Theoretical and experimental studies on PIBSA-based surfactants

By

Marina Mikhailovna van der Merwe

Submitted in partial fulfilment of the requirements of the degree

Philosophiae Doctor

In the Faculty of Natural and Agricultural Sciences

University of Pretoria

Supervisors: Professor Marilé Landman
Professor Petrus H. van Rooyen

June 2018

Pretoria

Dedicated to: Family and Friends

“The great obstacle to discoveries is not ignorance but the illusion of knowledge.”

Daniel J. Boorstin in*The Discoverers: A History of Man's Search to Know His World and Himself* (1983)

Declaration

I hereby declare that this dissertation, which I submit for the degree Philosophiae Doctor at the University of Pretoria, have not been submitted in whole or in part for consideration for any other degree or qualification in this, or any other university.

This dissertation is my own work, except where specific reference is made to the work of others as specified in the text and Acknowledgements.

Results obtained from this study have also been published in:
van der Merwe MM, Landman M, van Rooyen PH, Jordaan JHL, Otto DP (2017) Structural Assignment of Commercial Polyisobutylene Succinic Anhydride-based Surfactants. Journal of Surfactants and Detergents 20 (1):193-205.

Signature: 

Date: 20 June 2018

Presentations and posters

Molecular dynamics simulations of PIBSA-based surfactants at the supersaturated ionic interface of high internal phase emulsions (poster). CHPC 8th national meeting and conference, Skukuza, South Africa (2014).

Molecular dynamics simulations of a supersaturated salt solution (poster). ICTP water workshop, Trieste, Italy (2015).

Molecular Modelling of Additives for Highly Concentrated Emulsion Explosives (oral presentation). CHPC 9th national meeting and conference, Pretoria, South Africa (2015).

Empirical molecular modelling of the interactions of PIBSA-based surfactants with IV-$NH_4NO_{3(cr)}$ (poster). Australian Symposium on Computational Chemistry, Perth, Australia (2016).

Acknowledgements

Personal

I would like to thank my formal supervisors and long-time friends Prof Marilé Landman and Prof Petrus van Rooyen for your guidance and trust with this very challenging project; and informal supervisor and mentor - Dr Marc Meunier (Biovia) for training and continuous encouragement and support.

Special word of thanks to my friend – Stefan Coetzee, I often re-quote your words of wisdom, which helped me to get through this project; and my fellow students Roan, Lauren, Dominique and Ian for the cheerful chats and coffee breaks.

I would also like to thank my husband – Callie van der Merwe, for the immense moral and financial support during last 3 years of the study; and our children - Alexia and Vladislava for your faith and forgiveness! I could not have done this without you.

Official

Firstly, I would like to thank NRF for funding (Grant number 90216) and travel grant for attending Water workshop in Italy; and CHPC (SA) – for training and travel grants (Dr D. Moeketsi), use of National academic licence for Materials Studio and CHPC Tsessebe and Lengau clusters (Dr A. Lopis and Dr K. Govender).

Furthermore, I would like to thank Prof S. Scandolo, Dr A. Hassanali (ICTP, Italy) for electronic structure training, and discussions pertaining to simulations of ionic melts; Prof C. Vega (UCM, Spain) for discussions on nature of crystallization in HIPEs; Prof K. Range (LHUP, USA) for sharing unpublished research data on *ab-initio* modelling of aqueous Ammonium Nitrate; Dr R. Rausa (ENI S.p.A., Italy) for his valuable comments on published experimental work; and Prof J. Gale (Curtin University, Australia) for discussion on COMPASS parameterisation.

Finally, I would like to acknowledge BASF (SA) AEL and LAKE (SA) for providing samples of polymers and surfactants for experimental study; Dr Danie Otto and Dr Johan Jordaan (NWU, SA) for GPC and APCI-MS data acquisition; Dr Liezel van der Merwe (UP, SA) for assistance with DSC instrumentation; and Mr Eric Palmer for recording 2-D NMR spectra.

Summary

The polyisobutylene succinic anhydride (PIBSA) surfactants have been used for decades to attain kinetic stability in ammonium nitrate (AN) based emulsions. There are a number of studies concerned with the structure activity relationship and mechanism of surfactant rendered stability. However, the reported surfactant structures are inconsistent and a relation of structure to emulsion stability is yet to be established. This defined two main objectives of this thesis: to confirm the structure of PIBSA surfactants (the experimental study), and to establish a direct link between the structure and efficiency (the theoretical part).

Experimentally, based on the detailed analysis of the precursors and by chromatographic separation, the structure of the most effective surfactant in the series, the monoethanolamine (MEA) adduct of PIBSA (PIBSA-MEA), was resolved in this study. The proposed structure is consistent with the products of the classic Alder-ene thermal maleation step, followed by the regioselective ring fission of succinic anhydride. By analogy, structures were assigned to surfactants branded as PIBSA-IMIDE and PIBSA-UREA. Based on the nuclear magnetic resonance structural assignments, a novel *semi*-quantitative method was developed; and the estimated content of the surfactants, relative to the unreacted materials in the industrial concentrates, was found to be below 27 mole percent.

The theoretical study focused on the surfactant series with known efficacy: PIBSA-MEA, PIBSA-UREA, PIBSA-IMIDE and PIBSA-DEA. With practical application in mind, and based on our experimental results, model surfactants with a partly truncated side chain were used to study electronic structures with density functional theory (DFT), and to predict likely ionization states of the surfactants in the gas phase. The order of the calculated dipole moment, which was the highest in the amide-bearing surfactants (e.g. PIBSA-MEA and PIBSA-UREA), followed the experimental surface activity trend. Surface affinity of the untruncated surfactants with the simulated surfaces of aqueous ammonium nitrate, water, and growth faces of ammonium nitrate was then probed with Molecular Dynamics using condensed phase optimised Compass force-field. Surface adsorption energies were used to compare the efficacy. Discrimination between water and ammonium nitrate ions and the electrostatic interactions were found to be the key factors driving the values of the interaction energy within the surfactant-oxidizer system.

Abbreviations and symbols

General abbreviations	
1D and 2D	1- and 2-Dimensional (with reference to NMR)
Å	Angstrom
Anhydr.	Anhydrous
APCI	Atmospheric Pressure Chemical Ionization
ATR-FT-IR	Attenuated Total Reflection–Fourier Transform Infrared (spectroscopy)
b.l.	Bond length
b.o.	Bond order
B3LYP	Becke 3-Parameter (Exchange), Lee, Yang and Parr (correlation) functional
BFDH	Bravais-Friedel Donnay-Harker
c2p	Centre to plane distance (with reference to crystal)
ca.	Circa
Calc.	Calculated
CFF9X	Consistent Force-Field, X = 1, 3 or 5
Ch.	Charge
CMC	Critical Micelle Concentration
COMPASS(II)	Condensed-phase Optimized Molecular Potentials for Atomistic Simulation Studies (II stands for 2nd generation)
Coord.	Coordinates
COSY	Correlation Spectroscopy (2D-NMR experiment)
Da	Dalton
DEPTH	Distortionless Enhancement by Polarization Transfer (NMR experiment)
Der(s).	Derivative(s)
DFT	Density Functional Theory
d_{hkl}	Width of growth slice (with reference to crystal)
DNP	Double Numerical plus polarization (potential)
DPD	Dissipative Particle Dynamics
DSC	Differential Scanning Calorimetry
e.g.	For example
E_{ads}	Adsorption energy

E_{att}	Attachment energy
ESP	Electrostatic Potential
eV	Electron Volt
Exp.	Experimental
FF	Force Field
fs	Femtosecond
FT-IR	Fourier Transformed Infra-Red
GO	Geometry Optimisation
GPC	Gel Permeation Chromatography
Ha	Hartree
HB	Hydrogen Bond
HG	Head Group
HIP	High Internal Phase
HIPE	High Internal Phase Emulsion
HLB	Hydrophobic Lipophilic Balance
HMBC	Heteronuclear Multiple-Bond Correlation
HOMO	Highest Occupied Molecular Orbital
HPC	High Performance Computing
HSQC	Heteronuclear Single Quantum Correlation (2D-NMR experiment)
L	Litre
LJ	Lenard-Jones
LUMO	Lowest Unoccupied Molecular Orbital
MALLS	Multiple Angle Laser Light Scattering
Max.	Maximum
MD	Molecular Dynamics
MHz	Mega Hertz
mL	Millilitres
MM	Molecular Mechanics
Mn	Mean Molecular weight
NMR	Nuclear Magnetic Resonance
NOESY	Nuclear Overhauser Effect Spectroscopy (2D-NMR experiment)
PCFF	Polymer Consistent Force Field

PDI	Polydispersity Index
ppm	Parts per million
Prot.	Protonated
ps	Picoseconds
PXRD	X-ray Powder Diffraction
q	Coulomb (charge)
Qeq	Partial atomic charge by Rappe and Goddard's scheme
QM	Quantum Mechanics
RDF	Radial Distribution Function
Ref(s).	Reference(s)
SC	Super Cell
SCF	Self-Consistent Field
SPC	Single Point Charge (with reference to Water model)
SPC/E	Extended Simple Point Charge Model
Str.	Structure
TD	Thermal decomposition
TLC	Thin Layer Chromatography
vdW	van der Waals
w/o	Water-in-oil (with reference to emulsion)
wt %	Weight percentage
Acronyms of polymers and other chemical compounds	
AN	Ammonium Nitrate
DCM	Dichloromethane
EtoAc	Ethyl acetate
Hex.	Hexane
HR-PIB	Highly Reactive Polyisobutylene
IB	Isobutyl (repeat unit in polymers)
$[IB]_nSA$	$[Isobutyl]_{n=number\ of\ repeat\ units}$ Succinic anhydride
MAH	Maleic Anhydride
PIB	Polyisobutylene
PIBSA	Polyisobutylene succinic anhydride

PIBSA-*bis*-MEA	Polyisobutylenesuccin-*bis*-monoethanolamine
PIBSA-DEA	Polyisobutylenesuccin-diethanolamine
PIBSA-DEEA	Polyisobutylenesuccin-diethylethanolamine
PIBSA-IMIDE	Polyisobutylenesuccin-imide
PIBSA-MEA	Polyisobutylenesuccin-monoethanolamine
PIBSA-UREA	Polyisobutylenesuccin-urea
PIBSI	Polyisobutylenesuccin-imides
SA	Succinic anhydride
Succ.	Succinic
THF	Tetrahydrofuran
TMS	Trimethyl silane
W	Water
Subscripts used for designation of surfactant ionic form	
a	anionic
c	cationic
z	zwitterionic
Subscripts used for designation of physical state	
(aq)	aqueous
(cr)	crystalline
(g)	gaseous
(l)	liquid
(s)	solid

Table of contents

1 Introduction

Polyisobutylene succinic anhydride (PIBSA)-based surfactants (Scheme 1-1) are functionalized amphiphilic polymers and have been used by mining industries in explosive emulsion formulations since the late 1970's. Their high efficiency, low environmental impact and unique freezing properties render them suitable for a wide range of operating conditions [1-5]. Despite the attractive price point, the four decade-long market supremacy and unparalleled performance of currently available PIBSA-based surfactants, all leading manufactures continue to search for better performing additives, seeking product improvement and competitive advantages.

Experimental screening of novel emulsion additives is time-consuming and results in large amounts of chemical waste. For example, a typical pilot scale explosive emulsion sample for rheological and stability studies is prepared on several hundred grams scale and monitored daily for periods of time lasting several months [6-8]. Furthermore, studies of microstructure and interfacial interactions often rely on analytical methods, which are based on differentiation between specific isotopic forms, and require specialized synthesis and purification of test materials [9,10]. Despite the availability of advanced analytical techniques, the assignments of specific interactions between similar functional groups (in structure or size) still lack clarity and often are conjectural. For example, in X-ray diffraction studies of ammonium nitrate solutions (explosive emulsion oxidiser phase), the ammonium ion and water were reported indistinguishable due to their structural arrangement [9]; similarly, several overlapping areas for various emulsion components' key infrared vibrational frequencies (water, oxidizer phase, fuel oil and PIBSA surfactants) proved difficult in the assignment of specific cross-component interactions [11-14].

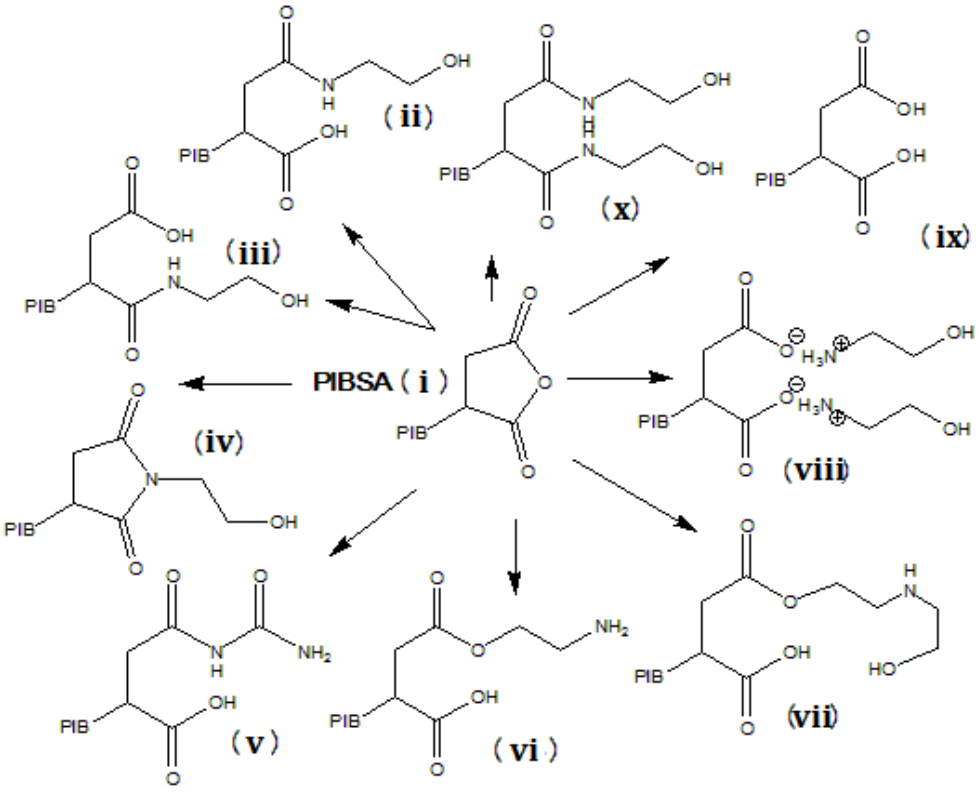

Scheme 1-1: PIBSA (i), PIBSA-derived surfactants (anti-clockwise i, ii, vi - isomers of PIBSA-MEA; iv - PIBSA-IMIDE; v - PIBSA-UREA; vii - PIBSA-DEA; x - PIBSA-bis-MEA) and some by-products (viii - PIBSA-MEA salt; ix - PIB-Succinic acid)

Alternative to traditional laboratory tests, simulation models can be used to predict the physicochemical properties and microstructure of the multicomponent systems, where experimental data is unavailable, inaccessible or ambiguous. With recent advances in High Performance Computing (HPC), the availability of parallelized computing codes and data submission pipelines, high throughput screening of novel ingredients with simulation models has become a routine practice [15,16]. Whilst the majority of useful findings concerning novel additives are proprietary, many advances in characterization and rheological aspects of micro-emulsions have been published [17-20]. However, successful cases of quantitative and qualitative simulation of surfactants and interfacial phenomena in highly concentrated emulsion explosive mixtures are lacking.

1.1 Chemical structure of PIBSA-based surfactants

PIBSA-based surfactants are produced by the nucleophilic substitution of the succinic ring in PIBSA, with an average molecular weight (*Mn*) of 950-1100 g mol^{-1} for the PIB side chain [1,2,21]. It was previously reported that two carbonyl groups of the anhydride are near-equivalent, and product mixtures of equal isomers, with PIB attached to the α-position from either of the two carbonyl groups, are obtained during substitution reactions [1,21,22]. In case of substitution with *bi*-functional amines (ethanolamine), in addition to some PIBSA hydrolysis products and their adducts, succinic esters are common by-products (**vi**, **viii** and **ix**, Scheme 1-1) in a slightly acidic reaction environment [1,3,21,23].

Some of the characteristic data (size, conformation of side chain and infrared frequencies) and efficacy trends for several PIBSA-based surfactants have been reported in literature [4,10,12,14,21,22,24,25]. However, there is large discrepancy in the structures of these surfactants, which differ in the structure of the link between PIB and the succinic anhydride ring, the number of isobutylene [IB] units in the PIB side chain and the relative position of the side chain as well as the -NH-R substituent (structures **ii** and **iii** Scheme 1-1; Scheme 1-2). It is generally accepted that products based on PIBs with an average molecular weight (*Mn*) of 1000 g $mole^{-1}$ are preferred in explosive emulsion formulations for their viscosity characteristics. Some ambiguity also exists in uses of generic names of the surfactant products. For example, Ganguly used a Lubrizol product, dubbed as 'LZX', and described it as the ester/salt product (*Mn* = 2500 g mol^{-1}) of the reaction of PIBSA with 2 moles of diethyl ethanolamine, with reference to explosive formulations and Lubrizol's patent by Forsberg [3,12]. The same product was described as a *bis*-MEA adduct (structure **x**, Scheme 1-1) by Kovalenko, with reference to the same patent by Lubrizol [26].

Generally, PIBSA-based surfactants are produced in a stepwise reaction starting with converting PIB to PIBSA, and then to PIBSA-derivatives. PIBSAs are produced by the thermal reaction of high-olefin content PIB (HR-PIB) and maleic anhydride, using a process patented in 1936 [27-30]. Alternatively, low-olefin content PIB, known as the 'conventional PIB', can be used in combination with chlorine to achieve lower anhydride yields, which is accompanied with the conventional PIB inherent variety of chain branching. From the price differential incentive, both types of PIB and PIBSA are utilized by industry [31]. In a

comprehensive synthetic study on the preparation of PIBSA from HR-PIB, NMR analysis of the products reported only 27 wt% yield in laboratory conditions, which will most likely be further reduced during scale up and in follow-up reactions of PIBSA derivatisation [32,33]. Apart from partial infrared data [12,21,25], no other spectroscopic data has been reported for the PIBSA-based surfactants shown in Scheme 1-1.

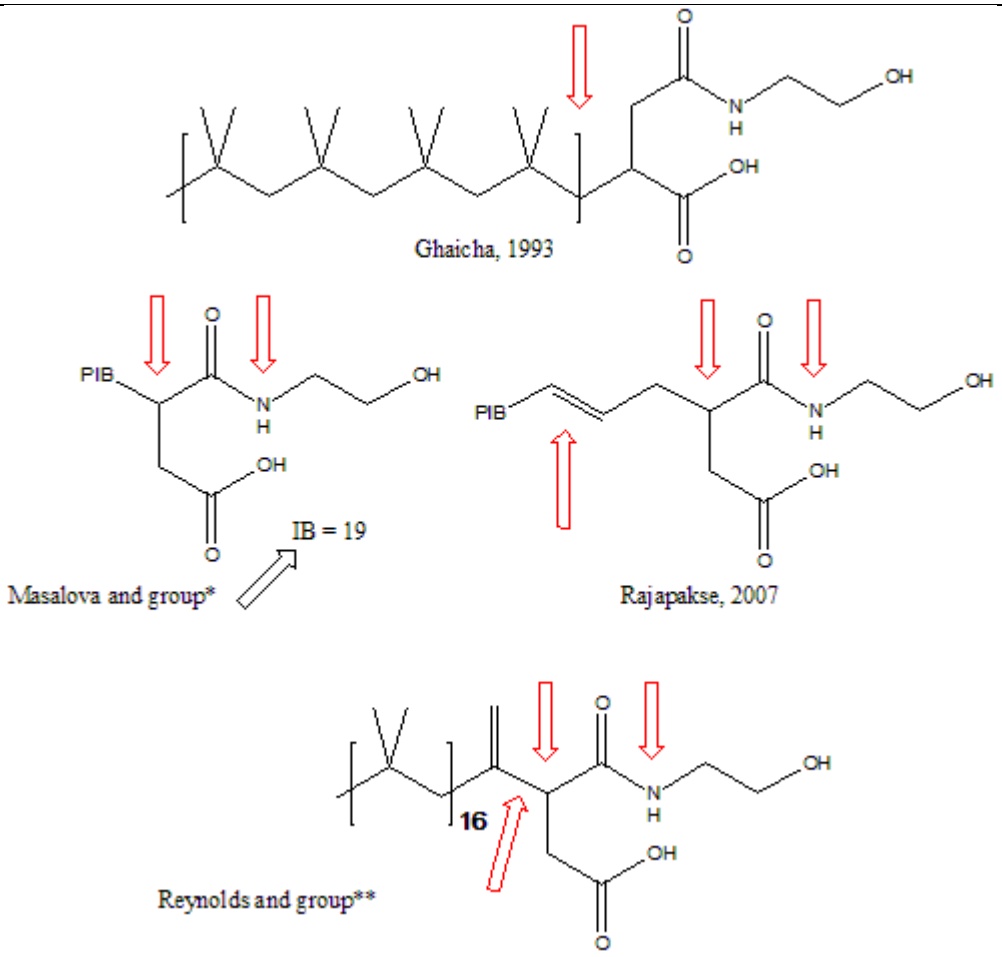

*Scheme 1-2: Structures of PIBSA-MEA reported by various researchers. [IB] - isobutylene repeat units; *[14]; **[34].*

The products in the thermal amination reaction of PIBSA are strongly dependant on temperature, pH, atmosphere, and method of combining reactants. In the presence of water, at atmospheric conditions and in the temperature range of 110-120 °C, the products are salt derivatives (structure **viii**; Scheme 1-1). In an anhydrous environment, under basic pH condition at elevated temperatures (*ca.* 140-160 °C) in an inert atmosphere, the products

are mainly PIBSA-amide derivatives (structures **ii**, **iii**, **iv**, **v** and **x**; Scheme 1-1). In an anhydrous, slightly acidic environment, ester/salt derivatives are produced [3]. Considering that the synthesis of PIBSA-surfactants is typically a 'one-pot reaction', the amount and the end-structure of the functionalized or active surfactant present in the industrial samples are questionable.

The source of PIB, used in the production of PIBSA and PIBSA-derived surfactants, is not always stated by the researchers and industry; and there seem to be general lack of concern with the underlying structural differences. Presence of unreacted PIBs, solvents, hydrocarbon oils and surfactant by-products in industrial concentrates would need to be considered in calculations of concentration-dependant properties of surfactants. These calculations are often based on the surfactant molar concentration, which, considering all the factors above, appears to be somewhat ambiguous. This is clearly seen from several studies by Masalova group, which utilised the same source of industrial concentrates of PIBSA-MEA and reported surfactant-specific properties e.g. the critical micelle concentration (CMC) with variability of 44-67 % (4.5×10^{-5} - 13.6×10^{-5}), as estimated from plots using surface tension methods [14,35,36].

Several analytical methods have been employed for an approximate estimation of active surfactant concentration, *i.e.* potentiometric titration, the Walch method (IR-based) and adaptations thereof [29,37]. These methods can not differentiate between active surfactant, by-products and hydrolysis products. A more accurate method of analysis of the industrial blends would be advantageous in studies of this class of surfactants. In this study we will aim to find a reliable technique to determine the concentration of active surfactant in the industrial surfactant blends unambiguously.

1.2 Role of surfactants in emulsion stability

Kinetic stability of High Internal Phase (HIP) explosive emulsions, which are inherently thermodynamically unstable, can be achieved by the use of surfactants and surfactant blends. These water-in-oil (w/o) emulsions typically consist of the oxidizer phase (*i.e.* ammonium nitrate salt) dispersed as micrometre-size droplets in the continuous phase (fuel oil), and where the content of the dispersed phase exceeds 80% of the total composition by

volume. The emulsion is produced by high-speed shear mixing of the two phases, resulting in formation of at least three kinds of interfaces: salt droplets, oil film and air bubbles. Surfactants are typically blended with the oil phase, and upon the emulsification and droplet refinement, they form micellar aggregates in the oil phase and monolayers at the aqueous droplet interface (Figure 1-1). Both of these microstructural elements are critical for the emulsion stability and shelf life [38]. Stability of emulsions is believed to be achieved through the following mechanisms [17,18]:

- Initial droplet refinement and prevention of droplet coalescence by shielding of two immiscible liquids or screening of unfavourable interactions by surfactant adsorbed at the droplet interface (mechanical barrier and reduction of surface tension) [18];
- Stabilisation of the aqueous droplets by a steric effect, rendered by surfactant aggregated into micelles, which suppresses the capillary waves at the droplet surface [38];
- Retardation of crystallization of supersaturated dispersed phase [40] (the mechanism of such stabilization is not understood);
- Depression of emulsion freezing point (irreversible, concentration dependent, not due to viscosity effects; and the mechanism is said to be surfactant dependant and is not yet understood) [12].

The choice of surfactant for emulsion stability is usually based on various criteria. Traditional approaches to the design of surfactants rely on multistep synthetic experiments, characterization and evaluation of performance by studying various physicochemical characteristics within the emulsion matrix. This is a very resource- and time-consuming as well as capital-intensive process. Previously reported comparative surfactant performance with respect to explosive emulsion stability can be summarized as follows:

- PIBSA-*bis*-MEA (**x**) > PIBSA-MEA (**i** and/or **iii**) [5];
- PIBSA-MEA (**ii** and/or **iii**) > PIBSA-DEA (**vii**) [21];
- PIBSA-UREA (**v**) > PIBSA-MEA (**ii** and/or **iii**) [4];
- PIBSA-MEA (**i** or **iii**) > PIBSA-UREA (**v**) > PIBSA-IMIDE (**iv**) [14,41-43].

Fresh HIP emulsion	*Aged HIP emulsion*

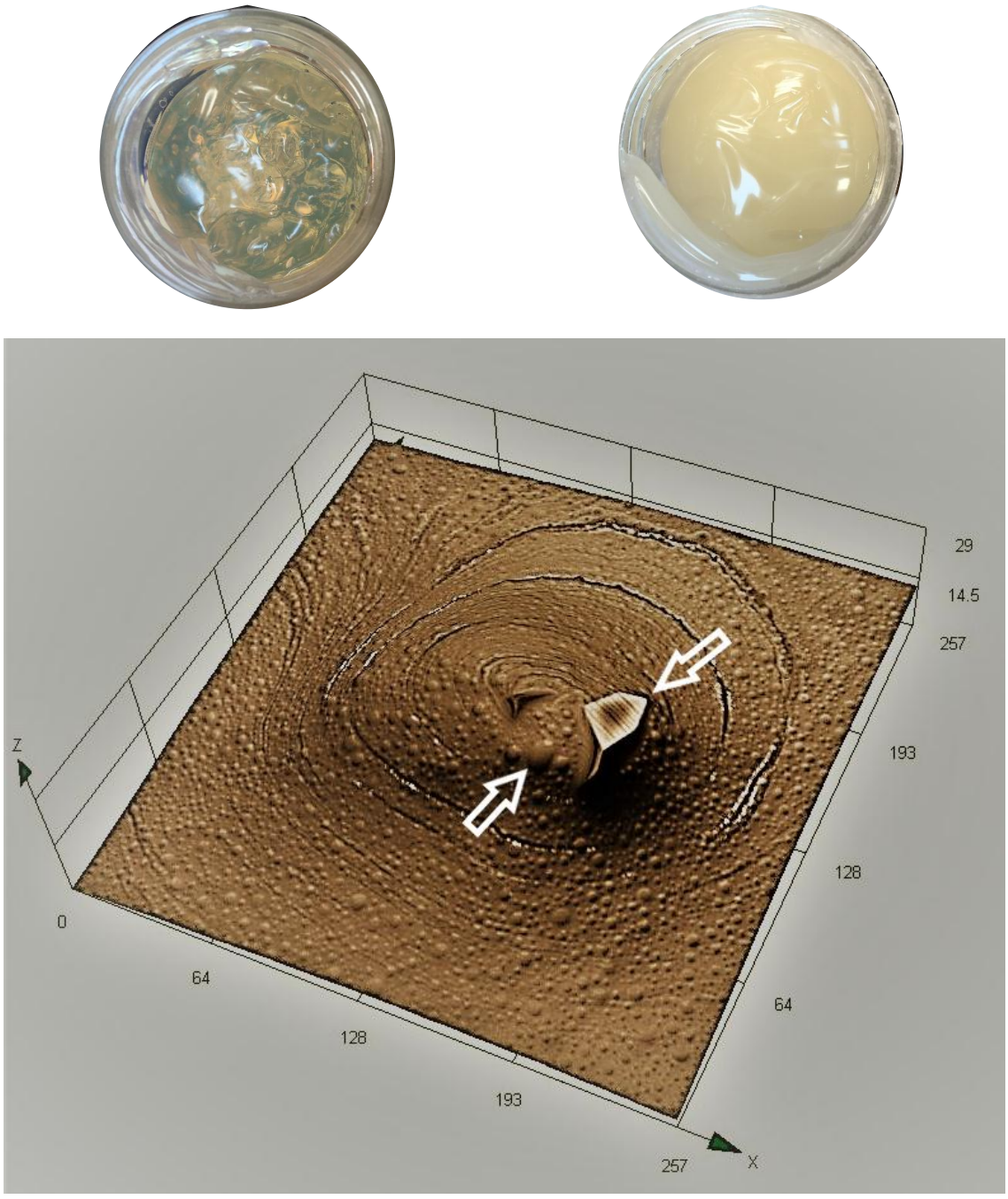

Figure 1-1: Photographic (above) images of fresh and aged HIPEs [39]. Polydispersity and spherical shapes of the droplets are clearly visible in the micrograph of the aged emulsion (below). White arrows point towards emerging oxidizer phase crystal in the centre of the image, and towards a coalesced emulsion droplet (bottom left).

The exact mechanism of emulsion stabilization and superior performance of some surfactants in the PIBSA-based surfactant class is still not completely understood**.** No firm scientific evidence to substantiate vast differences in the stability rendered by the series: PIBSA-MEA >> PISA-UREA >> PIBSA-IMIDE has been reported to date. This is mainly due to limitations of available analytical techniques in distinguishing between the similar functional groups in surfactant and salt ions, as well as water and the ammonium ion in the dispersed phase [9,44]. Further complications arise from complex ionization patterns of surfactant functional groups, pH factor-determined speciation of the emulsion matrix, the structural integrity of different surfactants [21] and analytical instrument operating conditions [22]. Some experimental studies of PIBSA-based and other surfactants with water and with concentrated ammonium nitrate (AN) solutions, suggested that strong surfactant:ammonium nitrate interactions, of either Coulombic or van der Waals nature, are likely to result in more stable emulsions [12,21,45-47]. Furthermore, fluorescence microscopy studies on the crystallization of ammonium nitrate and the interfacial phenomena of several surfactant systems suggested that the nucleation rate, crystallization and growth pattern at aqueous electrolyte interfaces are surfactant head group specific [48], pointing at a direct interactions of the surfactant head group with the salt. To some degree, the initial crystal growth retardation was also attributed to the surfactant.

Another point of importance is the relative interaction of surfactant head groups and water. Reynolds reported that in the emulsions formed with water/oil/PIBSA-surfactant, there was only 5 wt% surfactant adsorbed at the water-oil interface, and upon addition of salt to the water phase, surface loading was tripled (12-16 wt%) [22]. Another study on sulfonated surfactants used in the rapid removal of water to aid in the crystallization of ammonium nitrate prill, pointed that affinity of effective dehydrating agents to water was much higher than to salt [49]. This means that affinity of these surfactants to salt is higher than their affinity to water. On the other hand, the reversed difference in affinity may be used for dehydration, like in case of sulfonated surfactants, which are used for rapid removal of water and aid crystallization of ammonium nitrate prill. This class of dehydrating surfactants has much higher affinity to water than to ammonium nitrate salt. This difference in affinity

of certain surfactants to water and to salt could be accessed in a computational study and used as discriminating factor in the surfactant selection process.

Overall, gaining a better understanding of the mechanism and extent (strength) of surfactant functional groups engagement with the oxidiser phase could assist in the development of selection criteria for the novel surfactant candidates, based on the key head group interactions and geometric requirements to the relative position of such functional groups.

1.3 Molecular modelling

Theoretical prediction of the surfactant structure, properties, efficiency and aggregation can be achieved through the application of multi-scale molecular modelling tools [50,51]. Several successful multi-scale studies on engine oil additives, which are a different class of PIBSA-based dispersants (PIBSI), have been reported [52,53]. It was possible to predict aggregation properties of the highly complex oil deposits and model efficacy of deposit scrambling additives.

In addition to the structural ambiguity, PIBSA surfactants can exist in a number of ionisation forms, which were not previously characterised. In particular, the ionization of amide/urea adducts is not straightforward and the exact interactions of these head groups with aqueous salt could not be derived experimentally due analytical limitations. [21]. Using electronic structure methods, it would be insightful to calculate electron density distribution (partial atomic charges) and electrostatic potential maps for neutral and ionised forms of PIBSA surfactants and compare computed molecular vibrations with the reported experimental data (Raman and FT-IR fingerprints) [12]. To the best of our knowledge, no computation studies of PIBSA-derivatives, used in explosive emulsions, have been reported to date.

Besides the multiple interfaces, which exist in explosive emulsions, there are two types of aggregates within the emulsion matrix – droplets and reversed micelles (Figure 1-2). It was found that in the aged emulsions there was an overall depletion of surfactant loading at the droplet interface and in the number of the reverse micelles in the oil phase [22]. This was

attributed to a chemical change in the surfactant due to hydrolysis. The effects of the hydrolysis products on emulsion stability and crystallisation have not been evaluated in the past, apart from the reported tendency of the PIB-succinic acid to form insoluble salts with divalent ions (*e.g.* Ca^{2+}), which destabilise the emulsion.

Modelling interactions in such complex materials could require different levels of theory; from quantum mechanics to address electronic structure, to mesoscale calculations of the physicochemical properties of the micrometre-size aggregates and aggregation behaviour such as droplet coalescence (Figure 1-2) [16]. Whilst the self-assembly of surfactants and associated properties, such as interfacial tension and critical micelle concentration, can be accessed computationally, chemical details of the surfactants and their ionisation forms, which can be derived from electronic structure methods, are essential for mesoscale studies [54-56].

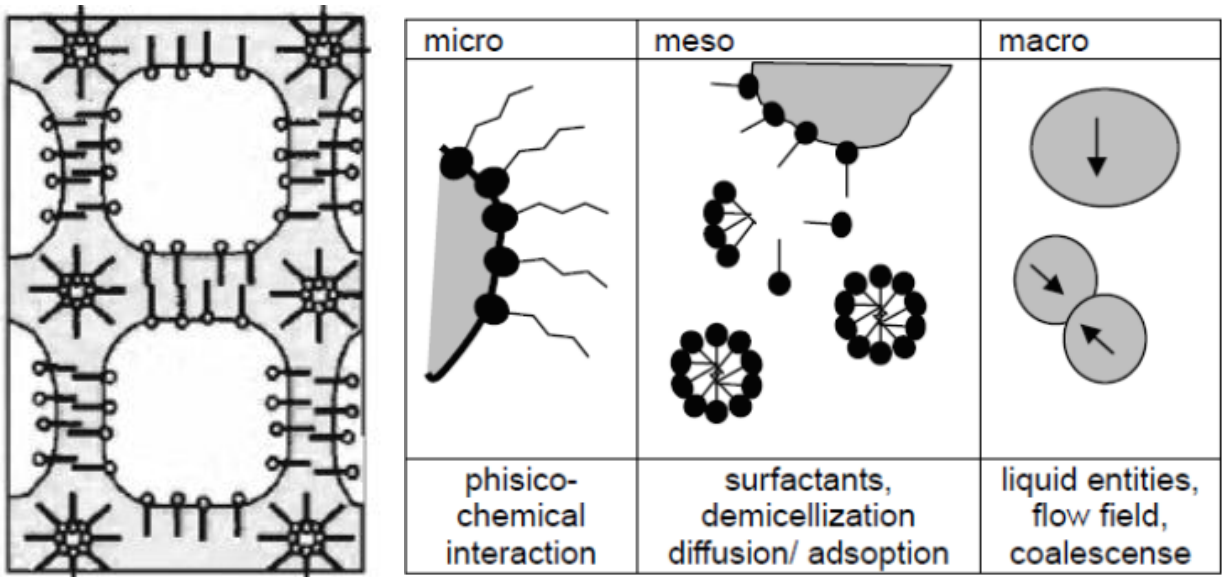

Figure 1-2: Reverse HIP emulsion droplets with adsorbed surfactant and reverse micelles (left), from Babak [18]; scales for molecular simulation of emulsions (right), from Krause [57].

The length scale amongst various explosive emulsion components is vastly different, and somewhat prohibitive for *ab initio* electronic structure methods, which can comfortably handle up to 100 atoms at a time. Considering the length scale of surfactants (300 atoms), fuel oil (20-50 atoms) and salt ions (up to 5 atoms), molecular modelling methods on atomic

rather than electronic scale seems more plausible. Such methods ignore electron-electron interactions and are known as classical methods, which are reliant on empirical potentials to describe bonding and non-bonding interactions between atoms. Some of the abovementioned methods are summarised below:

Quantum mechanics (QM), also known as *ab initio* (from first principles) level, is aimed at simulation of the electronic structure and reactivity of molecular or small cluster systems limited to a few hundred atoms [50,58,59]. Predicting the behaviour of large molecules in a condensed phase, such as interactions of surfactants with an emulsion matrix, with high-level *ab initio* calculations (accounting for electron correlation effect), is limited to small clusters (mainly to "two-body" interactions), due to the overall system size. Even with sufficient level of theory such calculations are inept at capturing polarization, which is an inherent property of "many-body" interactions, and which are important in condensed phases [60].

Molecular Mechanics (MM) remains a modelling method of choice on microscale level, applicable to large chemically versatile mixtures due to its atomistic resolution and relatively low computational cost [61-66]. The performance of the MM methods is highly reliant on the availability of accurate and reproducible force-fields (FF). The key feature of the FF for atomistic simulations is the ability to predict properties of mixtures without use of adjustable parameters for the unlike pair interactions over a range of operating temperatures and pressures [67]. One of the most advanced condense phase optimised force-fields used for modelling of energetic materials and with extended coverage of polymers, is Compass, which is available through the licenced materials modelling package Materials Studio™ (BIOVIA) [60,68-70].

Mesoscale modelling, also known as Dissipative Particle Dynamics (DPD), is a particularly useful tool, aimed at simulation of physical and chemical phenomena of complex mixtures at the length scales in the range 10 nm-100 μm [54,66,71-74]. This is applicable to polymer adsorption, polymer-surfactant interaction, phase separation, breakup and coalescence of droplets in the emulsion during processing and storage, crystal/nanoparticle growth and nucleation, bilayer stability and rapture, *etc.* [55,75-78]. However, for multifunctional molecules such as PIBSA derivatives, the basis of the DPD method, *i.e.* the

simplification of the system to a representation with fewer interaction sites, is not straightforward. Validation derived from a more detailed approach, resolving atom-atom interactions, is required.

1.4 Aims

The general selection process of novel surfactants (screening process) for improving the stability of explosive emulsions can benefit from a computational model and selection criteria, which is currently lacking. On the basis of our literature survey, the following questions should be answered:

- What is the structure and content; and what are the most likely ionization forms, of PIBSA-based surfactants used in explosive emulsion technology?
- What is the difference in surfactant rendered surface activity and subsequently, what is the mechanism of surface stabilization?
- What are the criteria to prioritise the selection of novel surfactants?
- To eliminate the identified knowledge gaps, the following aims of this study were set.

Experimentally, using separation and analytical methods:

i. Perform purification and structural characterisation of selected surfactants: PIBSA-MEA, PIBSA-UREA and PIBSA-IMIDE;
ii. Determine the concentration of active surfactant in the industrial surfactant blends.

Theoretically, through computer-based simulations:

iii. Characterise the electronic structure of surfactants *via* molecular modelling methods;
iv. Compare the calculated electronic structure of model surfactants with experimental data;
v. Using simulations, elucidate the mechanism of surface stabilization rendered by the series PIBSA-MEA, PIBSA-UREA, PIBSA-IMIDE and PIBSA-DEA and the effect of the surfactant head groups on different components of the ammonium nitrate based explosive emulsions.
vi. Develop a computational framework for the screening of surfactant additives for efficacy in stabilising explosive emulsions, and identify initial criteria for the selection of candidates.

1.5 References

1. Chattopadhyay AK (1990) Water-in-oil emulsion explosive. US Patent 4,919,179.

2. Chattopadhyay AK (1996) Emulsion explosive. US Patent 5,500,062.

3. Forsberg JW (1987) Water-in-oil emulsions. US Patent 4,844,756.

4. Boer WG (2003) Composition and emulsifier. US Patent 6,630,596.

5. McKenzie LF, Lawrence LD (1990) Emulsion explosives containing a polymeric emulsifier. US Patent 4,931,110.

6. Ferg EE, Simpson B (2013) Using PXRD and PONKCS to Determine the Kinetics of Crystallisation of Highly Concentrated NH4NO3 Emulsions. Journal of Chemical Crystallography 43 (4):197-206.

7. Masalova I, Malkin AY, Ferg E, Kharatiyan E, Taylor M, Haldenwang R (2006) Evolution of rheological properties of highly concentrated emulsions with aging —Emulsion-to-suspension transition. Journal of Rheology 50 (4):435-451.

8. Zahirovic S (2007) Interfacial tension study and rheological characterisation of water-in-oil emulsion explosives. PhD Thesis, The University of Melbourne.

9. Adya AK, Neilson GW (1991) Structure of a 50 mol kg-1 aqueous solution of ammonium nitrate at 373 K by the isotopic difference method of neutron diffraction. Journal of the Chemical Society, Faraday Transactions 87 (2):279-286.

10. Reynolds PA, McGillivray DJ, Gilbert EP, Holt SA, Henderson MJ, White JW (2002) Neutron and X-ray Reflectivity from Polyisobutylene-Based Amphiphiles at the Air–Water Interface. Langmuir 19 (3):752-761.

11. Wu HB, Chan MN, Chan CK (2007) FTIR Characterization of Polymorphic Transformation of Ammonium Nitrate. Aerosol Science and Technology 41 (6):581-588.

12. Ganguly S, Mohan VK, Bhasu VCJ, Mathews E, Adiseshaiah KS, Kumar AS (1992) Surfactant-electrolyte interactions in concentrated water-in-oil emulsions: FT-IR spectroscopic and low-temperature differential scanning calorimetric studies. Colloids and Surfaces 65 (4):243-256.

13. Al-Abadleh HA, Grassian VH (2003) FT-IR Study of Water Adsorption on Aluminum Oxide Surfaces. Langmuir 19 (2):341-347.

14. Masalova I, Kovalchuk K, Malkin AY (2011) IR Studies of Interfacial Interaction of the Succinic Surfactants with Different Head Groups in Highly Concentrated W/O Emulsions. Journal of Dispersion Science and Technology 32 (11):1547-1555.
15. Satyanarayana KC, Abildskov J, Gani R, Tsolou G, Mavrantzas VG (2010) Computer aided polymer design using multi-scale modelling. Brazilian Journal of Chemical Engineering 27:369-380.
16. Creton B, Nieto-Draghi C, Pannacci N (2012) Prediction of Surfactants' Properties using Multiscale Molecular Modeling Tools: A Review. Oil Gas Sci Technol – Rev IFP Energies nouvelles 67 (6):969-982.
17. Babak VG, Stébé M-J (2002) Highly Concentrated Emulsions: Physicochemical Principles of Formulation. Journal of Dispersion Science and Technology 23 (1-3):1-22.
18. Babak VG (2008) Highly concentrated emulsions. Physicochemical principles of the preparation and stability. Russian Chemical Reviews 77 (8):683-708.
19. Derkach SR (2009) Rheology of emulsions. Advances in Colloid and Interface Science 151 (1–2):1-23.
20. Yaron PN, Reynolds PA, McGillivray DJ, Mata JP, White JW (2010) Nano- and Microstructure of High-Internal Phase Emulsions Under Shear. The Journal of Physical Chemistry B 114 (10):3500-3509.
21. Ghaicha L, Leblanc RM, Chattopadhyay AK (1993) Influence of concentrated ammonium nitrate solution on monolayers of some dicarboxylic acid derivatives at the air/water interface. Langmuir 9 (1):288-293.
22. Reynolds PA, Gilbert EP, White JW (2001) High Internal Phase Water-in-Oil Emulsions and Related Microemulsions Studied by Small Angle Neutron Scattering. 2. The Distribution of Surfactant. The Journal of Physical Chemistry B 105 (29):6925-6932.
23. Scheiman M (1962) A review of monoethanolamine chemistry. Naval Research Lab Washington DC
24. Yakhoub HA, Masalova I, Haldenwang R (2010) Highly concentrated emulsions: Role of droplet size. Chemical Engineering Communications 198 (2):147-171.
25. Rajapakse A (2007) Drop size distributions and interfacial area in reactive liquid-liquid dispersions. PhD Thesis, RMIT Australia.

26. Kovalenko I, Kuprin V (2016) Emulsifier development for high-concentrated reverse emulsions. Праці Одеського політехнічного університету (1):72-80.
27. Tessier M, Maréchal E (1984) Synthesis of mono and difunctional oligoisobutylenes - III. Modification of α-chlorooligoisobutylene by reaction with maleic anhydride. European Polymer Journal 20 (3):269-280.
28. Walch E, Gaymans RJ (1994) Telechelic polyisobutylene with unsaturated end groups and with anhydride end groups. Polymer 35 (8):1774-1778.
29. Walch E, Gaymans RJ (1993) Synthesis of low-molecular-weight telechelic polyisobutylene. Polymer 34 (2):412-417.
30. Kennedy JP (1991) New functional polymers, blocks and thermoplastic elastomers by living carbocationic polymerization. Makromolekulare Chemie Macromolecular Symposia 51 (1):169-174.
31. Rivera-Tirado E, Aaserud DJ, Wesdemiotis C (2012) Characterization of polyisobutylene succinic anhydride chemistries using mass spectrometry. Journal of Applied Polymer Science 124 (4):2682-2690.
32. Balzano F, Pucci A, Rausa R, Uccello-Barretta G (2012) Alder-ene addition of maleic anhydride to polyisobutene: nuclear magnetic resonance evidence for an unconventional mechanism. Polymer International 61 (8):1256-1262.
33. Pucci A, Barsocchi C, Rausa R, D'Elia L, Ciardelli F (2005) Alder ene functionalization of polyisobutene oligomer and styrene-butadiene-styrene triblock copolymer. Polymer 46 (5):1497-1505.
34. Reynolds PA, Gilbert EP, White JW (2000) High Internal Phase Water-in-Oil Emulsions Studied by Small-Angle Neutron Scattering. The Journal of Physical Chemistry B 104 (30):7012-7022.
35. Kovalchuk K, Masalova I, Malkin AY (2010) Influence of electrolyte on interfacial and rheological properties and shear stability of highly concentrated W/O emulsions. Colloid J 72 (6):806-814.
36. Sanatkaran N, Masalova I, Malkin AY (2014) Effect of surfactant on interfacial film and stability of highly concentrated emulsions stabilized by various binary surfactant mixtures. Colloids and Surfaces A: Physicochemical and Engineering Aspects 461 (0):85-91.

37. Shen Y, Duhamel J (2008) Micellization and Adsorption of a Series of Succinimide Dispersants. Langmuir 24 (19):10665-10673.
38. Reynolds PA, McGillivray DJ, Mata JP, Yaron PN, White JW (2010) The stability of high internal phase emulsions at low surfactant concentration studied by small angle neutron scattering. Journal of Colloid and Interface Science 349 (2):544-553.
39. van der Merwe MM, Landman M (2015) Microscopic studies of high internal phase emulsions. University of Pretoria.
40. Malkin A, Masalova I (2007) A new mechanism of aging of highly concentrated emulsions: Correlation between crystallization and plasticity. Colloid J 69 (2):198-202.
41. Kovalchuk K, Masalova I (2012) Factors influencing the crystallisation of highly concentrated water-in-oil emulsions: A DSC study. South African Journal of Science 108 (3/4):01-05.
42. Masalova I, Foudazi R, Malkin AY (2011) The rheology of highly concentrated emulsions stabilized with different surfactants. Colloids and Surfaces A: Physicochemical and Engineering Aspects 375 (1–3):76-86.
43. Mudeme S, Masalova I, Haldenwang R (2010) Kinetics of emulsification and rheological properties of highly concentrated explosive emulsions. Chemical Engineering and Processing: Process Intensification 49 (5):468-475.
44. Adya AK, Neilson GW (1990) The structure of molten ammonium nitrate by isotopic difference method of neutron diffraction. Molecular Physics 69 (4):747-765.
45. Chattopadhyay AK, Ghaicha L, Oh SG, Shah DO (1992) Salt effects on monolayers and their contribution to surface viscosity. The Journal of Physical Chemistry 96 (15):6509-6513.
46. Chattopadhyay AK, Shah DO, Ghaicha L (1992) Double-tailed surfactants and their chain length compatibility in water-in-oil emulsions. Langmuir 8 (1):27-30.
47. Ghaicha L, Chattopadhyay AK, Tajmir-Riahi HA (1991) Behavior of stearic acid monolayers in presence of concentrated ammonium nitrate solution substrate. Langmuir 7 (10):2007-2009.
48. Yubai B, Munger G, Leblanc RM, Ghaicha L, Chattopadhyay AK (1996) Crystallization of Ammonium Nitrate under organized monolayers of various amphiphiles Journal of Dispersion Science and Technology 17 (4):391-405.

49. Chattopadhyay AK (2002) Effect of Polymeric Surfactants on the Behavior of Polycrystalline Materials with Special Reference to Ammonium Nitrate. In: Adsorption and Aggregation of Surfactants in Solution. Surfactant Science. CRC Press, pp 655-674.
50. Meunier M (2016) Industrial Applications of Molecular Simulations. CRC Press, Boca Raton.
51. Scocchi G, Posocco P, Fermeglia M, Pricl S (2007) Polymer−Clay Nanocomposites: A Multiscale Molecular Modeling Approach. The Journal of Physical Chemistry B 111 (9):2143-2151.
52. Mosey NJ, Muser MH, Woo TK (2005) Molecular mechanisms for the functionality of lubricant additives. Science 307 (5715):1612-1615.
53. Frigerio F, Rausa R (2008) Molecular modelling of additives for lubricants. Scienomics.
54. Groot RD (2000) Mesoscopic Simulation of Polymer-Surfactant Aggregation. Langmuir (16):7493-7502.
55. Groot RD (2003) Electrostatic interactions in dissipative particle dynamics-simulation of polyelectrolites and anionic surfactants. Journal of Chemical Physics 118 (24):11265-11277.
56. Groot RD, Warren PB (1997) Dissipative particle dynamics: Bridging the gap between atomistic and mesoscopic simulation. The Journal of Chemical Physics 107 (11):4423-4435.
57. Krause F, Li X, Fritsching U (2011) Simulation of Droplet-Formation and -Interaction in Emulsification Processes. Engineering Applications of Computational Fluid Mechanics 5 (3):406-415.
58. Hutter J, Iannuzzi M, Schiffmann F, VandeVondele J (2014) cp2k: atomistic simulations of condensed matter systems. Wiley Interdisciplinary Reviews: Computational Molecular Science 4 (1):15-25.
59. Sholl DS, Steckel JA (2009) Density Functional Theory: A Practical Introduction. 1st edn. Wiley.
60. Sun H (1998) COMPASS: An ab Initio Force-Field Optimized for Condensed-Phase ApplicationsOverview with Details on Alkane and Benzene Compounds. The Journal of Physical Chemistry B 102 (38):7338-7364.
61. Shen F, Lv P, Sun C, Zhang R, Pang S (2014) The crystal structure and morphology of 2,4,6,8,10,12-hexanitro-2,4,6,8,10,12-hexaazaisowurtzitane (CL-20) p-xylene solvate: a

joint experimental and simulation study. Molecules (Basel, Switzerland) 19 (11):18574-18589.
62. Mikami Y, Liang Y, Matsuoka T, Boek ES (2013) Molecular Dynamics Simulations of Asphaltenes at the Oil–Water Interface: From Nanoaggregation to Thin-Film Formation. Energy & Fuels 27 (4):1838-1845.
63. López-Chávez E, Pacheco-Sánchez JH, Martínez-Magadán JM, Castillo-Alvarado FdL, Soto-Figueroa C, García-Cruz I (2007) Methodology for Predicting the Phase Envelope of a Heavy Crude Oil and Its Asphaltene Deposition Onset. Petroleum Science and Technology 25 (1-2):19-39.
64. Sammalkorpi M, Karttunen M, Haataja M (2007) Structural Properties of Ionic Detergent Aggregates: A Large-Scale Molecular Dynamics Study of Sodium Dodecyl Sulfate. The Journal of Physical Chemistry B 111 (40):11722-11733.
65. Frigerio F (2010) Computer modeling and simulation of the nanoaggregation and solubility of crude oil asphaltenes. W Trans on Comp 9 (9):919-928.
66. Boek ES, Jusufi A, Löwen H, Maitland GC (2002) Molecular design of responsive fluids: molecular dynamics studies of viscoelastic surfactant solutions. Journal of Physics: Condensed Matter 14 (40):9413-9430.
67. Panagiotopoulos AZ (2001) Force Field Development for Simulations of Condensed Phases. AIChE symposium series, vol 325. American Institute of Chemical Engineers New York, N.Y.
68. Bunte SW, Sun H (2000) Molecular Modeling of Energetic Materials: The Parameterization and Validation of Nitrate Esters in the COMPASS Force Field. The Journal of Physical Chemistry B 104 (11):2477-2489.
69. Sun H, Jin Z, Yang C, Akkermans RLC, Robertson SH, Spenley NA, Miller S, Todd SM (2016) COMPASS II: extended coverage for polymer and drug-like molecule databases. Journal of Molecular Modeling 22 (2):47.
70. Sun N, Walz JY (2001) A Model for Calculating Electrostatic Interactions between Colloidal Particles of Arbitrary Surface Topology. Journal of Colloid and Interface Science 234 (1):90-105.

71. Boek ES, Coveney PV, Lekkerkerker HNW, van der Schoot P (1997) Simulating the rheology of dense colloidal suspensions using dissipative particle dynamics. Physical Review E 55 (3):3124-3133.
72. Fraaije JG, Tandon K, Jain S, Handgraaf JW, Buijse M (2013) Method of moments for computational microemulsion analysis and prediction in tertiary oil recovery. Langmuir 29 (7):2136-2151.
73. Boek ES, Coveney PV, Lekkerkerker HNW (1996) Computer simulation of rheological phenomena in dense colloidal suspensions with dissipative particle dynamics. Journal of Physics: Condensed Matter 8 (47):9509.
74. Zhu W, Xiao J, Zhu W, Xiao H (2009) Molecular dynamics simulations of RDX and RDX-based plastic-bonded explosives. Journal of Hazardous Materials 164:1082-1088.
75. Rekvig L, Frenkel D (2007) Molecular simulations of droplet coalescence in oil/water/surfactant systems. The Journal of Chemical Physics 127:134701.
76. Rekvig L, Hafskjold B, Smit B (2004) Molecular simulations of surface forces and film rupture in oil/water/surfactant systems. Langmuir 20 (26):11583-11593.
77. Rekvig L, Kranenburg M, Vreede J, Hafskjold B, Smit B (2003) Investigation of Surfactant Efficiency Using Dissipative Particle Dynamics. Langmuir 19 (20):8195-8205.
78. Shinoda W, DeVane R, Klein ML (2011) Coarse-grained force field for ionic surfactants. Soft Matter 7 (13):6178-6186.

2 Experimental studies on PIBSA-based surfactants

Abstract

Concentration of the surface active agents in industrial products is a common source of error. In order to compare efficiency of a number of polyisobutylene succinic anhydride (PIBSA) based surfactants, their concentration needs to be determined with a fair degree of certainty. Industrial samples of the monoethanolamine adduct of PIBSA (PIBSA-MEA) concentrate were used for chromatographic separation of the functionalized surfactant from the sample matrix. Complete spectroscopic assignments were based on detailed analysis of all the precursors and of the purified mixture of structural isomers. The structures of the double bond isomers were consistent with the expected addition products of the classic Alder-ene reaction derived PIBSA. The carbon-carbon connectivity of the succinamide head group to the bulky polymer tail of PIBSA-MEA was more complicated than previously thought, pointing towards regioselectivity in the nucleophilic substitution of PIBSA. By analogy, further structural assignments of two other surfactants, branded as PIBSA-IMIDE and PIBSA-UREA were made from the spectroscopic data recorded on crude industrial samples. Detailed nuclear magnetic resonance (NMR) assignments for all three surfactants reported here were utilized to develop a *semi*-quantitative ^{13}C-NMR based method for the estimation of the amount of the functionalized surfactant relative to the total PIB content in the industrial concentrates. The results highlight common sources of structure- and concentration dependent errors in high internal phase emulsion formulations.

2.1 Literature studies

Since the early 1990s, polyisobutylene succinic anhydride (PIBSA)-based surfactants have been used to render kinetic stability to high internal phase (HIP) water-in-oil emulsions [1-3]. The chemical structure of these amphiphilic molecules determines the nature of their interaction with the oil-water interface, the ability to form reverse micelles in the oil phase and their time-stabilizing efficiency [4,5]. The effective concentrations of these surfactants are usually determined by the emulsion stability limits, and typically are well in excess of their critical micelle concentration (CMC), to afford total surfactant concentration in the oil of 0.01–1.5 wt % [5,6]. Whilst the active surfactant loading at the water-oil interface is almost independent of dilution, the concentration of reverse micelles in the oil phase is "excess concentration"-dependent and proved to be critical for the HIP emulsion stability, especially at elevated temperatures [7].

The industrial method of production of PIBSA-based surfactants is typically a three-step process, starting from the manufacturing of PIB, followed by the addition of maleic anhydride (MAH) and further substitution/addition of other functional groups. Example of synthesis of PIBSA-MEA and PIBSA-UREA surfactants is given in Scheme 2-1 [3,8]. Further thermal treatment of the open ring structure can result in cyclization to imide-type head groups as in PIBSA-IMIDE surfactant. Chlorine-free PIBSAs of lower molecular weight and with a narrow polydispersity index (PDI) are generally preferred in HIP emulsion technology for their superior performance and viscosity characteristics.

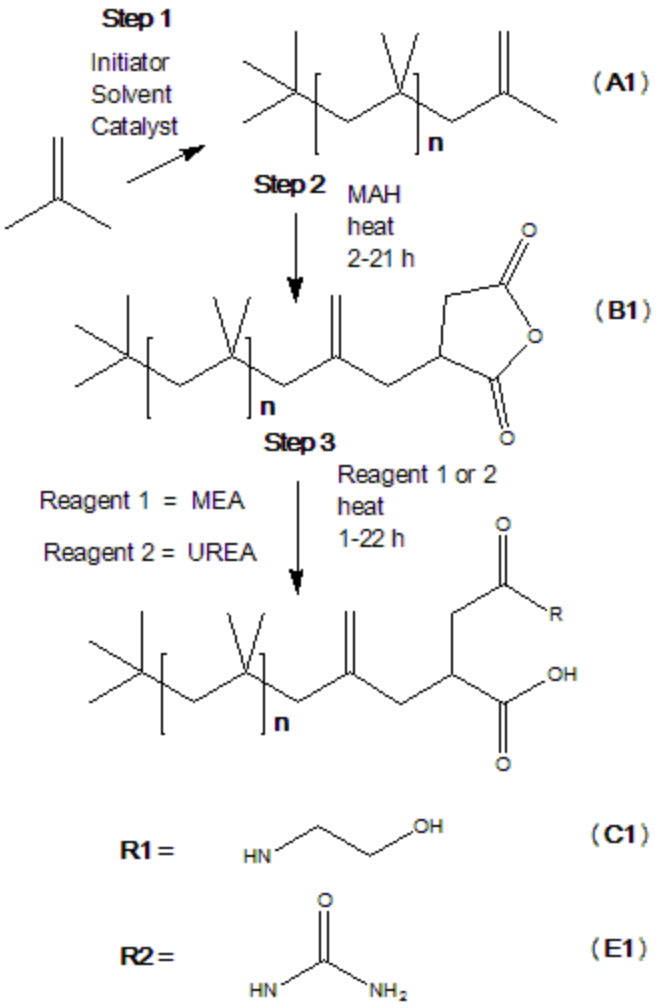

Scheme 2-1: Typical industrial process for preparation of PIBSA-based surfactants from HR-PIB (only major isomers of reactants and products are shown).

The viscosity of the oil phase is one of the key physicochemical parameters and can be greatly affected by the structure of the surfactant polar head group, average mass number (*Mn*), average molecular weight (*Mw*), the degree of functionalization and content of surface inactive products [9]. Mechanistic interpretation of surfactant performance is often based on model laboratory scale preparations, which fail to reproduce the complete macromolecular environment of the industrial mixtures, and may differ in their elementary and side reactions [10-12]. Furthermore, high thermal stability of HR-PIBs and PIBSAs can be affected by the duration of the exposure to the various catalysts and temperature cycles during formation of PIB-derived products [13].

Although most structural isomers of PIBSAs have been well characterized, the qualitative and quantitative analysis of commercial concentrates, which also contain unreacted starting materials, decomposition products and residual solvents, remains a challenging task [14-19]. Thus, having a better understanding of the chemical composition of the surfactant concentrates could be useful in quality control of the end products, choice of the synthetic intermediates and calculations of the concentration-dependent parameters such as the surfactant efficiency, interfacial tension and CMC.

2.2 Materials and Methods

The Glissopal® range of highly reactive (HR)-PIBs, produced by the BF_3-catalyzed process, as well as PIBSA were supplied by BASF (Midrand, RSA). Industrial samples of HR-PIB, PIBSA, PIBSA-MEA, PIBSA-IMIDE, PIBSA-UREA surfactant concentrates and a sample of diluent oil were supplied by a South African industry without any specifications. Reference sample numbers discussed in the text are given in Table 2-1.

Table 2-1: Inventory of the PIBs, PIBSAs, PIBSA derivatives and additives

Reference	Trade Name	Description
Sample 1	Glissopal®1000	HR-PIB, *Mn* =1000 g/mol
Sample 2	Glissopal®1300	HR-PIB, *Mn* =1300 g/mol
Sample 3	Glissopal®2300	HR-PIB, *Mn* =2300 g/mol
Sample 4	GlissopalSA®	PIBSA
Sample 5	Mosspar-H	Isoparaffinic oil
Sample 6	PIB	HR-PIB (unspecified *Mn*)
Sample 7	PIBSA	PIBSA
Sample 8	PIBSA-MEA	Polyisobutylene *N*-(2-hydroxyethyl) succinamide
Sample 9	PIBSA-IMIDE	Polyisobutylene *N*-(2-hydroxyethyl) succinimide
Sample 10	PIBSA-UREA	Polyisobutylene *N*-(urea) succinic acid imide

Chromatography: Sample 8 (5.02 g) was dissolved in 4 mL of hexane and purified using a 4 x 50 cm column packed with 100 g of silica gel_{60}. The column was packed with 500 mL of hexane (Hex), followed by elution with a stepwise gradient solvent mixture of Hex,

dichloromethane (DCM) and ethyl acetate (EtOAc) and washed with 1 L of EtOAc. Fractions of 6 mL aliquots were collected and combined by their relative thin layer chromatography (TLC) retention value, using UV_{254}, UV_{540} and 5 wt% phosphomolybdic spray reagent for detection. Pre-coated glass or aluminum silica gel TLC plates were used in all instances (F_{254} Merck or Sigma Aldrich). All solvents used for purification were distilled from chemically pure solvent grades. The solvent was removed under vacuum on a rotary evaporator at 60 °C.

NMR: NMR spectra were recorded on Bruker 300 and 400 MHz instruments at ambient temperature. All chemical shifts in the text, tables and figures are reported in δ (ppm), referred to tetramethylsilane (TMS) as external standard and referenced to the residual proton and carbon signals of $CDCl_3$ solvent at δ_H 7.24 ppm and δ_C 77.0 ppm, respectively. Routine analysis generally involved in 1D and 2D core procedures (^1H, ^{13}C, DEPTH, COSY, HSQC, HMBC and NOESY) was used for all samples. Samples were prepared with 60-70 mg in 0.5 mL of $CDCl_3$ (Merck) and filtered prior to analysis. Spectra were Fourier transformed, phase and baseline corrected by MestreNova (version 6.0.2) automated routines. Manual integration and selected peak normalization of the integrals by desired peak was applied to all spectra. The integration regions were spread over a range of at least 25 times of the line width (Hz) of the peak in both directions, and the data derived from the peak integration was taken as an average of three separate manual measurements to minimize experimental uncertainty [21].

ATR-FTIR: Mid-infrared spectra were recorded on a Bruker 70v Fourier transform infrared (FTIR) spectrophotometer, by placing the polymer samples in a diamond attenuated total reflection (ATR) cell. The resolution was 2 cm^{-1} and 32 scans were signal-averaged in each interferogram. Data was analyzed using OPUS software (version 7.5, Bruker). Spectra were smoothed with a Savitzky-Golay function algorithm, base-line corrected and normalized.

APCI-MS: Samples were introduced *via* the glass capillary directly into an atmospheric pressure chemical ionization (APCI) source and mass spectra were recorded using APCI, with drying gas temperature of 200 °C, nebulizer pressure of 1.6 bar and drying

gas of 8.0 L/min. Mass range scanned was m/z 50-3000 with maximum accumulation time of 0.2 min.

GPC-MALLS: Gel permeation chromatography (GPC) was carried out using a Hewlett–Packard 1100 series chromatograph interfaced with a DAWN digital signal processing (DSP) multi-angle laser light scattering (MALLS) (Wyatt Corp., Santa Barbara, CA) and refractive index (RI) detector for absolute molecular weight determination. GPC was calibrated in accordance with the universal calibration method with narrow range polystyrene standards. Samples were prepared at ±20 mg/mL, filtered (0.45 µm PTFE syringe) and injected straight after the preparation onto a series of GPC columns (Agilent PLgel™ 10 µm with pore size 105 Å, Agilent PLgel MIXED-C™ and a Phenomenex Phenogel™ 5 µm with a pore size of 100 Å), preceded with 0.5µm inline filter. Samples were eluted with distilled tetrahydrofuran (THF) at 1 mL/min. The specific refractive increment (dn/dc) was determined online between 0.090 to 0.100 ± 0.005 (Table A2-2). The *Mn*, *Mw* and PDI were calculated using ASTRA™ 4.73 (Wyatt Corp., Santa Barbara).

DSC: A Mettler Toledo differential scanning calorimetry (DSC) 1 instrument was used for DSC analyses. The polymer samples were weighed to 5 – 10 mg. Samples were subjected to a heat-cool temperature programme (-10 to 250 °C, heating/cooling rate of 10 K/min), flow rate of 60.00 mL/min and were purged with nitrogen gas.

2.3 Results and discussion

2.3.1 Structural study of surfactants and their precursors

The PIB and PIBSA reference samples (Table 2-1) were analyzed using APCI-MS, GPC-MALLs and 1D and 2D NMR experiments for reference purposes and for comparison to the results previously reported for the model reactions [15,18]. Relative concentrations of various double bond isomers in the samples of HR-PIB and PIBSA were established from the integral values of proton resonances [19]. PIBSA-MEA was selected as a model surfactant for purification and detailed structural studies. Structural assignments of the functionalized

PIBSA-IMIDE and -UREA were made from the analysis of crude industrial concentrates, and were based on the assignments of the model surfactant.

2.3.1.1 Analysis of HR-PIBs

The GPC-MALLS analysis of sample 1 gave *Mn* value of 1056 Da (19 isobutyl repeat units - IB) and *Mw*/*Mn* = 1.1 (*dn*/*dc* = 0.095), which compared well with the value reported in the BASF technical specification sheet (Tables A2-1 and A2-2); and *Mn* value of 975 Da (17 x IB) and *Mw*/*Mn* = 1.0 (*dn*/*dc* = 0.092) for sample 6. Such variation in *Mn* could lead to 10-15 % errors in values of the concentration dependent parameters frequently based on the assumption of the number of repeat units in the PIB side chain of the surfactant [20]. Samples 2 and 3 were also analyzed for method validation purposes and the results compared well with the technical specification values (Table A2-2).

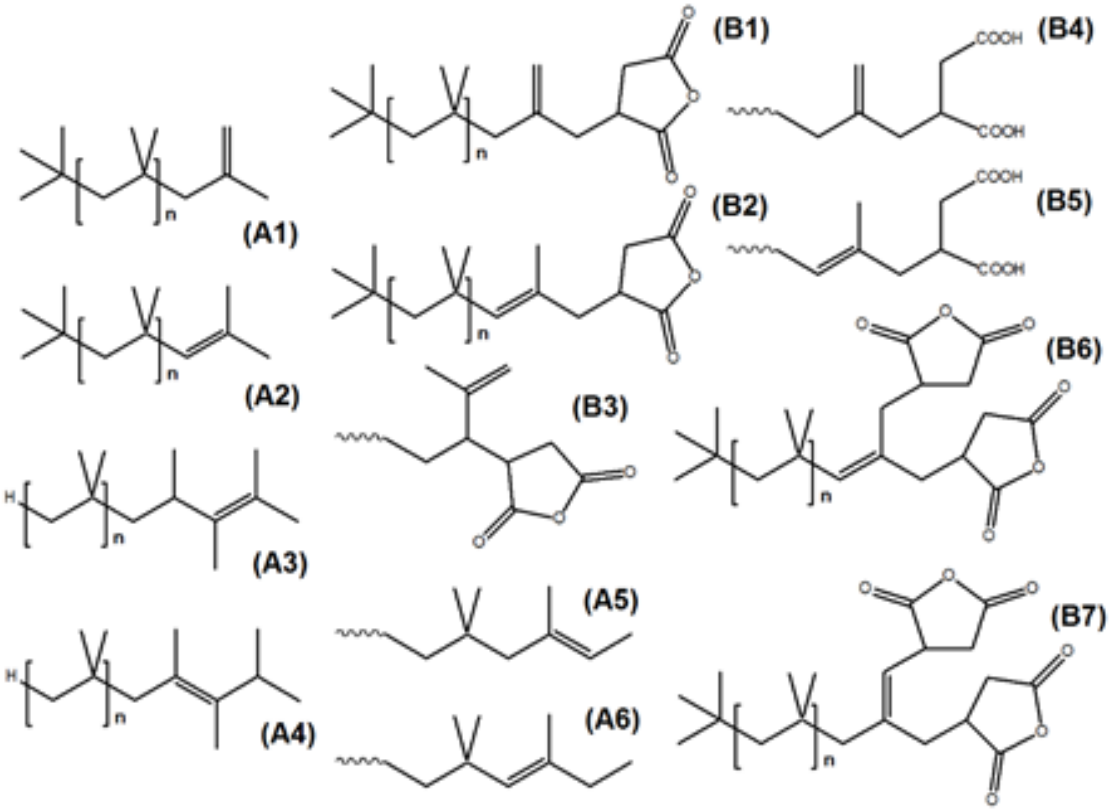

Scheme 2-2: HR-PIB isomers and rearrangement products (A1-A6) and PIBSA isomers and bi-products (B1-B7).

The APCI-MS analysis of the HR-PIB samples 1 and 6 showed main series of peaks spaced by 56 Da (1 x IB), with sample 6 having an additional series of peaks of the PIB with irregular carbon numbers, suggestive of a different synthetic route to that of sample 1 (Figs. A2-1 and A2-2). The ATR-FTIR absorbance profiles for both HR-PIB samples were identical and values are reported for cross reference purposes in Table 2-2. The ^{1}H- and ^{13}C-NMR spectra of samples 1 and 6 were very similar, composing of 86 and 87 % of the *exo*-olefin **A1**, 10 % of the *endo*-olefin **A2** and 3 and 4 % of the *tetra*-substituted isomers **A3** and **A4**, respectively (Scheme 2-2).

2.3.1.2 Analysis of PIBSAs

The GPC-MALLS analysis of sample 4 gave a *Mn* value of 1643 Da and *Mw*/*Mn* = 1.13 (*dn/dc* = 0.099), which compared well with the value reported in the BASF technical specification sheet (Table A2-1). Sample 7 gave lower *Mn* value of 1420 Da and *Mw*/*Mn* = 1.40 (*dn/dc* = 0.098). Overall, the GPC coupled with MALLs detection resulted in *Mn* values within a reasonable degree of accuracy for all PIB and PIBSA samples analysed, as compared to the BASF *in-house* method with the refractive index detector. The positive ion APCI spectrum of sample 7 showed two main series of peaks (Figure A2-3). The lower *Mw* series in the region of 200-400 m/z were separated by 14 Da (-CH_2-), which originate from carbocation rearrangement leading to the anomalous carbon numbers (C_3, C_5 *etc.*). This is more typical for the PIBSAs produced from $AlCl_3$ catalysed PIB, as reported by Harrison [17], but could also result from the thermal decomposition of PIB. The higher *Mw* series were separated by 56 Da and differed by 98 mass units from the starting regular carbon numbers PIB fragments ($C_{4n}H_{8n}$) with major molecular ions at m/z = 379, 435, 491 *etc.* The ATR-FTIR absorbance spectra of samples 4 and 7 were absolutely identical (Table 2-2).

Few differences between PIBSA samples 4 and 7 were noted in the carbonyl and olefin regions of the ^{13}C-NMR spectra. Two equally strong sets of the carbonyl peaks were observed in the spectra of sample 4 (δ_C 169.85 and 173.49 ppm; δ_C 178.52 and 181.04 ppm), which were assigned to the anhydride and the *di*-acid groups respectively, suggestive of significant anhydride hydrolysis (structures **B4** and **B5**, Scheme 2-2). Sample 7 presented with one set of carbonyl peaks of the succinic anhydride (δ_C 169.85 and 173.49 ppm). *Bis*-adduct **B6** was

detected in both PIBSA samples, whilst **B7** was not [15]. The positions of the resonances in the olefin region in both PIBSA samples were identical (δ_C 116.92, 126.65, 135.49, 141.02, 142.62 and 143.22 ppm) and compared well with the previously reported double bond isomers of classic Alder-ene PIBSA side chain **B1** and **B2** (Scheme 2-2), with 19 and 26 mol% of *exo*-PIBSA isomer **B1**; and 7 and 20 mol% of the unreacted *endo*-PIB **A2** respectively [14]. The unconventional PIBSA isomer **B3**, reported by Balzano [18] for the model thermal maleation reaction of Glissopal®1000, with characteristic methane carbon signals at δ_C 42.0 and 58.1 ppm (δ_H 3.00 and 2.67 ppm), was not detected in the two commercial PIBSA samples examined. Typically, PIBSA's undergo another heating cycle to remove water and increase its anhydride content prior to further derivatization.

2.3.1.3 Analysis of diluent oil

The diluent oils used in the final steps of production of PIBSA-based surfactants are usually selected from the category of $C_{14\text{-}20}$ hydrogenated petroleum distillates with boiling point ranging between 220-350 °C (e.g. Mosspar-H**,** Ash-H or Shell P833) [21]. The industrial diluent oil sample 5 was analyzed by ^{1}H and ^{13}C NMR spectroscopy (Figs. A2-7 and A2-8). The ^{13}C-NMR resonances were found in the region δ_C 11-40 ppm, which is typical for this hydrocarbon solvent category. Strongest peaks were situated at δ_C 14.1, 22.7, 29.7, 32.3 ppm (typical of *n*-paraffins) and at δ_C 37.5 ppm (quaternary carbons of *iso*-paraffins). A second set of considerably lower intensity signals appeared in groups of 2-4 around resonances at δ_C 20, 27, 33 (methyl substitutions on the hydrocarbon chain), δ_C 39 ppm and a single peak at δ_C 34.8 ppm. The appearance of the ^{1}H-NMR spectrum was almost identical to the spectrum of *n*-hexane and consisted of two distinct resonances: a broad resonance at δ_H 1.26 ppm for methane, methylene and crowded methyl protons and a characteristic multiplet at δ_H 0.86 ppm for the terminal methyl groups and other slightly more crowded germinal methyl groups of the hydrocarbon chain.

2.3.1.4 Analysis of PIBSA-MEA industrial concentrate

The industrial grade surfactant concentrate of PIBSA-MEA (sample 8) was selected for model studies. The GPC-measured *Mn* of 2552 Da (*Mw*/*Mn* = 1.5) was suggestive of

presence of a significant amount of higher *Mn* fully saturated oligomers, likely to result from the second order decomposition reactions of the PIB main chains in several synthetic cycles [22]. The positive ion APCI-MS spectrum indicated a mixture of isomeric units separated by 56 Da, which corresponded to the isobutyl (IB) repeat unit (C_4H_8) and showed a base peak at m/z = 198 Da $[M+H]^+$, followed by a series of peaks separated by 56 mass units (Figure A2-4). The calculated mass (M_{calc}) of 1277 g/mol for the PIBSA-MEA adduct was based on the molecular formula $H(IB)_{n-1}$-C_4H_6-$(C_2H_3COOH)CO$-NH-C_2H_4-OH with n = 19, for the PIB side chain of *Mn* = 1064 (estimated for samples 1 and 6 from the ^{13}C-NMR integral values). Differences in the calculated values of *Mn* between the GPC and APCI-MS can be ascribed to the source temperature of APCI-MS or the selectivity of the APCI-MS method toward the lower molecular weight ions, as previously reported for ESI-MS experiment [17]. The time factor in the sample preparation for the GPC analysis was also found to play an important role, as micelle formation in THF can be a source of the overestimation of *Mn* [23].

Fractionation of Sample 8 (for ^{1}H and ^{13}C NMR data refer to Figs. A2-9 and A2-10) afforded fractions **F1-F3**, which were analyzed by GPC-MALLs, APCI-MS, 1D and 2D NMR. The yields were as follows: fraction **F1** (light yellow - 1.63 g; 32.6 wt%), fraction **F2** (clear - 1.18 g; 23.6 wt%) and fraction **F3** (light brown - 1.2 g; 24 wt%) with total column recovery of just over 80 wt%.

Fraction **F1** was identified as a mixture of diluent oil and low molecular weight PIB products, which is known in industry as the 'light polymer' or 'light distillate'. GPC-MALLs analysis of this fraction gave poor resolution and *Mw*/*Mn* could not be calculated. The APCI-MS spectrum (Figure A2-5), with the base peak at *m/z* = 97 Da $[M+H]^+$ and several major molecular ions at *m/z* = 165, 261 and 448 Da, compared well with the previously reported data for the thermal decomposition products of PIB [17,24]. Fully saturated hydrocarbon constituents of the diluent oil were not detected by APCI-MS due to the lack of ionization.

Examination of the ^{1}H- and ^{13}C-NMR spectra allowed identification of several unsaturated terminal structures of PIB by comparison with chemical shift values reported for model olefins [13]. Other than the typical unreacted PIBs (**A2-A4**), *tri*-substituted end group structures **A5** and **A6** were found to be present, with **A6** in a relatively large amount

(Scheme 2-2). ^{1}H-NMR analysis proved difficult to distinguish between resonances of various end groups of PIB scission products, hexane and mineral oil. The ^{1}H-NMR resonances of the *tri*-substituted and isopropyl end groups in PIB were observed in low field region, as previously reported [24,25], with maximally crowded methyl protons of low *Mn* thermal decomposition products (TD) resonating around δ_H 1.24 ppm (Figure 2-1).

Fraction **F2** was identified as a mixture of functionalized PIBSA isomers **C1** - **C3** (Figure 2-1). GPC-MALLS analysis of this fraction gave *Mn* = 1616 Da and *Mw*/*Mn* = 1.51 (*dn*/*dc* = 0.092), which were within reasonable agreement with the calculated molecular weight for a product derived from sample 6. Major molecular ions in the positive ion APCI spectrum (*m*/*z* = 113, 198, 254, 310, 366, 422 and 478; Figure A2-6) were separated by 56 Da (base peak *m*/*z* = 198 Da $[M+H]^+$), and the oligomers differed by 98 Da from the regular carbon number PIB side chain ($C_{4n}H_{8n}$) fragments [17].

Major isomer **C1** (Figure 2-1) was identified by 1D and 2D NMR as the *exo*-PIB-*N*-(2-hydroxyethyl) succinamide denoted as PIBSA-MEA (olefin side chain: δ_C 143.49 and 116.08 ppm). The ^{13}C-NMR resonance signals of the secondary amide side chain appeared at δ_C 41.67 for N-CH_2 and 60.68 ppm for O-CH_2 (Figure A2-11). Two single peaks at δ_C 177.31 ppm for -CH_2-C=O and 180.46 ppm for >CH-C=O were assigned to the open ring succinic moiety. Carbon-carbon connectivity along the PIB side chain was derived from the ^{13}C-NMR peak intensities and integration values, heteronuclear NMR maps and by comparison with the previously published data by Harrison [19].

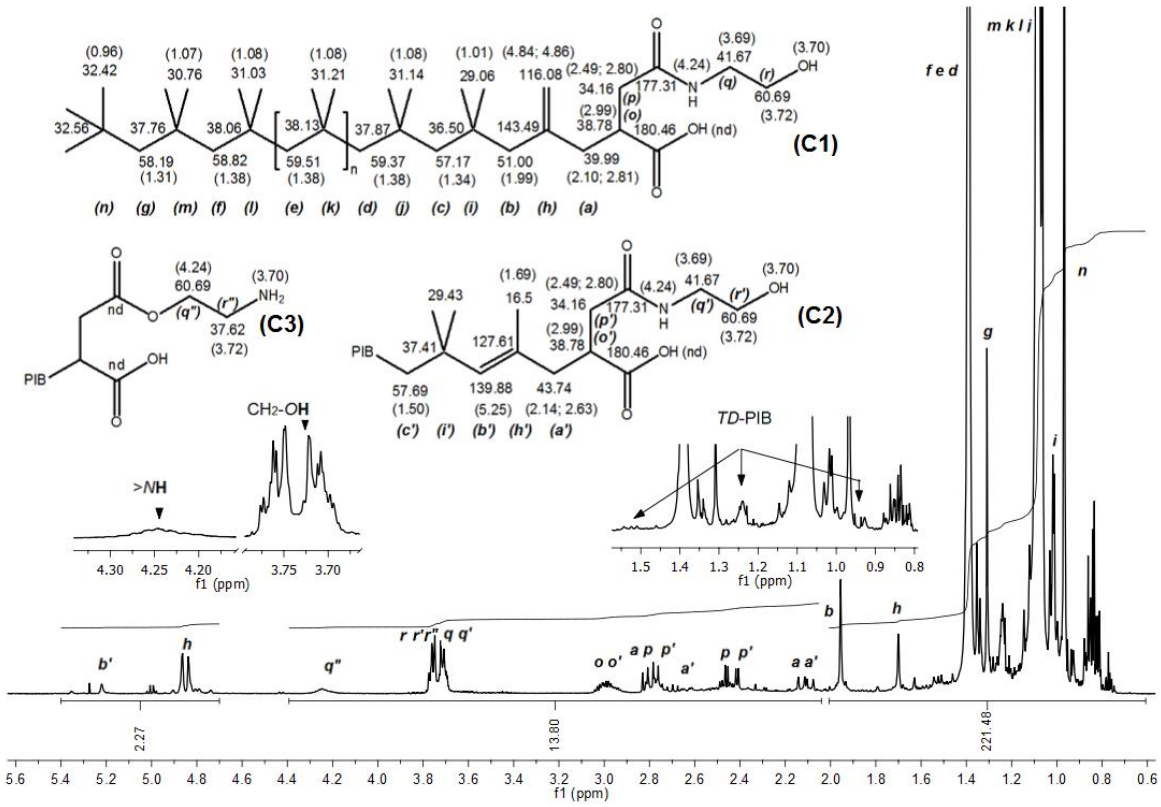

Figure 2-1: ^{1}H-NMR spectrum (400 MHz, $CDCl_3$) and structures of PIBSA-MEA surfactant isomers C1-C3. Carbon and proton (in brackets) chemical shifts are quoted in ppm.

The previously unassigned carbon shift of moderately crowed methylene group ***j*** appeared at δ_C 59.37 ppm (s, 2H, δ_H 1.34 ppm). The position of the amide proton was derived from proton-proton coupling of the HN- and -CH_2 protons in the 2D COSY plot ($J_{H\text{-}H}$, δ_H 3.72 – 4.24 ppm), and it was further confirmed by the NOESY experiment with a strong correlation observed for the resonance peaks at δ_H 3.72 and 4.24 ppm (Figure A2-12). The HMBC ($J_{H\text{-}C}$) correlations of the amide-carrying carbonyl group (δ_C 177.31 ppm) to the succinic methylene protons ***p*** (δ_H 2.49 and 2.70 ppm) and to the *N*-methylene protons ***q*** (δ_H 3.69 ppm) were suggestive of some regioselectivity of the nucleophilic ring opening reaction, which was previously characterized as an equal mixture of isomers, with the PIB chain adjacent or one carbon removed from the carboxylic acid residue [2,7]. This may be due to some intramolecular interactions, the effect of a bulky ring substituent (steric hindrance during nucleophilic attack) or of the molecular environment of the reaction matrix.

Key chemical shifts for the two minor isomers **C2** and **C3** were derived from the HSQC and HMBS NMR maps (Figure A2-13). For the *endo*-PIB-*N*-(2-hydroxyethyl) succinamide **C2,** with a *tri*-substituted olefin PIB side chain (δ_C 127.61 and 139.88 ppm), the methyne vinyllic proton ***b'*** was observed at δ_H 5.25 ppm and the allylic ring adjacent methylene protons ***a'*** - at δ_H *2.14 and 2.63 ppm* (δ_C 43.74 ppm). For the isomer **C3**, the ester methylene carbon ***q"*** was observed at δ_C 60.7 ppm (δ_H 4.2 ppm) and the primary amine bound carbon ***r"*** - at δ_C 37.62 ppm (2H, m δ_H 3.72 ppm).

The ^{1}H-NMR spectrum of the fraction **F3** was characteristic of a fully saturated PIB. Its dark brown color was consistent with the increase in the refractive index with carbon number in the thermal decomposition (TD) products of PIB as previously reported [18,26]. Temperature cycle of the thermal maleation reaction of PIB ranges from 150-200 °C, whilst the onset of thermal degradation of the BF_3 process PIB and PIBSA is in the region of 240 °C [18,27]. Higher order of thermal decomposition observed in this sample is likely to be due to the prolonged exposures of feedstock to high temperature and catalysts in the production process. Further investigation of this fraction was outside of the scope of this paper.

2.3.1.5 Structural assignments of PIBSA-IMIDE isomers

Structures of PIBSA-IMIDE isomers **D1** and **D2** (Figure 2-2) were assigned from the NMR analysis of sample 9 following the chemical shift trends of the model compounds **C1** and **C2** (Figure 2-1).

All proton and carbon chemical shifts were very similar to PIBSA-MEA, with no change in the chemical shift of the closed ring carbonyl groups (δ_C *177.29 and 180.43 ppm;* Figure A2-13). This could be due to the intramolecular hydrogen bond formation of the amide hydrogen with the acid carbonyl group in PIBSA-MEA open ring structure. The proton-proton COSY/NOESY correlation for the amide-methylene protons was absent (Figure A2-12).

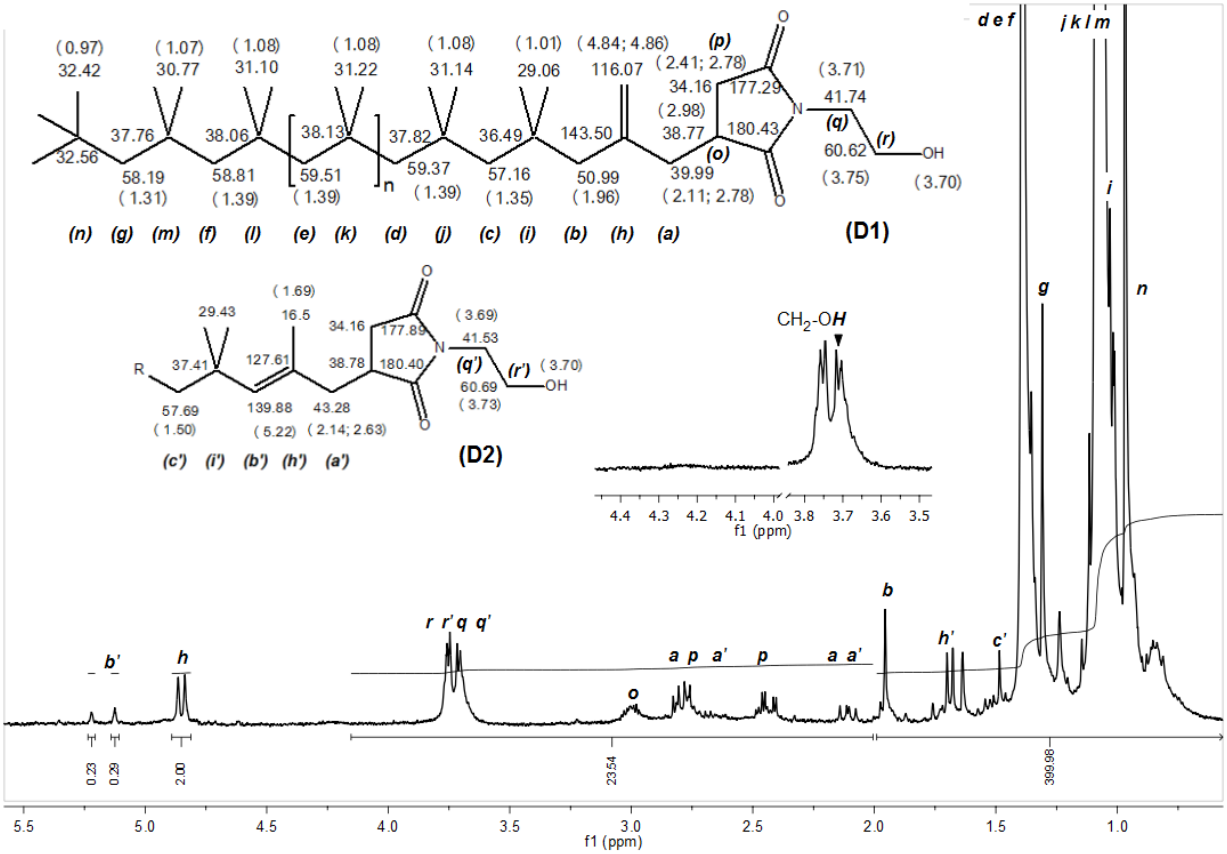

Figure 2-2: ^{1}H-NMR (400 MHz, $CDCl_3$) spectrum of sample 9 and structures of PIBSA-IMIDE surfactant isomers D1 and D2. Carbon and proton (in brackets) chemical shifts are quoted in ppm.

2.3.1.6 Structural assignments of PIBSA-UREA isomers

Structures of the PIBSA-UREA adducts **E1** and **E2** (Figure 2-3) in sample 10 were assigned on the basis of 1D and 2D NMR of the industrial concentrate and by the analogy to the model compounds **C1** and **C2** (Figure 2-1). Sample 10 contained a large amount of diluent oil. The slightly more pronounced downfield shift of all resonances in the head group and the PIB chain was attributed to the electron density shift and polarization effects in the extended partial π-bond system of the *N*-acylurea group (**E1**). A few key chemical shifts of the minor isomer **E2** were assigned as δ_C 128.19 and 140.00 ppm (d, 1H, δ_H 5.25 ppm) for the olefinic resonance ***b'*** and δ_C 43.74 ppm (dd, 2H, δ_H 2.14 and 2.63 ppm) for the vinylic ring adjacent methylene ***a'*** (Figure A2-14).

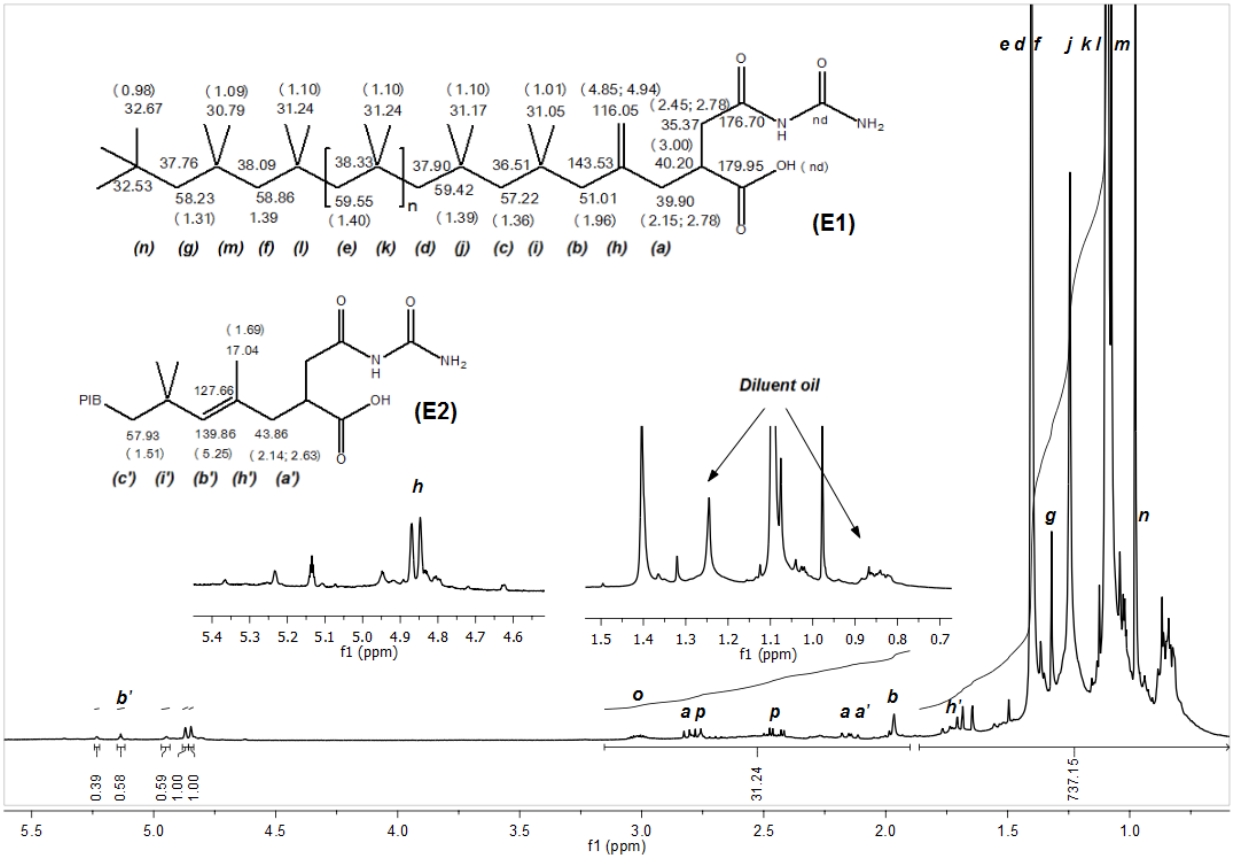

Figure 2-3: ^{1}H-NMR (400 MHz, $CDCl_3$) spectrum of PIBSA-UREA (Sample 10).

2.3.2 ATR-FTIR analysis of PIB, PIBSA and PIBSA surfactants

Qualitative ATR-FTIR analysis of PIB, PIBSA, additives, industrial concentrates and purified surfactants (Figures A2-16 to A2-23) resulted in a few interesting conclusions, which were somewhat different from the previously reported data in terms of the functional group assignments (Table 2-2). Adsorption band at 890 cm^{-1} of the exocyclic double bond of the unreacted *exo*-PIB **A1** was observed in both PIBSA samples but not in the PIBSA derivatives, unlike the more stable isomer **A2** (*endo*-PIB), which was present in all of the products of the PIB derivatization process. These findings are consistent with the ^{1}H- and ^{13}C-NMR results. In PIBSA samples 4 and 7, the adsorption band of the $>C=CH_2$ of the PIB side chain has shifted to 920 cm^{-1}, which is in good agreement with the predicted value [28].

Absorption values of the carbonyl stretching in PIBSA and PIBSA derived samples varied from 1702 - 1779 cm^{-1} depending on the type of carbonyl present, and were in good agreement with the previously reported data [25]. The ester isomer **C3** with the characteristic adsorption at 1740 cm^{-1} was not detected by FTIR in any of the PIBSA-MEA samples [2]. The absorption band at 1073 cm^{-1}, previously ascribed to that of the primary C-*O*(H) in acetamide [11], was also present in HR-PIB but absent from the purified PIBSA-MEA fraction **F2** (I.R. 2950, 2892, 1702, 1471, 1391, 1364, 1227, 1169, 949, 921 and 652 cm^{-1}). The acyl (O-H) stretching of the hydrolyzed *di*-acid by-products **B4** and **B5** of PIBSA (sample 4), typically found as a broad band at 2500-3100 cm^{-1}, was not detected by the FTIR [14]. This is mainly due to the sensitivity of the instrument.

The N-H stretching vibrations of this class of amides, usually found in the region of 3140-3500 cm^{-1}, were not detected in any of the PIBSA derivatives investigated [11]. This could be due to the tendency of these head groups to form conformational intramolecular hydrogen bonds. Previously reported bands for an amide stretching at 1550 and 1635 cm^{-1} were also not observed in PIBSA-MEA or PIBSA-IMIDE samples [28].

Such detailed I.R. fingerprinting of these surfactants can be particularly useful in the FTIR guided studies of the interfacial interactions of these surfactants with the oxidizer salts such as Ammonium Nitrate. The quantitative IR analysis of the surfactant concentrates as proposed by Walch [25] resulted in the substantially overestimated *Mn* values. This is probably due to the presence of the unreacted PIBs, higher *Mn* decomposition products of PIBs and the diluent oil (sample 5 IR spectrum: 2957, 2923, 2863, 2361, 1591, 1460, 1376, 1071 and 728 cm^{-1}), as the PIB chain is unlikely to grow in the thermal maleation of PIB, ring substitution or condensation reactions.

Table 2-2: IR frequencies (cm^{-1}) and assignments for HR-PIB, PIBSA and PIBSA-derivatives

	HR-PIB Samples 4 and 7	**PIBSA** Samples 4 and 7	**PIBSA MEA** Sample 8	**PIBSA IMIDE** Sample 9	**PIBSA UREA** Sample 10
PIB tail (main chain)					
$=CH_2$ asym. str.	-	3080	-	-	-
CH str.	-	2980	-	-	-
CH str.	2950	2950	2950	2951	2950
	-	-	-	-	2923
CH str.	2892	2890 2720	2892	2887	-
CH str.	2361	2361	n.o	2361	n.o
n.a.	1591	-	1593	1591	1597
CH bend	1471	1465	1471	1471	1466
CH_3 swing	1388	1385	1391	1390	1387
CH_3 swing	1364	1360	1364	1363	1364
CH bend crowded $-CH_2-$	1227	1225	1227	1227	1227
n.a.	1073	1071	1070	1070	1073
>C=CHR	949	950	949	n.o.	950
C=C stretch	-	920	921	921	n.o.
$>C=CH_2$ wag PIB	890	890	-	-	-
Head Group					
sym. str. anhydr.	-	1860	-	-	-
>C=O		1785	-	1776	1779
	-	-	1702	1700	1715
$H_2N-C=O$	-	-	-	-	1666
C=O str. anhydr.	-	1640	-	-	-
$C-(CH_2)$ bend	-	1160	1169	1169	1169
Anhydr.	-	715	-	-	-
N-H wag	-	-	652	691	635

n.o. – not observed
n.a. – not assigned

2.3.3 Semi-quantitative analysis of PIBSA surfactants from ^{13}C-NMR

In PIBs, methyl and methylene carbons having the same degree of steric hindrance and crowding are known to have essentially the same chemical shifts in $CDCl_3$ regardless of the total carbon number and chain length [26]. In the ^{13}C-NMR spectra of HR-PIB (samples 1 and 6), there were six distinct signals in the region δ_C 50-60 ppm. Signals of the isolated terminal methylene at δ_C 58.2 and its nearest neighbour at 58.8 ppm are well separated from the bulk and from the signals near the double bond end of the PIB chain at δ_C 51 or 57 ppm for the *exo*-isomer **C1** and at δ_C 43.7 ppm for the *endo*-isomer **C2** (Figure A2-15). Relative values of the integrals of carbon signals at δ_C 58.2 and 58.8 ppm were nearly the same as the sum of integrals of the allylic methylenes of **A1** and **A2** PIB isomers (Table 2-3). In PIBSA samples 4 and 7, relative intensities of these terminal methylene peaks were significantly higher than that of the allylic and ring methylenes due to the presence of the unreacted PIBs and its thermal decomposition products (Figure 2-4). Similar pattern was observed for the

relative intensities of the characteristic quaternary carbon signals and geminal methyl groups. This trend allowed to estimate the content of the surfactant in the industrial concentrate from the relative values of the integrals of the distinct methylene carbon resonances of the functionalized polymer to that of the isolated terminal or adjacent to terminal methylene groups (Table 2-3).

It is assumed that NMR signal intensities scale linearly with the compound concentration. From Figure 2-4, if the content of HR-PIB *exo*-isomer is x mol%, and if the integral corresponding to the methylene carbon denoted c is normalized to 1, then x is directly proportional to the values of the integrals corresponding to ***g*** or ***f*** carbon signals and amounts to 83 mol%, which is in the same range as the (86 mol%) derived from ^{1}H-NMR. Then the number of the corresponding IB units in the *exo*-PIB chain is the sum of scaled values of integrals ***c***, ***d*** + ***e***, ***f***, ***g*** plus 3 (for ***a***, ***b*** and ***n*** fragments). In the current example it equals to 19 (M_{calc} HR-PIB = 1064), which is slightly higher than the *Mn* value of 975 Da determined by GPC. This underestimation of *Mn* by GPC is not uncommon considering that the instrument was calibrated with polystyrene and not the PIB standards [29]. For PIBSA and PIBSA derivatives, the content of the *endo*-isomer is higher and the carbon signal corresponding to ***c'*** is more prominent. Thus the total amount of the functionalized polymer is proportional to the sum of integrals ***c*** and ***c'***, and mol% of the functionalized polymer in this example is 100×(1+0.3)/2.5 = 52 , and the number of IB units in the PIB side chain of PIBSA is 19. In case of PIBSA-MEA, the content of the functionalized polymer was calculated to be 36 mol% and the number of IB units in the PIB side chain amounted to just over 18, which is within reasonable agreement with the yield of chromatographic separation. The normalization of the methylene signals of the functionalized head group ***p*** = ***p'*** result in the combined estimate of the *exo*- and *endo*-isomers, and corresponded well with the results above.

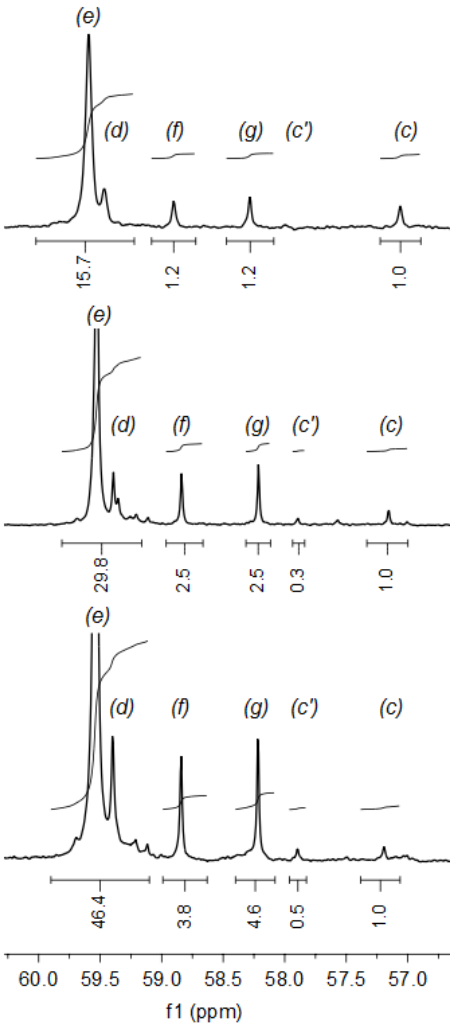

Figure 2-4: ^{13}C-NMR (300 MHz, $CDCl_3$) integrated spectral region from 56.5 – 60.5 ppm of PIB (sample 6 - top), PIBSA (sample 7 - middle) and PIBSA-MEA (sample 8 bottom).

This method can prove useful in the calculations of conversion rates, and the accuracy can be improved by calibration with diluent oils or by using an internal standard such as di-methylformamide [17].

Relative amount of the functionalized PIBSA-MEA isomers of the total PIB sample content was found to be in the range of 17-36 mol%; with 28-32 mol% for PIBSA-IMIDE and 22-25 mol% for PIBSA-UREA, based on analysis of the six batches of industrial surfactant concentrates (PIBSA-MEA, PIBSA-IMIDE and PIBSA-UREA), manufactured between 2011-

2015. Relative content of the functionalized surfactant was independent of the manufacturing date.

Table 2-3: Normalized integration values of the ^{13}C-NMR crowded methylene spectral peaks of PIB derivatives for semi-quantitative analysis

PIB chain atom label	HR-PIB Sample 6		PIBSA Sample 7		PIBSA-MEA Sample 8		PIBSA-MEA (Sample 8 fraction F2)	
	^{13}C res. δ, ppm	Int. value	^{13}C res. δ, ppm	Int. value	^{13}C res. δ, ppm	Int. value	^{13}C res. δ, ppm	Int. value
e; d	59.57; 59.45	15.7	59.5; 59.3	29.8	59.5; 59.4;	46.4	59.51; 59.37	18.7
f	58.88	1.2	58.8	2.5	58.84	3.8	58.82	1.5
g	58.26	1.2	58.2	2.5	58.22	4.6	58.19	1.5
c	57.04	1.0	57.1	1.0	57.19	1.0	57.17	1.0

Progressive thermal degradation from PIB to PIBSA-based derivatives was evident in all PIBSA and industrial surfactant samples examined. The results of this study have shown that batch-to-batch variation in the concentration of active surfactant in industrial concentrates can be significant and should be considered when comparing surfactant efficiency based on concentration-dependent physicochemical parameters. Poor conversion rates and thermal decomposition products can constitute up to 65 wt% of the surfactant concentrates, and can thus affect calculated values of CMC by up to two orders of magnitude. Since the concentration of the functionalized surfactant in the emulsion can have a significant effect on performance and shelf life, taking into account sample manufacturing history and accurate estimation of the surfactant concentration in industrial products are essential. The effects of large amounts of non-adsorbing polymers and higher *Mn* decomposition products on the overall viscosity characteristics of the oil phase, and subsequently the emulsion stability, should also be carefully considered.

2.3.4 DSC study of PIB, PIBSA and PIBSA derivatives

All polymer samples remained amorphous throughout the heating-cooling cycle. A gradual heat flow rise was observed in samples 1, 6, 9 and 10 from 0 - 240 °C, with the PIB samples showing the steepest climb, but no obvious phase transition. PIBSA samples 4 and

7, crude PIBSA-MEA (sample 8) and purified PIBSA-MEA (sample 8: fraction **F2**) had almost no enthalpy change in the temperature regimen used, indicating better thermal stability (Figure A2-24).

2.4 References

1. Ganguly S, Mohan VK, Bhasu VCJ, Mathews E, Adiseshaiah KS, Kumar AS (1992) Surfactant—electrolyte interactions in concentrated water-in-oil emulsions: FT-IR spectroscopic and low-temperature differential scanning calorimetric studies. Colloids and Surfaces 65 (4):243-256.
2. Ghaicha L, Leblanc RM, Chattopadhyay AK (1993) Influence of concentrated ammonium nitrate solution on monolayers of some dicarboxylic acid derivatives at the air/water interface. Langmuir 9 (1):288-293.
3. Chattopadhyay AK (1990) Water-in-oil emulsion explosive. US Patent 4,919,179.
4. Derkach SR (2009) Rheology of emulsions. Advances in Colloid and Interface Science 151 (1-2):1-23.
5. Reynolds PA, McGillivray DJ, Mata JP, Yaron PN, White JW (2010) The stability of high internal phase emulsions at low surfactant concentration studied by small angle neutron scattering. Journal of Colloid and Interface Science 349 (2):544-553.
6. Babak VG, Stébé M-J (2002) Highly Concentrated Emulsions: Physicochemical Principles of Formulation. Journal of Dispersion Science and Technology 23 (1-3):1-22.
7. Reynolds PA, Gilbert EP, White JW (2001) High Internal Phase Water-in-Oil Emulsions and Related Microemulsions Studied by Small Angle Neutron Scattering. 2. The Distribution of Surfactant. The Journal of Physical Chemistry B 105 (29):6925-6932.
8. Boer WG (2003) Composition and emulsifier. US Patent 6,630,596.
9. Reynolds PA, Reid CA (1991) Effect of nonadsorbing polymers on the rheology of a concentrated nonaqueous dispersion. Langmuir 7 (1):89-94.
10. Stoliarov SI, Lyon RE, Nyden MR (2004) A reactive molecular dynamics model of thermal decomposition in polymers. II. Polyisobutylene. Polymer 45 (25):8613-8621.

11. Bubálik M, Beck Á, Baladincz J, Hancsók J (2009) Development of deposit control additives for diesel fuel. Petroleum & Coal 51 (3):167-175.
12. Shaikh SK (2017) Adducts of low molecular weight PIB with low polydispersity and high vinylidene content US Patent 9,598,655.
13. Spěváček J, Toman L, Vlěk P (1995) 13C NMR characterization of unsaturated terminal structures in oligoisobutylenes. Polymer Bulletin 34 (4):461-467.
14. Tessier M, Maréchal E (1984) Synthesis of mono and difunctional oligoisobutylenes - III. Modification of α-chlorooligoisobutylene by reaction with maleic anhydride. European Polymer Journal 20 (3):269-280.
15. Tessier M, Maréchal E (1984) Synthesis of mono and difunctional oligoisobutylenes - IV. Modification of α,ω-dichlorooligoisobutylene by reaction with maleic anhydride. Preliminary study on block polycondensation. European Polymer Journal 20 (3):281-290.
16. Tessier M, Maréchal E (1986) Structural study of telechelic oligoisobutylenes in relation with the experimental conditions of their synthesis. European Polymer Journal 22 (11):889-901.
17. Harrison JJ, Mijares CM, Cheng MT, Hudson J (2002) Negative Ion Electrospray Ionization Mass Spectrum of Polyisobutenylsuccinic Anhydride: Implications for Isobutylene Polymerization Mechanism. Macromolecules 35 (7):2494-2500.
18. Balzano F, Pucci A, Rausa R, Uccello-Barretta G (2012) Alder-ene addition of maleic anhydride to polyisobutene: nuclear magnetic resonance evidence for an unconventional mechanism. Polymer International 61 (8):1256-1262.
19. Harrison JJ, Young DC, Mayne CL (1997) 2D-INADEQUATE Structural Assignment of Polybutene Oligomers. The Journal of Organic Chemistry 62 (3):693-699.
20. Masalova I, Kovalchuk K, Malkin AY (2011) IR Studies of Interfacial Interaction of the Succinic Surfactants with Different Head Groups in Highly Concentrated W/O Emulsions. Journal of Dispersion Science and Technology 32 (11):1547-1555.
21. Mata JP, Reynolds PA, Gilbert EP, White JW (2013) Extended Q-range small angle neutron scattering from inverse micellar solutions of PIBSA—Micelle and molecular scattering. Colloids and Surfaces A: Physicochemical and Engineering Aspects 418 (0):157-164.

22. David C (1975) Chapter 1 Thermal Degradation of Polymers. In: Bamford CH, Tipper CFH (eds) Comprehensive Chemical Kinetics, vol 14. Elsevier, pp 1-173.
23. Pirouz S, Wang Y, Chong JM, Duhamel J (2015) Chemical Modification of Polyisobutylene Succinimide Dispersants and Characterization of Their Associative Properties. The Journal of Physical Chemistry B 119 (37):12202-12211.
24. Dimitrov P, Emert J, Hua J, Keki S, Faust R (2011) Mechanism of Isomerization in the Cationic Polymerization of Isobutylene. Macromolecules 44 (7):1831-1840.
25. Walch E, Gaymans RJ (1993) Synthesis of low-molecular-weight telechelic polyisobutylene. Polymer 34 (2):412-417.
26. Warren RW, Gates DS, Driscoll GL (1971) NMR identification of C11 to C40 branched hydrocarbons derived from the decomposition of polyisobutylene. Journal of Polymer Science Part A-1: Polymer Chemistry 9 (3):717-746.
27. Lehrle RS, Duncan R, Liu Y, Parsons IW, Rollinson M, Lamb G, Barr D (2002) Mass spectrometric methods for assessing the thermal stability of liquid polymers and oils: study of some liquid polyisobutylenes used in the production of crankcase oil additives. Journal of Analytical and Applied Pyrolysis 64 (2):207-227.
28. Walch E, Gaymans RJ (1994) Telechelic polyisobutylene with unsaturated end groups and with anhydride end groups. Polymer 35 (8):1774-1778.
29. Chance RR, Baniukiewicz SP, Mintz D, Strate GV, Hadjichristidis N (1995) Characterization of Low-Molecular-Weight Polymers: Failure of Universal Calibration in Size Exclusion Chromatography. International Journal of Polymer Analysis and Characterization 1 (1):3-34.

3 Computational study of PIBSA-based surfactants

Abstract

The objective of this section of the project was to characterise the interactions of a series of PIBSA-based surfactants with various components of HIPE emulsions using molecular modelling methods. The study focused on three surfactants with known efficacy: PIBSA-MEA, PIBSA-UREA and PIBSA-IMIDE, which were compared with the well-reviewed product PIBSA-DEA. Quantum and classical mechanics codes were used for model building, geometry optimisation and molecular dynamics (MD) to study modes of surface adsorption; all these codes are contained within a single platform materials modelling suite - Material Studio™. The surface affinity of several low energy conformers of hypothetically possible ionised forms of the polymeric surfactants *i.e.* neutral, protonated (cationic), deprotonated (anionic) and zwitterionic, was probed on simulated surfaces of aqueous ammonium nitrate, pure water, and predicted growth faces of crystalline ammonium nitrate. Averaged values of the interaction energies were used for efficacy comparison. According to the hypothesis tested, *i.e.* comparative adsorption of additives to the surface of the supersaturated solution of salt and to water as well as crystal growth inhibition, it was found that all experimentally active surfactants had lower adsorption energies to water than to the model salt solution. Hydrogen bonds between ions were found to show the strongest interactions with the salt solution. The inhibition of crystal growth was inherent only to PISA-UREA. Correlations in *ab initio* calculated vibrational frequencies allowed the description of an ionisation mechanism of amide-bearing surfactant groups. A mechanism of oxidiser phase metastability was also proposed.

3.1 Literature study

3.1.1 Emulsion: Aspects of composition, microstructure and stability

3.1.1.1 Composition

High internal phase emulsions (HIPEs), which are used as blasting agents, typically consist of a large fraction (> 75 wt %) of the aqueous dispersed phase droplets containing oxidiser salt (w), which are separated by a thin layer of the continuous or oil (o) phase, and these are the w/o emulsions. The dispersed phase is a supersaturated solution (*ca.* 80 wt %) of ammonium nitrate (NH_4NO_3, AN) while the oil phase contains fuel or diesel (*ca.* 5 wt %). The remainder of the emulsion matrix is made up of water or oil soluble additives (*ca.* 15 wt %), comprising surface active agents (surfactants), crystal habit modifiers, buffers, and detonation catalysts. The aqueous oxidizer phase is usually buffered with citric or acetic acid to keep the pH between 3.5-4.5, in order to support the gassing reaction and desired order of detonation. Surfactants are used to assist with emulsification, droplet refinement and emulsion stability. The fudge point, at which AN starts to crystallise, is used to determine the required concentration of the salt in the emulsion, depending on the intended application. For surface formulations, concentrations corresponding to a fudge point of ~60 °C are used. Underground formulations are required to be more sensitive and generate higher energy outputs.

3.1.1.2 Emulsion microstructure and length scale

From the objective of investigating the mode of interaction of PIBSA-based surfactants and the oxidiser phase, microstructural characteristics of the emulsion would determine the special requirements of the simulation system. Reynolds and co-workers carried out a series of neutron diffraction experiments to investigate the microstructure of the PIBSA-surfactant stabilised HIPEs [1,2]. Some of the relevant characteristics reflective of the length scale of the surfactant and emulsion are summarised as follows: Droplet size, reported as the Sauter mean diameter - D_{32}, is typically 1-30 μm (1.0×10^4 to 3.0×10^5 Å), with a calculated droplet surface area of 1.3×10^9 to 1.1×10^{12} Å^2. Droplets are separated by

the continuous oil film of 1000-1500 Å [2,3]. The conformation(s) of the PIBSA-based surfactants in the dielectric environment of the oxidiser phase (*ca.* 16) is reported to be fully extended reaching an approximate length of 30 Å [4]. The molecular area occupied by PIBSA-based surfactant head groups at the interface, as reported by various authors, was around 140-220 $Å^2$ [1,3,5-7].

3.1.1.3 Emulsion stability

The metastability of the supersaturated dispersed phase inside the emulsion droplets is achieved with kinetic control by droplet refinement and with interface stabilisation by surfactants. Without added surfactant, AN emulsions are short lived and tend to crystallise. In surfactant-stabilised aged emulsions, the percentage crystallinity on aging reaches up to 30 wt % [8]. A number of laboratory-scale studies have been reported where the performance of model emulsion formulations stabilised by various PIBSA-based surfactants have been compared [9-13]. In the series PIBSA-MEA, PIBSA-UREA and PIBSA-IMIDE, PIBSA-MEA stabilised emulsions have shown superior performance by remaining stable over 52 week periods [14], and emulsion stability was shown to follow the same trend as the interfacial tension γ [12]:

PIBSA-MEA (> 52 weeks) > PIBSA-UREA (17 weeks) > PIBSA-IMIDE (16 weeks)

Structure-activity investigations of a laboratory synthesised PIBSA-DEA, also abbreviated by Ghaicha *et al.* as PSDA [10], were inconclusive concerning the mechanism of surface stabilisation, but provided some useful experimental details and order of stability for the pair PIBSA-MEA (PSMA) > PIBSA-DEA. However, a systematic study comparing various PIBSA-based surfactants is lacking to date.

Ganguly *et al.* drew an analogy of the emulsified solution of NH_4NO_3 and metastable supercooled water [15], with the latter presenting both modes of nucleation: bulk-homogenous, which is initiated by thermal fluctuation of the critical nucleus, and heterogeneous, which may be initiated by a surface, a surfactant or an impurity. Depending on the choice of the surfactant, both modes have been observed in surfactant-stabilised

HIPEs [16]. For homogenous nucleation, the nucleation rate ($\boldsymbol{J}$) is inversely proportional to the droplet average volume (V_d) and droplet lifetime (τ) [17].

$$\boldsymbol{J \propto \frac{1}{\tau V_d}} \qquad \textit{Eq. 3-1}$$

By contrast, in HIPEs stabilised with PIBSA surfactants, stability is higher in emulsions with smaller droplets, and scales with the droplet surface area [14]. This is typical of the heterogeneous type of nucleation, which occurs at one of the interfaces, and the nucleation rate follows Eq. 3-2, where A_d is the surface area of the droplets [17].

$$\boldsymbol{J \propto \frac{1}{\tau A_d}} \qquad \textit{Eq. 3-2}$$

It was found that for molecular crystals like AN, the smaller the surface energy, the slower the normal growth rate [18]. From the heterogeneous nucleation theory, the nucleation event is believed to be a non-spontaneous event due to the energy cost of the nuclei formation *vs* the free energy gain per unit volume. The critical size of nuclei (r_c) determines the absolute nucleation rate and depends on surface tension γ (Eq. 3-1), where ΔG_{sl} is the free energy difference between bulk liquid and solid (Eq. 3-3). Thus normal crystal growth rates are also proportional to γ. This could play a major role in the mode of surfactant-rendered stability.

$$\boldsymbol{r_c = \frac{2\gamma}{\Delta G_{sl}}} \qquad \textit{Eq. 3-3}$$

The strength of the bonding at the interface is strongly dependent on the structure and chemistry of the substrate surface. If the atomic structure of the substrate surface closely matches a particular crystal growth plane of the nucleating phase so that lattice strain is minimised and, in addition, the substrate presents a set of chemical functionalities that promote strong bonding to the nucleus, then the enthalpic contribution to the interfacial free energy becomes small, and nucleation occurs preferentially on that crystal plane [19].

It was shown that the surfactants, which are able to mediate crystal growth, affect mainly the thermodynamics of the processes involved. Edge energy of the cluster is

decreased due to saturation of the dangling bonds by the surfactant atoms. However, some surfactants saturate only some dangling bonds in the newly forming cluster, which increases the work in formation of the critical nucleus and renders remaining dangling bonds inaccessible for growth propagation by steric hindrance. This is typically followed by the increase in the E_{edge} of the surfactant cluster due to the segregation of the surfactant layer. The latter should be considered for the multifunctional PIBSA-based surfactants, which could form particularly strong hydrogen bonds with both ions of the salt substrate.

Results of another literature study on amphiphilic monolayer systems with concentrated AN solutions indicated that the crystallisation of AN was influenced by the nature of the molecules present in the monolayers [20]. The changes in the functionalities of the polar head groups produced significant differences in nucleation as well as the growth pattern of AN crystals, as observed by photoelectron microscopy. An additive can modify crystal habit by creating surface defects and dislocations, which result in altering of lattice energies. An additive that lowers the crystal lattice energy (which generally happens with organic surface-active agents) also reduces the bond strength between the crystals and crystal-bound water. An example of such behaviour is found for polystyrene sulfonate (PSS), which is used in the production of AN prill [4]. Reducing the size of AN crystals to almost unit cell, PSS possesses a unique mechanism of removing water from an AN droplet. Regardless of the crystallising phases of AN, the PSS, being a multifunctional molecule, interacts with various sites on the crystallising AN planes and isotopically reduces the size of the forming crystals. However, within the emulsion context, removal of water and formation of such crystallites would be highly undesirable and would affect detonation properties of the emulsion.

Formation of nano-suspensions during emulsion aging in PIBSA surfactant-stabilised emulsion formulations was reported by Malkin *et al.* [21]. This implies that, post the initial retardation of crystallisation, surfactants may selectively affect fast growing faces of the salt, resulting in formation of small isotropic crystallites. The ability of a surfactant to interact with growth faces of crystalline material could be used as one of the stabilisation criterions for the additive [22].

3.1.2 Surfactant

3.1.2.1 Surface activity

Surface activity of a molecule is a measure of its ability to accumulate at the interface, when the free energy of the adsorbed state (ΔG_{ads}) is significantly lower than that of the unadsorbed state [23]. It depends on the change in the interaction energies of the surface and the adsorbate and entropy effects [24]. A general ranking based on the capability of functional groups of associative colloid behaviour in amphiphilic/water systems was proposed by Laughlin [25]. He used surfactant affinity to water in his thermodynamic classification of 'operative' surfactant functional groups known as hydrophilic-lipophilic balance (HLB). According to HLB, the 'operative' hydrophilic groups may be organised into five subclasses, and these were ranked in order of relative hydrophilicity as follows:

anionic ~ cationic > zwitterionic > semipolar > single bond

Charged species should be more strongly adsorbed at the interface, causing interfacial tension to drop. Modelling of the surface interactions with various ionisation forms of surfactant should therefore prove useful.

3.1.2.2 Surfactant ionisation and susceptibility to hydrolysis

Surfactants, which are capable of ionisation, may exist in different forms, once mixed with water or an aqueous oxidiser phase. The head groups of the PIBSA surfactants under consideration are mono-substituted bi-functional esters (PIBSA-DEA); bi-functional amides (PIBSA-MEA), cyclic imides (PIBSA-IMIDE) and acylureides (PIBSA-UREA). PIBSA-IMIDE can be considered as a non-dissociative surfactant. PIBSA derivatives with succinic acid moiety would only partially dissociate in water due to the presence of the highly hydrophobic side chain. In a basic environment, PIBSA-DEA may be deprotonated on the acid and/or amine side, although the latter is a highly unlikely situation considering the relative **N-H**/CO**O-H** bond strengths. Proton removal would largely depend on the base. Deprotonation of PIBSA-MEA and PIBSA-UREA would result in formation of the carboxylate anion only, as the amide protons are not very acidic due to the partial double bond character of **C-N**. In an acidic

environment, the secondary amine of PIBSA-DEA is likely to undergo quaternisation [10]. In PIBSA-MEA and PIBSA-UREA, *O*-protonation of the amide carbonyl would be the spatially and energetically preferred form [26-28].

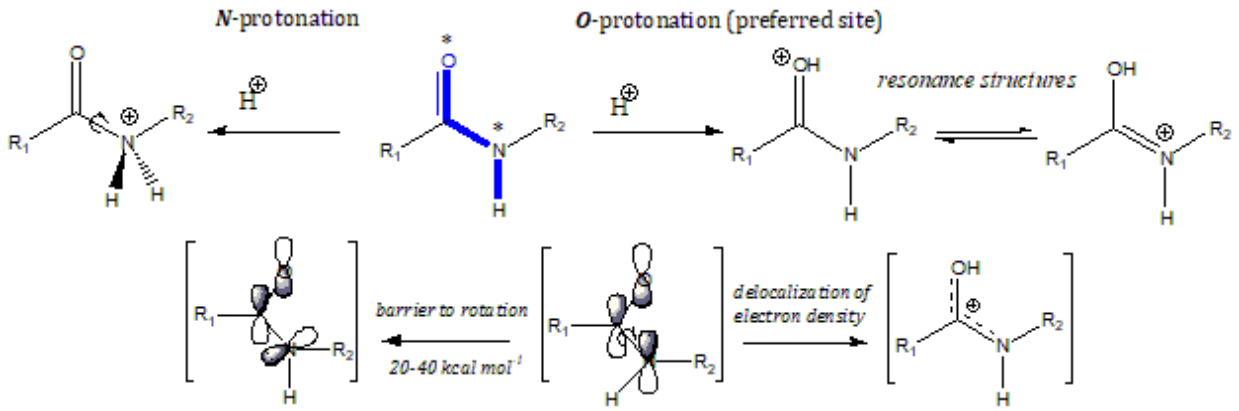

Scheme 3-1: Protonation sites in amides. Two orbital alignment scenarios leading to protonation at oxygen or nitrogen* sites. Typical anti-orientation of carbonyl oxygen and amide proton is depicted in blue. Image adopted from Nanubolu [28].*

Furthermore, linear secondary amides have mainly *anti* orientation with respect to the carbonyl oxygen and amide hydrogen, with a significant barrier to rotation (10-40 kcal $mol^{-1)}$ C-N bond (Scheme 3-1). The *anti* orientation is more energetically favoured, which is owed to the same electronic effects as the *γ*-effect in hydrocarbons [29-31]. *Syn*-amides are of very rear occurrence, and exist mainly in a hindered or cyclic form, like in lactams [30,32]. Both *syn* and *anti* amides are capable of ionization, where an oxygen of the amidic carbonyl is the likely protonation site [32]. In PIBSA-UREA, the proton could associate with either of the two carbonyl groups of the succinureide moiety. Depending on the relative nature of the surfactant and pH environment, zwitterionic ionisation can be achieved in surfactants with donor/acceptor head group capabilities.

3.1.2.3 Computational studies of PIBSA-based surfactants

Computational studies of PIBSA-based surfactants and especially within context of the explosive emulsion formulations are very scarce in literature. Masalova *et al.* reported

calculations of the head group size for the series PIBSA-MEA, PIBSA-UREA and PIBSA-IMIDE using molecular mechanics ACD freeware 3-D optimisation [12]. Kovalchuk *et al.* reported a DFT study of the solvation of the model linear chain hydrocarbon derivatives of succinimide, using B3LYP as functional [33].

3.1.3 Ammonium nitrate

3.1.3.1 Solid Ammonium Nitrate

Ammonium Nitrate (AN) is a polymorphic solid which is known to exist in seven crystalline forms in the temperature range 0 – 187 °C [34,35]. At standard atmospheric conditions, the orthorhombic phase *IV* (-18 to 32 °C) and tetragonal phase *II* (84 – 125 °C) are of importance to this study. The crystallographic coordinates for these two crystal phases were reported by Lucas and Choi [36,37]. The coordinates of hydrogenous *IV*-AN were derived from neutron single crystal measurements. For deuterated *II*-AN, Rietveld profile-refinement of neutron diffraction measurements were done. A stable anhydrous liquid state of AN was also found in atmospheric aerosols as supermicron size particles [38]. The lifetime and efflorescence behaviour of such particles were simulated in laboratory conditions. The stability of the anhydrous liquid state was found to be highly dependent on the purity of water used in the sample preparation, and water impurities were responsible for seeding the crystallisation of AN. Computationally, AN was stable in a molten state between T= 169-189 °C with onset of thermal decomposition at 202 °C [39].

In PIBSA surfactant-stabilised emulsions, AN crystallises in predominantly the tetragonal *II*-AN form, which gradually undergoes phase transition *II* → *IV* [8]. This phenomenon is believed to occur as a result of stereochemical correspondence with the surfactant functional groups. It could be hypothesised that surfactant head groups have different affinities to the morphologically important *II*-AN and *IV*-AN growth faces.

3.1.3.2 *Structure of aqueous Ammonium Nitrate*

The density for equimolar AN:W was reported by Thompson *et al.* who derived solubility and density isotherms for AN solutions in water, which covered dilute to supersaturated concentration ranges [40]. Experimental, calculated and extrapolated density values for $AN_{(s)}$, $AN_{(l)}$ and $AN_{(aq)}$ are given in Table 3-1.

Table 3-1: Calculated and experimental densities for solid and liquid phases, and aqueous solutions of AN under normal pressure and temperature range of 255-475 K

Solution ID (molar ratio)	c (wt %) AN	T, K	Density, g cm^{-3} (exp. or calc.)	Reference
IV-AN	100	255 – 357	1.725_{exp}	Cross ref. from [41]
II-AN	100	357 – 398	1.646_{exp}	Cross ref. from [41]
I-AN	100	398 -442	1.591_{exp}	Cross ref. from [41]
AN *(Ionic melt)*	100	442-475	$1.428 - 1.408_{exp}$	[39]
AN:W *(2:1)*	89.88	373.15	1.405_{calc}	Extrapolated from [40]
AN:W *(1:1)*	80.14	333.15	1.371_{exp}	[40]
AN:W *(1:2)*	68.96	298.15	1.316_{calc}	Extrapolated from [40]

Conventionally the oxidiser phase has been viewed as a supersaturated solution of ammonium nitrate salt [42,43]. Braunstein regarded an equimolar solution of AN as an ionic melt [44]. Such systems are considered as non-dissociating for water. Protic ionic liquid mixtures have been reported to create similar dielectric environments as neat ionic liquids, due to a strong electrostatic screening of water by the ions, as reported for AN and methyl-ammonium nitrate [4,45]. In the latter ionic liquid, the cation is directionally hydrogen-bonded to water, and tetrahedral coordination of water to the network of methyl-ammonium nitrate is reported.

One of the most generalised and widely accepted thermodynamic theories of associative equilibria in the highly concentrated aqueous solutions of salts, is the thermodynamic "*quasi-lattice*" theory of association [44], which adopts the view that only the cation is hydrated. Some experimental and theoretical calculations suggest that the cationic hydration energy is stronger than that of the anion. However, results of cryoscopic

measurements for AN:W system by Keenan suggest that hydration of the nitrate anion may well exist [46]. Peleg's experimental results for liquid AN-W mixtures (0.4-1.4 molar ratio range) were in agreement with Braunstein's assumption that for an AN:W system, water is held predominantly by the cation for up to an AN-W ratio of 1, with additional W molecules possibly hydrating some anions [47].

The micro structure of aqueous solutions of AN was studied experimentally by X-Ray and neutron diffraction techniques [34,48,49]. X-Ray studies of aqueous AN solutions generally failed to differentiate between NH_4^+ and H_2O species and were thus unable to provide a resolved local ionic structure. Study of an equimolar deuterated solution (50 mol kg^{-1} ND_4NO_3 in D_2O) is of particular interest for this study in terms of structural parameters and ion coordination [48]. The results indicated that ND_4^+ and NO_3^- ions are stable in solution and have relatively weak hydration shells. The separation of the nitrogen centres in this cation-anion pair of 6.1 Å was derived from 2nd order difference isotopic substitution methods. However, this study was carried out at 100 °C. The molecular dynamics and density of such a system would be vastly different from the supercooled equimolar solution of AN inside the microdroplets in the commercial emulsion formulations, which are kinetically stable at ambient temperature.

Previously reported computational studies on the structural aspects of concentrated solutions of ammonium, nitrate and water are mostly limited to small clusters of A-W_{1-10} or N-W_{1-10} [50-54]. Aspects of phase transition, thermal decomposition and nitrosation reactions are also reported [39,55,56]. Several groups have worked on the development of ammonium nitrate-specific potentials (force-fields), for the calculation of thermophysical properties [57] and reactive force-fields, to study proton transfer reactions and decomposition chemistry [41,53].

Simulations of AN in the gas phase have shown that the $NH_4^+ - NO_3^-$ ion-pair is highly unstable [50], and the equilibrium structure of AN in the gas phase is the nitric acid–ammonia complex ($NH_3 - HNO_3$) [51]. However, in acidic solution, it exists almost exclusively as NH_4^+ and NO_3^- ions [55], and proton transfer can be ignored. An energy calculation on the solvated (explicit water model) ion-pair structure, with the dielectric

permittivity of air (ϵ *ca.*1), afforded a total energy that is 27.46 kcal mol^{-1} above that of the gas-phase hydrogen-bonded structure, suggesting that water effectively stabilised the ion-pair. Thus water is likely to render a similar stabilisation of the ion-pair at the interface of two low dielectric environments in the real emulsion situation, where AN ions are exposed to the interface between oil (e.g. dodecane, ϵ *ca*. 2) and air (ϵ *ca*. 1).

3.1.4 Water and water models

The microscopic nature of liquid water and water surfaces is not completely understood and there is an on-going experimental and computational effort to advance the knowledge, characterise and simulate its structure [58]. Many simple and complex, polarisable and non-polarisable, tetrahedral and planar water models have been developed in the last 50 years. For classical Molecular Dynamics (MD) simulations, a water monomer can be treated as rigid or as flexible. In rigid models, the bond angle H-O-H and all bond lengths are constrained to a selected set of parameters, which are often based on experimental data or ideal geometry [59-61]. In the flexible approach, geometric parameters are force-field dependent. The dynamic properties amongst water models can differ significantly when simulated under the same conditions [62]. The dipole moment can be affected by the variation of point charges, which are also known to affect the overall potential energy of the system. For the purpose of evaluation of a specific model, the radial distribution functions (RDF) may be compared to the reported data for some of the most widely used models (e.g. SPC or SPC/E) and experimental results [59].

3.1.5 Computational methods

3.1.5.1 Case studies

Konkel and Myerson used Material Studio™ and Compass FF to study the efficiency of polysorbate-type surfactants in stabilising pharmaceutical nano-suspensions [22]. Their *rapid adsorption model* was based on the *binding energy* of the surfactant to the fast growing

crystal faces of the drug. The results correlated well with the experimental stability and shelf-life of various nano-suspension based drug formulations.

Scocchi simulated interatomic interactions in the nylon-6 polymer with a surface of nanocomposite system (Cloisite 20A) using Material Studio™ and Compass FF, which was a compromise between accuracy and availability of the force field parameters for all atom types present in the molecular model [63]. A *slab model* (pseudo 2-D periodic system) of the optimised single polymer molecule–surface complex was used to calculate *interaction energy*. The predicted structure of the polymer-clay nanocomposite system obtained from the developed simulation procedure was in excellent agreement with previous experimental and atomistic simulation results.

Shen and co-workers studied the effect of a solvent on growth morphology of explosive CL-20 crystals using *slab model* with Compass force field in Material Studio™ package [64]. Crystal growth inhibition was predicted from the relative values of the *attachment energy* to the *simulated growth faces* of CL-20 crystals ($\boldsymbol{E_{att}}$) and the *adsorption energy* ($\boldsymbol{E_{ads}}$) of a solvent to the same. Predicted *growth inhibition* of some crystal faces by the solvent was in good agreement with the experimentally derived morphology of CL-20, crystallized from this solvent.

3.1.5.2 Slab model

The slab model, schematically represented in Figure 3-1, is one of the most exploited models for surface modelling [65]. In essence, the periodic boundary conditions are applied in all three dimensions with sufficient volume of vacuum left above the surface in one dimension normal to the surface, to impose zero tailing of electron density between the top and bottom of the layers in the periodic supercell. Such model can be applied to study periodic and amorphous systems.

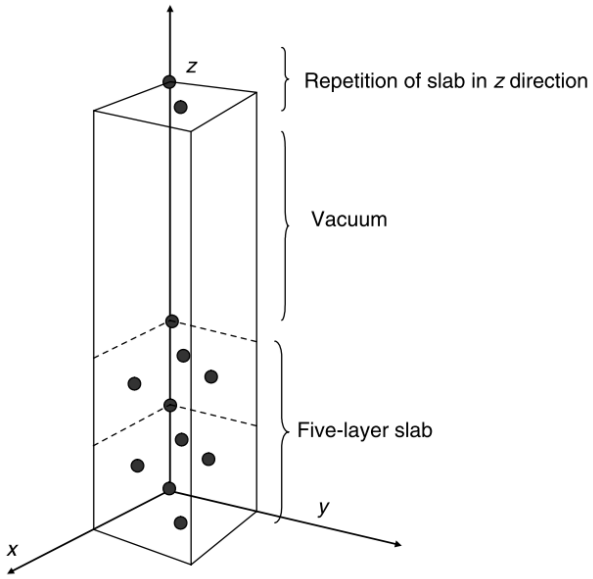

Figure 3-1: Slab model reproduced from Sholl et al. [65].

3.1.5.3 Force Fields

A force-field generally expresses the potential energy of a system as a sum of valence (geometric), cross-term, and non-bonding interactions (van der Waals and Coulombic). There are a variety of FFs supported by the Material Studio™ simulation platform, including several generics as well as a state of the art FF - CompassII.

CompassII (condensed-phase-optimised molecular potentials for atomistic simulation studies (II-second generation)) is the first force field, which was parameterised with *ab initio* and empirical methods. It is based on the earlier consistent valence (CFF9X) and polymer consistent (PCFF) Class-II force fields [66]. Its valence parameters and partial atomic charges were derived by fitting to *ab initio* data; the van der Waals (vdW) parameters were derived from MD simulations of molecular liquids, which were fitted to a wide range of experimental observables for organic compounds containing H, C, N, O, S, P, halogen atoms and ions, alkali metal cations, and several divalent metal cations. The functional forms of this FF are of the consistent FF-type. The non-bond interactions in Compass include the Lennard-Jones (LJ) 9-6 function for the van der Waals (vdW) term and Coulombic function for electrostatic interactions (Table A3-1) [67]. There is no separate term for hydrogen bonding,

and it is modelled by the same non-bond functions. CompassII enables an accurate and simultaneous prediction of structural, conformational, vibrational, and thermophysical properties for a broad range of molecules in isolation and in condensed phases. It was specially optimised to model energetic materials, and is believed to be one of the most accurate FFs for alkyl nitrates, despite the large discrepancy with experiment in the values of elastic coefficients and the LJ well depth parameters [68,69].

Another FF worthy of considering for the scope of the current study is the *Dreiding* [70]. This is a generic all-purpose FF, which affords reasonable predictions for organic, biological and main-group inorganic molecules, and it is accessible through a number of computational platforms (e.g. LAMMPS). General force constants and valence parameters in Dreiding are based on simple hybridisation rules, and bond lengths are derived from the atomic radii. Dreiding consists of the LJ potential for the vdW interactions, atomic monopoles and a distance-dependent Coulombic term for electrostatic interactions between partial atomic charges, and the LJ 12-10 potential for hydrogen bonding (Table A3-1).

3.1.5.4 Partial atomic charges

Partial charges exist even in charge-neutral species and reflect the difference in electronegativity between the atoms from which the molecule is composed. In classical method-based simulations, atomic charges may be assigned by a force-field or estimated using other available methods. In the CompassII FF, the partial charge is defined for each atom type, and it is a collective term, which is the sum of so-called bond increments (representing the charge separation between two valence-bonded atoms) of all atoms that are valence-bonded to the atom in question [67]. For force fields like Dreiding, with no inherent partial atomic charges, two methods for calculating approximate atomic point charges (based on electronegativity) are available within Material Studio™: Gasteiger and QEq [71,72]. Choice of the FF is often based on the accuracy of the predicted partial charges.

When evaluating performance of a FF, the Coulomb terms could be assessed through comparison of partial charges derived from density functional theory (DFT) simulations (e.g. Mulliken partitioning) or experimental methods (e.g. NMR chemical shifts). Mulliken charge

analysis uses spin density and atomic overlap matrices for charge partitioning [73]. Amongst other well-known computational methods, the Hirshfeld method of charge and spin analysis is based on the deformation density [74], and the electrostatic potential (ESP)-fitted charge assignment, which deduces charges from the positions of the atomic nuclei and the electron density [75].

3.2 Aims

PIBSA-based surfactants are claimed to provide metastability to high internal phase emulsions by means of a mechanical barrier and the reduction of surface tension of the supersaturated dispersed solution of ammonium nitrate salt. Numerous studies of PIBSA-surfactant stabilised emulsions were not able to elucidate ionisation behaviour in the series PIBSA-MEA, PISA-UREA and PIBSA-IMIDE. Neither were they able to deduce the mechanism responsible for the vast differences in stability rendered by the series. The experimental challenges and the existing ambiguity in the structure of the modern surfactant concentrates, as well as in the microstructure of the oxidiser phase at ambient temperatures, have provided sufficient motivation for undertaking a multi-scale computational study to address the following:

- To gain a better understanding of the mode of interaction of the widely used commercial surfactants with various components of emulsion, with emphasis on the surfactant hydrophilic functional groups by resolving atom-atom interactions with the substrate;
- To develop a multi-scale computational model based on a single materials modelling platform, for rapid screening and optimisation of the novel surfactants for application in high internal phase water-in-oil emulsions.

3.3 Models

3.3.1 General computational methods

All molecular modelling studies were carried out within a single modular platform - Biovia Material Studio™ (version 16.1). *Crystal Builder*, *Polymer Builder* and *Amorphous Cell* modules of Material Studio™ were used to construct various components of the model systems using the CHPC cluster. Density functional theory (DFT) code *DMol³* and molecular mechanics code *Forcite* were used for geometry optimisation and dynamics tasks. The *Adsorption Locator* module was used to study interactions of surfactants with various surface models. *Reflex* module was used to plot experimental data and simulate XPD patterns of model crystals. *Morphology* module was used to compute crystal growth morphology. Detailed descriptions of parameter sets are given below for the specific tasks.

3.3.1.1 Structural characterisation and hydrogen bonding

The local structure of ions (1st, 2nd and 3d) was characterised by calculation of radial distribution functions (RDF). Models were checked for agreement with gas phase clusters before using in liquid phase simulations. For solids, the intermolecular distance O---H limit for hydrogen bonding was less than 2.38 Å [76]. For amorphous structures, geometric criteria for hydrogen bonding between any pairs was applied to the intermolecular distance O---H to be less than 2.45 Å, and the angle between the O---O and O---H vectors to be less than 30° [77]. The distance between atoms participating in hydrogen bonding can be employed to assign the hydrogen bond strength [78].

3.3.1.2 Calculation of surface roughness

Surface roughness is a way of assessing surface irregularities, which may be present in the form of creases and cusps, and which affects the adsorption modes of surfactants and crystal growth. Normal crystal growth rate of a rough interface is generally higher than that of a smooth interface [79]. Surface roughness was estimated as the ratio of the accessible solvent surface, at a specified solvent radius, to the geometric surface area of the slab (in amorphous structures) or as a ratio of *Connolly* surface area to the geometric area (for crystal

surfaces). These are standard algorithms available in the Material Studio™ software package [80,81]. External accessibility of solvent is determined by a flooding algorithm that fills from the external faces of the field as implemented in *Solvent task* of *Visualizer* tools of Material Studio™ [82]. The same set of parameters was used for solid and amorphous surfaces, with a grid interval of 0.25 Å, a van der Waals scale factor of 1 and initial solvent radius of 1.4 Å.

3.3.2 Simulation of Surfactants

Simulation of PIBSA-based surfactants was based on three models, which differed by the size of the side chain attached to the functionalised succinic moiety. The input structures in **polymeric model** were based on the structures derived in Chapter 2, with 16 isobutylene repeat units ($[IB]_{16}$), connected to the succinic moiety by the isobutyl link, and *ca.* 220 atoms in total. This model was used for the surface adsorption studies.

In **semi-truncated model** of surfactants, the side chain consisted of $[IB]_{1\text{-}4}$, and had the same head-tail connection as the polymeric model, with total number of atoms of *ca.* 70. These surfactants were used for *ab initio* electronic structure studies.

The **truncated model of** surfactants had side chain reduced to the methyl-group, and consisted of *ca.* 25 atoms. This model was used for the rapid surface adsorption studies.

To label various ionisation states of the surfactants (*i.e.* cationic, anionic and zwitterionic), a first letter of the specific state was added after the abbreviated name of the surfactant (e.g. in PIBSA-MEAa, letter 'a' stands for the deprotonated or anionic ionisation state of PIBSA-MEA).

3.3.2.1 Polymeric and truncated model surfactants

The geometries of the polymeric and truncated model surfactants were first optimized in Forcite using the Smart algorithm and automatic force-field atom typing and charge assignments with CompassII (v. 1.2) [66,67,83]. For reference purposes, the geometry of HR-PIBSA was also optimized with Dreiding force field, using automatic atom typing and Gasteiger and QEq methods for charge assignment [66]. Electrostatic and van der

Waals interactions were treated with the atom-based summation and cubic spline truncation methods (cut-off = 18.5 Å; spline width = 1 Å; buffer width = 0.5 Å).

The *Quench dynamics* task of the *Forcite* module was used to find local minima of the polymeric surfactant structures, where searching of conformational space is done by alternating periods of dynamics simulation with a quench period, in which the structure is minimised using the Smart algorithm. For dynamics, atoms were assigned random velocity profiles to, and a constant-temperature/constant volume (NVT) ensemble was used with the Nosé-Hoover-Langevin (NHL) thermostat to maintain system temperature at 298 K [84]. Equations of motion were integrated with the Verlet algorithm with time steps of 0.1 fs and 100 step intervals between the quenches, for a total run time of 10 ps [85]. CompassII (v. 1.2) FF was used with the atom-based summation and cubic spline truncation methods with cut-off distance of 18.5 Å (spline width - 1 Å; Buffer width - 0.5 Å) for electrostatic and van der Waals interactions.

3.3.2.2 Geometry optimisation for semi-truncated model surfactants

The DFT *DMol³* model engine (v. 2016) with B3LYP exchange-correlation potential and DNP basis set (file 3.5) was used for geometry optimisation calculations [86]. Convergence tolerance was set to fine (with ΔE =1e-5, maximum force = 0.002 Ha Å^{-1} and maximum displacement as 0.005 Å), maximum iterations to 150 and maximum step size was 0.3 Å. Electronic parameter settings were as follows: integration was set to fine, SCF tolerance to fine, core treatment for all electrons, orbital cut-off to fine and solvent was set to vacuum. Atomic charges were derived from subsequent population analyses using Mulliken, Hirshfeld, and ESP-fitted charge analysis methods as implemented in *DMol³* of Material Studio™. Bond orders were assigned using the Mayer algorithm [87]. The magnitude of total dipole moment was calculated from the dipole moment vectors, as part of the *DMol³* GO run. The *DMol³* GO task was run in parallel using 192 cores.

3.3.3 Simulation of Ammonium Nitrate crystal growth faces

3.3.3.1 Initial coordinates and input structures

Unit cells of *II*-AN and *IV*-AN were built from the crystallographic coordinates as reported by Lucas and Choi respectively [36,37]. The coordinates of hydrogenous *IV*-AN were derived from neutron single crystal measurements and for deuterated *II*-AN, from the Rietveld profile-refinement of neutron diffraction measurements. For *II*-AN , the structure with 'orientation *a'* [36] of the two interchangeable orientations of *II*-AN was used in this study. *Reflex* module of Material Studio™ was used to simulate powder diffraction patterns for comparative analysis of the XPD patterns.

3.3.3.2 Geometry optimisation of Ammonium Nitrate crystal phases with DMol^3

Geometry optimisations of *II*-AN and *IV*-AN unit cells were done using the *DMol*^{3} module (v. 2016) with lattice optimisation. B3LYP exchange-correlation potential with DNP basis set (file 3.5) and revised Perdew, Burke and Enzerhof (RPBE) functional were used for geometry optimisation calculations [86]. Convergence tolerance was set to fine (ΔE =1e-5; max. force = 0.002 Ha Å^{-1}; max. displacement as 0.005 Å; max. iterations to 50 and max. step size was 0.3 Å). Electronic parameter settings were as follows: all electrons core treatment, restricted spin polarisation, SCF tolerance and integration grid were set to fine, orbital cut-off was set to fine and global cut-off was set to 3.4 Å. Atomic charges were derived from subsequent population analyses using Mulliken, Hirshfeld and ESP-fitted charge analysis methods as implemented in *DMol*^{3} of Material Studio™. The *DMol*^{3} task was run in parallel using 8 cores.

3.3.3.3 Geometry optimisation of Ammonium Nitrate crystal phases with Forcite

The Smart algorithm with ultra-fine convergence tolerance was used for geometry optimisation as implemented in the *Forcite* module of Material Studio™ [88]. Automatic force-field atom typing and charge assignments were used with CompassII (v. 1.2) and Gasteiger or QEq charge analysis schemes, when using the Dreiding force-field. Electrostatic and van der Waals interactions were treated with the Ewald summation method [89,90].

3.3.3.4 *Crystal growth morphology of II-AN and IV-AN*

Crystal growth morphologies for *II*-AN and *IV*-AN phases were calculated with Bravais–Friedel–Donnay–Harker (BFDH) and the Growth morphology methods as implemented in the *Morphology* module of the Material Studio™ modelling package (theoretical aspects reviewed in SI-A3) [91].

Default parameters with ultra-fine calculations quality were used in the study of the crystal morphologies of *II*-AN and *IV*-AN. CompassII (v. 1.2) FF and FF-assigned partial atomic charges were used in all calculations. The Ewald summation method was used to treat electrostatic interactions (accuracy of 1e-5 kcal mol^{-1} and buffer width of 5 Å). An atom-based method was used for control of the van der Waals interactions (cut-off of 18.5 Å, buffer width of 0.5 and spline width of 1 Å). The face list generator d_{hkl} minimum was set to 0.8. The ratio of the largest diameter to the smallest diameter orthogonal to it is the calculated aspect ratio for the predicted morphology.

Crystal growth faces with appreciable surface area were cleaved along the main face to a width of nd_{hkl} to achieve surface depth of *ca.* 30 Å. Growth surfaces were rebuilt as 2-D periodic supercells to *ca.* 30 Å a side. The 3-D slabs were constructed by adding *ca.* 100 Å of vacuum above the surface in the *c*-direction. All atoms in the slab were constrained. Slabs were used for the adsorption studies without any further geometry optimisation. The value of $\boldsymbol{E_{att}}$ was used in conjunction with the surface adsorption energy $\boldsymbol{E_{ads}}$ to quantitatively compare the effect of surfactants on growth of the morphologically important crystal faces (Section 3.3.7).

3.3.4 *Simulation of Aqueous Ammonium Nitrate*

The selected equimolar composition of the aqueous oxidiser phase (55.5 mol kg^{-1}) corresponded to an industrial product with a fudge point of 65 °C. The density of the solution was calculated from the solubility and density isotherms adopted from Thompson *et al.* [40]. The geometries of the input structures of the ions (NO_3^- and NH_4^+) and water (H_2O) were

optimised in *Forcite* with the Smart algorithm and ultra-fine convergence tolerance using CompassII FF and FF-assigned atom types and partial atomic charges. These structures were used for building a simulation cell.

The *Amorphous Cell* module was used to load multiple frames of the cubic simulation cell to a specified density with 9 ion-pairs of salt and 9 molecules of water, using 2000 loading steps per frame (a = b = c *ca.* 10.2 Å). The cell was confined along the c-lattice vector and the Ewald summation method was used for controlling electrostatics (accuracy of 1 x 10^{-5} kcal mol^{-1}; buffer width of 0.5 Å). An atom-based method was used for the van der Waals interactions (repulsive cut-off of 18.5 Å and buffer width of 0.5 Å). The lowest energy frame was used to construct an orthorhombic supercell from 4 x 4 x 3 cubic cells (a = b *ca.* 40 Å and c = 30 Å). The supercell was cleaved along the (001) direction and the resultant surface was used for the construction of a vacuum slab (denoted as "9x9x9SC").

3.3.5 Simulation of Water

The water monomer was treated as flexible and used with CompassII FF and FF-assigned parameters for atom types and partial charges. The starting configuration was a cubic box with side length of *ca*. 30 Å, which was packed using the confined layer task of *Amorphous Cell* with 900 water molecules, to achieve a density of 0.997 g mol^{-1} [60,92]. The P_1 symmetry of the initial packing was randomised using a MD run in Forcite. The simulation cell was equilibrated at constant-volume and constant-temperature regime (NVT ensemble) with randomly assigned atom velocities (Maxwell-Boltzmann distribution). The Newton equations of motion were integrated with the Verlet leapfrog algorithm using a time step of 0.1 fs and 10 000 dynamics steps (1 ps) [85]. The temperature was set to 298 K and held constant using the Nosè thermostat, as implemented in Forcite [93].

Long range electrostatic interactions and van der Waals interactions were treated with the Ewald summation method (with ultra-fine accuracy, buffer width of 0.5 Å and repulsive cut-off of 12 Å). The same dynamics parameters were used in the production run, with time step of 1 fs, and atom velocities taken from the last frame of the equilibration run

trajectory. The bulk structure of the water simulation cell was characterised by calculating ∠(HOH) and radial distribution functions (g(OO), g(HH) and g(OH)) as implemented in Materials Studio. The final frame from the MD run was used to construct the vacuum slab by cleaving the simulation cell along the (001) plane and building a vacuum slab (denoted as "W900") for the surface adsorption studies.

3.3.6 Slab models

Surfaces were translated into slab models by cleaving simulated cubic or orthorhombic cells along the (001) plane. A vacuum layer of *ca.* 100 Å was added above the top atomic layer of the surface in the z-direction to screen the interactions of the adsorbate from the bottom of the surface slab. The positions of the atoms in the middle of the slab (below and above two surfaces in the z-direction) were fixed by applying constraints to the Cartesian and fractional coordinates using the Rattle algorithm [94]. These atoms are inaccessible to the adsorbates and their dynamics are assumed to have little or no effect on the surface adsorption. This allows to increase the time step and speed up the surface adsorption simulations.

The partially constrained slab was relaxed using a GO run in *Forcite* with the Ewald summation method for electrostatics and atom-based cut-off for the van der Waals interactions. For the periodic structures of *II*-AN and *IV*-AN growth faces, fractional positions of all the atoms within the lattice were fixed without further geometry optimisations.

3.3.7 Surface adsorption studies

Simulated Annealing task within the Adsorption Locator module was used to simulate the loading of the adsorbates or adsorbate mixtures into the vacuum slab, with containing a pseudo-surface [95]. Monte Carlo searches of the configurational space of the substrate-adsorbate system [96], which was subjected to an annealing protocol, were used to identify

possible low energy adsorption sites [97]. The annealing protocol (with concurrent geometry optimisation of the adsorbate) consisted of 5 heating cycles (500 steps per cycle), using 100 000 loading steps for the polymeric and 10 000 for the truncated adsorbates. The automated temperature control was applied with default annealing temperature cycle parameter values of T_{max} = 600 K and T_{final} = 100 K. Charges were assigned by CompassII and long range interactions were treated with the Ewald summation method with accuracy of 1e-5 kcal mol^{-1} and buffer width of 0.5 Å for Coulombic interactions; and with the atom-atom summation method for the van der Waals interactions, which were truncated at 18.5 Å (using the cubic spline method with spline width of 1 Å and buffer width of 0.5 Å).

The adsorption energy $\boldsymbol{E_{ads}}$ is composed of two parts: the energy of adsorbing the sorbate onto the surface in its input conformation and a small deformation energy due to relaxation of the sorbate in the presence of the surface. The adsorption energy $\boldsymbol{E_{ads}}$ was calculated as follows:

$$E_{ads} = E_{total} - (E_{internal} + E_{deformation}) \qquad \textit{Eq. 3-4}$$

The difference between the $\boldsymbol{E_{ads}}$ as calculated by *Adsorption Locator* and $\boldsymbol{E_{att}}$ as calculated for the same face by the Growth morphology predictor was used to evaluate the effect of an adsorbate on the predicted external morphology (crystal habit), which is generated automatically from the list of faces and centre-to-face distances. In case of $|\boldsymbol{E_{ads}}| > |\boldsymbol{E_{att}}|$ the growth inhibition of that crystal growth face by the adsorbate is said to be achieved.

3.3.8 Approximations

The approximations used in this study are listed below:

a) The use of a non-reactive force-field presumes no chemical change in the system (*i.e.* proton transfer, hydrolysis *etc.*);
b) The pH effects in the aqueous AN phase were ignored. The pH factor was artificially introduced into the polymer and model molecule head groups by addition or removal of a proton;

c) Based on the relatively close values of the dielectric constants of ϵ (air) = 1, ϵ (vac) = 1 and ϵ (oil) = 2, all surface adsorption calculations were run in vacuum;
d) When modelling the interface of the emulsion droplet, the emulsion was presumed to be mono-dispersed and the curvature of the interface was considered to be 0, based on the relevant size of the simulation cell cross section cap area (*ca*. 9 x 10^2 Å^2) to the surface area of the average emulsion droplet with d_{32} of 10 μm (*ca.* 3 x 10^{10} Å^2);
e) In a vacuum slab model of the surfaces, the motion of the atoms that are a few Å below the surface were assumed to not impact the dynamics of the sorbate to any great degree;
f) In growth morphology calculations, interactions with the crystal edges were not considered.

3.4 Results and Discussion

3.4.1 Simulation of Surfactants

The objective of the computational study of PIBSA surfactants was to derive their electronic structure, predict most likely ionisations states and to gain better understanding of the structure activity relationships. Three models, with varied number of atoms in the linear side chain, were considered. The **polymeric model** was based on the major product of thermal maleation of the highly reactive (HR) PIB, and contained 16 isobutylene repeat units ($[IB]_{16}$) (Scheme 3-2). The size of these polymers (*ca*. 220 atoms) was prohibitive of the high quality *ab initio* calculations, and some extent of the side-chain truncation was mandatory. The **semi-truncated** model (*ca*. 70 atoms) contained 4 isobutylene repeat units ($[IB]_4$) and was used for the *ab initio* calculations of the electronic structure. The fully **truncated** model (ca. 25 atoms), was used for the rapid screening of surface activity.

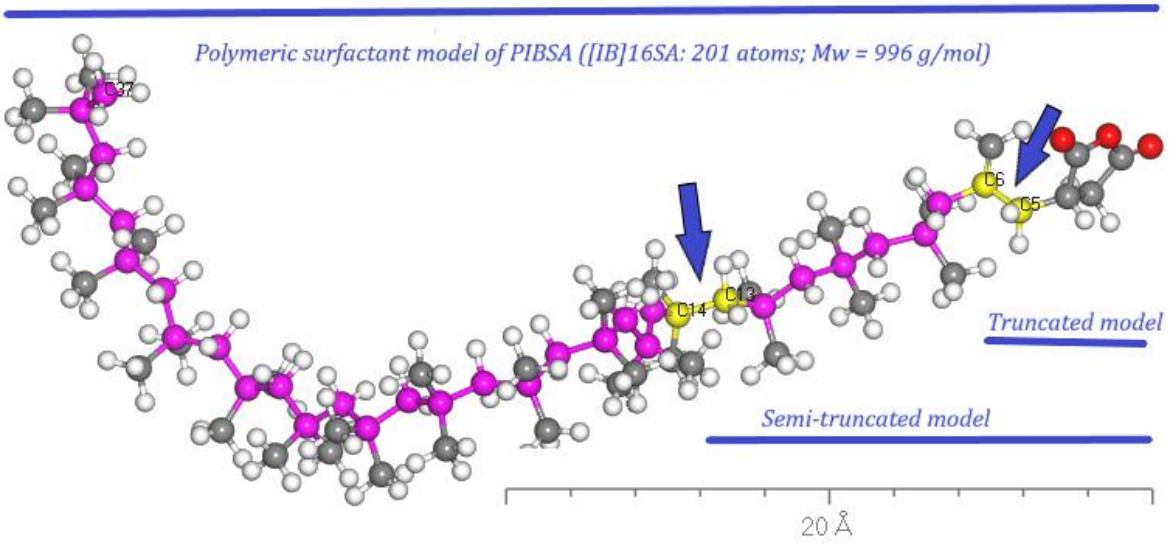

Scheme 3-2: PIBSA models in ball and stick representation. Colour legend: Hydrogen – white, Carbon – grey, Oxygen – red and Isobutylene backbone – magenta. Yellow joints indicate place of truncation.

3.4.1.1 Geometry optimisation and calculation of partial atomic charges of semi-truncated and truncated PIBSA with DMol³ and Forcite

The geometry of the succinic anhydride derivatives with a $[IB]_{1\text{-}4}$ side chain, starting with isobutyl succinic anhydride ($[IB]_1SA$) and extending the side chain by one [IB] unit at a time, was optimised with *DMol³* and partial charges were assigned using Hirshfield, Mulliken and ESP analysis methods as implemented in *DMol³* (Table A3-4). The numbering scheme and colour legends are presented in Scheme 3-3.

The effect of lengthening of the carbon side chain on the electronic density in the succinic anhydride moiety became less pronounced after the addition of the second IB fragment. Separate geometry optimisation run with Forcite was followed for the methyl-substituted succinic anhydride (CH_3SA) and partial atomic charges are listed in Table 3-2. The expected difference in the electron density between C1 and C4 atoms correlated well with the ^{13}C-NMR results obtained in our structural studies of the industrial PIBSA samples. The larger electron density on C4 ($\Delta q_{C4} q_{C1}\ ca.\ 0.1\ eV$) could be one of the contributing factors to the regioselectivity observed in the industrial PIBSA derivatives (Chapter 2).

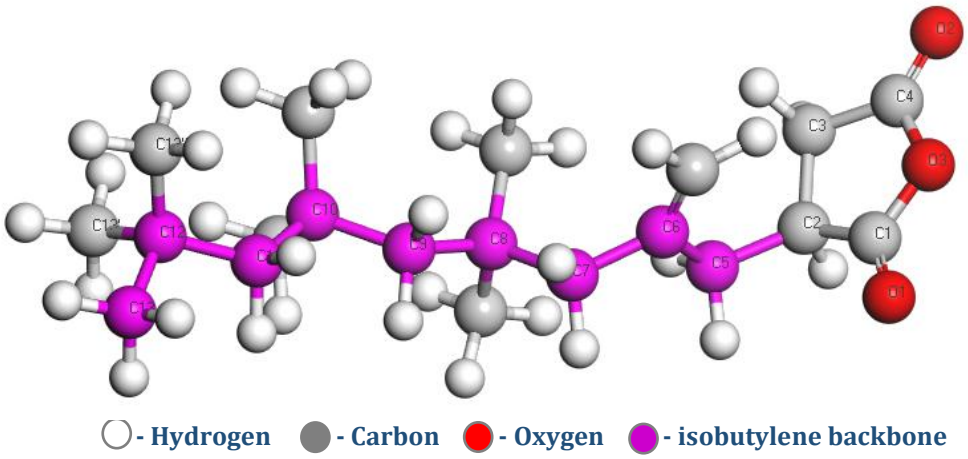

Number scheme for semi-truncated model of PIBSA

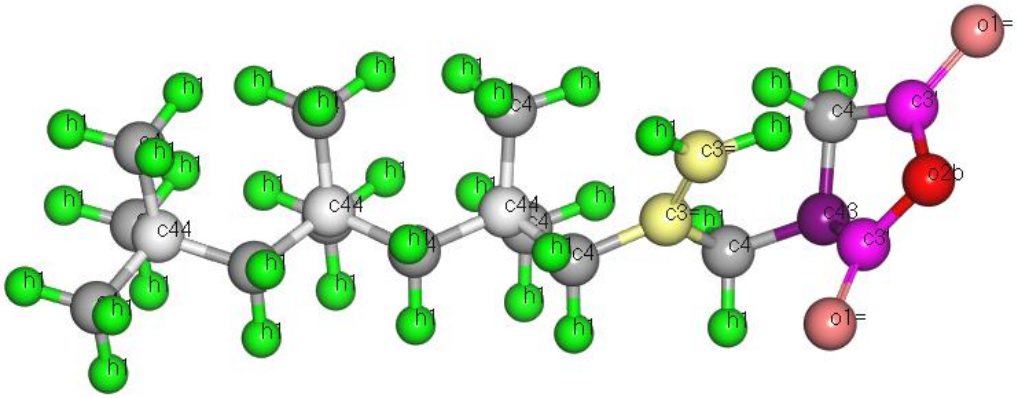

CompassII atom types for semi-truncated model of PIBSA

Scheme 3-3: Ball and stick representations for the semi-truncated model of PIBSA ([IB]$_4$SA) (above) and CompassII atom types (below). Numbers on hydrogen atoms are omitted; only linear side chain carbons and oxygens are numbered.

For the [IB]$_n$SA and CH_3SA compounds, partial charges on O atoms of the anhydride were identical for O2 and O3 atoms and differed by 0.016 *eV* for O1. Quantum charge analysis with the Mulliken method resulted in a more symmetrical density distribution, as expected, and varied significantly from the ESP fitted distribution, whilst the Hirshfeld distribution was largely underestimated. The geometry of the semi-truncated [IB]$_4$SA was optimised in a separate calculation with Forcite, using CompassII and Dreiding force fields. Partial atomic charges were automatically assigned by CompassII; and Gasteiger and QEq charge analysis methods were used with Dreiding force field (Table 3-2), as implemented in Materials Studio™ [71,72].

Table 3-2. Partial atomic charges and atom types for [IB]$_4$SA

Head group	***Compass II***		***Dreiding***			***DMol^3***		
	Atom type	**CompassII, q, *eV***	**Atom type**	**Gasteiger, q, *eV***	**QEq, q, *eV***	**Mulliken, q, *eV***	**Hirshfeld, q, *eV***	**ESP, q, *eV***
C1	c3'	0.562	C_R	0.272	0.614	0.610	0.221	0.577
C2	c43	-0.053	C_3	0.059	-0.146	-0.229	-0.005	0.137
C3	c4	-0.106	C_3	0.047	-0.242	-0.224	-0.049	-0.513
C4	c3'	0.562	C_R	0.269	0.593	0.595	0.223	0.692
O1	o1=	-0.450	O_2	-0.266	-0.472	-0.385	-0.245	-0.438
O2	o1=	-0.450	O_2	-0.266	-0.464	-0.386	-0.251	-0.460
O3	o2b	-0.224	O_R	-0.244	-0.522	-0.482	-0.114	-0.396
Tail								
C5	c4	-0.106	C_3	-0.019	-0.237	-0.116	-0.043	-0.592
C6	c3=	0.000	C_2	-0.076	0.016	0.078	0.028	0.537
C7	c4	-0.106	C_3	-0.027	-0.202	-0.117	-0.047	-0.683
C8	c44	0.000	C_3	-0.031	0.027	-0.149	0.048	0.818
C9	c4	-0.106	C_3	-0.043	-0.181	-0.053	-0.049	-0.576
C10	c44	0.000	C_3	-0.034	0.030	-0.153	0.048	0.794
C11	c4	-0.106	C_3	-0.043	-0.166	-0.046	-0.051	-0.514
C12	c44	0.000	C_3	-0.038	0.030	-0.151	0.048	0.750
C13*	c4	-0.159	C_3	-0.060	-0.394	-0.131	-0.098	-0.563

* For terminal methyl groups C-(CH_3)$_3$, the average value of the 3 charges is quoted.

Comparing quantum ESP fitted charges with those determined with force-fields, for Dreiding atom types, charges calculated with QEq method were more realistic than charges derived from the Gasteiger method. From the QEq charge analysis, the absolute value of the electron density on carbonyl carbon C1 was higher than on C4. The same was observed for the carbonyl oxygens O1 and O2. On other hand, CompassII-assigned charges were more symmetrical than ESP fitted charges, placing the same charge on both carbonyl carbons and oxygens, which is typical for CompassII [68]. The absolute values of the charges assigned by CompassII to the key atoms *i.e.* O1 and O2, which are likely to interact with polar molecules in the adsorption studies, were in reasonable agreement with the ESP-assigned charges.

3.4.1.2 *Calculation of partial atomic charges and valence parameters for semi-truncated model surfactants*

Valence parameters for the semi-truncated neutral forms of [IB]$_4$SA-IMIDE, [IB]$_4$SA-MEA, [IB]$_4$SA-UREA and [IB]$_4$SA-DEA were derived from *Geometry Optimisation* runs with *DMol*^{3} (Table 3-3).

Table 3-3: Bond distances for semi-truncated [IB]$_4$SA-derivatives from DMol^3

[IB]$_4$SA-IMIDE	[IB]$_4$SA-MEA	[IB]$_4$SA-UREA	[IB]$_4$SA-DEA
	trans-conformation	***cis-trans-coformation***	
r(C1-O1) = 1.201 Å	r(C1-O1) = 1.209 Å	r(C1-O1) = 1.204 Å	r(C1-O1) = 1.209 Å
r(C4-O2) = 1.212 Å	r(C4-O2) = 1.223 Å	r(C4-O2) = 1.225 Å	r(C4-O2) = 1.206 Å
r(C3-C4) = 1.5135 Å	r(C3-C4) = 1.523 Å	r(C4'-O4) = 1.212 Å	r(C3-C4) = 1.5142 Å
r(C1-N) = 1.389 Å	r(C4-N) = 1.362 Å	r(C3-C4) = 1.508 Å	r(C22-N) = 1.459 Å
r(C4-N) = 1.395 Å	r(N-C21) = 1.463 Å	r(C4-N1) = 1.385 Å	r(N-C23) = 1.463 Å
r(N-C21) = 1.459 Å	r(N-H) = 1.014 Å	r(C4'-N1) = 1.410 Å	r(N-H) = 1.01 Å
	cis-conformation	r(C4'-N2) = 1.374Å	
	r(C1-O1) = 1.209 Å	r(N1-H) = 1.011 Å	
	r(C4-O2) = 1.221 Å	r(N2-H_a) = 1.007 Å	
	r(C3-C4) = 1.523 Å	r(N2-H_b) = 1.008 Å	
	r(C4-N) = 1.370 Å		
	r(N-C21) = 1.463 Å		
	r(N-H) = 1.011 Å		

[IB]$_4$SA-IMIDE: In the equilibrium gas phase conformation of the [IB]$_4$SA-IMIDE, the two carbonyl groups and nitrogen atom of the imide ring (O1-C1-N-C2-O2) were found to lie in a common plane, as can be clearly seen from the dihedral angles of 0^0 for ∠(O2-C4-N-C21) and 3^0 for ∠(O1-C1-N-C21). Weak hydrogen bond between O2 and H-O3 (∠(O2---H-O3) = 123^0; 2.48 Å) is likely to be responsible for the elongation of the C4-O2 double bond and slight reduction in its double bond character (bond length = 1.212 Å; bond order = 1.85). The proximity of the two oxygen atoms (*i.e.* O2 and O3) afforded broad electronegative domain, as can be seen from the computed electrostatic potential (Scheme 3-4).

- Oxygen **- Nitrogen** **- Carbon** **- Hydrogen** **------ - hydrogen bond**

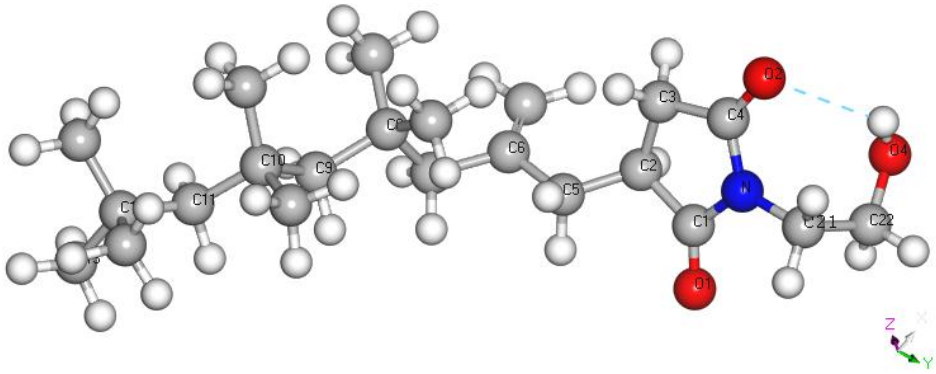

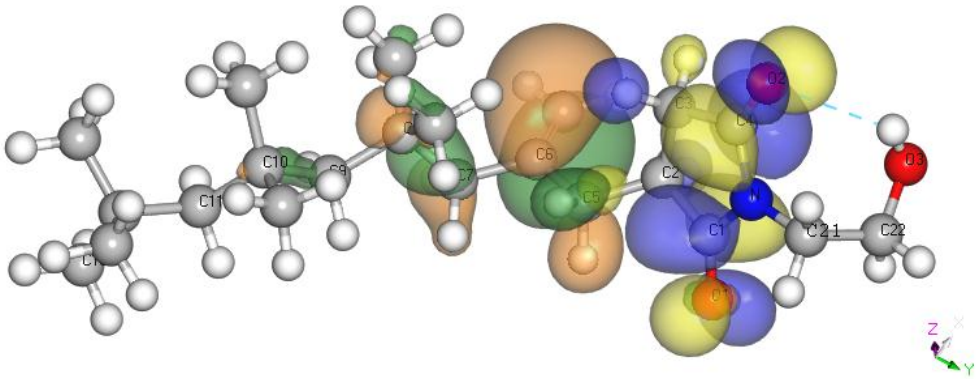

Isosurface colour map*: *LUMO *Yellow - (-) values, blue - (+) values;* ***HOMO*** *- Brown - (-) values, green - (+) values*

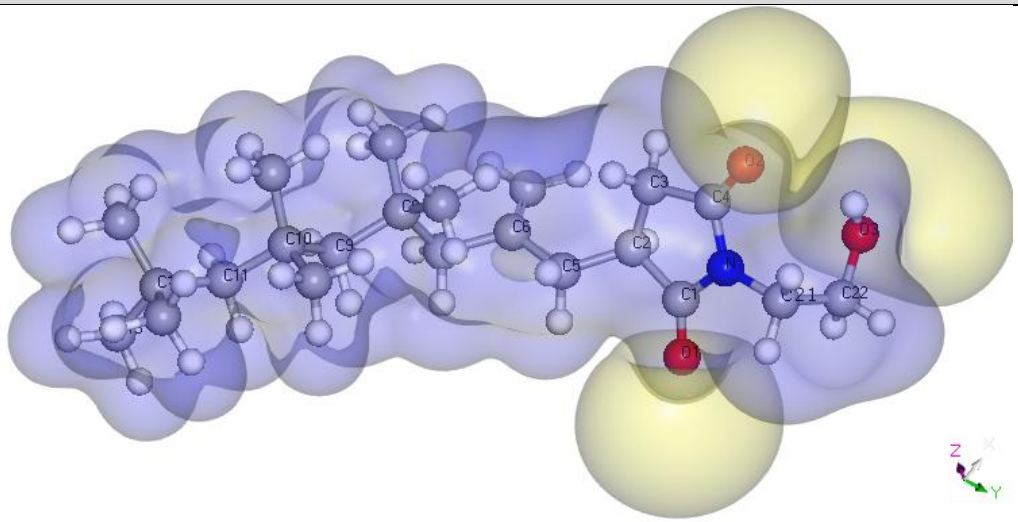

Isosurface colour map*: Yellow - (-) values, blue - (+) values*

Scheme 3-4: Numbering and colour scheme for [IB]$_4$SA-IMIDE (top); HOMO-LUMO isosurface (middle) and calculated electrostatic potential (bottom).

Quantum and FF-assigned partial atomic charges, and atom typing for the head group of [IB]$_4$SA-IMIDE are listed in Table 3-4. The increase in partial charge on the O2 oxygen, as compared to [IB]$_4$SA is due to the charge transfer from the nitrogen and the delocalisation of electrons from its lone pair, making this site a better hydrogen bond acceptor. Two distinct stretching vibrations for the carbonyl groups of the succinimide head group (1710 and 1840 cm^{-1}; Figure A3-1) were observed in the calculated Raman spectrum of [IB]$_4$SA-IMIDE.

Table 3-4. Partial atomic charges and atom types for head group of [IB]$_4$SA-IMIDE

Atom number	***Compass II***		***DMol^3***		
	Atom type	***CompassII*, q, *eV***	**Mulliken, q, *eV***	**Hirshfeld, q, *eV***	**ESP, q, *eV***
C1	c3'	0.450	0.568	0.189	0.476
C2	c43	-0.053	-0.234	-0.007	0.078
C3	c4	-0.106	-0.209	-0.051	-0.576
C4	c3'	0.450	0.561	0.190	0.562
O1	o1=	-0.450	-0.464	-0.277	-0.496
O2	o1=	-0.450	-0.484	-0.281	-0.510
>**N**-	n3m	-0.223	-0.467	-0.031	-0.083
N-**C**H$_2$-C	c4	0.117	0.010	0.001	-0.355
C-**C**H$_2$-O	c4o	0.054	0.178	0.024	0.190
C-**O**-H	o2h	-0.570	-0.537	-0.247	-0.631
C-O-**H**	h1o	0.410	0.272	0.139	0.420

From CompassII representation of [IB]$_4$SA to [IB]$_4$IMIDE, the *sp^3* oxygen bridge atom type for anhydride' *O3* ('**o2b**') was replaced by the *sp^3* nitrogen type ('**n3m**') for the anhydrous amide; and three additional atom types were added for the *N*-ethanolamine side chain (Table 3-4). The *sp^3* hybridized '**n3m**' atom type failed to account for the succinimide ring rigidity and for the delocalization of the electron density. Subsequently, force-field assigned partial atomic charge on the imide nitrogen was overestimated by 0.14 *eV*, when compared to the ESP-assigned charge. This resonance and intramolecular HB-stabilised IMIDE derivative is unlikely to undergo protonation in the acidic environment.

[IB]$_4$SA-MEA: The minimum energy equilibrium gas phase structure of [IB]$_4$SA-MEA, with intramolecular hydrogen bond (∠(N-H---O1) = 140^0; b.l. = 2.08 Å), was the expected ***trans*-conformation** with respect to the amide hydrogen and amidic carbonyl. It presented a classic case of the amide orbital mixing and polarisation around the amidic moiety.

Table 3-5: Partial atomic charges and atom types for head groups of [IB]$_4$SA-MEA, [IB]$_4$SA -UREA and [IB]$_4$SA -DEA

Atom number	**[IB]$_4$-MEA**				**[IB]$_4$-UREA**			**[IB]$_4$-DEA**		
	CompassII		***DMol^3***		***CompassII***		***DMol^3***	***CompassII***		***DMol^3***
	Atom type	**q, *eV***	**ESP, q, *eV***	**ESP, q, *eV***	**Atom type**	**q, *eV***		**Atom type**	**q, *eV***	**ESP, *q, eV***
			trans	***cis***						
C1	c3’	0.495	0.570	0.513	c3’	0.495	0.664	c3’	0.495	0.404
C2	c43	-0.053	0.187	0.404	c43	-0.053	-0.034	c43	-0.053	0.357
C3	c4	-0.106	-0.591	-0.462	c4	-0.106	-0.256	c4	-0.106	-0.607
C4	c3’	0.450	0.730	0.733	c3’	0.450	0.577	c3’	0.562	0.755
C4’	-	**-**	**-**	**-**	c3”	0.532	0.758	-	**-**	**-**
O1	o1=	-0.450	-0.579	-0.517	o1=	-0.450	-0.503	o1=	-0.450	-0.489
O2	o1=	-0.450	-0.481	-0.586	o1=	-0.450	-0.532	o1=	-0.450	-0.569
O3	o2c	-0.455	-0.531	-0.601	o1=	-0.500	-0.533	o2c	-0.455	-0.530
O3-H	h1o	0.410	0.351	0.453	h1o	0.410	0.406	h1o	0.410	0.452
O4	h1o	-0.570	-0.576	-0.628	o2c	-0.455	-0.577	o2s	-0.272	-0.206
O4-**H**	o2h	0.410	0.371	0.404	-	-	-	-	-	-
O5	-	-	-	-	-	-	-	o2h	-0.570	-0.665
N/N1	n3mh	-0.574	-0.533	-0.632	n3mh	-0.367	-0.590	n3h1	-0.727	-0.867
N/N1-**H**	h1n	0.351	0.344	0.331	h1n	0.351	0.368	h1n	0.353	0.407
N2	-	-	-	-	n3mh	-0.718	-0.847	-	**-**	-
N2-**Ha**	**-**	**-**	**-**	**-**	h1n	0.351	0.374	-	**-**	**-**
N2-**Hb**	**-**	**-**	**-**	**-**	h1n	0.351	0.399	-	**-**	**-**

The sp^2 character of the nitrogen was evident from the near trigonal planar geometry (∠ (H-N-C4) = 119 °; ∠ (H-N-C21) = 116 °; ∠ (C4-N-C21) = 121 °), with carbon C21 lying just 6° off the common plane. Strong polarization of the amide moiety was supported by the charge shift from nitrogen to carbonyl oxygen (Table 3-5), and the magnitude of the calculated dipole moment of 6.28 Debye, which was the strongest in the series. Such

polarization would typically lead to the formation of very strong hydrogen bonds with neighbours and/or other polarisable molecules [27,29,30]. The protonation site of this amide moiety is likely to be exclusively at O2.

The calculated electrostatic potential map of the *trans*-[IB]$_4$SA-MEA is shown in Scheme 3-5. In the gas phase optimised geometry, a large negatively charged domain around O2 and O4 is sterically available for hydrogen bond formation with HB-donor sites, whilst the smaller domain on the opposite side around O1 is more sterically hindered. The geometry optimised structure of the *cis*-isomer was 8.5 kcal mol^{-1} higher in energy than the *trans*-isomer (Scheme A3-1). The expected sp^2 geometry of nitrogen appeared somewhat distorted (∠ (H-N-C4) = 112°; ∠ (H-N-C21) = 115° and ∠ (C4-N-C21) = 129°); and carbon C21 was found to lie 18° off the common plane, which the amide nitrogen shares with the attached hydrogen and carbonyl moiety (∠(O2-C4-N-C21) = 162°).

Furthermore, a larger negative charge on the nitrogen atom (q_N = -0.632 *eV*), when compared to the *trans*-isomer, is a result of the twisted geometry and poor orbital overlap. Such deviation from planarity and the increased *sp*^{3}-character would make amidic nitrogen prone to *N*-protonation; thus two possible protonation sites of *cis*-[IB]$_4$SA-MEA need to be considered (*i.e.* O2 and N) [26,28,98]. This is also likely to increase its susceptibility to hydrolysis, when compared to polarisation-stabilised amides.

A few differences were noted in the calculated Raman spectra of *cis* and *trans* isomers of [IB]$_4$SA-MEA, which are mainly due to the intramolecular hydrogen bond in the trans isomer: ((C1=O1) 1750$_{cis}$/1710$_{trans}$ cm^{-1}; (N-H) 3740$_{cis}$/3600$_{trans}$ cm^{-1}, (C-N) 3590$_{cis}$/3530$_{trans}$ cm^{-1} and 3830$_{cis}$/3810$_{trans}$ cm^{-1}; Figure A3-2).

- Oxygen **- Nitrogen** **- Carbon** **- Hydrogen** **------ - hydrogen bond**

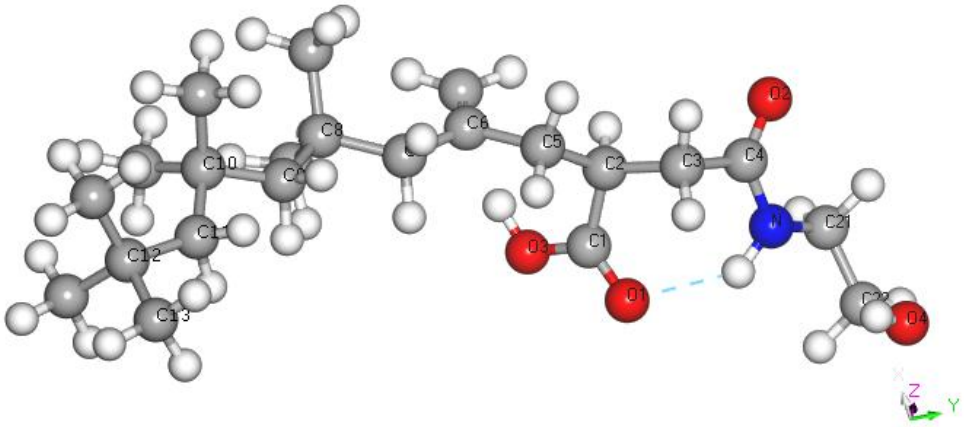

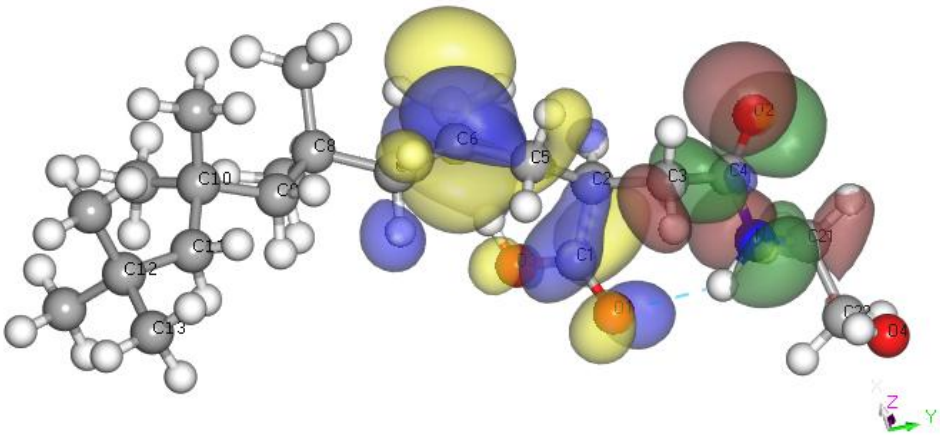

***Isosurface colour map**: **LUMO** Yellow - (-) values, blue - (+) values; **HOMO** - Brown - (-) values, green - (+) values*

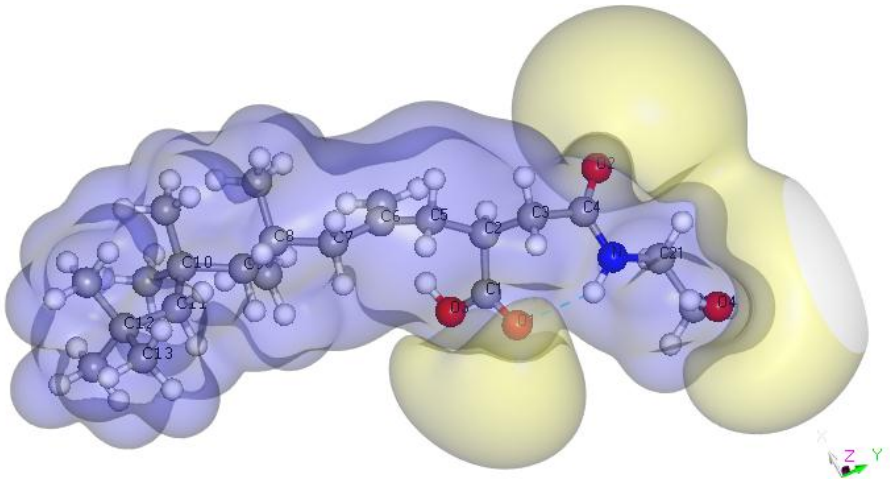

***Isosurface colour map**: Yellow - (-) values, blue - (+) values*

Scheme 3-5: Numbering and colour scheme for $[IB]_4$SA-MEA (top); HOMO-LUMO isosurface (middle) and calculated electrostatic potential (bottom).

IB]$_4$SA-UREA: From the four possible isomers (Table 3-6), the lowest energy conformation was *cis-trans* with respect of the position of the amidic hydrogen relative to the two C=O amidic bonds. In this conformation, and similarly to *cis*-[IB]$_4$SA-MEA, the O2-C4-N1-H arrangement deviated from planar. However, the delocalisation of the lone pair electron density on N1 over the amidic and ureide moieties (q_{N1} = -0.590; q_{C4} = -0.577; q_{O2} = -0.532 *eV*), aids to head group polarisation (total dipole moment = 5.2 Debye) and renders N1 an unlikely protonation site.

The additional stabilisation of this conformation is from the strong intramolecular hydrogen bonding of the amidic carbonyl (∠(O4---H-O3) =148°; b.l. = 1.88 Å; Scheme 3-6). Geometric arrangement of the terminal -NH_2 was closer to pyramidal (∠ (H_a-N2-H_b) = 115°; ∠ (H_b-N2-C4') = 114°; ∠ (H_a-N2-C4') = 120°), as previously reported for free urea, with substantial negative charge localisation on the terminal nitrogen N2 (q_{N2} = - 0.847 *eV*), making N2 capable of acting as a hydrogen bond donor or acceptor [98]. Such a geometric arrangement allows [IB]$_4$SA-UREA three potential sites for protonation: O2, O4 and terminal N2. The calculated electrostatic potential map is indicative of strong polarisation with two oppositely charged and equally sized electron donor/acceptor domains (Scheme 3-6). Three distinct stretching vibrations of the carbonyl groups of the succinureide head group (1720, 1820 and 1830 cm^{-1}) and a strong N-H vibration at 3600 cm^{-1} were present in the calculated Raman spectrum of [IB]$_4$SA-UREA (Figure A3-4).

- Oxygen **- Nitrogen** **- Carbon** **- Hydrogen** **------ - hydrogen bond**

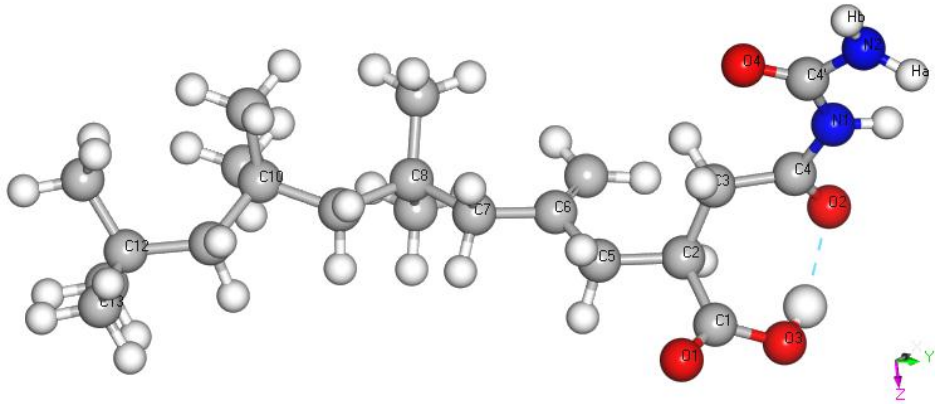

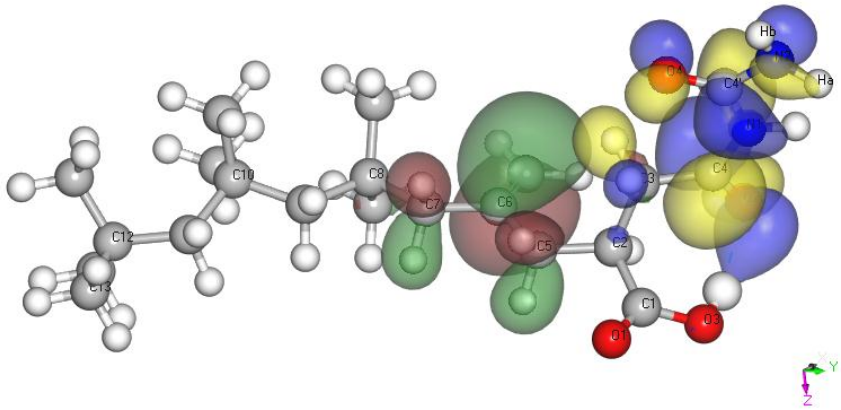

Isosurface colour map*: *LUMO *Yellow - (-) values, blue - (+) values;* ***HOMO*** *- Brown - (-) values, green - (+) values*

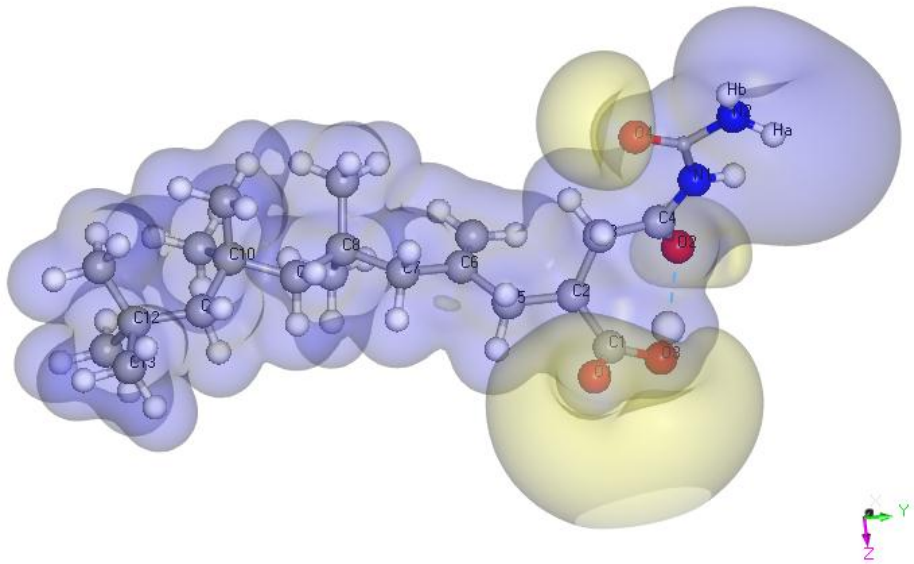

Electrostatic potential isosurface colour map*: Yellow - (-) values, blue - (+) values*

Scheme 3-6: Numbering and colour scheme for [IB]$_4$SA-UREA (top); HOMO-LUMO isosurface (middle) and calculated electrostatic potential (bottom).

Table 3-6: Conformations of [IB]$_4$SA-UREA (cis/trans position of amide hydrogen with respect to C=O), calculated SCF Energy and total dipole moment from DMol^3 calculations

Conformation	**Structure**	***SCF, Ha***	***Total Dipole,* Debye**
cis-trans	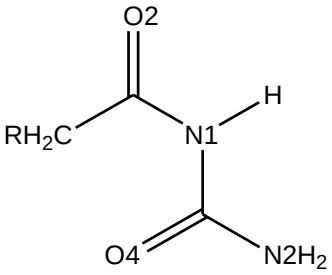	-1306.7790	5.49
cis-cis	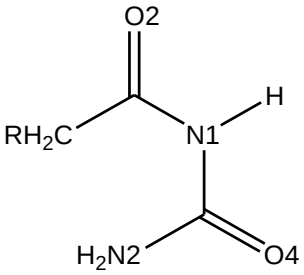	-1306.7750	3.23
trans-cis	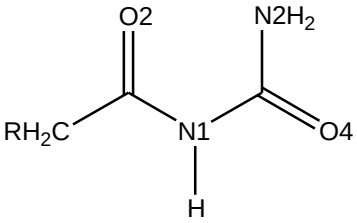	-1306.771	4.16
trans-trans	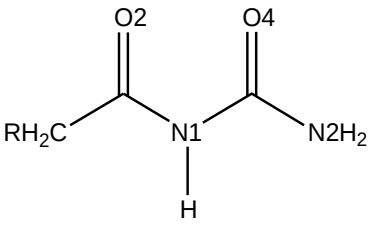	-1306.770	7.14

[IB]$_4$SA-DEA: In the case of [IB]$_4$SA-DEA, the ester carbonyl presented with a typical bond length (C4-O2) of 1.20 Å and a bond order of 2. Substantial negative charge was located on the amine nitrogen (q_N = -0.867 eV), with a lone pair readily available for hydrogen bonding or protonation, and which was also evident from the negative charged domain in the calculated electrostatic potential isosurface (Scheme 3-7). Three other negatively charged domains (around O1, O2 and O5) were scattered around the head group, providing multiple hydrogen bond acceptor sites. These sites were also of a relatively smaller size than more localized negatively charged domains in [IB]$_4$SA-MEA and [IB]$_4$SA-UREA.

From the calculated Raman spectrum of [IB]$_4$SA-DEA, three stretching vibrations of carbonyl groups appeared at 1720, 1800 and 1830 cm^{-1}; and a distinct peak at 3560 cm^{-1}, corresponding to the N-H vibration (Figure A3-5).

Based on the calculated total dipole moment of the minimum energy structures (Table 3-7), the semi-truncated series can be arranged in the following order:

[IB]$_4$SA-MEA-trans > [IB]$_4$SA-UREA-cis-trans > [IB]$_4$SA-MEA-cis PIBSA-DEA > [IB]$_4$SA-IMIDE

Relative internal stability in the series, based on the calculated HOMO-LUMO energy gap renders [IB]$_4$SA-MEA-*cis* the most stable, followed by [IB]$_4$SA-MEA-*trans,* [IB]$_4$SA-IMIDE; with [IB]$_4$SA-UREA-*cis-trans* being the least stable in the series (Table 3-7).

- Oxygen **- Nitrogen** **- Carbon** **- Hydrogen** **------ - hydrogen bond**

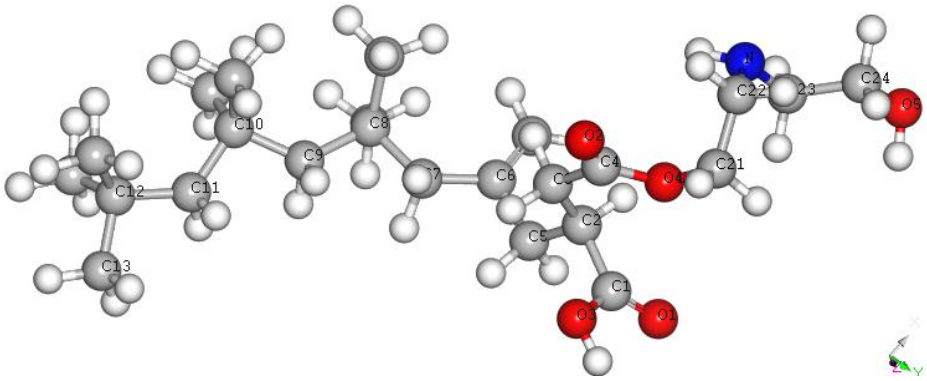

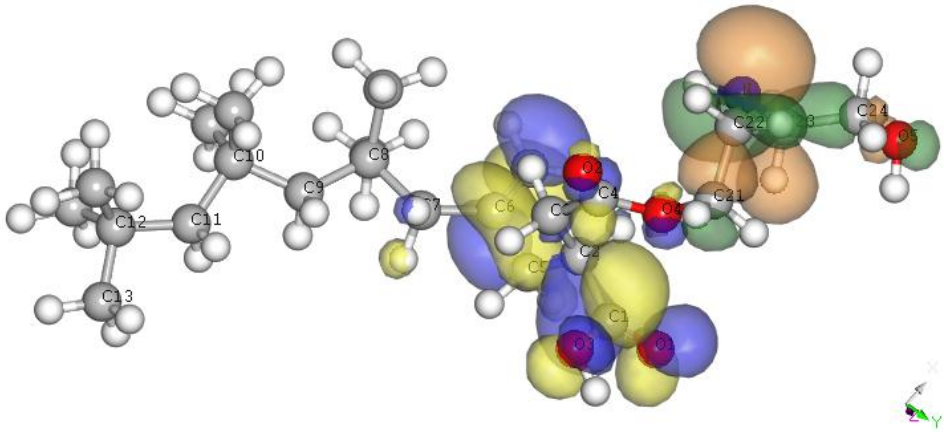

***Isosurface colour map**: **LUMO** Yellow - (-) values, blue - (+) values; **HOMO** - Brown - (-) values, green - (+) values*

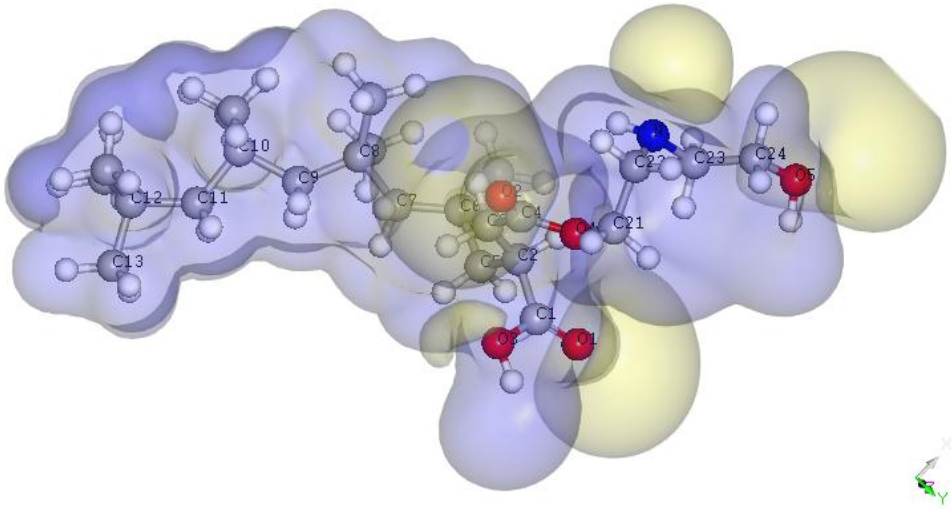

***Isosurface colour map**: Yellow - (-) values, blue - (+) values*

Scheme 3-7: Numbering and colour scheme for [IB]$_4$SA-DEA (top); HOMO-LUMO isosurface (middle) and calculated electrostatic potential (bottom).

Table 3-7: Calculated dipole moment, HOMO and LUMO energies and energy gaps for semi-truncated [IB]$_4$SA-derivatives

	HOMO, Ha	LUMO, Ha	HOMO-LUMO gap, *eV*	Total dipole moment, Debye
[IB]$_4$SA-MEA(*trans*)	-0.251445	-0.025176	6.16	6.28
[IB]$_4$SA-MEA(*cis*)	-0.244663	-0.014267	6.27	3.79
[IB]$_4$SA-UREA (O2O4-*cis-trans*)	-0.249878	-0.044098	5.59	5.49
[IB]$_4$SA-IMIDE	-0.255175	-0.030463	6.11	2.96
[IB]$_4$SA-DEA	-0.230427	-0.019620	5.97	3.05
[IB]$_4$SA-MEA(*trans*)$_{O\text{-}protonated}$	-0.350168	-0.187078	4.44	63.26
[IB]$_4$SA-MEA(*trans*)$_{N\text{-}protonated}$	-0.348020	-0.202451	3.96	66.18
[IB]$_4$SA-UREA (O2O4-*cis-trans*)$_{O2\text{-}protonated}$	-0.344668	-0.226920	3.20	67.65
[IB]$_4$SA-UREA (O2O4-*cis-trans*)$_{O4\text{-}protonated}$	-0.335355	-0.231066	2.84	77.72
[IB]$_4$SA-DEAc	-0.327925	-0.153058	4.76	81.26
[IB]$_4$SA-DEAa	-0.062685	0.106514	3.63	70.57

3.4.1.3 DFT and Forcite studies on the protonated forms of PIBSA-MEA and PIBSA-UREA

The objective of the DFT study of PIBSA-based surfactants was to predict their geometry and partial charge distribution, as well as to gain further understanding of their mechanism of action in HIPEs. Other incentives were to evaluate the performance of CompassII FF, and to calculate Raman frequencies for ionised forms in aid of the interpretation of complex spectra of the formulated emulsions. Two possible ionisation forms of the semi-truncated forms of PIBSA-MEA and PIBSA-UREA converged with DFT geometry optimisation, and were subsequently analysed with DMol^3 and Forcite.

[IB]$_4$MEA$_{O\text{-}protonated}$: Elongation of the carbonyl double bond and loss of some double bond character were evident from the *DMol^3* geometry optimised structure (b.l. (O2-C4) = 1.32 Å); the amide bond shortened and presented with partial double bond character (b.l (N1-C4) = 1.29 Å); an intramolecular hydrogen bond of medium strength measured 1.79 Å (∠ (N-H…O1) = 152°; Scheme 3-8). A slight decrease in bond length was observed between C3-C4 (1.49 Å) in the ionized state when compared to its native neutral form (1.52 Å), with

a significant amount of negative charge shifted from the lone pair of the amide *N* to the C3 carbon (Δq = -0.260 *eV*; Table 3-8).

In the calculated Raman spectrum, the carbonyl vibration at 1810 cm^{-1} peak has disappeared, and the signal at 1750 cm^{-1} has increased in intensity. The peak corresponding to the N-H vibration at 3590 cm^{-1} in the unprotonated form has shifted by 10 cm^{-1} to a higher wave number (Figure A3-3). A similar situation was reported by Ghaicha, where a 10 cm^{-1} frequency shift of the peak at 3425 cm^{-1} towards higher frequency was observed in the FT-IR spectrum of PIBSA-MEA monolayers at the aqueous salt interface [10,16]. This finding is suggestive that, in the acidic environment, the PIBSA-MEA surfactant undergoes the expected *O*-protonation.

With Forcite, the two possible ways of representing *O*-protonated carbonyl group are depicted in Scheme 3-3 for CH_3SA-MEAc. The CompassII-assigned partial atomic charges for the partial double bond structure representation are listed in Table 3-8. The CompassII-assigned partial charges on all heteroatoms, compared reasonably well to the quantum distribution. However, the total charge in this force field representation was near zero, mainly due to the differences in quantum/FF atomic charges on C2, C3 and C4 atoms (Table 3-5).

From a structure representation point of view, using a double bond for the amide-bearing carbonyl group (C4=O2) to build *O*-protonated amide form resulted in the different atom type assigned to *O2* ('**o**'). This affected the partial atomic charge on C4, which also significantly deviated from the quantum distribution (q_{C4} = $0.045^{\text{CompassII}}$/0.547^{ESP} *eV*, Table 3-8). The overall molecular charge in this representation was near zero (these calculations are not included). Automatic FF atom type and charge assignments were not adequate for this structural arrangement.

● - Oxygen ● - Nitrogen ● - Carbon ○ - Hydrogen ------ - hydrogen bond

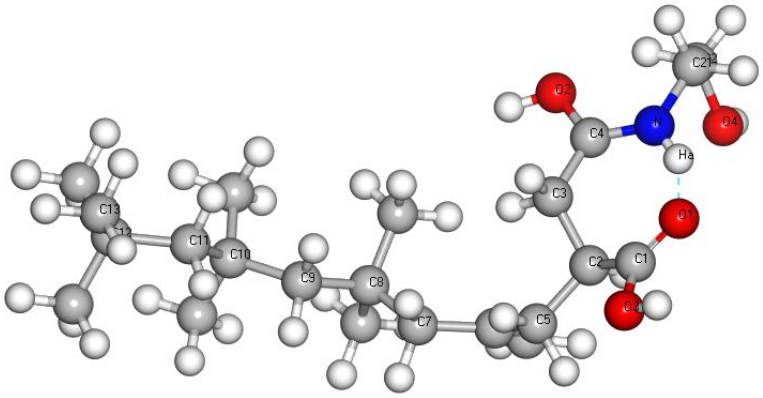

[IB]$_4$SA-MEA$_{O\text{-}protonated}$

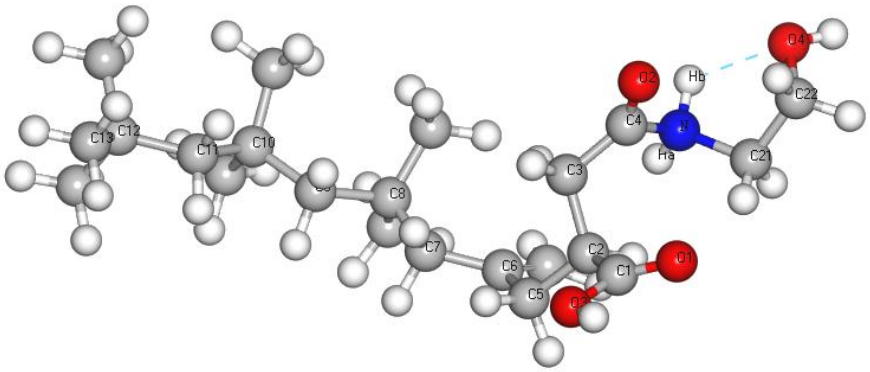

[IB]$_4$SA-MEA$_{N\text{-}protonated}$

Scheme 3-8: DMol^3-optimised geometries and atom numbering of O- and N-protonated forms of [IB]$_4$SA-MEA.

● - Oxygen ● - Nitrogen ● - Carbon ○ - Hydrogen ------ - hydrogen bond

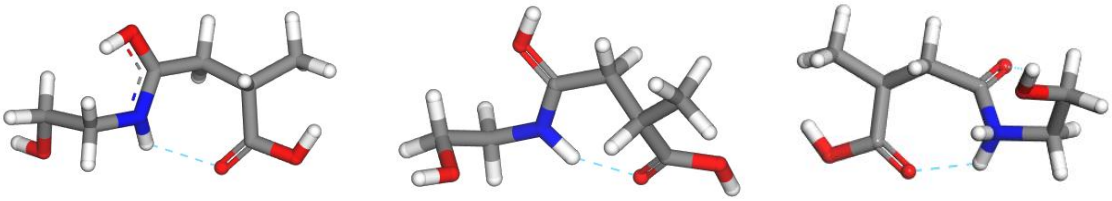

CH$_3$SA-MEA$_{O\text{-}protonated}$ (partial double bond)	***CH$_3$SA-MEA$_{O\text{-}protonated}$*** (double bond)	***CH$_3$SA-MEA$_{N\text{-}protonated}$***

Scheme 3-9: CompassII representation of protonated CH$_3$-MEAc forms.

[IB]$_4$MEA$_{N\text{-}protonated}$: With *N*-protonation of the amide and removal of partially delocalised electrons to form an N-H bond the carbonyl group, the bond order of O2-C4 changed to 2.00. Subsequently, the b.l reduced from 1.22 Å in the neutral form to 1.18 Å (Scheme 3-8). Substantial elongation of the amide bond (*N-C4*) and subsequent reduction in the bond order (b.l. = 1.56 Å; b.o. = 0.73) were observed as a result of ionisation. A high intensity peak at 1950 cm^{-1} was noted in the calculated Raman spectrum (Figure A3-3). The absolute values of the ESP-assigned charges on the hydroxyl group were affected by ionisation; however this effect is not reflected in the CompassII-assigned charges (Table 3-8).

Table 3-8: Partial atomic charges and atom types for the protonated forms of [IB]$_4$MEA

Atom number	[IB]$_4$-MEA$_{O2\text{-}protonated}$			[IB]$_4$-MEA$_{N\text{-}protonated}$		
	DMol^3	CompassII		DMol^3	CompassII	
	ESP, q, *eV*	Atom type	q, *eV*	ESP q, *eV*	Atom type	q, *eV*
C1	0.510	c3'	0.495	0.474	c3'	0.495
C2	0.436	c43	-0.053	0.468	c43	-0.053
C3	-0.727	c4	-0.106	-0.587	c4	-0.106
C4	0.547	c3	0.126	0.609	c3'	0.583
C21	-0.197	c4	0.081	-0.143	c4	0.301
C22	0.183	c4o	0.054	0.033	c4o	0.054
O1	-0.535	o1=	-0.450	-0.493	o1=	-0.450
O2	-0.417	o2h	-0.437	-0.328	o1=	-0.450
O2-**H**	0.424	h1o	0.410	-	-	-
O3	-0.563	o2c	-0.455	-0.563	o2c	-0.455
O3-**H**	0.492	h1o	0.410	0.481	h1o	0.410
O4	-0.637	o2h	-0.570	-0.633	o2h	-0.570
O4-**H**	0.436	h1o	0.410	0.459	h1o	0.410
N	-0.216	n3	-0.640	-0.273	n4+	-0.100
N–**H$_a$**	0.346	h1n	0.353	0.334	h1n	0.280
N–**H$_b$**	-	-	-	0.268	h1n	0.280
Net Charge, eV	**1**	**-**	**0**	**1**	**-**	**1**

The CompassII-assigned charge for the amidic nitrogen ('**n4+**' atom type) was fair, compared to the ESP assigned charge (q_N = -0.100$^{\text{CompassII}}$/-0.273$^{\text{ESP}}$ *eV*). The FF calculated charges on the amide protons – H_a and H_b ('**h1n**' atom type) were in good agreement with

the quantum distribution ($q_{Ha=}q_{H,b}$ = 0.280^{CompassII}/q_{Ha} = 0.334^{ESP} and q_{Hb} = 0.268^{ESP} *eV*). The net charge on *N*-protonated CH_3SA-MEA in the force field representation was 1 *eV*.

The two stable isomers of [IB]$_4$SA-UREA were the *O*-protonated forms, where the proton is placed at either of the two acylureide carbonyl oxygens O2 or O4 (Scheme 3-10). Geometry optimisation run with DMol^3 of the N2-protonated [IB]$_4$SA-UREA resulted in repositioning of the proton within bonding distance of carbonyl O4. The FF representation of the *N*-protonated form of this isomer will be considered in Section 3.4.1.4.

[IB]$_4$UREA$_{O2\text{-}protonated}$: Geometric parameters and bond orders for the O2-protonated acylureide moiety were arranged as follows: reduction of bond orders of O2-C4 (b.o = 1.21; b.l. = 1.31 Å) and N1-C4' (b.o. = 0.83; b.l 1.48 Å), and acquired partial double bond character between C4-N1 (b.o. =1.38; b.l. = 1.30) and between C4' and N2 (b.o. = 1.22; b.l = 1.34 Å) presented as expected. The high intensity peaks at 1260 and 1400 cm^{-1} were observed on the Raman spectrum; three distinct C-O peaks around 1800 cm^{-1} (1650, 1670 and 1900 cm^{-1}); and significantly diminished peak intensities from 3000 to 3600 cm^{-1} (Figure A3-4). This ionisation form, in the gas phase state, had a slightly lower SFC than its *O4*-protonated isomer.

In CompassII representation (Scheme 3-11), with the partial double bonded structure between *O2-C4-N1*, for the secondary amide, FF-assigned partial charges, compared reasonably well to the quantum distribution (Table 3-7). However, the net molecular charge in the force field representation of the *O2*-protonated amide was near zero, mainly due to the parameterisation of the '**c3**' atom type assigned to carbonyl' *C4* at the protonation site, which subsequently affected the partial atomic charges on both adjacent atoms (*i.e. C3* and *N1*). When a protonated C-O group was represented with a double bond, the atom type assigned to *O2* changed to '**o**', like in the case of [IB]$_4$SA-MEA$_{O\text{-}protonated}$; and partial atomic charge on C4 deviated even further from the quantum distribution (q_{C4} = 0.045^{CompassII}/0.531^{ESP} *eV*). The overall molecular charge in this representation remained near zero (these calculations are omitted).

[IB]$_4$UREA$_{O4\text{-}protonated}$: A notable feature for this isomer was the intramolecular hydrogen bond (b.l. = 1.42 Å, ∠(O2-H---O1) =173°). The bond order for the succinamide carbonyl (O2-C4) was close to double bond character (b.o. = 1.94; b.l. = 1.22 Å); the bond order for N1-C4 was 0.92**,** with a reduced bond length when compared to the neutral form (1.44 Å); the bond between N1-C4' shortened, with a reduced bond order of 1.15 (b.l. = 1.35 Å); partial double bond character between C4'-O4 with a bond order of 1.33 and bond length of 1.28 Å was observed. Such an arrangement around the succinamide group would allow formation of a stronger hydrogen bond with the surface substrate due to amide bond polarisation. The amide bond to N2 of the urea moiety (C4'-N2) was shortened and the bond order acquired partial double bond character (b.l. 1.32 Å; b.o. of 1.32), with N2 having assumed a sp^2 hybridised state with ∠ (H_a-N2-H_b) of 119°, ∠ (H_b-N-C4') of 118° and ∠ (H_a-N-C4') of 123°.

Table 3-9: Partial atomic charges and atom types for the protonated forms of [IB]$_4$SA-UREA

Atom number	[IB]$_4$-UREA$_{O2\text{-}protonated}$			[IB]$_4$-UREA$_{O4\text{-}protonated}$		
	DMol^3	CompassII		DMol^3	CompassII	
	ESP, q, *eV*	Atom type	q, *eV*	ESP q, *eV*	Atom type	q, *eV*
C1	0.647	c3'	0.495	0.645	c3'	0.495
C2	0.044	c43	-0.053	0.130	c43	-0.053
C3	-0.369	c4	-0.106	-0.248	c4	-0.106
C4	0.531	c3	0.126	0.637	c3'	0.450
C4'	0.761	c3"	0.532	0.840	c3	0.231
O1	-0.498	o1=	-0.450	-0.478	o1=	-0.450
O2	-0.454	o2c	-0.437	-0.418	o1=	-0.450
O2-**H**	0.452	o2h	0.410	-	-	-
O3	-0.497	o2c	-0.455	-0.474	o2c	-0.455
O3-**H**	0.411	h1o	0.410	0.434	h1o	0.410
O4	-0.470	o1=	-0.500	-0.508	o2c	-0.436
O4-**H**	-	-	-	0.455	o2h	0.410
N1	-0.437	n3	-0.469	-0.693	n3mh	-0.455
N1-**H**	0.400	h1n	0.353	0.413	h1n	0.351
N2	-0.855	n3mh	-0.718	-0.878	n3	-0.806
N2-**Ha**	0.423	h1n	0.353	0.374	h1n	0.351
N2-**Hb**	0.450	h1n	0.353	0.399	h1n	0.351
Net charge, eV	***1***	***-***	***0***	***1***	***-***	***0***

- Oxygen **- Nitrogen** **- Carbon** **- Hydrogen** **------ - hydrogen bond**

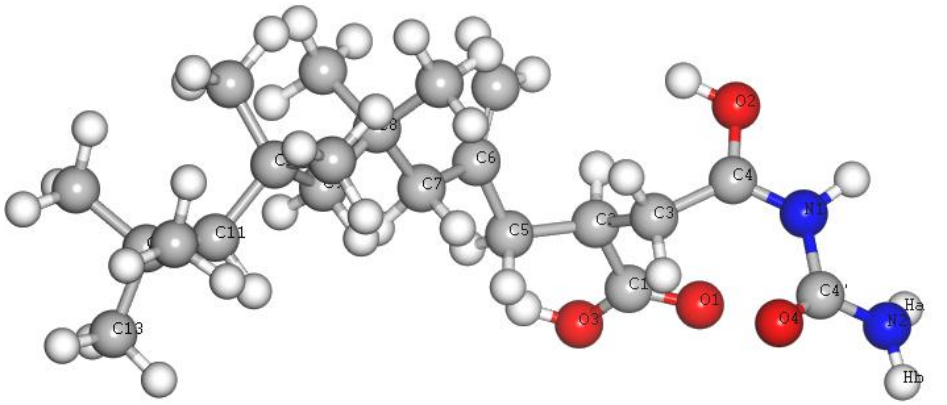

[IB]$_4$SA-UREA*O2-protonated*

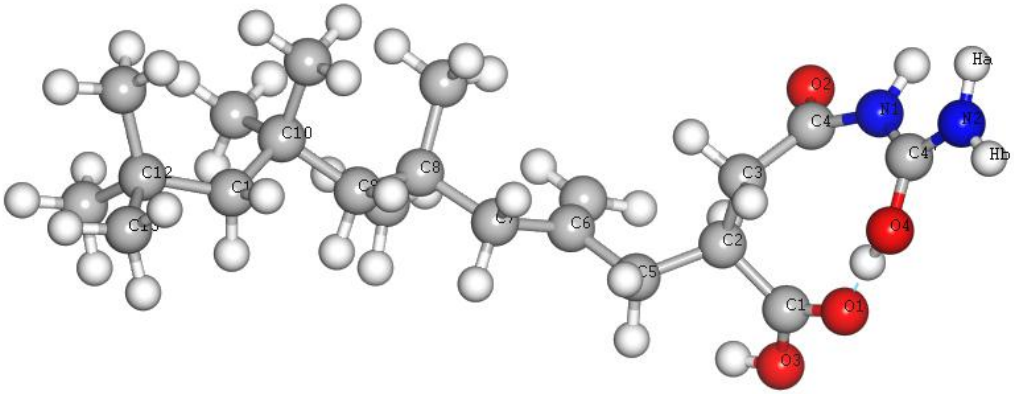

[IB]$_4$SA-UREA*O4-protonated*

Scheme 3-10: DMol^3-optimised geometries and atom numbering of O-protonated forms of [IB]$_4$SA-UREA.

The high intensity peaks at 1260 and 1560 cm^{-1} (1270 and 1500 cm^{-1} in the molecular form) were observed in the Raman spectrum corresponding to O-H and N-H bending vibrations, respectively; three distinct C-O peaks around 1800 cm^{-1} (1720, 1740 and 1840 cm^{-1}) were ascribed to the O4-protonated amide arrangement; a characteristic high intensity vibrational frequency peak appeared at 2310 cm^{-1}; and flattening of the amide stretching (N-H) and O-H peaks around 3000- 3600 cm^{-1} was also prominent (Figure A3-4).

● - Oxygen	● - Nitrogen	● - Carbon	○ - Hydrogen	------ - hydrogen bond

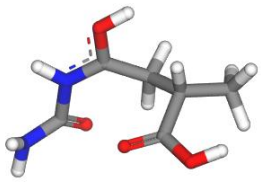	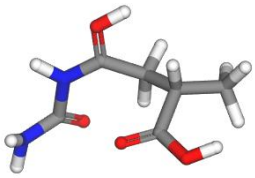	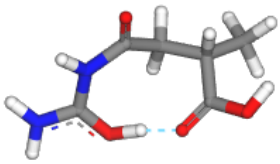	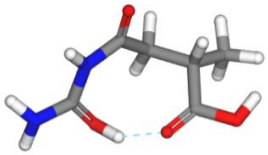
CH_3SA-$UREA_{o2\text{-}protonated}$ (partial double bond)	***CH_3SA-$UREA_{o2\text{-}protonated}$*** (double bond)	***CH_3SA-$UREA_{o4\text{-}protonated}$*** (partial double bond)	***CH_3SA-$UREA_{o4\text{-}protonated}$*** (double bond)

Scheme 3-11: Structures and various representations of semi-truncated- and truncated protonated CH_3SA-UREAc.

The total charge in the FF representation for this ionisation form was near zero, and the differences in quantum/FF atomic charges on C4' (q_{C4} = 0.840/0.231 *eV*; Table 3-9). All *N*-protonated forms of the model surfactants containing atom type '**n4+**' were optimised using automatic FF parameters for all energy contributors containing this atom type, i.e. bond stretch, angle bend, torsion and inversion terms. The negative charge-bearing carbonyl oxygens (O=C-O$^-$), present in the anionic form of PIBSA-derivatives are typed as '**o1-d**', and FF-derived partial charges were in good agreement with the quantum distribution.

3.4.1.4 Forcite geometry optimisation of polymeric and truncated surfactant forms for surface adsorption studies

The truncated structures of PIBSA surfactants and their ionised forms are depicted in Scheme 3-12 and 3-13.

For PIBSA polymeric forms, the side chain contained $[IB]_{16}$ repeat units linked to the succinic moiety by isobutenyl. Overall, automatically assigned atom types and charges in the molecular forms of the surfactants reproduced quantum distribution reasonably well.

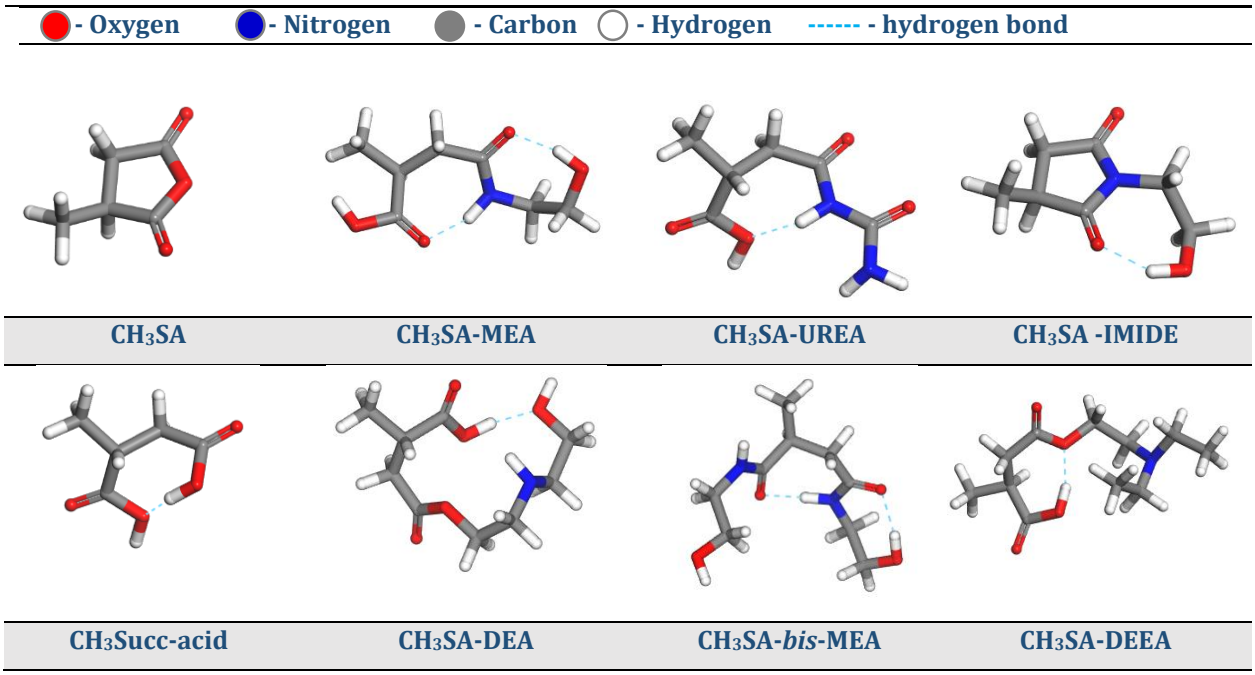

Scheme 3-12: Stick model of CompassII-optimised geometries of Methyl Succinic anhydride and derivatives (dashed blue lines represent intramolecular hydrogen bond).

For the FF representations of the polymeric and truncated ionisation forms, the parameters were the same as discussed in the previous sections, where the extent of side chain on the assignment of head group charge did not affect partial charges of the head group.

● - Oxygen	● - Nitrogen	● - Carbon	○ - Hydrogen	------ - hydrogen bond

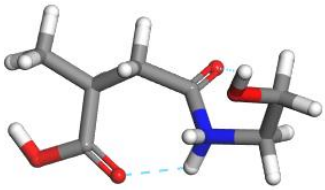	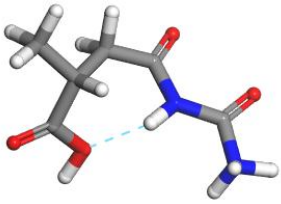	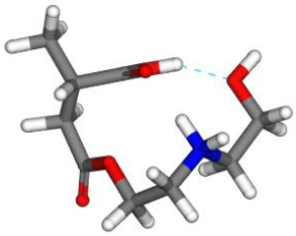
$CH_3SA\text{-}MEA_{N\text{-}protonated}$	**$CH_3SA\text{-}UREA_{N\text{-}protonated}$**	**$CH_3SA\text{-}DEAc$**
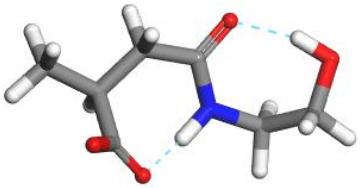	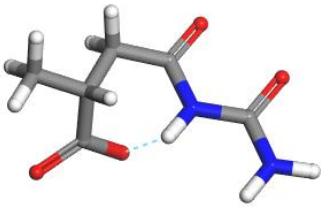	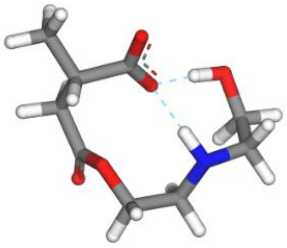
$CH_3SA\text{-}MEAa$	**$CH_3SA\text{-}UREAa$**	**$CH_3SA\text{-}DEAa$**
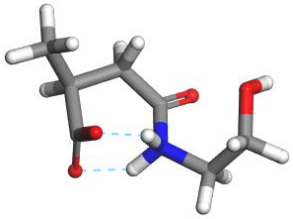	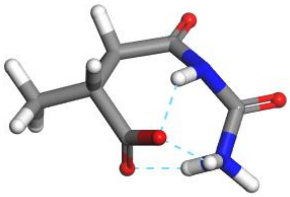	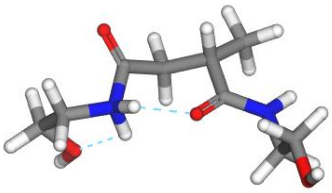
$CH_3SA\text{-}MEAz$	**$CH_3SA\text{-}UREAz$**	**$CH_3SA\text{-}bis\text{-}MEAc^*$**

*Scheme 3-13: Stick model of CompassII-optimised geometries of various ionisation forms of Methyl Succinic anhydride derivatives (subscripts: **c**-cationic form; a- anionic form; **z**- zwitterionic form; *-one of the two possible ionisation sites). Dashed blue lines represent intramolecular hydrogen bond.*

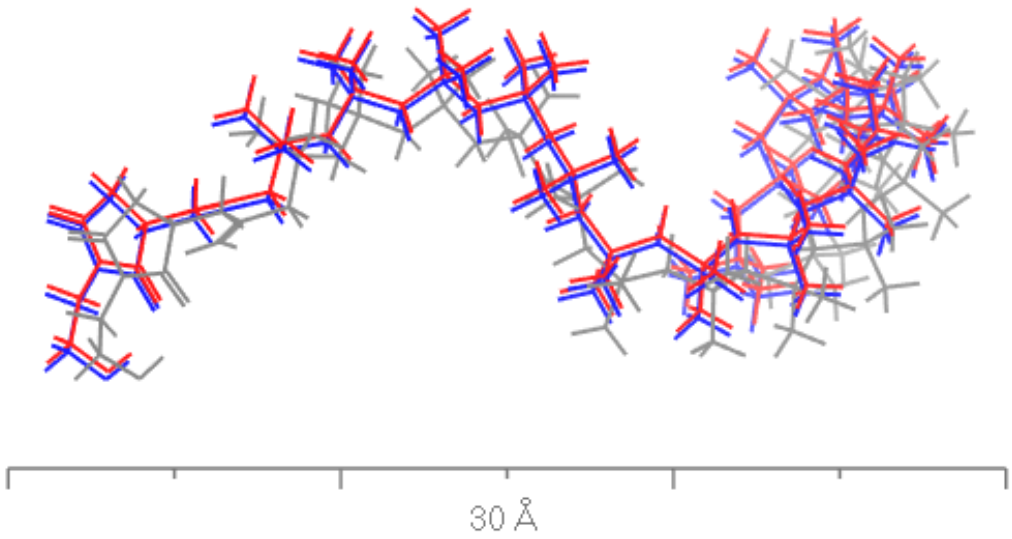

Figure 3-2: Overlaid structures of the three selected low energy conformers of PIBSA-IMIDE extracted from quench dynamics trajectory. Two of the conformers (red and blue) are almost superimposable.

The last step was to sample low energy conformations of the polymeric model surfactants (surfactants with $[IB]_{16}$SA-side chain), using quench dynamics simulations. Local minimum energy converged conformations were extracted from the 10 ps trajectory (Figure 3-2) and used in the surface adsorption studies. The Hamiltonian energy difference between the different conformers was less than 1 kcal mol^{-1}. The largest contribution to the energy came from the electrostatic and torsion energy terms.

3.4.2 Simulation of Ammonium Nitrate crystal growth morphology

3.4.2.1 Initial coordinates

Plots of the experimental coordinates of *II*-AN and *IV*-AN are depicted in Figure 3-3. For *IV*-AN, values of *d* spacing were in excellent agreement with the experimental results [99,100]. As can be clearly seen from the Reflex-calculated XPD spectra for crystals of *IV*-AN compared well to the overlaid experimental XPD spectra recorded for ground *IV*-AN prill, and other experimental results [100]. However, automatic assignments of some reflections for *IV*-AN were significantly different for the peaks with *d* values at 3.96 Å, which was assigned to

(110), 3.66 Å to (011), 2.48 Å to (201). 2.47 Å to (002), 2.27 Å to (102) and 2.26 Å to (211). The (210) reflection was listed by Reflex as absent. Calculated assignments and predicted absent reflections were in good agreement with other experimental results reported for orthorhombic *IV*-AN [101,102]. This set of experimental coordinates for *IV*-AN, as reported by Choi, was used for geometry optimisation and the calculations of crystal growth morphology [37].

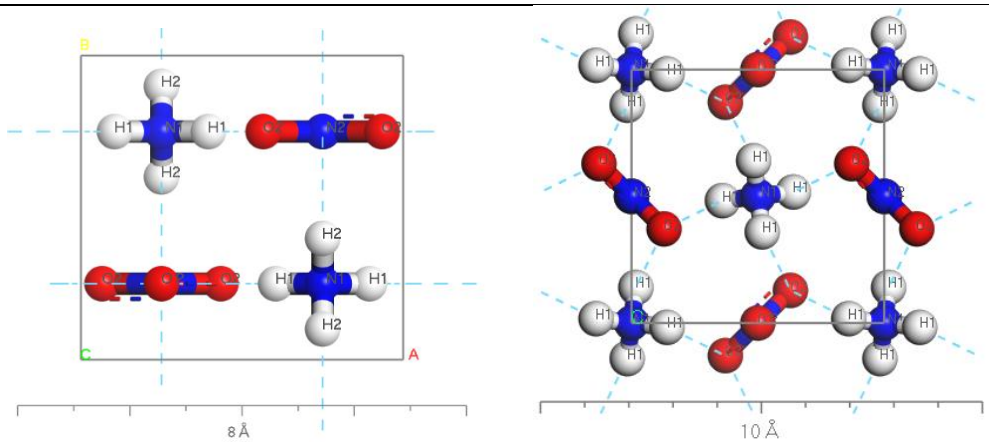

***IV*-AN, *Pmmn* [37]** **| *II*-AN, *orientation a*, *P42$_1$m* [36]**

*Figure 3-3: Unit cells of crystal phases of IV- and II-*AN.

For *II*-AN (Figure 3-4), predicted values of 2θ for the two equivalent orientations *a* and *b,* as reported by Lucas, were identical [36]. Atomic coordinates corresponding to orientation-*a* were used for geometry optimisation and the calculation of crystal growth morphology of *II*-AN [99,100].

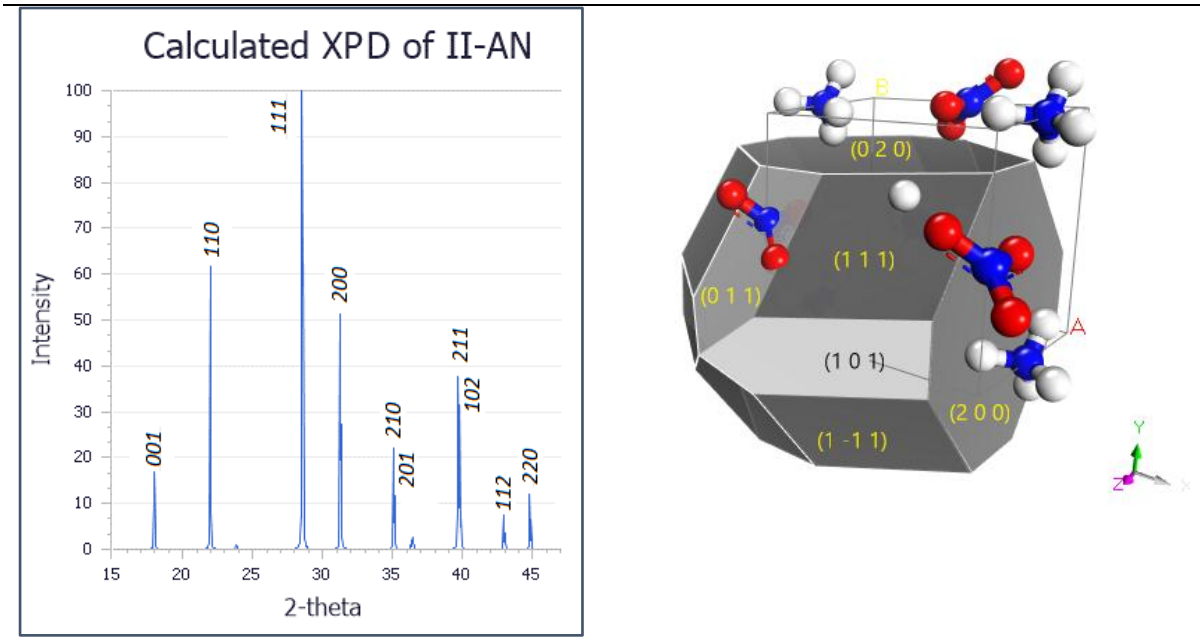

*Figure 3-4: Calculated XPD pattern for orientation a of II-*AN *crystal cell with Reflex-assigned reflections (left); and growth morphology habit calculated with CompassII FF (right). Growth face indices are in brackets.*

3.4.2.2 Geometry optimisation and partial atomic charges

Geometries of AN ions were optimised with *Forcite*, using CompassII and Dreiding FFs. Automatically assigned atom types and partial charges are summarised in Table 3-10 and structural parameters are listed in Table A3-5. Separate geometry optimisation was performed with *DMol³* and partial charges were calculated using the ESP fit.

The values of partial atomic charges for NH_4^+ and NO_3^- calculated by *DMol³* were in good agreement with literature data [39,57,103]. CompassII-assigned charges reproduced the quantum distribution fairly well for H_2O and NO_3^-. The partial atomic charge for atom type '**n4+**' of NH_4^+ deviated significantly from the values calculated with *DMol³* and from those previously reported [57]. This could be due to the inadequate bond increment for '**h1+**'/'**n4+**' as a result of FF parameterisation.

Table 3-10: Partial atomic charges and atom types for Ammonium Nitrate and Water

Atom type (ion)	**CompassII atom type [67]**	**CompassII, q, *eV***	**Dreiding atom type [70]**	**Dreiding, QEq, q, *eV***	***DMol³* ESP fit, q *eV***
N (NH_4)	n4+	-0.120	N_3	-0.756	-0.824
H (NH_4)	h1+	0.280	H_A	0.319	0.456
N (NO_3)	n3-	0.661	N_R	0.393	0.734
O (NO_3)	o12	-0.554	O_2	-0.310	-0.578
O (H_2O)	o2*	-0.820	O_3	-0.706	-0.806
H (H_2O)	h1o	0.410	H_A	0.353	0.403

The values of partial charges calculated with the QEq method for atom types N_3 and H_A, assigned to NH_4^+ by Dreiding FF, were in fairly good agreement with the quantum distribution, but deviated significantly for N_R and O_3 atom types, assigned to NO_3^-. Valence parameters derived from CompassII were in fair agreement with the experimental values [36,37]. Bond lengths for non-equivalent pairs N1-H1 and N1-H2, and N1-O1 and N1-O2 were nearly equal from CompassII calculations, which is typical for FF inherent utilisation of scalar isotropic atomic polarisabilities.

Overall, the geometry optimisation of *II*-AN and *IV*-AN crystal cells with CompassII resulted in a near isotropic cell contraction in all directions, which is a consequence of shortening of intermolecular distances between '**h1+**' and '**o12** ' atom types (H1---O1, H2---O1 and H1---O2) with equivalent total reduction in unit cell volume of *ca.* 28 % for *II*-AN and *IV*-AN.

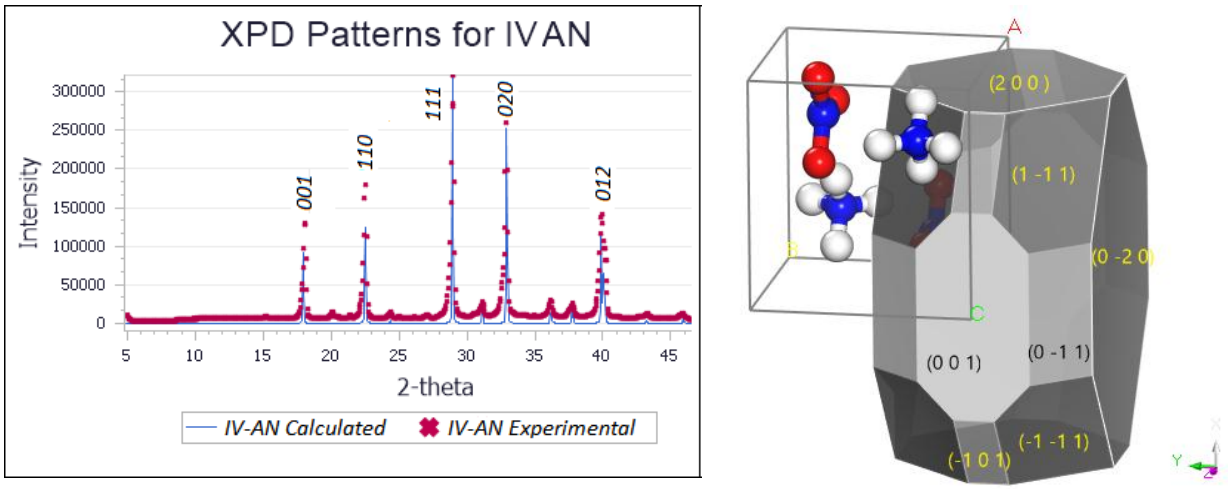

*Figure 3-5: Calculated XPD pattern for orientation a of IV-*AN *crystal cell with Reflex-assigned reflections (left); and growth morphology habit calculated with CompassII FF (right). Growth face indices are in brackets.*

The most likely reason for the shortcoming of CompassII in computing the non-bonded parameters for AN crystal forms, is the soft 6-9 function inherent to LJ potential used in CompassII for the A-N pair [68,69].

For the purpose of this study, crystal cells were used without geometry optimisation and partial atomic coordinates were fixed.

3.4.2.3 Calculation of crystal growth faces with MORPHOLOGY module

The crystal morphologies of *II*-AN and *IV*-AN (in vacuum) were predicted with *BFDH* and *Growth morphology* methods, using CompassII and Dreiding FFs (Tables 3-10 and A3-6). The choice of FF had pronounced effect on predicted crystal morphology (Figure A3-6). CompassII was used to derive stable crystal faces, d_{hkl}, centre-to-plane (c2p) distance between the growth origin and the growth face, total area and $\boldsymbol{E_{att}}$ are listed in Table 3-11. Corresponding growth morphology faces were used in surface adsorption study (Scheme 3-14).

*Table 3-11: Calculated habit faces with BFDH and Growth morphology methods for II- and IV-*AN *(in vacuum) with CompassII*

BFDH				Growth morphology			
hkl	**d_{hkl} Å**	**c2p distance, Å**	**Total facet area, %**	**d_{hkl}**	**c2p distance, Å**	**Total area, %**	**E_{att}, kcal mol^{-1}**
***IV*-AN**							
(0 0 1)	4.94	20.23	23.39	4.94	53.45	8.83	-53.45
(1 1 0)	3.95	25.32	44.67	-	-	-	-
(1 0 1)	3.75	26.69	17.04	3.75	59.40	3.84	-59.40
(0 1 1)	3.66	27.34	14.16	3.66	49.98	8.12	-49.98
(1 1 1)	-	-	-	3.09	52.16	27.05	-52.16
(2 0 0)	2.87	34.81	0.74	2.87	51.95	16.46	-51.95
(0 2 0)	-	-	-	2.72	30.07	35.71	-30.07
Aspect ratio	*1.743*			*2.067*			
***II*-AN**							
(0 0 1)	4.93	20.27	22.83	-	-	-	-
(1 1 0)	4.04	24.73	47.02	-	-	-	-
(1 0 1)	3.74	26.77	30.15	3.74	56.86	19.52	-56.86
(1 1 1)	-	-	-	3.1274	53.10	15.54	-53.10
(1 1 -1)	-	-	-	3.1274	53.10	15.54	-53.10
(2 0 0)	-	-	-	2.8596	41.15	49.40	-41.15
Aspect ratio	*1.744*			*1.825*			

The predicted growth morphology generally did not resemble the experimental morphology, although some of the slower growing faces corresponded to the high intensity reflections for both *II*-AN and *IV*-AN in the calculated and experimental XPD patterns (Figure 3-4 and Figure 3-5). For *IV*-AN, the aspect ratio of 2, calculated with *Growth Morphology* method, indicated somewhat flattened crystal morphology. In practice, needle-shaped crystals are prevalent morphological form of *IV*-AN in ambient conditions, and which is also the main crystal form of AN in PIBSA - stabilized aged emulsions [4,8,102].

Based on the calculated crystal growth morphology of *IV*-AN, (020) appeared to be one of the slower growing faces (lowest E_{att}) and accounted for more than 35 % of the crystal surface.

Table 3-12: Surface roughness of II-AN and IV-AN growth faces

Growth face index	Cross section area of simulation cell, Å²	Solvent accessible surface area, Å²	Surface roughness index
***IV*-AN**			
(1 0 1)	1124.68	1433.71	1.27
(1 1 1)	1501.30	1697.50	1.13
(2 0 0)	806.24	943.76	1.17
(0 2 0)	851.75	917.70	1.10
(0 1 1)	844.29	1004.34	1.19
(0 0 1)	1124.69	1366.21	1.21
***II*-AN**			
(1 0 1)	863.90	1141.27	1.32
(1 1 1)	883.59	925.62	1.12
(2 0 0)	846.33	958.85	1.13

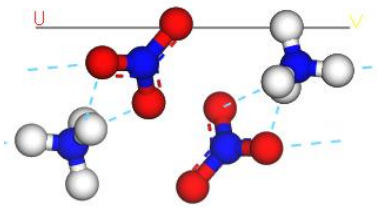

II-AN *(101)*

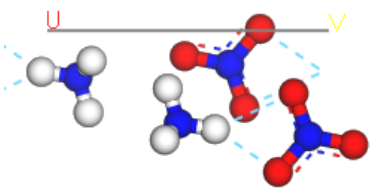

IV-AN *(101)*

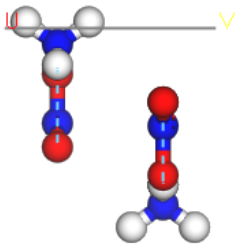

IV-AN *(001)*

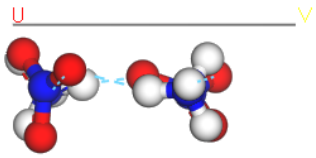

II-AN *(111)*

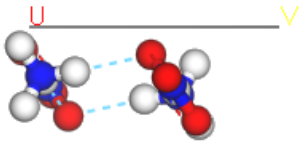

IV-AN *(111)*

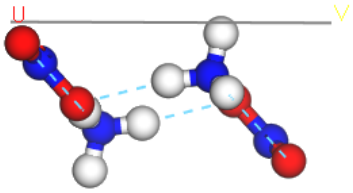

IV-AN *(011)*

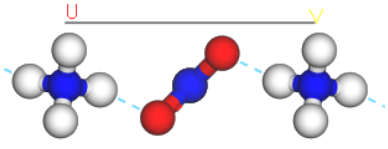

II-AN *(200)*

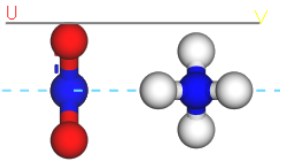

IV-AN *(200)*

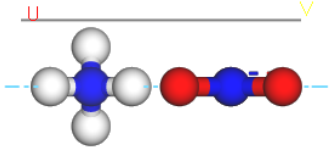

IV-AN *(020)*

Scheme 3-14: Growth faces of II-AN and IV-AN calculated with Growth Morphology method.

In terms of the calculated growth surface roughness (Table 3-12), the order of the values followed the order of E_{att} (Table 3-11). The fastest growth face (101) had the highest values of surface roughness for both crystal phases of AN. Crystal growth surfaces, of approximately 30x30x30 Å, were built from the predicted crystal growth faces of II-AN and IV-AN and used for construction of vacuum slabs for the surface adsorption studies.

3.4.3 Simulation of Aqueous Ammonium Nitrate

The intramolecular parameters and numbering scheme for the geometry-optimised input structures of ammonium nitrate and water are summarised in Table 3-13. Values of bond lengths and angles, derived from geometry optimisation with CompassII, were in good agreement with those calculated with DMol^3 and previously reported data [53,104]. A confined cubic simulation cell was packed with 9 ion pairs of ammonium nitrate (AN) and nine molecules of water (W) with a density of 1.37 g mol^{-1}. A supercell was constructed by repeating the 9x9x9SC simulation cell four times in the *a*- and *b*-directions and three times in the *c*-direction. The concentration profile for 9x9x9SC is given in Figures A3-7 and A3-8.

The total radial distribution function (RDF) was dominated by the narrow peaks corresponding to the intramolecular interatomic distances: 0.97 Å (O_W-H_W), 1.01 Å (N_A-H_A), 1.25 Å (N_N–O_N), 1.49 Å (O_W-O_W), 1.65 Å (H_A-H_A) and 2.17 Å. In the previously reported experimental study of the deuteriorated equimolar solution of A:N:W (100 ^{0}C), the intramolecular interactions O-D in (D_2O), N1-D and N2-O were said to occur at such close distances that it was not possible to distinguish between them from the total *g(r)* at 1.06(2) Å [48]. Analysis of RDFs between atom sets allowed to determine a number of key intermolecular distances for this system: 3.43 Å (N_A-N_A and N_N-N_N), 4.09 Å (N_A-O_W) and 4.55 Å (N_A–O_W), which were fairly close to the experimental values of 3.4 and 3.5 Å for N_A-N_A and N_N-N_N; and 4 and 5 Å for the hydration shells of ammonium and nitrate, respectively [48].

Table 3-13: Schematic representation, numbering scheme and intramolecular geometric parameters for the ammonium ion (NH_4^+), nitrate ion (NO_3^-) and water (H_2O)

NH_4^+	***CompassII geometric parameters***	***DMol³ geometric parameters***	***Reference geometric parameters***
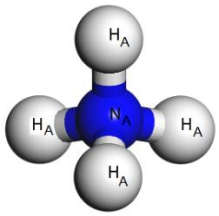	N_A-H_A = 0.957 Å H_A---H_A = 1.649 Å ∠ H_A-N-H_A = 109.471	N_A-H_A = 1.025 Å H_A---H_A = 1.674 Å ∠ H_A-N-H_A = 109.471	N_A-H_A = 1.006/1.0252 Å [50]/[105] ∠ H_A-N-H_A = 109.5/109.47 ^{0}
NO_3^-			
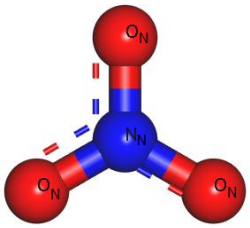	N_N–O_N = 1.257 Å O_N---O_N = 2.178 Å ∠ O_N-N_N-O_N = 120.0 ^{0}	N_N–O_N = 1.256 Å O_N---O_N = 2.175Å ∠ O_N-N_N-O_N = 120.0 ^{0}	N_N–O_N = 1.220 Å [50] ∠ O_N-N_N-O_N = 120.0 ^{0}
H_2O			
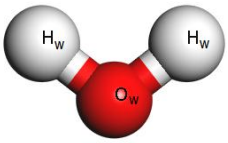	O_w–H_w = 0.957 Å H_w---H_w = 1.514 Å ∠ H_w-O_w-H_w = 104.52 ^{0}	O_w – H_w = 0.972 Å H_w---H_w = 1.521 Å ∠ H_w-O_w-H_w = 102.880^0	O_w – H_w = 1.0 Å [106] ∠ H_w-O_w-H_w = 109.47^0

The N_A-N_N distribution had 2 major peaks; at 3.45 and 5.60 Å. Shorter separation is likely to be due to direct bonding between A-N ions, as previously reported [44,49]. The only geometrically plausible structural arrangement to afford a separation of 5.6 Å is if the ions are simultaneously solvated by water N_A-H_A---O_w-H_w---O_N-N_N, which implies hydration of the nitrate anion. These results are in the range of the previously reported values of interatomic distance between two nitrogen centers *r*(N_A-N_N) in the high temperature crystal phase of *V*-AN (3.8 Å), molten ammonium nitrate salt (4.5 Å), and in a deuterated equimolar solution of ammonium nitrate at 100 ^{0}C (6.1 Å) [34,48].

The hydrogen bonding distance for H_{A}---O_{w} was found to be between 1.49-1.61 Å, which correlated well with the *ab initio* small cluster studies of an A:N:W system 1.51-1.70 Å [107]; and between 1.63-1.66 for A-W clusters [108]. Based on good general agreement of structural parameters of the periodic simulation cell it was considered as a good starting model for surface adsorption studies. The supercell was cleaved along the (001) direction and translated to a vacuum slab by extending the cell in the C-direction by 100 Å.

3.4.4 Simulation of Water

The RDFs - *g*(OO), *g*(HH) and *g*(OH) of W900 of the randomised amorphous simulation cell are shown in (Figure A3-10), and compared reasonably with the experimentally reported data for water at standard atmospheric conditions (exp./current results): *g*(OO) = 2.88/2.71Å; *g*(OH) = 1.85/1.77 Å [59,60,62]. The results compared well with the original rigid SPC/E model by Berendsen (model/current results): *g*(OO) = 2.75/2.71 Å; *g*(OH) = 1.77/1.77 Å [61]. The water surface was approximated by translation of the cleaved simulation cell by 100 Å in the C-direction. The concentration profile for W900 is given in Figure A3-9.

3.4.5 Surface adsorption studies

The total interaction energies E_{ads} for the lowest energy adsorbate-surface arrangement for PIBSA-based polymeric and truncated surfactant models, their ionisation and hydrolysis products, and some common surface inactive compounds are presented in Table 3-14 and Table 3-15, for amorphous surfaces; and in Tables A3-8 and A3-8, for solid surfaces.

3.4.5.1 Adsorption study on surfaces of aqueous salt and water

The order of surface activity for the neutral forms of he polymeric series, which was based on the absolute value of $|E_{ads}|$ to 9x9x9SC, correlated well with the experimentally observed trend of the emulsion stability, *i.e.* PIBSA-MEA > PIBSA-UREA > PIBSA-IMIDE. PIBSA-MEA exhibited the strongest interaction with the aqueous salt surface (E_{ads} = -63.59 kcal mol^{-1}), followed by PIBSA-UREA (E_{ads} = -56.71 kcal mol^{-1}) and PIBSA-IMIDE (E_{ads} = -43.11 kcal mol^{-1}). Surface inactive compounds *i.e.* dodecane and HR-PIB had similarly low affinity to either liquid surface, and could easily be differentiated from the surface active compounds. The ΔE_{ads} between the two interfaces was relatively small (*ca.* 3 and 5 kcal mol^{-1}) respectively.

Table 3-14. Adsorption energies of PIB derivatives and their truncated forms to liquid surfaces

Neutral forms of PIBSA derivatives	**E_{ads} to W900, kcal mol^{-1}**	**E_{ads} to 9x9x9SC, kcal mol^{-1}**	**ΔE_{ads}, kcal mol^{-1}**	***Neutral forms of CH_3SA-derivatives***	**E_{ads} to W900, kcal mol^{-1}**	**E_{ads} to 9x9x9SC, kcal mol^{-1}**	**ΔE_{ads}, kcal mol^{-1}**
HR-PIB	-22.93	-27.91	-4.98	Dodecane	-9.12	-12.01	-2.89
HR-PIBSA	-19.97	-51.07	-31.1	CH_3SA	-14.03	-21.94	-7.91
HR-PIBSucc acid	-31.88	-37.14	-5.26	CH_3Succ acid	-20.72	-21.64	-0.92
PIBSA-MEA	-49.84	-63.60	-13.76	CH_3SA-MEA	-23.23	-41.67	-18.44
PIBSA-UREA	-36.20	-56.72	-20.52	CH_3SA-UREA	-22.75	-45.27	-22.52
PIBSA-IMIDE	-28.11	-43.11	-15.00	CH_3SA-IMIDE	-15.06	-24.75	-9.69
PIBSA-DEEA	-35.07	-56.12	-21.05	CH_3SA-DEEA	-21.99	-40.42	-18.43
PIBSA-DEA	-37.16	-61.25	-24.09	CH_3SA-DEA	-19.64	-32.38	-12.74
PIBSA–*bis* MEA	-47.04	-50.49	-3.45	CH_3SA-*bis* MEA	-24.53	-44.33	-19.8

The interaction energies of the PIBSA-MEA and PIBSA-DEA pair with the water interface also corresponded well with the experimental trend [10], with PIBSA-MEA having the strongest affinity to water (-49.84 kcal mol^{-1}). This could be due to the additional stabilisation of the amide through the internal hydrogen bonding, which is lacking in the ester derivative. This case is discussed in more details in Section 3.4.5.2.

Considering surface activity in terms of the number of functional groups in the head of the surfactant, for PIBSA-MEA and PIBSA-*bis*-MEA, it was found that the additional amide

and hydroxyl functionalities in the latter afforded reduced surface binding to aqueous salt (Table 3-14). Conversely, for the pair PIBSA-DEA and PIBSA-DEEA (PIBSA adduct of *di*-ethyl ethanolamine, Scheme 3-12), which differ by the substituents on the amine' nitrogen, presence of the additional hydroxyl group in the former, resulted in a slightly better surface binding of PIBSA-DEA ($\Delta \boldsymbol{E_{ads}}$ (9x9x9SC) = 5 kcal mol^{-1}). This picture changed significantly for the ionised forms of these surfactants (Table 3-15), where $\boldsymbol{E_{ads}}$ to aqueous salt became proportional to the number of the ionisable sights. However, the relative surface activity of PIBSA-DEEA and PIBSA-UREA were found to be within 1 kcal mol^{-1}, despite the difference in the number of the functional groups in their head groups.

The PIB-Succinic acid, the likely hydrolysis product of PIBSA-derived surfactants, was found to have equally low $\boldsymbol{E_{ads}}$ to both liquid surfaces (Table 3-14, $\Delta \boldsymbol{E_{ads}}$ = 5.26 kcal mol $^{-1}$), which is in line with its poor experimental surface activity as reported by Ghaicha [10].

From a point of view of the initial hypothesis, all surface active compounds exhibited much lower interaction energies with water than with the aqueous salt. This criterion may be used in the initial screening of the potential surfactant candidates. Overall, the order of surface activity for the neutral forms of functionalised surfactants was as follows:

PIBSA-MEA > PIBSA-DEA > PIBSA-UREA ≈ PIBSA-DEEA > PIBSA-IMIDE

The truncated model compounds followed a similar order of activity, although the interaction energies were of lower magnitude than in the polymeric model and there were some differences in the binding modes (Figure 3-6). A shift in the centre of mass and change in the conformation of the polymeric side chain bring in additional stabilisation and result in higher adsorption energies than in the corresponding truncated model compounds (Figure A3-11).

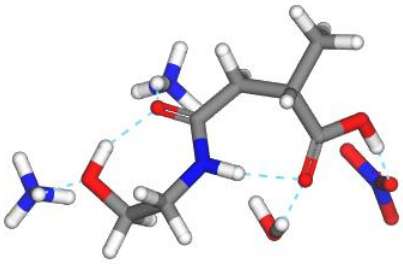

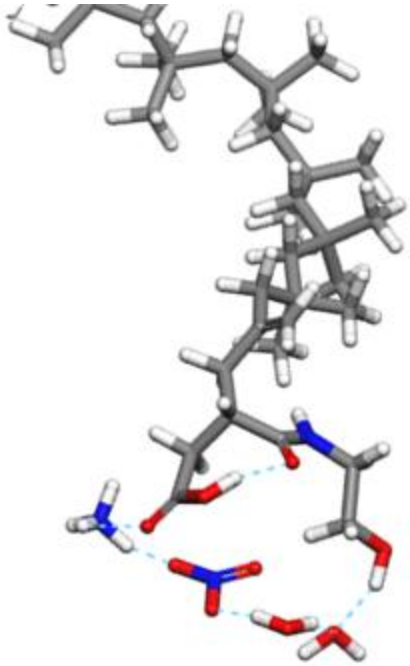

E_{ads} (9x9x9SC) = -41.66 kcal mol^{-1}	E_{ads} (9x9x9SC) = -55.62 kcal mol^{-1}

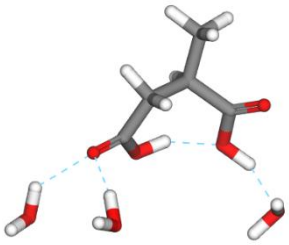

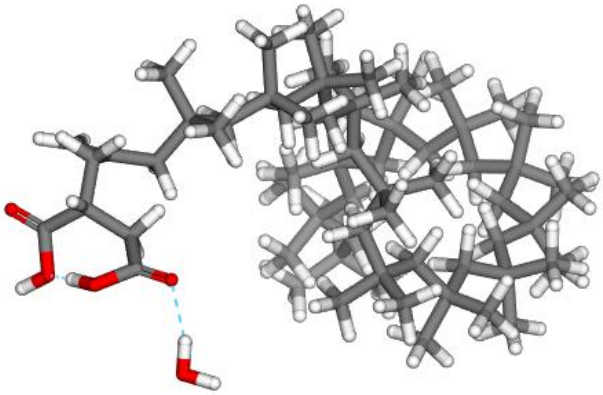

E_{ads} (W900) = -20.72 kcal mol^{-1}	E_{ads} (W900) = -31.88 kcal mol^{-1}

Figure 3-6: Adsorption modes of CH_3SA-MEA (top left) and PIBSA-MEA (top right) to 9x9x9SC. Adsorption modes of CH_3-Succinic acid (bottom left) and PIB-Succinic acid (bottom right) to W900.

Since the Adsorption Locator code is not parallel, an average 10-fold shortening in calculation time could be achieved for the truncated structures. When comparing the ionised forms of surfactants (ΔE_{ads}), the energy difference between polymeric and truncated models becomes less significant, than in their corresponding neutral forms, as the values of the E_{ads} to aqueous salt (9x9x9SC) are of much larger magnitude (Table 3-15).

Table 3-15. Adsorption energies of the ionised polymers and their truncated forms liquid surfaces

Ionized forms of PIBSA derivatives	***E_{ads}* to W900, kcal mol^{-1}**	***E_{ads}* to 9x9x9SC, kcal mol^{-1}**	**ΔE_{ads}, kcal mol^{-1}**	***Ionized forms of CH_3SA-derivatives***	***E_{ads}* to W900, kcal mol^{-1}**	***E_{ads}* to 9x9x9SC, kcal mol^{-1}**	**ΔE_{ads}, kcal mol^{-1}**
PIBSA-MEA$_{N\text{-}prot.}$	-75.00	-159.13	84.13	CH_3SA –MEA$_{N\text{-}prot.}$	-50.54	-130.23	79.69
PIBSA-MEAa	-72.51	-141.47	68.96	CH_3SA -MEAa	-63.37	-132.32	68.95
PIBSA-MEAz	-52.24	-79.72	27.48	CH_3SA -MEAz	-42.83	-46.12	3.29
PIBSA-UREA$_{N\text{-}prot.}$	-69.94	-148.54	78.60	CH_3SA -UREA $_{N\text{-}prot.}$	-65.44	-146.72	81.28
PIBSA-UREAa	-58.44	-145.57	87.13	CH_3SA -UREAa	-52.65	-131.34	78.69
PIBSA-UREAz	-32.32	-58.99	26.67	CH_3SA -UREAz	-34.47	-48.69	14.22
PIBSA-DEAc	-55.72	-137.32	81.60	CH_3SA –DEAc	-49.92	-123.84	73.92
PIBSA-DEAa	-75.59	-149.48	73.89	CH_3SA –DEAa	-60.36	-130.14	69.78
PIBSA-*bis*-MEA$_{N\text{-}prot.}$	-63.59	-135.49	71.90	CH_3SA-*bis*-MEA$_{N\text{-}prot.}$	-53.53	-131.44	77.91
PIBSA-*bis*-MEA$_{N,N\text{-}prot}$	-299.99	-449.74	149.75	CH_3SA-*bis*-MEA$_{N,N\text{-}prot.}$	-113.45	-253.46	140.01

Overall, for the tested surfactants in the polymeric model, the order of E_{ads} was in line with the experimental emulsion stability trend:

PIBSA-MEA$_{N\text{-}prot.}$ > PIBSA-UREA$_{N\text{-}prot}$ > PIBSA-DEA$_c$ > PIBSA-IMIDE

However, this outcome is subjective to the validity of the CompassII force-field. Overall, the order of the HLB theory applied to the range considered. Several most probable ionisation forms, which could not be modelled due to the lack of FF parameterisation, will have to be reconsidered.

All ionised surfactants shared one common feature in their binding modes, which is binding of charge-bearing functional groups of a surfactant head group to the oppositely charged surface ions. Unlike their unionised states, which involved at least one head group – water interaction, ionised head groups, typically, did not bind to water. The deprotonated (negatively charged) head groups formed strong hydrogen bonds with ammonium cations and protonated (positively charged) head groups were hydrogen-bonded to the nitrate anions; with the latter showing stronger adsorption energies to the aqueous salt interface

owing to a larger charge - charge separation($\Delta|q|$). This however, is subjective to the force-field used in this study.

3.4.5.2 PIBSA-MEA/PIBSA-DEA case study

From the study of Ghaicha and co-workers [10] on the adsorption of PIBSA-MEA and PIBSA-DEA at the air-water and air-aqueous salt interfaces (at pH = 2; 4.6; 5.8 and 8) several parallels could be drawn with regard to the adsorption modes observed by FT-IR, relative molecular sizes of adsorbate head groups and the nature of surface stabilisation. However, the exact effect of the pH on the ionisation state of the surfactants could not be determined. Experimentally, PIBSA-DEA was said to form a stronger monolayer and occupy a smaller area (77.2 Å^2) than PIBSA-MEA (81.7 Å^2) at the air-water interface [10]. This order is reversed at the air-AN_{aq}-interface (55 wt %; pH = 4.7), where PIBSA-DEA occupied a larger molecular surface area of 221 Å^2 *vs* 180 Å^2 for PIBSA-MEA (Table 3-15).

In relation to the molecular surface area at the air-water and air-AN interfaces, our results were in agreement with the experimental results reported for PIBSA-DEA and PIBSA-MEA monolayers (Figure 3-7). The $\boldsymbol{E_{ads}}$ (9x9x9SC) for the protonated PIBSA-$MEA_{N\text{-}protonated}$ was found to be the strongest amongst the ionised surfactants considered. In both polymeric and truncated models, the adsorption mode involved strong hydrogen bonding of the protonated amide and nitrate anion. Similarly, in PIBSA-DEA_c, the protonated secondary amine was hydrogen-bonded to a nitrate anion. The distance between the surfactant bound ions at the aqueous salt interface was smaller for the *N*-protonated MEA derivative than in the protonated DEA derivative (Figure 3-7), as observed experimentally. However, this observation could be incidental, as the exact ionisation of the amide group near the ionic interface is not known. Better binding capacity of PIBSA-MEA with salt ions, as reported for high surface pressure conditions, is likely to originate from the polarisation of the *O*-protonated amide, which results in the increased strength of interactions with surrounding hydrogen bond-donors/acceptors, similar to that in proteins.

In the basic environment, where the deprotonation of the succinic carboxyl is assumed, the distance between the ions bound to the head group of the R-MEAa was found

to be smaller than in R-DEAa, as per previously reported experimental results [10]. These findings can be considered significant in terms of the validity of the force field and the adsorption model, at least in the case of the unambiguously ionised PIBSA-DEA.

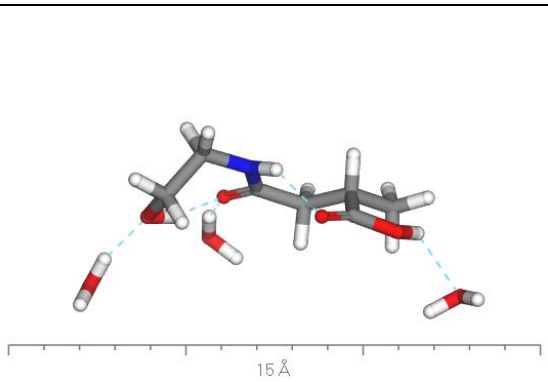

$CH_3SA\text{-}MEA_n$

$r_{Ow1\text{-}Ow2}$ = 10.47Å; *Eads* (W) = -23.23 kcal mol^{-1}

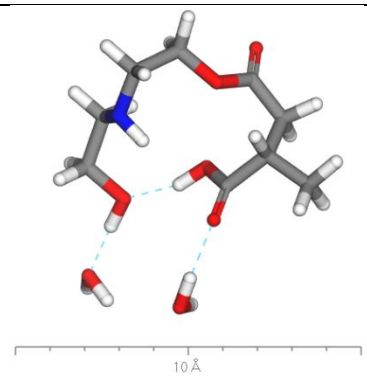

$CH_3SA\text{-}DEA_n$

$r_{Ow1\text{-}Ow2}$ = 5.99 Å; *Eads* (W) = -19.63 kcal mol^{-1}

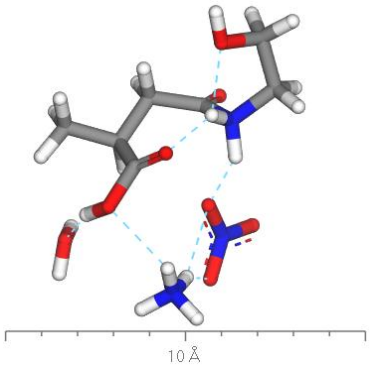

$CH_3SA\text{-}MEA_{N\text{-}protonated}$

$r_{N1\text{-}N2}$ = 3.18 Å; *Eads* (AN:W) = -130.23 kcal mol^{-1}

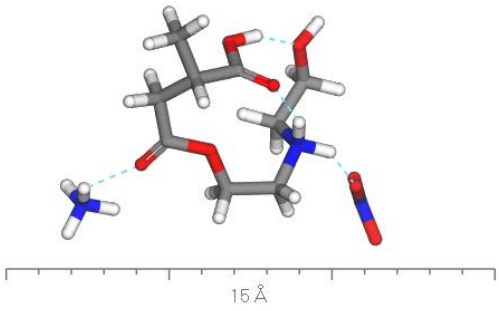

$CH_3SA\text{-}DEA_c$

$r_{N1\text{-}N2}$ = 8.59 Å; *Eads* (AN:W) = -123.84 kcal mol^{-1}

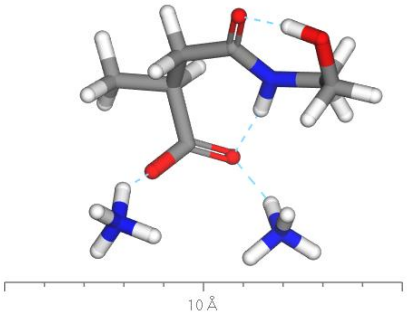

$CH_3SA\text{-}MEA_a$

$r_{N1\text{-}N2}$ = 4.65 Å; *Eads* (AN:W) = -132.32 kcal mol^{-1}

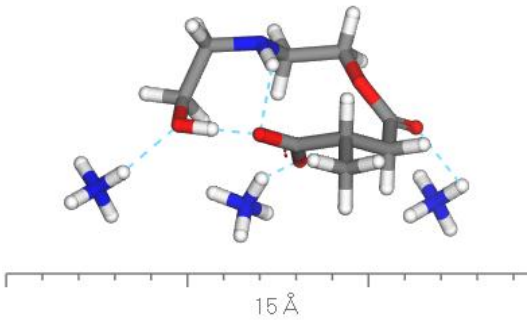

$CH_3SA\text{-}DEA_a$

$r_{N1\text{-}N2} \sim r_{N1\text{-}N3}$ = 9.4 Å; *Eads* (AN:W) = - 130.14 kcal mol^{-1}

Figure 3-7: Adsorption modes of some protonated and deprotonated forms of CH_3SA-MEA and CH_3SA-DEA to W900 and to AN:W surfaces.

*3.4.5.3 Adsorption to growth faces of II-*AN *and IV-*AN

The objective of the adsorption study to growth faces of II-AN and IV-AN was to evaluate the potential of surfactant efficiency at crystal growth inhibition. A further incentive was to gain insight into the experimentally observed phenomenon of predominant crystallization of *II*-AN from the PIBSA-surfactant stabilized emulsions.

In the polymeric model, for most functionalized surfactants, the difference in the affinity to *II*-AN and *IV*-AN crystal growth faces (101), (111) and (200) was notable (Table A3-7), and the absolute values of $\boldsymbol{E_{ads}}$ to growth faces of *II*-AN were smaller than to growth faces of *IV*-AN, implying stronger effect on growth retardation of the latter (Figure 3-9). The absolute values of the adsorption energies of all experimentally efficient surfactants were larger than the attachment energies of the corresponding growth faces of *II*-AN and *IV*-AN ($\boldsymbol{E_{ads}}>\boldsymbol{E_{att}}$), which is suggestive of their potential efficiency at crystal growth inhibition (Figure 3-9). By contrast, an adverse relationship ($\boldsymbol{E_{ads}}<\boldsymbol{E_{att}}$) was found for the PIB succinic acid (HR-PIB$_{Succ}$), which is known to have inferior efficacy to the amide/imide/amine-functionalized PIBSA surfactants [6].

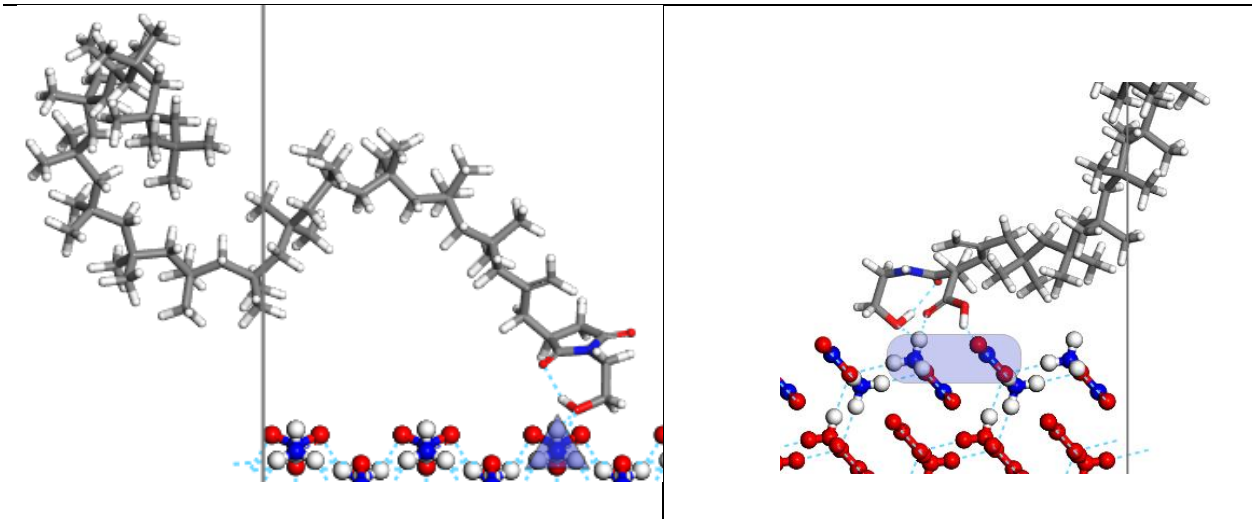

PIBSA-IMIDE	PIBSA-MEA

Figure 3-8: Adsorption modes of PIBSA-IMIDE and PIBSA-MEA on to (011) growth surface of IV-AN. Shaded areas show differences in the extent of surface binding, with one HB to ammonium for PIBSA-IMIDE and three HB to ammonium and nitrate ions for PIBSA-MEA.

Furthermore, for the cationic and anionic surfactant forms, values of the adsorption energies to all growth faces of AN were substantially smaller than to the surface of aqueous ammonium nitrate (Tables A3-7 and A3-8).

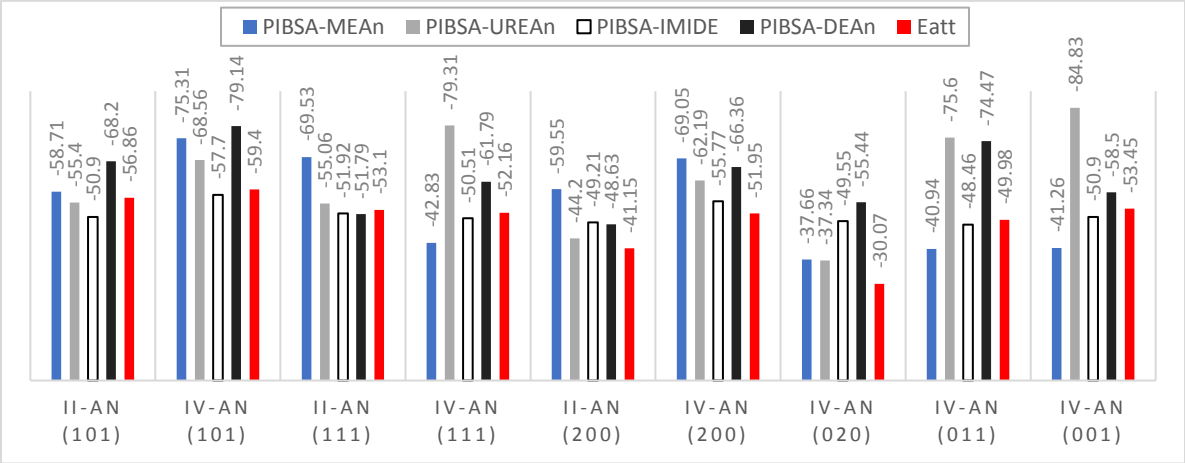

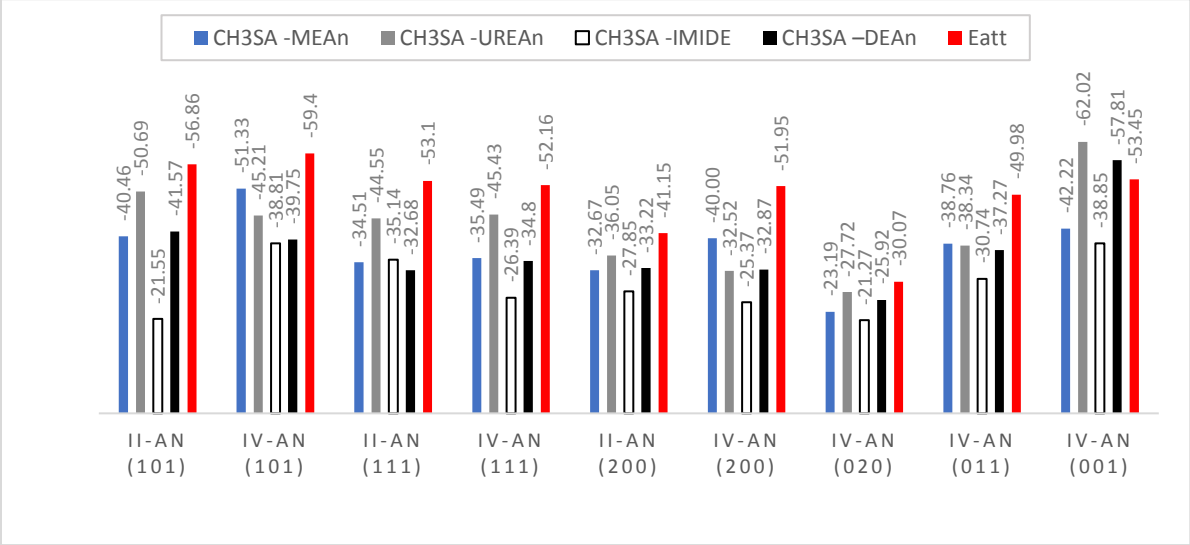

*Figure 3-9: Plots of E_{att} for II-*AN *and IV-growth faces and E_{ads} for polymeric (above) and truncated (below) surfactant models.*

This is due to the differences in the spatial arrangement of the surface ions, and more favourable head group orientation at the aqueous ammonium nitrate surface. This observation embeds some confidence in the CompassII force field. The $[IB]_{16}$SA-UREA had the strongest interaction with all of the solid growth faces of *II*-AN and *IV*-AN forms, with $\boldsymbol{E_{ads}}$ to (111), (011) and (001) of *IV*-AN having the largest absolute values, and growth inhibition

properties as $|E_{ads}|>|E_{att}|$. This would likely present experimentally in the form of isotropic crystals in the aged emulsions. PIBSA-MEA had a similar effect on faces (101), (111), (200) and (011) for *IV*-AN.

The modes of adsorption of $[IB]_{16}$SA-MEA and $[IB]_{16}$SA-IMIDE surfactants onto (011) growth face of *IV*-AN, depicted in Figure 3-8, show quite narrow domains of the interaction of the head groups with the dangling bonds of the adjacent A and N ions. Such versatility and wide range in adsorption modes could lead to smaller and more isotropic crystallites over time and possibly formation of nano-suspensions, as previously reported for PIBSA-stabilised HIPSs [21].

The *N*-protonated polymeric form of PIBSA-MEA had the strongest adsorption energies to AN growth faces, which were larger than E_{att}. In contrast, the protonated PIBSA-DEA showed more selective behaviour with only one strong interaction with (101) of *IV*-AN. It would be interesting to compare these results to E_{ads} of the more likely *O*-protonated amide form of PIBSA-MEA, which were not completed due to shortcomings of the force-field charge assignment.

Generally, stabilisation of the polymeric chain at the liquid interfaces resulted in larger absolute values of E_{ads}. The general trend in E_{ads} was relatively preserved between the polymeric and truncated surfactant models (Figure 3-9).

3.5 References

1. Mata JP, Reynolds PA, Gilbert EP, White JW (2013) Extended Q-range small angle neutron scattering from inverse micellar solutions of PIBSA—Micelle and molecular scattering. Colloids and Surfaces A: Physicochemical and Engineering Aspects 418 (0):157-164.
2. Reynolds PA, McGillivray DJ, Gilbert EP, Holt SA, Henderson MJ, White JW (2002) Neutron and X-ray Reflectivity from Polyisobutylene-Based Amphiphiles at the Air–Water Interface. Langmuir 19 (3):752-761.

3. Reynolds PA, Gilbert EP, White JW (2001) High Internal Phase Water-in-Oil Emulsions and Related Microemulsions Studied by Small Angle Neutron Scattering. 2. The Distribution of Surfactant. The Journal of Physical Chemistry B 105 (29):6925-6932.
4. Chattopadhyay AK (2002) Effect of Polymeric Surfactants on the Behavior of Polycrystalline Materials with Special Reference to Ammonium Nitrate. In: Adsorption and Aggregation of Surfactants in Solution. Surfactant Science. CRC Press, pp 655-674.
5. Reynolds PA, Gilbert EP, White JW (2000) High Internal Phase Water-in-Oil Emulsions Studied by Small-Angle Neutron Scattering. The Journal of Physical Chemistry B 104 (30):7012-7022.
6. Reynolds PA, Henderson MJ, Holt SA, White JW (2002) Interfacial Structure of a High Internal Phase Emulsion near a Solid Surface. Langmuir 18 (24):9153-9157.
7. Foudazi R, Masalova I, Malkin AY (2010) The role of interdroplet interaction in the physics of highly concentrated emulsions. Colloid J 72 (1):74-92.
8. Ferg EE, Simpson B (2013) Using PXRD and PONKCS to Determine the Kinetics of Crystallisation of Highly Concentrated NH4NO3 Emulsions. Journal of Chemical Crystallography 43 (4):197-206.
9. Rutherford CE (1990) The Destabilising Effects of various Cations on a Surfactant Derivative of Poly Iso-butenyl Succinic Anhydride. MSc Thesis, University of Natal.
10. Ghaicha L, Leblanc RM, Chattopadhyay AK (1993) Influence of concentrated ammonium nitrate solution on monolayers of some dicarboxylic acid derivatives at the air/water interface. Langmuir 9 (1):288-293.
11. Masalova I, Foudazi R, Malkin AY (2011) The rheology of highly concentrated emulsions stabilized with different surfactants. Colloids and Surfaces A: Physicochemical and Engineering Aspects 375 (1–3):76-86.
12. Masalova I, Kovalchuk K, Malkin AY (2011) IR Studies of Interfacial Interaction of the Succinic Surfactants with Different Head Groups in Highly Concentrated W/O Emulsions. Journal of Dispersion Science and Technology 32 (11):1547-1555.
13. Zahirovic S (2007) Interfacial tension study and rheological characterisation of water-in-oil emulsion explosives. PhD Thesis, The University of Melbourne.
14. Tshilumbu NN (2009) The effect of type and concentration of surfactant on stability and rheological properties of explosive emulsions. MSc Thesis, CPUT.

15. Ganguly S, Mohan VK, Bhasu VCJ, Mathews E, Adiseshaiah KS, Kumar AS (1992) Surfactant-electrolyte interactions in concentrated water-in-oil emulsions: FT-IR spectroscopic and low-temperature differential scanning calorimetric studies. Colloids and Surfaces 65 (4):243-256.
16. Ghaicha L, Chattopadhyay AK, Tajmir-Riahi HA (1991) Behavior of stearic acid monolayers in presence of concentrated ammonium nitrate solution substrate. Langmuir 7 (10):2007-2009.
17. Taborek P (1985) Nucleation in emulsified supercooled water. Physical Review B 32 (9):5902-5906.
18. Dhanaraj G, Byrappa K, Prasad V, Dudley M (2010) Springer handbook of crystal growth. Springer-Verlag, Berlin Heidelberg.
19. De Yoreo JJ, Vekilov PG (2003) Principles of Crystal Nucleation and Growth. Reviews in Mineralogy and Geochemistry 54 (1):57-93.
20. Yubai B, Munger G, Leblanc RM, Ghaicha L, Chattopadhyay AK (1996) Crystallization of Ammonium Nitrate under organized monolayers of various amphiphiles Journal of Dispersion Science and Technology 17 (4):391-405.
21. Malkin A, Masalova I (2007) A new mechanism of aging of highly concentrated emulsions: Correlation between crystallization and plasticity. Colloid J 69 (2):198-202.
22. Konkel JT, Myerson AS (2008) Empirical molecular modelling of suspension stabilisation with Polysorbate 80. Molecular Simulation 34 (10-15):1353-1357.
23. Hiemenz PC (1986) Principles of colloid and surface chemistry. 2nd edn. M. Dekker, New York.
24. McClements DJ (2016) Food emulsions: principles, practices, and techniques. 3d edn. CRC Press, Boca Raton.
25. Laughlin RG (1981) HLB, from a thermodynamic perspective. Journal of the Society of Cosmetic Chemists 32 (6):371-392.
26. Janssen MJ (1961) The structure of protonated amides and ureas and their thio analogues. Spectrochimica Acta 17 (5):475-485.
27. Birchall T, Gillespie R (1963) Nuclear Magnetic Resonance Studies of The Protonation Of Weak Bases In Fluorosulphuric Acid: II. Amides, Thioamides, And Sulphonamides. Canadian Journal of Chemistry 41 (10):2642-2650.

28. Nanubolu JB, Sridhar B, Ravikumar K (2012) Resonance-assisted amide protonation in dutasteride hydrochloride salt. CrystEngComm 14 (7):2571-2578.
29. Jiao D, Barfield M, Hruby VJ (1993) Ab initio IGLO study of the syn/anti dependence of the 13C NMR chemical shifts in simple amides. Magnetic Resonance in Chemistry 31 (1):75-79.
30. Murthy ASN, Rao KG, Rao CNR (1970) Molecular orbital study of the configuration protonation, and hydrogen bonding of secondary amides. Journal of the American Chemical Society 92 (12):3544-3548.
31. Levy GC, Nelson GL (1972) Carbon-13 NMR study of aliphatic amides and oximes. Spin-lattice relaxation times and fast internal motions. Journal of the American Chemical Society 94 (14):4897-4901.
32. Szostak M, Yao L, Day VW, Powell DR, Aubé J (2010) Structural Characterization of N-Protonated Amides: Regioselective N-Activation of Medium-Bridged Twisted Lactams. Journal of the American Chemical Society 132 (26):8836-8837.
33. Kovalchuk K, Landman M, Masalova I (2012) A Computational Study of the Succinimide Derivative Surfactant. Journal of Dispersion Science and Technology 34 (6):778-784.
34. Adya AK, Neilson GW (1990) The structure of molten ammonium nitrate by isotopic difference method of neutron diffraction. Molecular Physics 69 (4):747-765.
35. Dunuwille M, Yoo C-S (2013) Phase diagram of ammonium nitrate. The Journal of chemical physics 139 (21):214503.
36. Lucas BW, Ahtee M, Hewat AW (1979) The crystal structure of phase II ammonium nitrate. Acta Crystallographica Section B 35 (5):1038-1041.
37. Choi CS, Mapes JE, Prince E (1972) The structure of ammonium nitrate (IV). Acta Crystallographica Section B 28 (5):1357-1361.
38. Lightstone JM, Onasch TB, Imre D, Oatis S (2000) Deliquescence, Efflorescence, and Water Activity in Ammonium Nitrate and Mixed Ammonium Nitrate/Succinic Acid Microparticles. The Journal of Physical Chemistry A 104 (41):9337-9346.
39. Velardez GF, Alavi S, Thompson DL (2004) Molecular dynamics studies of melting and solid-state transitions of ammonium nitrate. The Journal of Chemical Physics 120 (19):9151-9159.

40. Thompson AR, Molstad MC (1945) Solubility and Density Isotherms - Potassium and Ammonium Nitrates in Isopropanol Solutions. Industrial & Engineering Chemistry 37 (12):1244-1248.
41. Shan T-R, van Duin ACT, Thompson AP (2014) Development of a ReaxFF Reactive Force Field for Ammonium Nitrate and Application to Shock Compression and Thermal Decomposition. The Journal of Physical Chemistry A 118 (8):1469-1478.
42. Kovalchuk K, Masalova I (2012) Factors influencing the crystallisation of highly concentrated water-in-oil emulsions: A DSC study. South African Journal of Science 108 (3-4):00-00.
43. Foudazi R, Masalova I, Malkin AY (2011) Flow behaviour of highly concentrated emulsions of supersaturated aqueous solution in oil. Rheologica Acta 50 (11):897-907.
44. Braunstein J (1971) Chapter 4 - Statistical Thermodynamics of Molten Salts and Concentrated Aqueous Electrolytes. In: Petrucci S (ed) Ionic Interactions, vol 22. Academic Press, pp 179-260.
45. Zahn S, Thar J, Kirchner B (2010) Structure and dynamics of the protic ionic liquid monomethylammonium nitrate ($[CH_3NH_3][NO_3]$) from ab initio molecular dynamics simulations. The Journal of Chemical Physics 132 (12):124506.
46. Keenan AG (1957) Cryoscopic Behavior of H_20 and HNO_2 in Fused Ammonium Nitrate. The Journal of Physical Chemistry 61 (6):780-782.
47. Peleg M (1971) Association equilibriums of silver and chloride ions in liquid ammonium nitrate-water mixtures. I. Molar ratio range water:ammonium nitrate 0.4-1.4 at 110°. The Journal of Physical Chemistry 75 (13):2060-2064.
48. Adya AK, Neilson GW (1991) Structure of a 50 mol kg^{-1} aqueous solution of ammonium nitrate at 373 K by the isotopic difference method of neutron diffraction. Journal of the Chemical Society, Faraday Transactions 87 (2):279-286.
49. Walker PAM, Lawrence DG, Neilson GW, Cooper J (1989) The structure of concentrated aqueous ammonium nitrate solutions. Journal of the Chemical Society, Faraday Transactions 1: Physical Chemistry in Condensed Phases 85 (6):1365-1372.
50. Nguyen M-T, Jamka AJ, Cazar RA, Tao F-M (1997) Structure and stability of the nitric acid–ammonia complex in the gas phase and in water. The Journal of Chemical Physics 106 (21):8710-8717.

51. Cagnina S, Rotureau P, Fayet G, Adamo C (2013) The ammonium nitrate and its mechanism of decomposition in the gas phase: a theoretical study and a DFT benchmark. Physical Chemistry Chemical Physics 15 (26):10849-10858.
52. Dunlap BI, Doyle RJ (1996) Ammonium Nitrate Cluster Ions. The Journal of Physical Chemistry 100 (13):5281-5285.
53. Alavi S, Thompson DL (2002) Theoretical study of proton transfer in ammonium nitrate clusters. The Journal of Chemical Physics 117 (6):2599-2608.
54. Dang LX, Chang TM, Roeselova M, Garrett BC, Tobias DJ (2006) On NO3--H2O interactions in aqueous solutions and at interfaces. J Chem Phys 124 (6):66101.
55. da Silva G, Dlugogorski BZ, Kennedy EM (2006) An experimental and theoretical study of the nitrosation of ammonia and thiourea. Chemical Engineering Science 61 (10):3186-3197.
56. Opoku MK, Dlugogorski BZ Preparation and characterisation of potassium ammonium nitrates. In: IX ISHIPMIE, Cracow, Poland, 2012.
57. Sorescu DC, Thompson DL (2001) Classical and Quantum Mechanical Studies of Crystalline Ammonium Nitrate. The Journal of Physical Chemistry A 105 (4):720-733.
58. Ouyang JF, Bettens RP (2015) Modelling Water: A Lifetime Enigma. Chimia 69 (3):104-111.
59. Soper AK (2000) The radial distribution functions of water and ice from 220 to 673 K and at pressures up to 400 MPa. Chemical Physics 258 (2):121-137.
60. Soper AK, Phillips MG (1986) A new determination of the structure of water at 25°C. Chemical Physics 107 (1):47-60.
61. Berendsen HJC, Grigera JR, Straatsma TP (1987) The missing term in effective pair potentials. The Journal of Physical Chemistry 91 (24):6269-6271.
62. Mark P, Nilsson L (2001) Structure and Dynamics of the TIP3P, SPC, and SPC/E Water Models at 298 K. The Journal of Physical Chemistry A 105 (43):9954-9960.
63. Scocchi G, Posocco P, Fermeglia M, Pricl S (2007) Polymer−Clay Nanocomposites: A Multiscale Molecular Modeling Approach. The Journal of Physical Chemistry B 111 (9):2143-2151.
64. Shen F, Lv P, Sun C, Zhang R, Pang S (2014) The crystal structure and morphology of 2,4,6,8,10,12-hexanitro-2,4,6,8,10,12-hexaazaisowurtzitane (CL-20) p-xylene solvate: a

joint experimental and simulation study. Molecules (Basel, Switzerland) 19 (11):18574-18589.
65. Sholl DS, Steckel JA (2009) Density Functional Theory: A Practical Introduction. 1st edn. Wiley.
66. Sun H, Jin Z, Yang C, Akkermans RLC, Robertson SH, Spenley NA, Miller S, Todd SM (2016) COMPASS II: extended coverage for polymer and drug-like molecule databases. Journal of Molecular Modeling 22 (2):47.
67. Sun H (1998) COMPASS: An ab Initio Force-Field Optimized for Condensed-Phase Applications Overview with Details on Alkane and Benzene Compounds. The Journal of Physical Chemistry B 102 (38):7338-7364.
68. Bunte SW, Sun H (2000) Molecular Modeling of Energetic Materials: The Parameterization and Validation of Nitrate Esters in the COMPASS Force Field. The Journal of Physical Chemistry B 104 (11):2477-2489.
69. Borodin O, Smith GD, Sewell TD, Bedrov D (2008) Polarizable and Nonpolarizable Force Fields for Alkyl Nitrates. The Journal of Physical Chemistry B 112 (3):734-742.
70. Mayo SL, Olafson BD, Goddard WA (1990) DREIDING: a generic force field for molecular simulations. The Journal of Physical Chemistry 94 (26):8897-8909.
71. Gasteiger J, Marsili M (1980) Iterative partial equalization of orbital electronegativity—a rapid access to atomic charges. Tetrahedron 36 (22):3219-3228.
72. Rappe AK, Goddard WA (1991) Charge equilibration for molecular dynamics simulations. The Journal of Physical Chemistry 95 (8):3358-3363.
73. Mulliken RS (1955) Electronic Population Analysis on LCAO–MO Molecular Wave Functions. I. The Journal of Chemical Physics 23 (10):1833-1840.
74. Hirshfeld FL (1977) Bonded-atom fragments for describing molecular charge densities. Theoretica chimica acta 44 (2):129-138.
75. Singh UC, Kollman PA (1984) An approach to computing electrostatic charges for molecules. Journal of Computational Chemistry 5 (2):129-145.
76. Hamilton W, Ibers JA (1968) Hydrogen bonding in solids. Benjamin, New York.
77. Wang J, Kalinichev AG, Kirkpatrick RJ (2009) Asymmetric Hydrogen Bonding and Orientational Ordering of Water at Hydrophobic and Hydrophilic Surfaces: A Comparison

of Water/Vapor, Water/Talc, and Water/Mica Interfaces. The Journal of Physical Chemistry C 113 (25):11077-11085.
78. Zahn S, Wendler K, Delle Site L, Kirchner B (2011) Depolarization of water in protic ionic liquids. Physical Chemistry Chemical Physics 13 (33):15083-15093.
79. Dhanaraj G (2010) Springer handbook of crystal growth. vol Book, Whole. Springer, Heidelberg.
80. Connolly M (1983) Solvent-accessible surfaces of proteins and nucleic acids. Science (New York, NY) 221 (4612):709-713.
81. Connolly ML (1983) Solvent-accessible surfaces of proteins and nucleic acids. Science 221 (4612):709-713.
82. Voorintholt R, Kosters MT, Vegter G, Vriend G, Hol WGJ (1989) A very fast program for visualizing protein surfaces, channels and cavities. Journal of Molecular Graphics 7 (4):243-245.
83. Sun N, Walz JY (2001) A Model for Calculating Electrostatic Interactions between Colloidal Particles of Arbitrary Surface Topology. Journal of Colloid and Interface Science 234 (1):90-105.
84. Samoletov AA, Dettmann CP, Chaplain MA (2007) Thermostats for “slow” configurational modes. Journal of Statistical Physics 128 (6):1321-1336.
85. Verlet L (1967) Computer "Experiments" on Classical Fluids. I. Thermodynamical Properties of Lennard-Jones Molecules. Physical Review 159 (1):98-103.
86. Becke AD (1993) Density-functional thermochemistry. III. The role of exact exchange. The Journal of Chemical Physics 98 (7):5648-5652.
87. Mayer I (1986) Bond orders and valences from ab initio wave functions. International Journal of Quantum Chemistry 29 (3):477-483.
88. Karasawa N, Goddard WA (1989) Acceleration of convergence for lattice sums. The Journal of Physical Chemistry 93 (21):7320-7327.
89. Ewald PP (1921) Die Berechnung optischer und elektrostatischer Gitterpotentiale. Annalen der Physik 369 (3):253-287.
90. Tosi MP (1964) Cohesion of Ionic Solids in the Born Model**Based on work performed under the auspices of the U.S. Atomic Energy Commission. In: Seitz F, Turnbull D (eds) Solid State Physics, vol 16. Academic Press, pp 1-120.

91. Docherty R, Clydesdale G, Roberts KJ, Bennema P (1991) Application of Bravais-Friedel-Donnay-Harker, attachment energy and Ising models to predicting and understanding the morphology of molecular crystals. Journal of Physics D: Applied Physics 24:89.
92. Kell GS (1975) Density, thermal expansivity, and compressibility of liquid water from 0° to 150°. Correlations and tables for atmospheric pressure and saturation reviewed and expressed on 1968 temperature scale. Journal of Chemical & Engineering Data 20 (1):97-105.
93. Nosé S (1984) A molecular dynamics method for simulations in the canonical ensemble. Molecular Physics 52 (2):255-268.
94. Andersen HC (1983) Rattle: A "velocity" version of the shake algorithm for molecular dynamics calculations. Journal of Computational Physics 52 (1):24-34.
95. Černý V (1985) Thermodynamical approach to the traveling salesman problem: An efficient simulation algorithm. Journal of Optimization Theory and Applications 45 (1):41-51.
96. Frenkel D, Smit B (2002) Understanding molecular simulation: from algorithms to applications. 2nd edn. Academic Press, San Diego.
97. Metropolis N, Rosenbluth AW, Rosenbluth MN, Teller AH, Teller E (1953) Equation of State Calculations by Fast Computing Machines. The Journal of Chemical Physics 21 (6):1087-1092.
98. Platts JA, Maarof H, Harris KD, Lim GK, Willock DJ (2012) The effect of intermolecular hydrogen bonding on the planarity of amides. Physical chemistry chemical physics : PCCP 14 (34):11944-11952.
99. Herrmann MJ, Engel W (1997) Phase Transitions and Lattice Dynamics of Ammonium Nitrate. Propellants, Explosives, Pyrotechnics 22 (3):143-147.
100. Vargeese AA, Joshi SS, Krishnamurthy VN (2009) Effect of method of crystallization on the IV–III and IV–II polymorphic transitions of ammonium nitrate. Journal of Hazardous Materials 161 (1):373-379.
101. Hendricks SB, Posnjak E, Kracek FC (1932) Molecular rotation in the solid state. The variation of the crystal structure of ammonium nitrate with temperature. Journal of the American Chemical Society 54 (7):2766-2786.

102. Seiyama T, Yamazoe N (1968) Misroscopic observation of phase transitions of ammonium nitrate. Journal of Crystal Growth 2 (5):255-266.
103. Mort KA, Wilde PJ, Jackson RA (1999) Computer modelling of ammonium nitrate: I. Development of potentials and calculation of lattice properties. Journal of Physics: Condensed Matter 11 (20):3967.
104. Goebbert DJ, Garand E, Wende T, Bergmann R, Meijer G, Asmis KR, Neumark DM (2009) Infrared Spectroscopy of the Microhydrated Nitrate Ions NO3−(H2O)1−6†. The Journal of Physical Chemistry A 113 (26):7584-7592.
105. Pickard, Dunn ME, Shields GC (2005) Comparison of Model Chemistry and Density Functional Theory Thermochemical Predictions with Experiment for Formation of Ionic Clusters of the Ammonium Cation Complexed with Water and Ammonia; Atmospheric Implications. The Journal of Physical Chemistry A 109 (22):4905-4910.
106. Berendsen HJC, Postma JPM, van Gunsteren WF, Hermans J (1981) Interaction Models for Water in Relation to Protein Hydration. In: Pullman B (ed) Intermolecular Forces: Proceedings of the Fourteenth Jerusalem Symposium on Quantum Chemistry and Biochemistry held in Jerusalem, Israel, April 13–16, 1981. Springer Netherlands, Dordrecht, pp 331-342.
107. Range K (2009) Benchmark calculations of Ammonium Nitrate ions in aqueous solution. The 237th ACS National Meeting. Salt Lake City, UT.
108. Pickard D, Shields ME, George C (2005) Comparison of Model Chemistry and Density Functional Theory Thermochemical Predictions with Experiment for Formation of Ionic Clusters of the Ammonium Cation Complexed with Water and Ammonia; Atmospheric Implications. The Journal of Physical Chemistry A 109 (22):4905-4910.

4 Conclusions and Outlook

The series of surfactants, examined in this study, was amphiphilic molecules with polar head-groups and non-polar polymeric tails. Head-groups were amide, ester and imide derivatives of polyisobutylene succinic anhydride (PIBSA). The reported structures of these surfactants are inconsistent and there are no reports concerning composition of the industrial concentrates used in some experimental studies. Ambiguity in the reported surfactant structures and variation in the available starting materials necessitated the experimental structural studies conducted in Chapter 2. The operating environment for the mining explosive emulsions, where this series of surfactants are used for droplet refinement and emulsion stability, is typically acidic. The ionization states of these surfactants were not previously reported. Subsequently, no solid evidence-based mechanism of how PIBSA-surfactants stabilise emulsion formulations, has been proposed to date. The main objectives of theoretical study in Chapter 3 were to predict likely ionisation forms of a series of PIBSA-based surfactants, and to establish a relationship between surfactant structure and the emulsion stability.

4.1 Conclusions to Chapter 2

Surfactant structure

To determine the structure of the surfactants, it was possible to purify the PIBSA-monoethanolamine surfactant (PIBSA-MEA) from the industrial concentrate and characterise it by means of nuclear magnetic resonance (NMR) and infrared spectroscopy as well as mass spectrometry. By analysis of synthetic precursors, and by analogy to the assignments of PIBSA-MEA, structural assignments were made for PIBSA-IMIDE and PIBSA-UREA surfactants from the NMR spectra of their industrial concentrates. To the best of our knowledge this is the first report of the complete structural assignments for these three surfactants.

Determination of the average molecular weight (*Mn*) of PIBs and PIBSA with GPC-MALLs was in good agreement with the expected values (within ca. 6 % range). However, for

the PIBSA-derived surfactant concentrates, GPC analysis significantly overestimated the *Mn* in all samples, which we believe is due to the presence of higher *Mn* products in the industrial products, as previously reported [1]. Formation of surfactant aggregates in the mobile phase of the GPC eluent, which could potentially affect the *Mn*, is also plausible, but a less likely event, due to the shear effects of the stationary phase, which could even lead to C-C bond breaking, as previously reported for high *Mn* PIBs [2].

Mass spectrometry proved useful in the identification of the nature of the PIB used in the production of PIBSA-based surfactants. Ion fragments separated by 56 mu are being characteristic of the HR-PIB precursors, and afforded higher surfactant yields than those derived from the conventional PIB, with the characteristic ion fragments, separated by 14 mu. From the analysis of multiple batches of surfactant samples, we found that products, manufactured from the highly reactive polyisobutylene precursors, had higher concentrations of functionalised surfactants, than those manufactured from the conventional PIB.

For the major PIBSA-MEA isomer, polymeric side chain was found to be connected to the succinic moiety *via* the secondary methyl group of the isobutylene link (PIB-**$CH_2C(=CH_2)CH_2$**-Succ) with *exo*-double bond. An unexpected finding in the structural study of PIBSA-MEA surfactant was the fact that only one (***C***-type Scheme 1.1) of the two possible isomers was present in all of the industrial mixtures, in contrast to the expected equimolar mixture of isomers ***C*** and ***C'*** [3,4]. This was clearly evident from the long range heteronuclear correlation in the HMBC NMR spectrum of PIBSA-MEA. This implies that the ring-opening reaction of PIBSA with ethanolamine is regioselective in the temperature regimen used in an industrial process. Kinetic nature of the selectivity of the ring scission in the unsymmetrically substituted succinic anhydrides was also reported by Galust'yan [5]. This is a first report of the regioselectivity in nucleophilic PIBSA substitution.

A detailed assignment of the I.R. frequencies was valuable in relating previously published results [3] of the interfacial interactions of the PIBSA-MEA surfactant with the acidic solution of ammonium nitrate to the specific ionisation form at the carbamide oxygen atom. This is a first report of this ionisation form of the PIBSA-MEA surfactant. The ionisation

forms of other surfactants in the series could not be confirmed experimentally due to lack of the interfacial data. The experimental values of Raman frequencies could be useful in comparison to the calculated Raman intensities of PIBSA surfactants (Chapter 3) and their ionisation forms. Unfortunately, due to time and instrument constraints, experimental Raman spectra of PIBSA surfactants could not be recorded.

Surfactant content

To quantify the amount of the functionalized PIBSA-MEA surfactant, we capitalized on the simplicity of the nuclear magnetic resonance ^{13}C-NMR spectral region between 56 – 62 ppm, which is far upfield from the deshielded methylene groups situated on or close to the succinic residue of surfactant head group. This method allowed us to derive an approximate number of [IB] repeat units in the PIB side chain of the surfactants and to find relative concentration of the functionalized polymers to the unreacted PIB in the industrial concentrates. The maximum amount of the functionalized surfactant present in the industrial concentrates was 27 mol % of the total polymer content, in the samples derived from the HR-PIB, and less than 17 mol % in the samples derived from the conventional PIB. This semi-quantitative method is unique in principle and can be used for analysis of *mono*- or *bis*-substituted PIBSA-based surfactants, either in the form of concentrates or extended to pre-diluted surfactant/oil mixtures, by introducing internal standards.

Thermal stability

The purified PIBSA-MEA was shown to have a superior thermal stability profile in the DSC study, when compared to its polymeric precursors (*i.e.* PIB and PIBSA), and industrial surfactant concentrates of PIBSA-MEA, PIBSA-UREA and PIBSA-IMIDE. The fact that the thermal stability profile for a purified surfactant was vastly different from its concentrate leads us to the conclusion that in a more concentrated form, the intermolecular interactions between surfactant head-groups containing polarised amide bonds could be responsible for the increased thermal stability of PIBSA-MEA surfactant. Such intermolecular interactions are of great importance in the context of explosive emulsions, where only functionalized surfactants get adsorbed at the interface as monolayers.

4.2 Conclusions to Chapter 3

Ionisation forms of surfactants from electronic structure

Based on the practical examples of PIBSA-surfactants with known efficacy in stabilising HIPEs (*i.e.* PIBSA-MEA, PIBSA-UREA and PIBSA-DEA), we used the *ab initio* DFT code (DMol^3) to calculate geometric and electronic parameters of the model surfactants (< 100 atoms). With focus on the surfactant head-groups, we truncated the PIB side chain to just four repeat units ([IB]$_4$). Their likely ionisation forms were the geometry optimised structures with the lowest values of local energy minima.

In the gas phase, the expected *trans* configuration of the amide hydrogen with respect to the carbonyl oxygen of the succinic moiety predominated over the *cis* in the *N*-monosubstituted secondary amides, *i.e.* PIBSA-MEA and PIBSA-UREA. The geometric requirement for the amide protonation at the carbonyl oxygen in [IB]$_4$SA-MEA-*trans* was satisfied, and consequently, the *O*-protonated isomer was found to be of lower energy than the *N*-protonated form. The deviation from planarity in PIBSA-MEA-*cis* would likely lead to the *N*-protonated amide in the acidic environment. However, there is no evidence of the existence of the *trans-cis* interconversion in real systems. For PIBSA-UREA, the lowest energy configuration of the secondary amide moiety with respect to the amidic carbonyl (O2) was *trans*; and with respect to the ureide carbonyl - it was *cis*. The [IB]$_4$SA-UREA-(*trans-cis*)$_{O2\text{-}protonated}$ was the lowest energy model ionisation form of PIBSA-UREA. Furthermore, the sp^3 hybridised terminal amide group of the [IB]$_4$SA-UREA lacked typical secondary amide stability, and thus, is the most obvious leaving group and likely site for surfactant decomposition [6,7].

In the absence of a systematic experimental study, we propose the following order of the calculated surfactant stability (based on the values of HOMO-LUMO gap), with PIBSA-UREA and PIBSA-DEA being the most unstable in the series:

[IB]$_4$SA-MEA >> [IB]$_4$SA -IMIDE > [IB]$_4$SA –DEA > [IB]$_4$SA -UREA

The order of the calculated dipole moment for the cationic and anionic forms of the $[IB]_4$SA-DEA ($[IB]_4$SA-DEAc > $[IB]_4$SA-DEAa), and for the pair $[IB]_4$SA-DEAc >> $[IB]_4$SA-$MEA_{O\text{-protonated}}$ is in good agreement with the previously published experimental results for the PIBSA-DEA and PIBSA-MEA [3]. Examination of the reported experimental behaviour of the protonated forms of PIBSA-DEA and PIBSA-MEA in monolayers adsorbed at the acidic aqueous ammonium nitrate interface, where PIBSA-MEA had higher collapse pressure than PIBSA-DEA, was indicative of a stronger bonding to the surface by the former. We believe that this is due to the resonance effects and polarization of the amide moiety, which lead to a stronger hydrogen bond between the ionised head-group and the nitrate anion (NO_3^-), as was seen in the case of the urea nitrate crystals (b.l (C=O-H---O=N) = 1.57-1.61 Å)) [8,6,9-11]. It is reasonable to propose that the charge- and resonance-stabilized *O*-protonation of the amidic carbonyl, is the key structural feature responsible for the superior surface binding of the PIBSA-MEA and PIBSA-UREA surfactants.

Formation of the ion-pairs between surfactant head-group and ammonium nitrate, also suggested by Ghaicha, and particularly with the nitrate anion, would render it an increased stability in a low dielectric environment at the oil-ammonium nitrate interface [6,10]. The protonated amide group would also contribute to the overall positive surface potential of the oxidizer phase droplets and repulsive retardation of droplet coalescence and increased emulsion stability [3].

From the above considerations, it can be concluded that the overall surfactant efficiency in this series is determined by the polarised nature of the secondary amide domain, intrinsic dipole moment and surfactant stability. This mechanism of surface stabilization seems highly plausible and a further study is required to test its validity.

Surface adsorption

In the emulsion preparation, surfactants are added to the oil phase, and during the mixing with the oxidiser salt solution (aqueous solution of ammonium nitrate) they adsorb onto the oxidiser salt droplets. Surfactant efficiency at stabilising explosive emulsions is highly dependent on the structure of the head-group [3,12,13]. Our approach to the *in-silico* evaluation of the surfactant efficiency at stabilising explosive emulsions was to simulate

their adsorption onto the various components constituting the explosive emulsion (water, oxidiser salt and oxidiser salt solution). We used Molecular Mechanics code Forcite, which is intended for the simulation of the large systems (thousands of atoms). Forcite utilises the force-filed potentials, which are able to resolve chemical details of the interatomic interactions.

On the example of PIBSA, two different force-fields, *i.e.* CompassII and Dreiding were compared by means of the calculated partial charges derived from the force-field and *ab initio* methods (DMol^3). Considering the variability of the chemical environments, and the overall performance, both force fields had suffered a few shortcomings, which could be attributed, mainly, to the partial atomic charge algorithms. Generally, the parameters calculated by CompassII force-field were in good agreement with the *ab initio* results and this force-field was selected for the simulation of the polymeric surfactants and oxidiser phase components (*i.e.* ammonium nitrate and water). However, CompassII lacked parameters to accurately represent the *O*-protonated amide functionalities in PIBSA-MEA and PIBSA-UREA.

Adsorption energies of the full size polymeric surfactants and non-surfactants were used to establish the order of surfactant efficiency, which correlated well with the previously published experimental results. By studying preferential binding sites of the surfactants to water and to an equimolar aqueous solution of ammonium nitrate (oxidiser phase), it was possible to draw a few mechanistic and structure–activity conclusions:

- The interaction energies of all molecular and ionised forms of surfactants with the oxidizer phase (aqueous ammonium nitrate) were greater than their interaction energies with water; and water was expelled from the solvation sheath of the ionised surfactant head-groups as previously suggested by Ghaicha [3].
- The anionic and cationic surfactant forms had far greater interaction energies ($\boldsymbol{E_{ads}}$) with the simulated aqueous ammonium nitrate salt than their molecular forms, and differed significantly in their binding modes to aqueous salt and to water. This change in the head-group conformation is consistent with the previously reported experimental results [3]. At the aqueous ammonium nitrate surface, molecular

(unionised) forms of the surfactant head-groups formed several hydrogen bonds with the dangling bonds of the ammonium nitrate ions and water. Mode of surfactant binding to water was mainly monodentate and non-specific, either via one- or two-site hydrogen bonds to donor or acceptor sites.

- Binding modes of the ionized PIBSA-surfactants involved Coulombic interactions and an ion-pair formation between the surfactant charge-bearing functional groups and ammonium nitrate ions, as previously suggested from the experiment [3].
- Evaluation of the ionization forms of the surfactants containing *O*-protonated secondary amide functionalities was not possible due to the lack of parameters for such atom types in the CompassII force-field.
- Structure-activity relationship between the different surfactant forms followed the Laughlin's HLB-based efficiency trend [14]:
  - **cationic ≈ anionic >> zwitterionic > neutral**

Furthermore, when we compared values of the adsorption energy (E_{ads}) of surfactants to the ammonium nitrate growth faces and the corresponding attachment energies (E_{att}) for these growth faces, only PIBSA-UREA was found to affect all growth faces of *II-AN* and *IV-AN*. This implies that the mode of emulsion stabilization for PIBSA-based surfactants is unlikely to be through direct crystal growth inhibition.

Finally, using fully truncated surfactant model allowed to speed up surface adsorption calculations and proved useful in the pre-screening of the potential surfactant activity at an interface. Although the mode of binding was not always the same between the two models (polymeric and truncated), the trend in surface activity between the two models was very similar, particularly for the ionized surfactant forms.

Overall, our computational framework allowed to make predictive judgments as to which hypothesis was most valid and thus set a direction for the experimental testing of the new candidates by providing initial guidance. From the surface adsorption study, it was possible to differentiate between the surface active and surface inactive molecules, and the predicted activity corresponded well with the experimental activity trends. This allowed to gain an understanding of the relative effects of the various functional groups with respect to the

intra- and inter-molecular interactions and to the surfaces of the individual emulsion components. The selection criteria for surfactant candidates can be defined as follows:

1) Surfactant head group should contain a secondary amide (manual selection);
2) Surfactant should have greater adsorption energy to the aqueous ammonium nitrate than to water (adsorption study);
3) Refining of the surfactant candidates can be based on their polarizability, calculated dipole moment (molecular and ionised forms) and stability (*ab initio* study).

4.3 Outlook on future work

General

The potential of the PIB-succinamide derivatives to undergo *trans*/*cis* isomerisation at the aqueous salt interface needs to be investigated to gain further insight to the complex ionisation and decomposition patterns. Raman and NMR techniques, in conjunction with our experimental and computational results, may be used to study such isomerism in solution [15].

Modelling framework: validation and benchmarking

- Benchmarking study of PIBSA-based surfactants with various combinations of functional groups using current simulation framework and systematic experimental validation study is also required.

Modelling framework: steps towards improvement

- Further work needs to be done to either improve CompassII parameterisation of ammonium nitrate and ionised forms of the amides, or to probe several alternative force-fields;
- Rigid water models need to be considered in the surface adsorption framework;
- Large scale *ab initio* molecular dynamics study of equimolar solution of aqueous ammonium nitrate is essential to gaining a better understanding of the valence and geometric parameters in such system. The simulation cell constructed for surface

adsorption studies could be used as the initial set of coordinates for *ab initio* simulations.

Modelling framework: extension

- Obtain surfactant conformations from solvation in model oil; and incorporate model oil (e.g. dodecane) into the oxidizer simulation cell (in place of vacuum), and run surface adsorption calculations to understand effects of solvation on surfactant adsorption modes;
- Study adsorption of multiple surfactants and co-surfactants using current simulation frame-work (simplified monolayer system);
- Conduct a mesoscale study on self-assembly of PIBSA-based surfactants and compute macroscopic physicochemical parameters (e.g. cmc).

4.4 References

1. Walch E, Gaymans RJ (1994) Telechelic polyisobutylene with unsaturated end groups and with anhydride end groups. Polymer 35 (8):1774-1778.

2. Chance RR, Baniukiewicz SP, Mintz D, Strate GV, Hadjichristidis N (1995) Characterization of Low-Molecular-Weight Polymers: Failure of Universal Calibration in Size Exclusion Chromatography. International Journal of Polymer Analysis and Characterization 1 (1):3-34.

3. Ghaicha L, Leblanc RM, Chattopadhyay AK (1993) Influence of concentrated ammonium nitrate solution on monolayers of some dicarboxylic acid derivatives at the air/water interface. Langmuir 9 (1):288-293.

4. Reynolds PA, Gilbert EP, White JW (2001) High Internal Phase Water-in-Oil Emulsions and Related Microemulsions Studied by Small Angle Neutron Scattering. 2. The Distribution of Surfactant. The Journal of Physical Chemistry B 105 (29):6925-6932.

5. Galust'yan GG, Levkovich MG, Abdullaev ND (2000) The Direction of Ring Fission of Unsymmetrically-substituted Succinic Anhydrides. 1. Interaction of α-Tetrahydrofurylsuccinic Anhydride with Benzylamine and 2,5-Xylidine. Chemistry of Heterocyclic Compounds 36 (12):1402-1408.

6. Tokmakov IV, Alavi S, Thompson DL (2006) Urea and urea nitrate decomposition pathways: a quantum chemistry study. The journal of physical chemistry A 110 (8):2759-2770.

7. Alexandrova AN, Jorgensen WL (2007) Why Urea Eliminates Ammonia Rather than Hydrolyzes in Aqueous Solution. The Journal of Physical Chemistry B 111 (4):720-730.

8. Guevara-Vela JM, Romero-Montalvo E, Costales A, Pendas AM, Rocha-Rinza T (2016) The nature of resonance-assisted hydrogen bonds: a quantum chemical topology perspective. Physical Chemistry Chemical Physics 18 (38):26383-26390.

9. Nanubolu JB, Sridhar B, Ravikumar K (2012) Resonance-assisted amide protonation in dutasteride hydrochloride salt. CrystEngComm 14 (7):2571-2578.

10. Harkema S, Feil D (1969) The crystal structure of urea nitrate. Acta Crystallographica Section B 25 (3):589-591.

11. Emsley J (1980) Very strong hydrogen bonding. Chemical Society Reviews 9 (1):91-124.

12. Ghaicha L, Chattopadhyay AK, Tajmir-Riahi HA (1991) Behavior of stearic acid monolayers in presence of concentrated ammonium nitrate solution substrate. Langmuir 7 (10):2007-2009.

13. Yubai B, Munger G, Leblanc RM, Ghaicha L, Chattopadhyay AK (1996) Crystallization of Ammonium Nitrate under organized monolayers of various amphiphiles Journal of Dispersion Science and Technology 17 (4):391-405.

14. Laughlin RG (1981) HLB, from a thermodynamic perspective. Journal of the Society of Cosmetic Chemists 32 (6):371-392.

15. Hu X, Zhang W, Carmichael I, Serianni AS (2010) Amide Cis–Trans Isomerization in Aqueous Solutions of Methyl N-Formyl-d-glucosaminides and Methyl N-Acetyl-d-glucosaminides: Chemical Equilibria and Exchange Kinetics. Journal of the American Chemical Society 132 (13):4641-4652.

Appendices

A2. Appendix to Chapter 2

Table A2-1: Technical specification of BASF products Glissopal® and GlissopalSA®***

Properties (unit)	Method	Glissopal® 1000	Glissopal® 1300	Glissopal® 2300	GlissopalSA®
Mn	GPC	1000	1300	2300	-
PDI	GPC	1.6	2.0	1.8	-
Alfa (*exo*)	^{13}C-NMR	88	87	80	-
Beta (*endo*)	^{13}C-NMR	6	7	8	-
Tetra-substituted	^{13}C-NMR	1.5	1.5	2	-
Bis-maleation, %	BASF method	-	-	-	16
Saponification mg KOH/g	BASF method	-	-	-	87
Activity, %	BASF method	-	-	-	78
Water, mg/kg	Karl-Fisher	25	25	25	-
Viscosity, mm^2/s	DIN51562	4650	15000	48000	-
Viscosity, 100 C, mm^2/s	DIN51562	190	500	1500	480
Density, 20 C, g/cm^3	DIN51757	0.89	0.89	0.90	0.92

* Technical Information Bulletin - TI/EVD 1186 e December 2005
** Technical Information Bulletin - TI/EVO 2066 e April 2013

Table A2-2: GPC-MALLs analysis of PIB and PIBSA

Reference	Trade name	dn/dc	Mn	Mw	PDI
Sample-1	Glissopal®1000	0.095	1077	1191	1.1
Sample-2	Glissopal®1300	0.10	1378	2363	1.7
Sample-3	Glissopal®2300	0.10	2681	3607	1.3
Sample-4	Glissopal®SA	0.099	1576	1920	1.2
Sample-6	HR-PIB	0.092	1267	1295	1.0
Sample-7	PIBSA	0.098	1700	1900	1.1

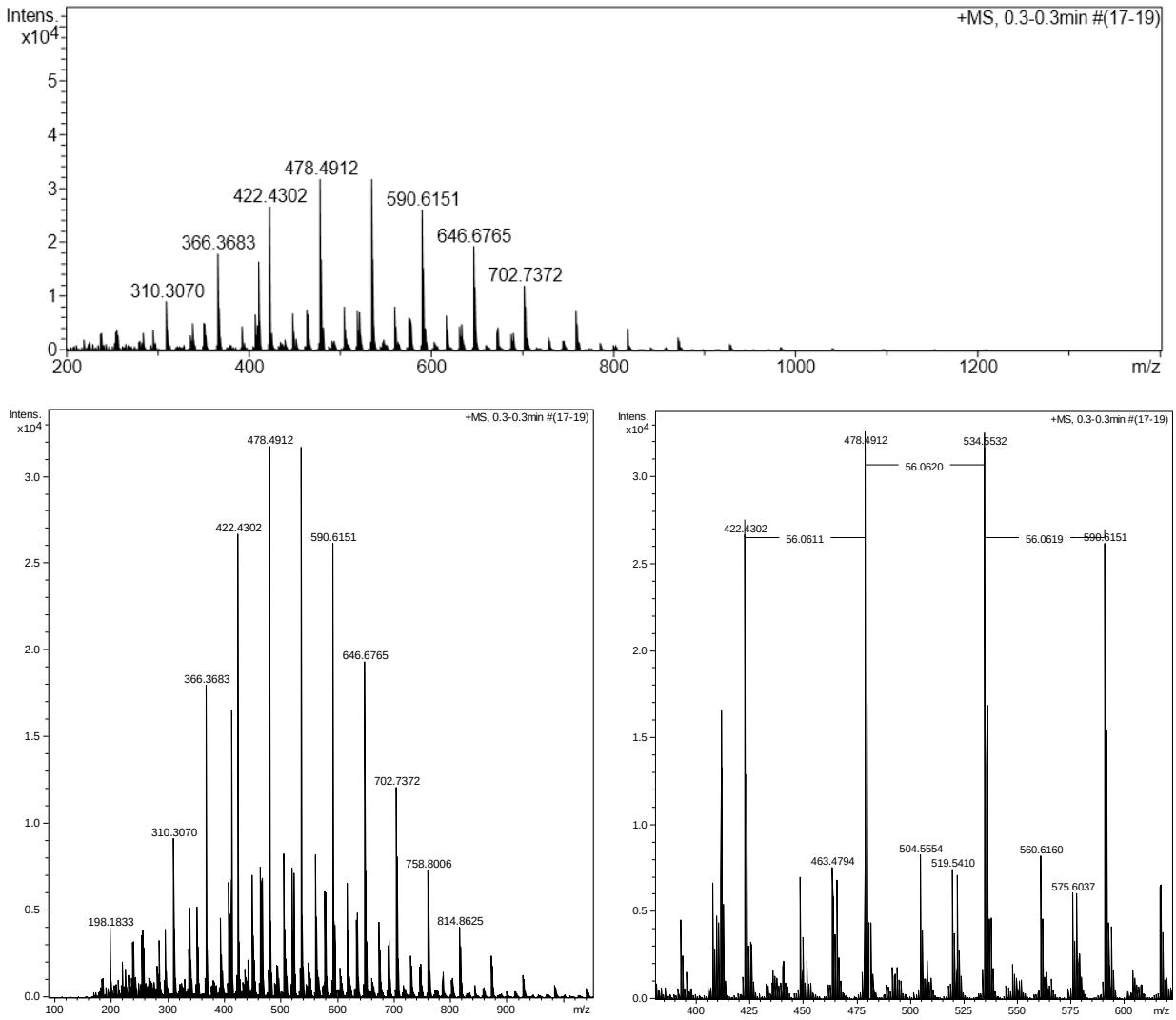

Figure A2-1: Positive mode APCI mass spectra of PIB sample-6.

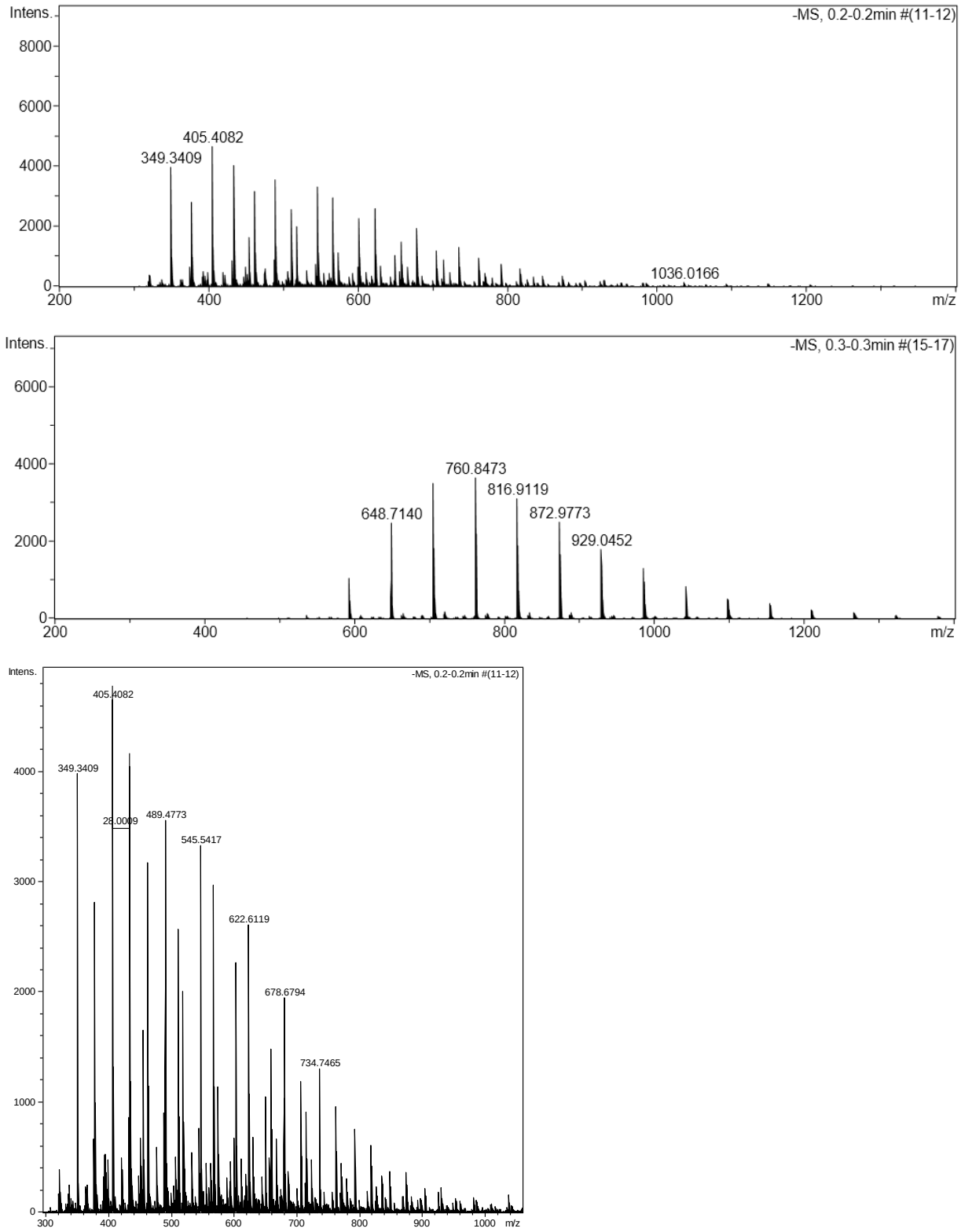

Figure A2-2: Negative mode APCI mass spectra of PIB sample-6.

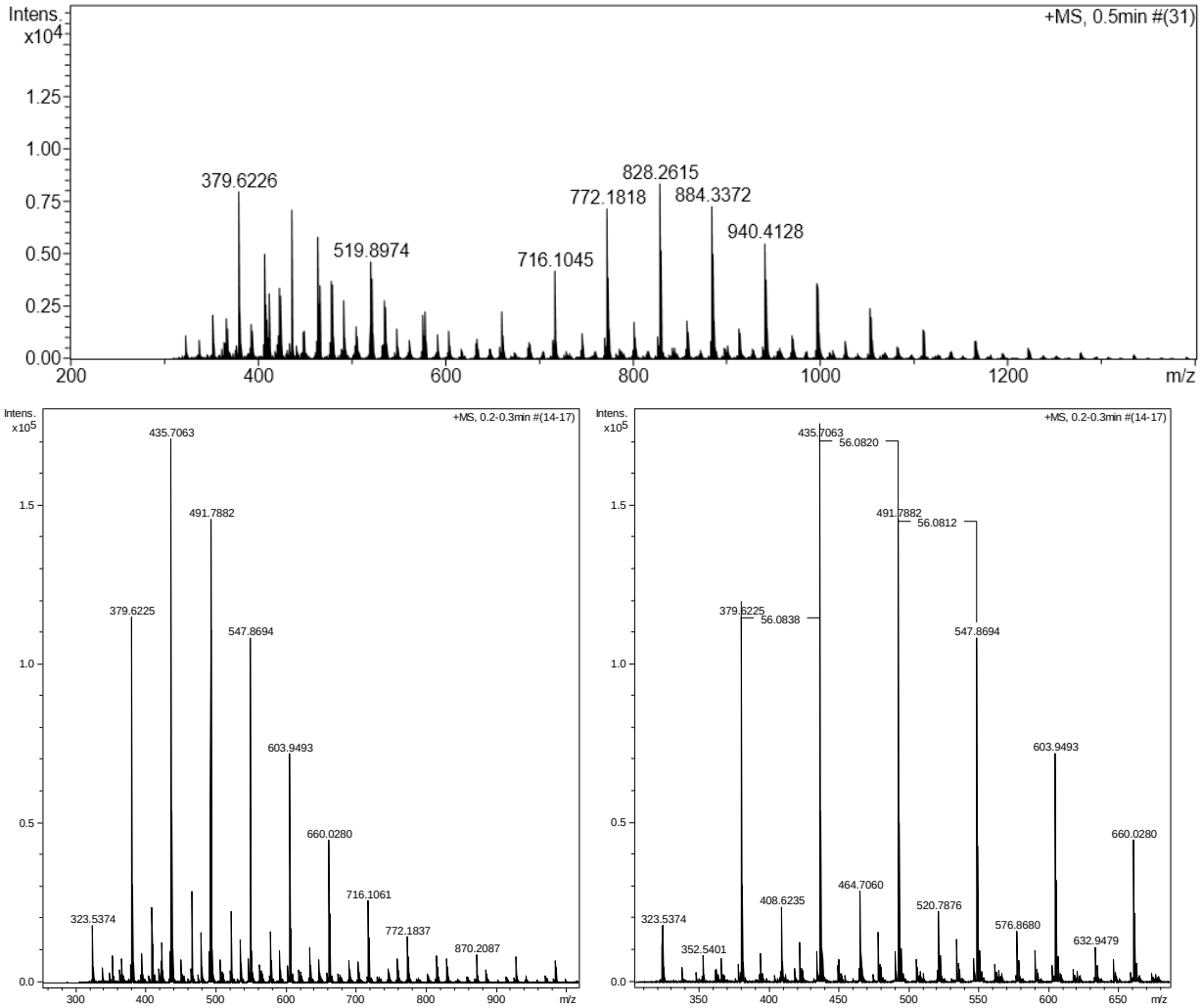

Figure A2-3: Positive mode APCI mass spectra of PIBSA sample-7.

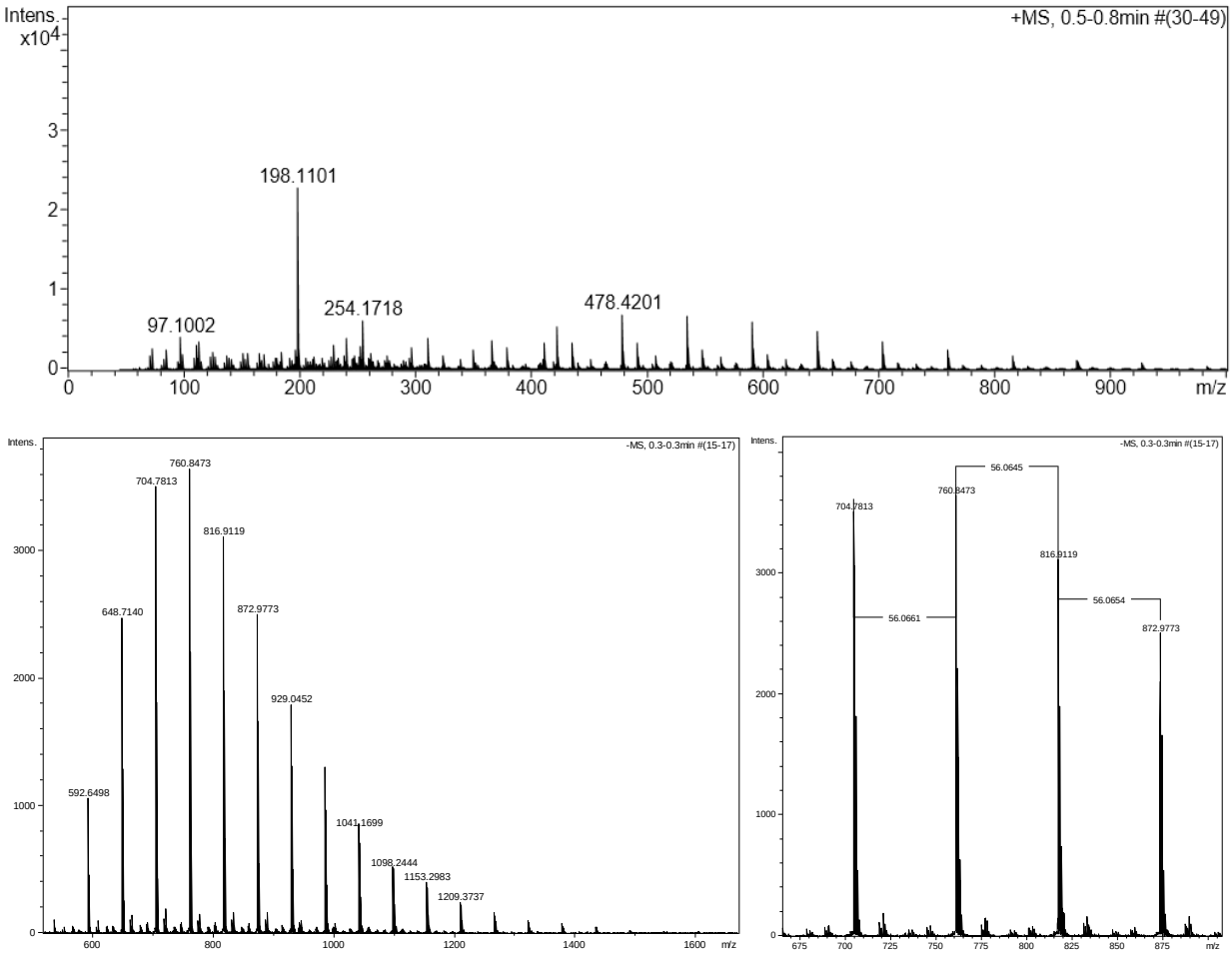

Figure A2-4: Positive mode APCI mass spectra of PIBSA-MEA sample-8.

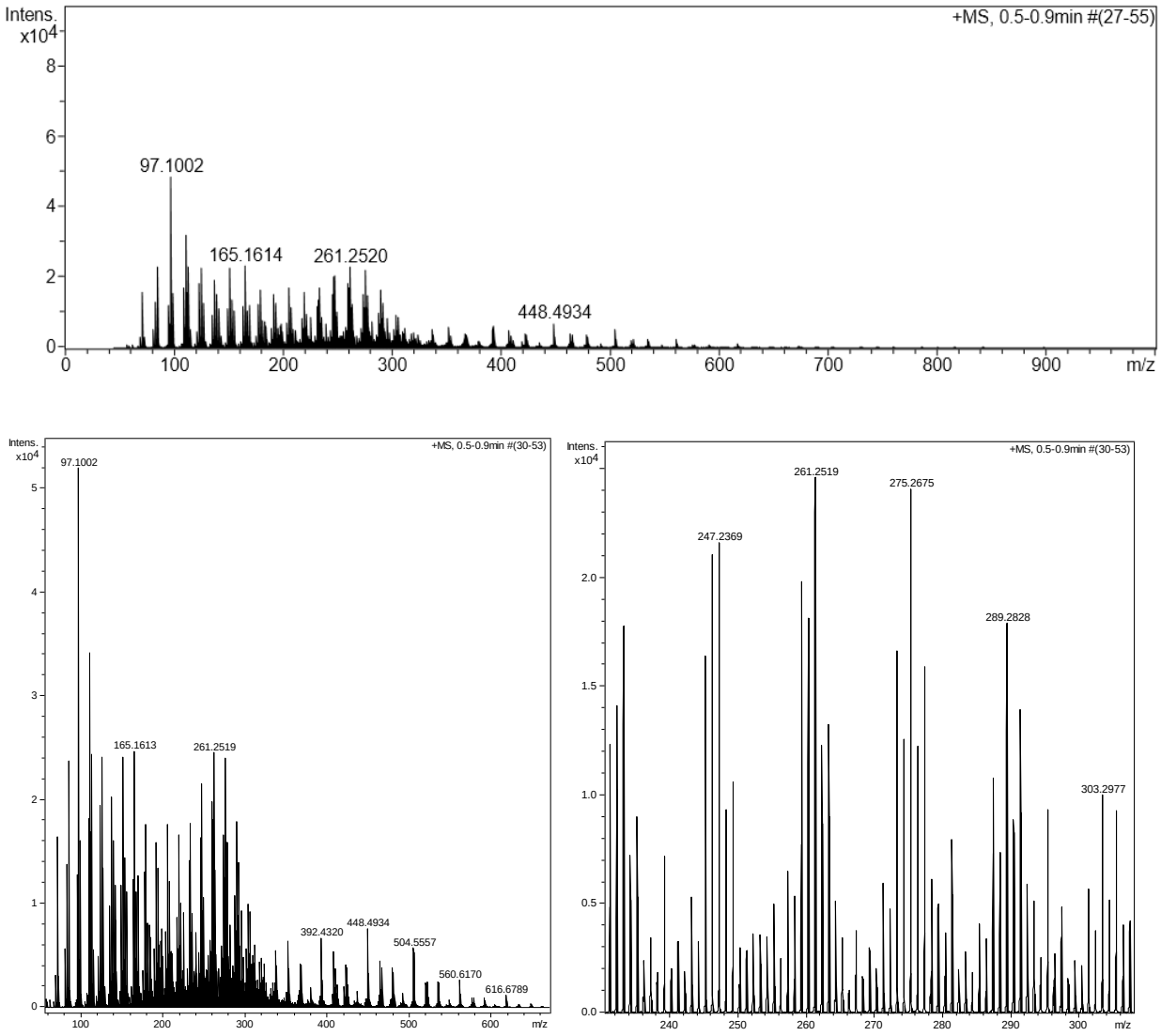

Figure A2-5: Positive ion APCI mass spectra of sample-8/fraction-F1.

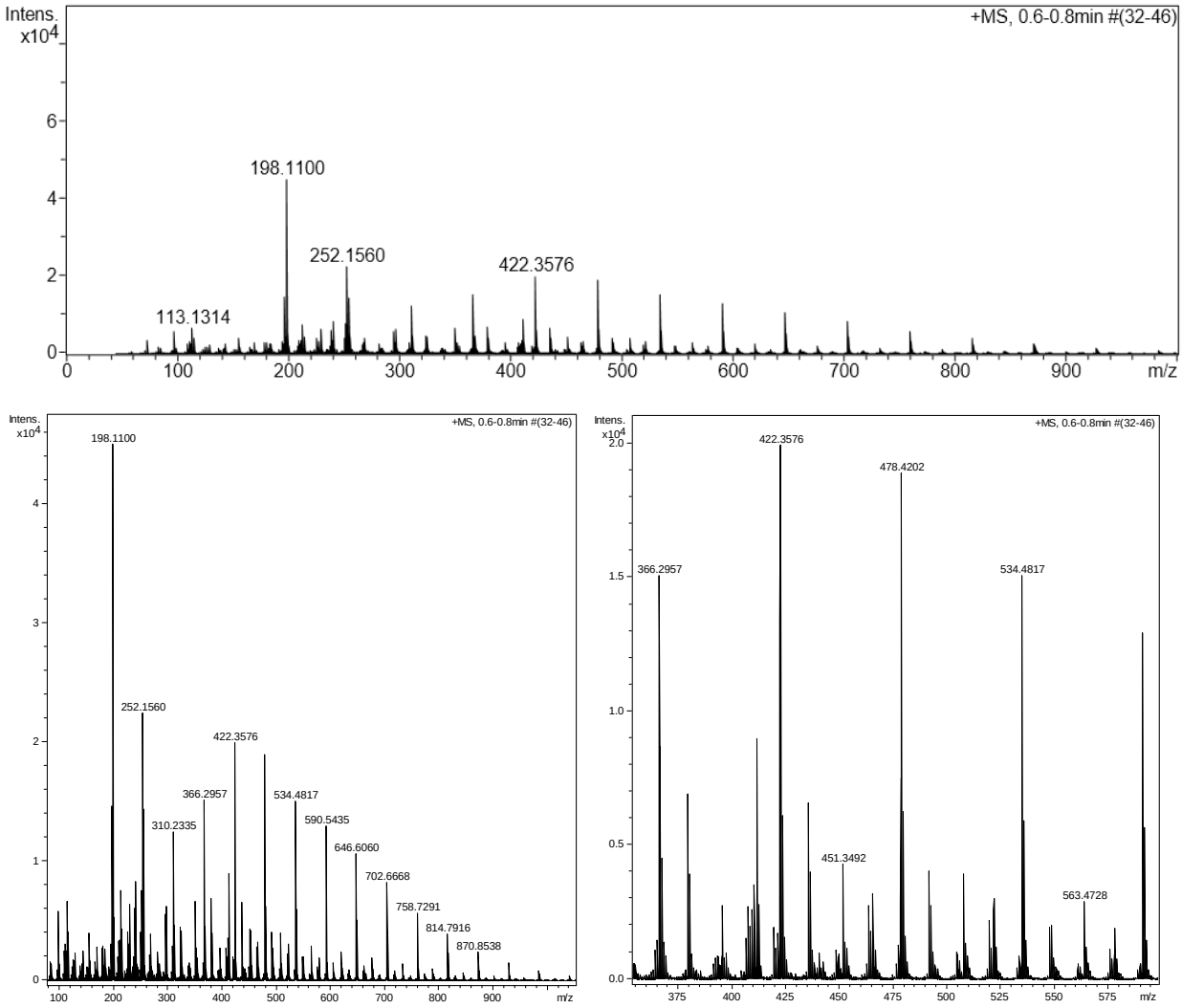

Figure A2-6: Positive mode APCI mass spectra of PIBSA-MEA sample-8/fraction-F2.

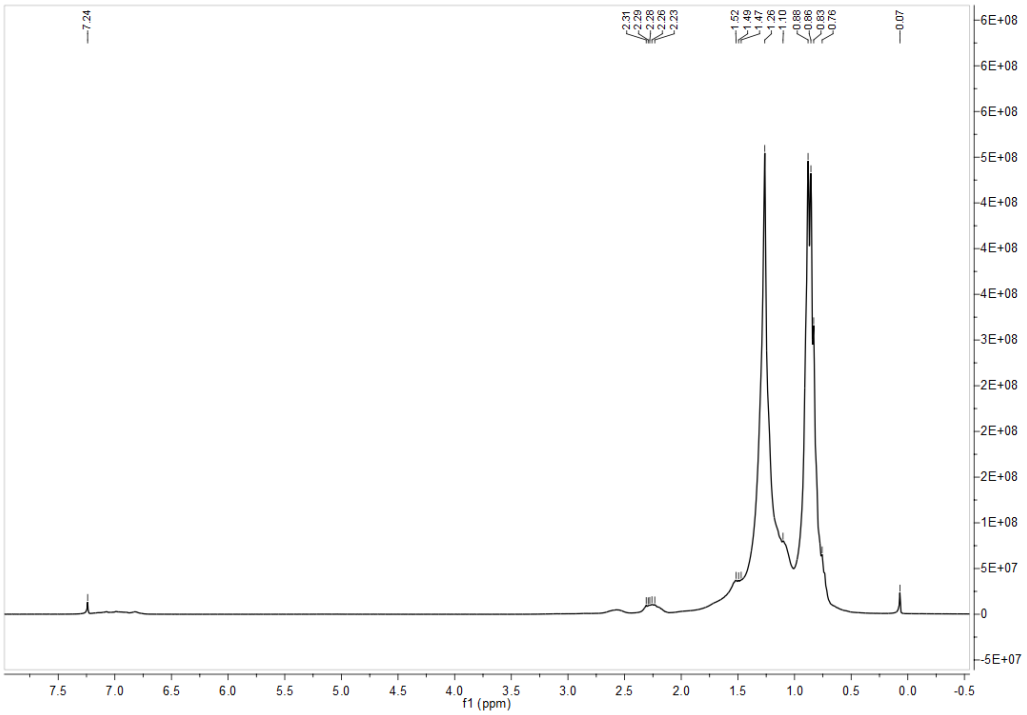

Figure A2-7:[1]H-NMR (300 MHz, CDCl[3]) spectrum of diluent oil (sample-5).

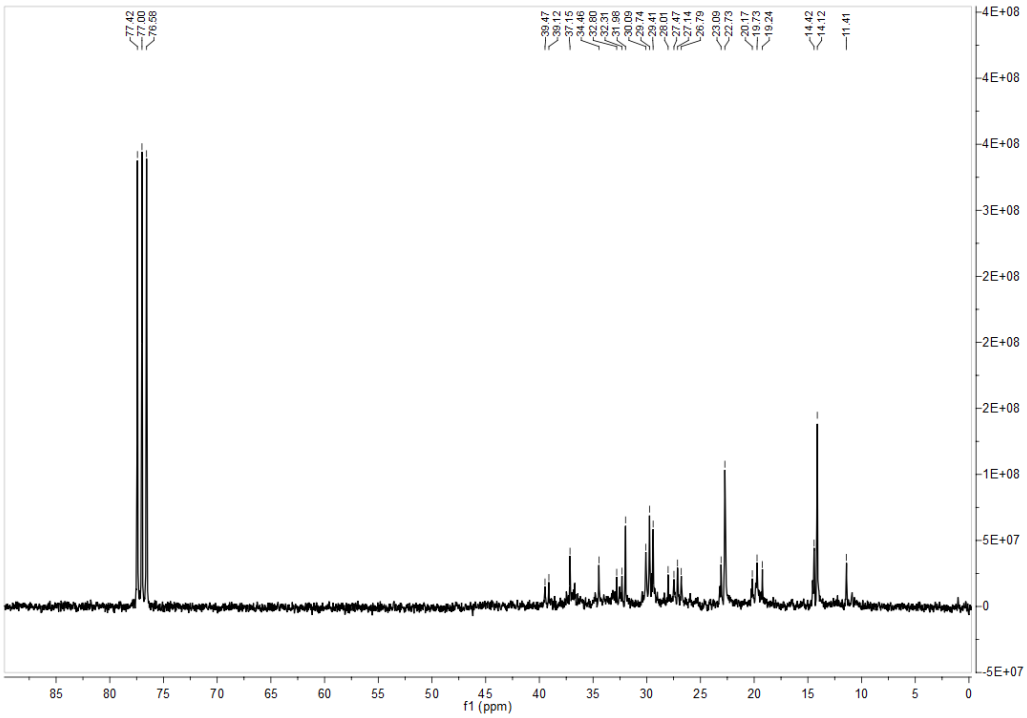

Figure A2-8: [13]C-NMR (300 MHz, $CDCl_3$) spectrum of diluent oil (sample-5).

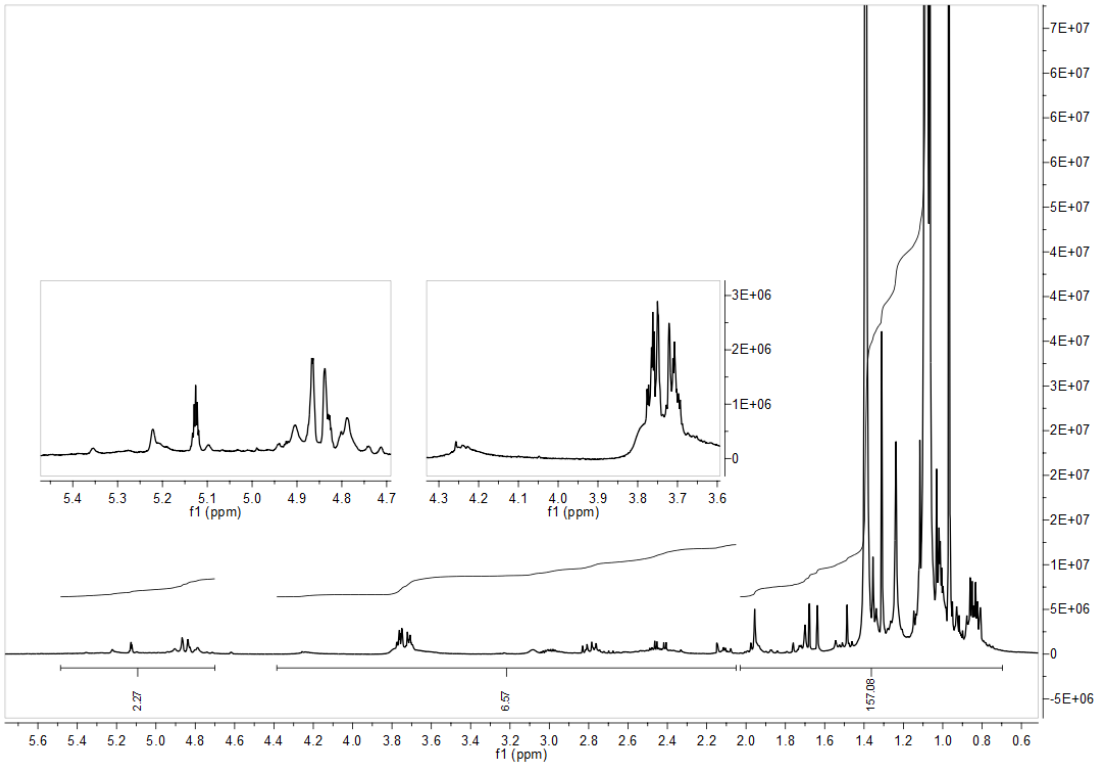

Figure A2-9: ^{1}H-NMR (400 MHz, $CDCl_3$) spectrum of PIBSA-MEA surfactant (sample-8).

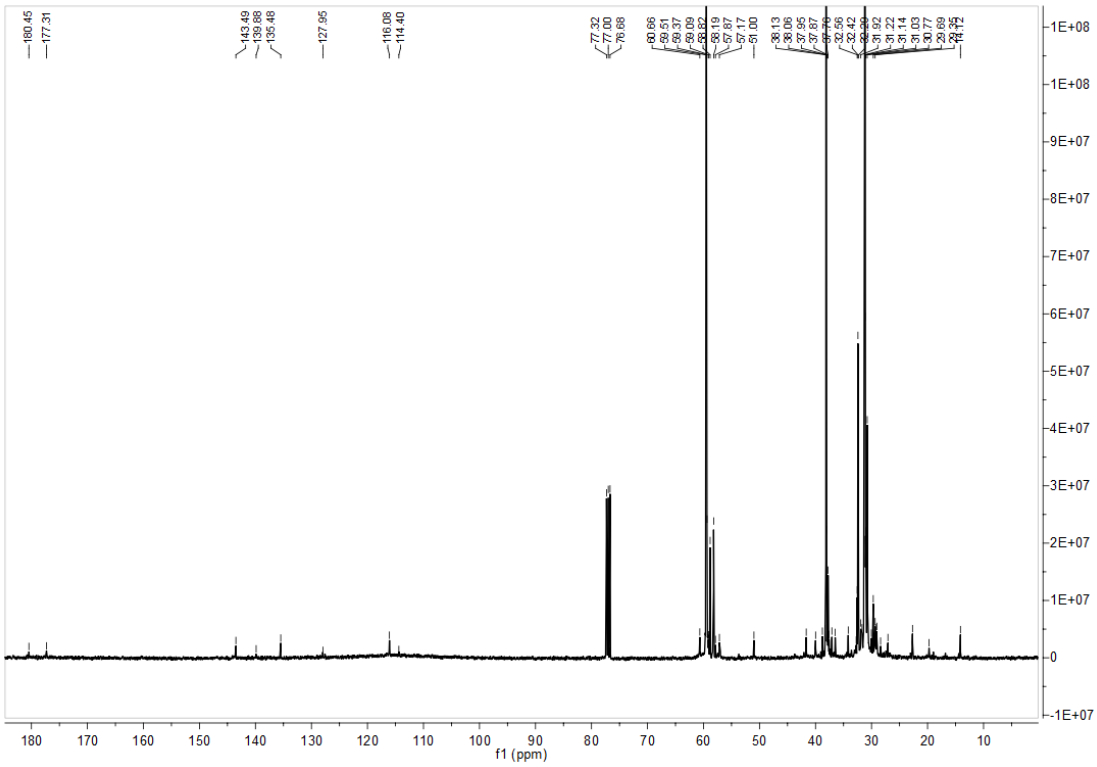

Figure A2-10: ^{13}C-NMR (400 MHz, $CDCl_3$) spectrum of PIBSA-MEA surfactant (sample-8).

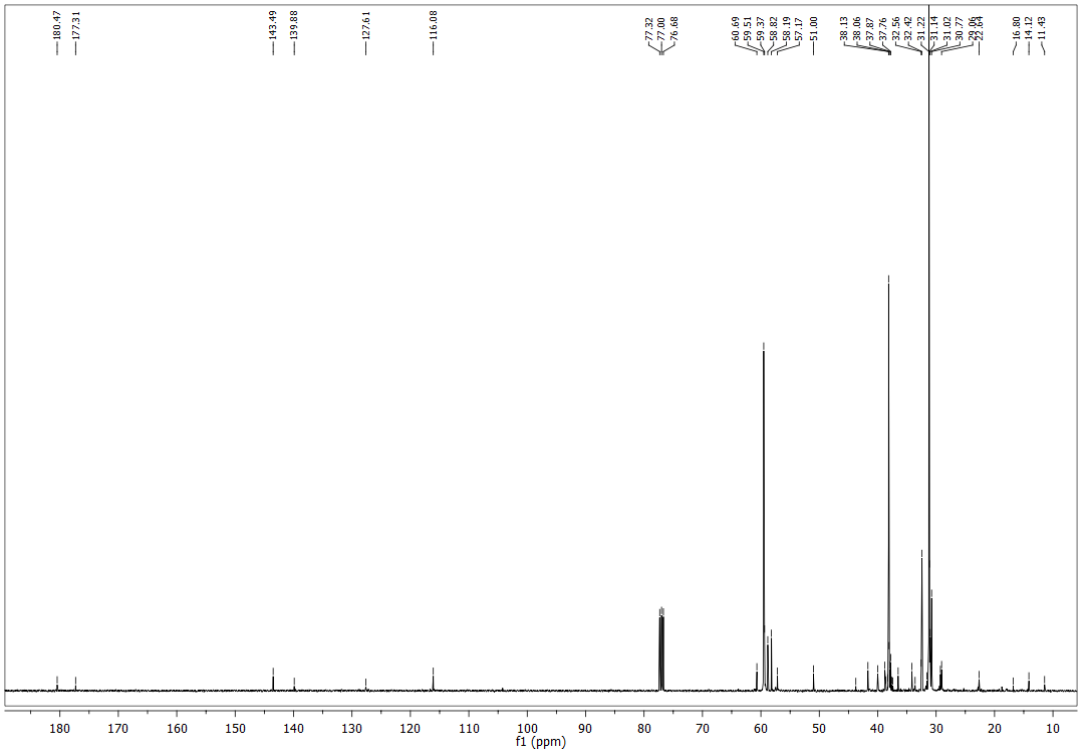

Figure A2-11: ^{13}C-NMR (400 MHz, $CDCl_3$) spectrum of purified PIBSA-MEA (sample-8/fraction F2).

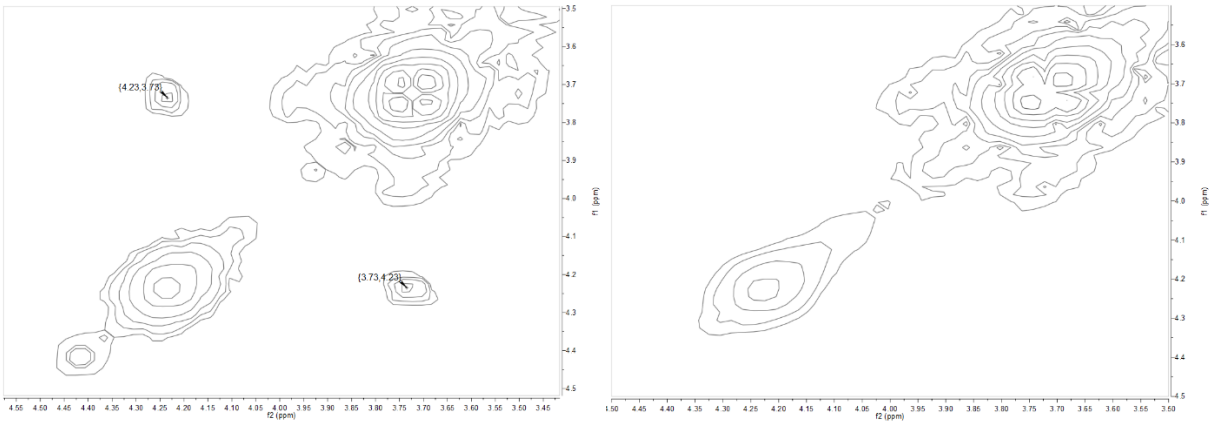

Figure A2-12: Expanded ^{1}H-^{1}H COSY NMR (400 MHz, $CDCl_3$) maps of PIBSA-MEA sample-8/fraction F2 (left) and PIBSA-IMIDE sample-9 (right).

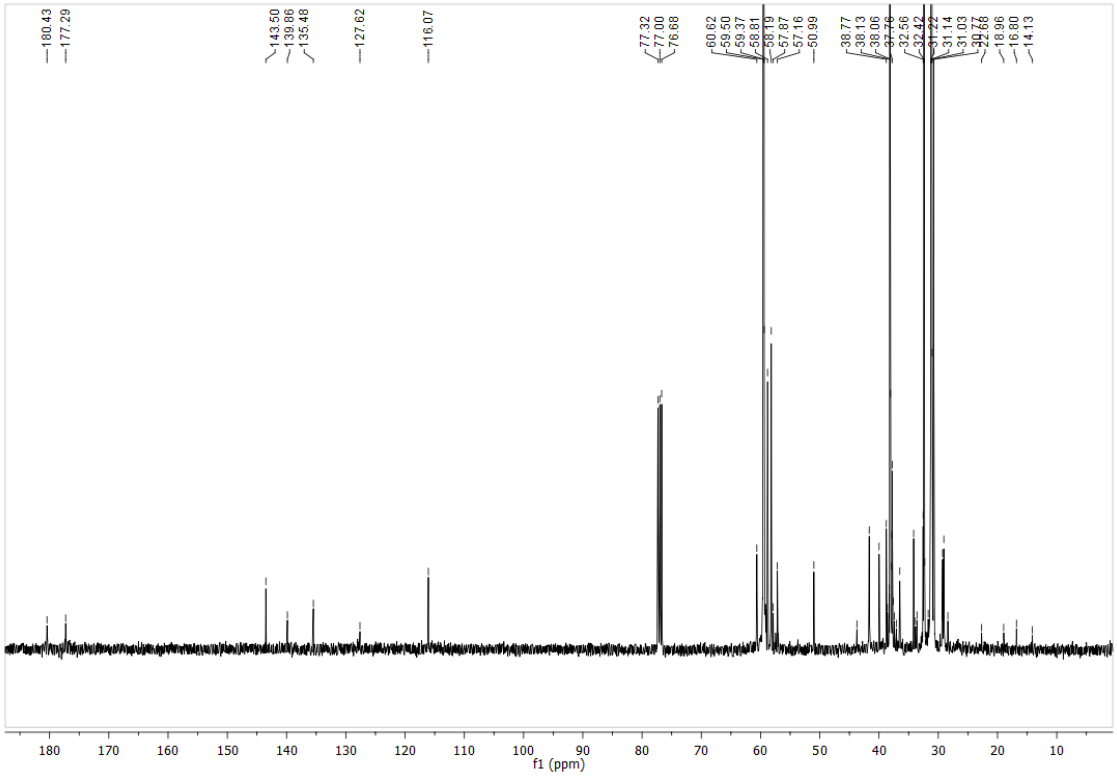

Figure A2-13: ^{13}C-NMR (400 MHz, $CDCl_3$) spectrum of PIBSA-IMIDE (sample-9).

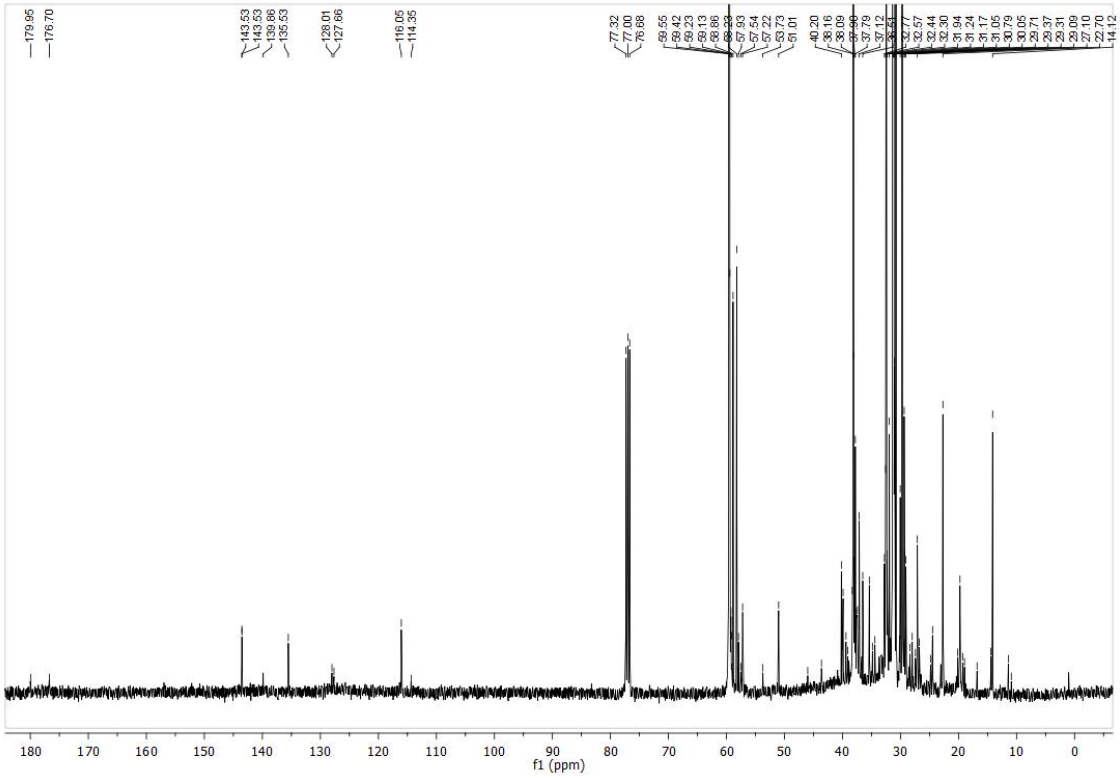

Figure A2-14: ^{13}C-NMR (400 MHz, $CDCl_3$) spectrum of PIBSA-UREA (sample-10).

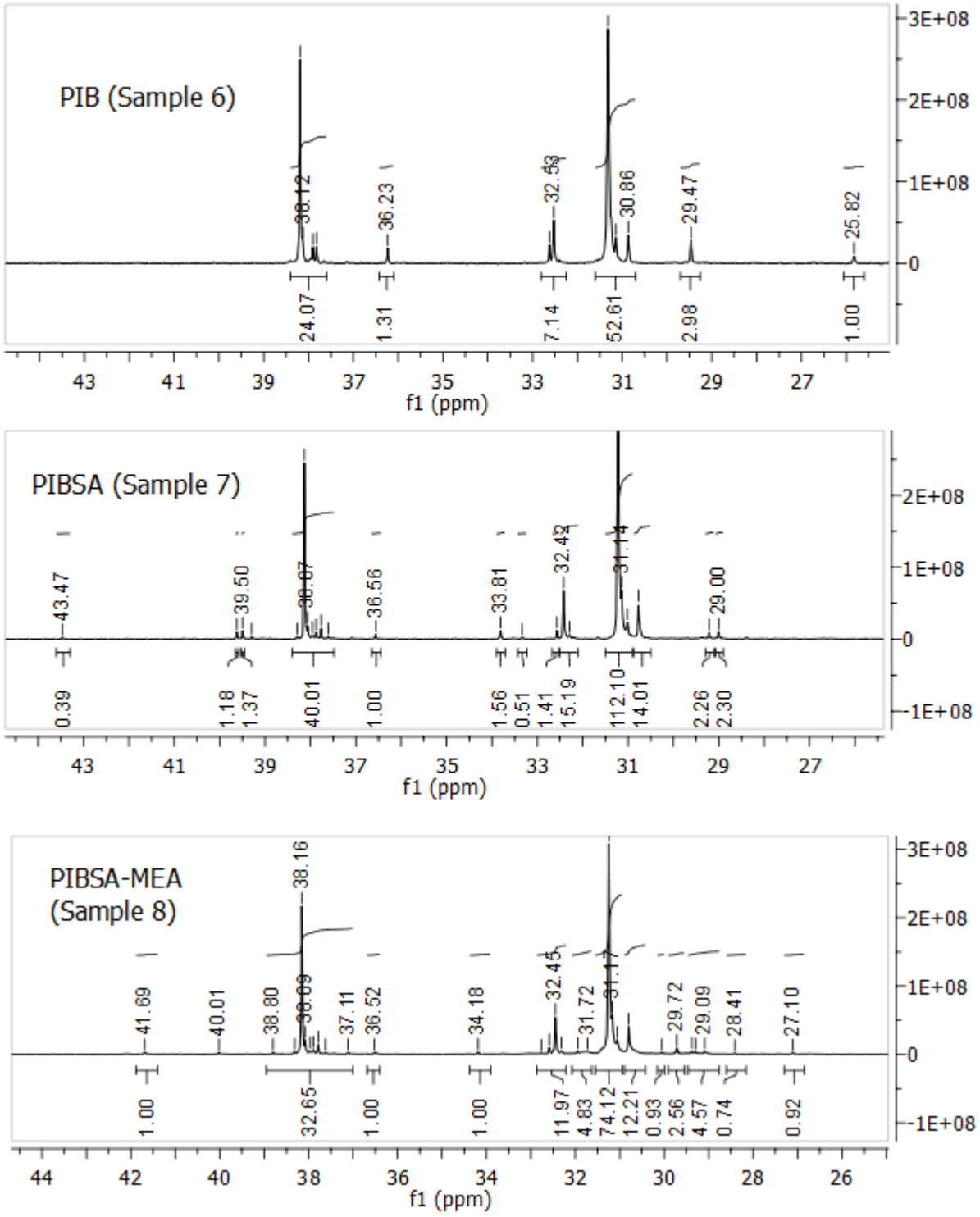

Figure A2-15: Integration of ^{13}C-NMR (400 MHz, $CDCl_3$) aliphatic spectral peaks of PIB (sample-6), PIBSA (sample-7) and PIBSA-MEA (sample-8).

FT-IR spectra

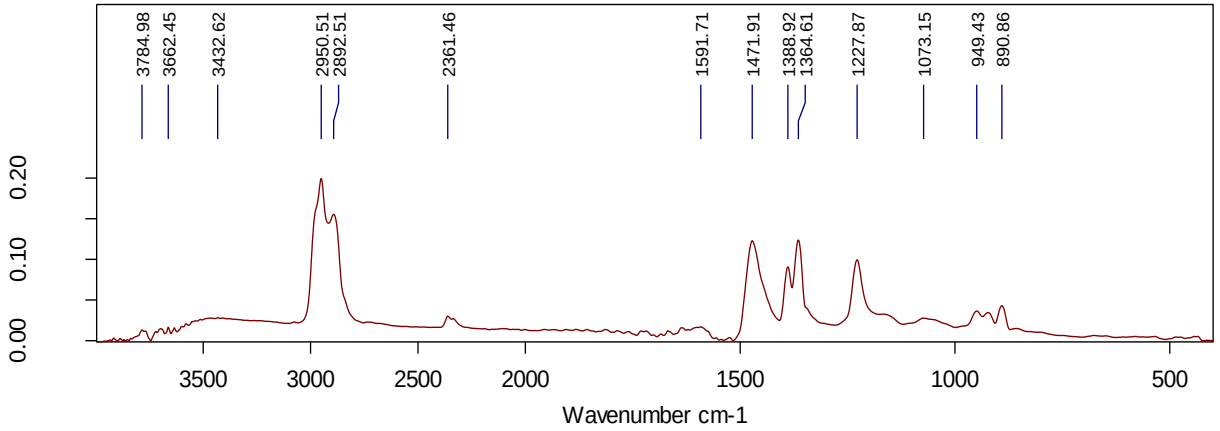

Figure A2-16: FT-IR spectrum of MM-II-001B Lake PIB (sample 6).

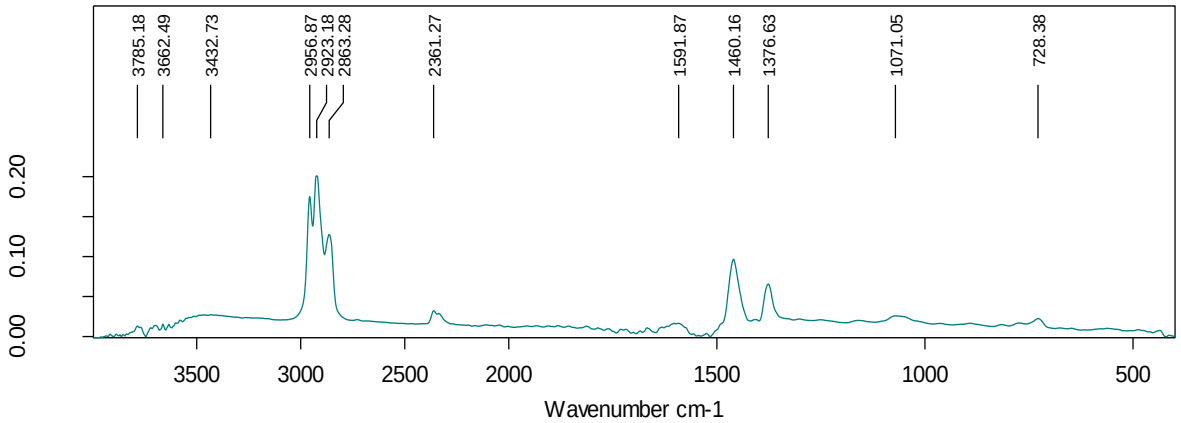

Figure A2-17: FT-IR spectrum of diluent oil (sample-5).

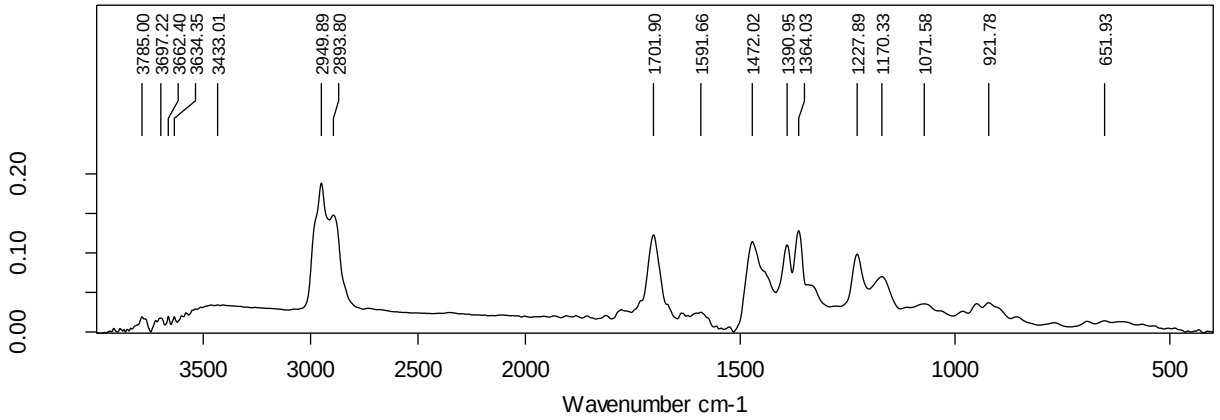

Figure A2-18: FT-IR spectrum of PIBSA-IMIDE (sample-9).

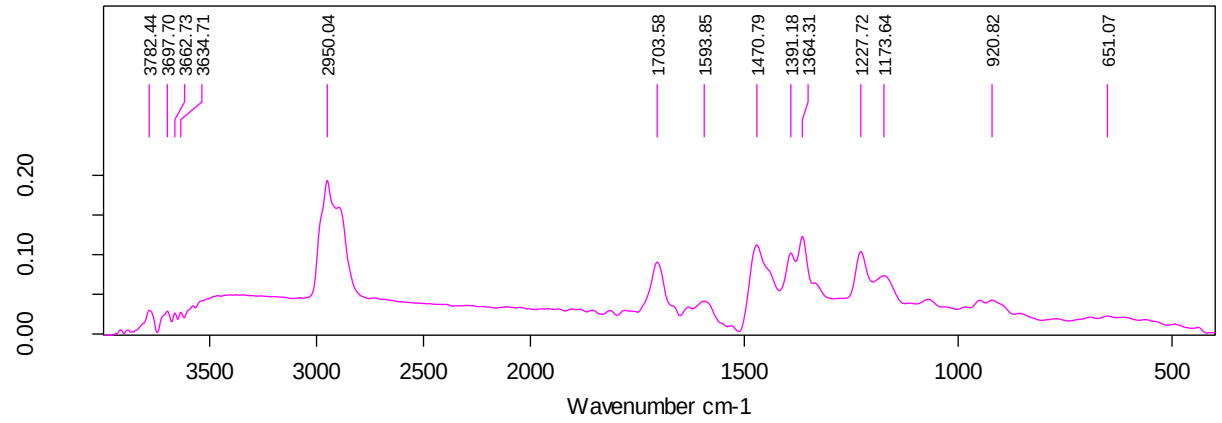

Figure A2-19: FT-IR spectrum of PIBSA-MEA concentrate (sample-8).

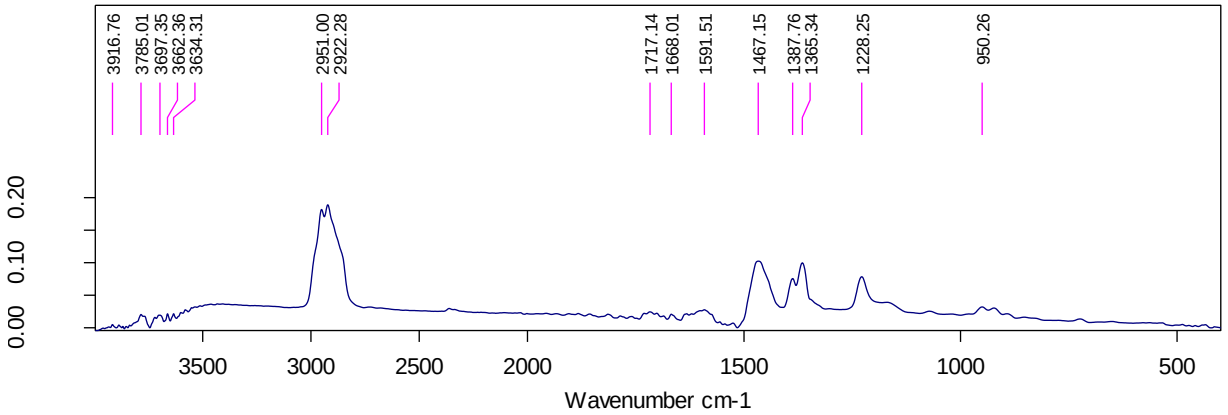

Figure A2-20: FT-IR spectrum of PIBSA-MEA (sample-8/ fraction F1).

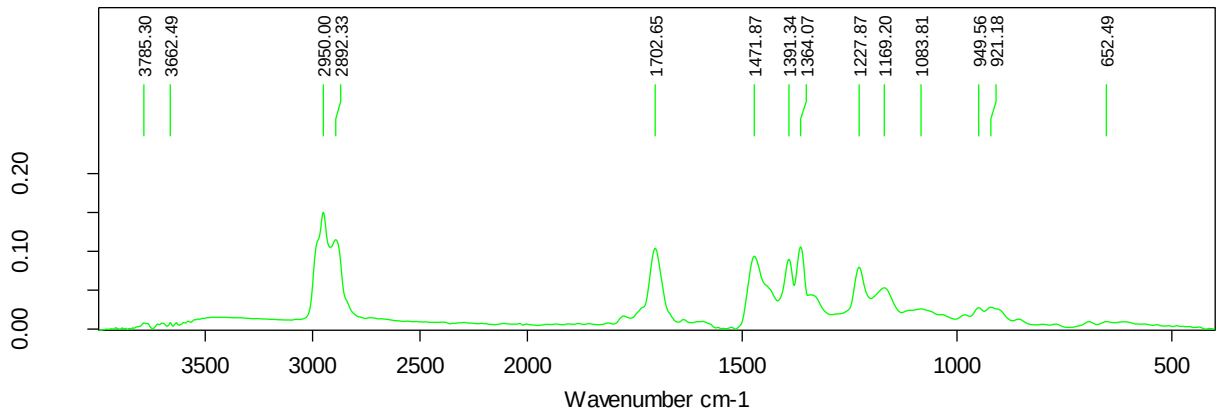

Figure A2-21: FT-IR spectrum of PIBSA-MEA (sample-8/fraction F2).

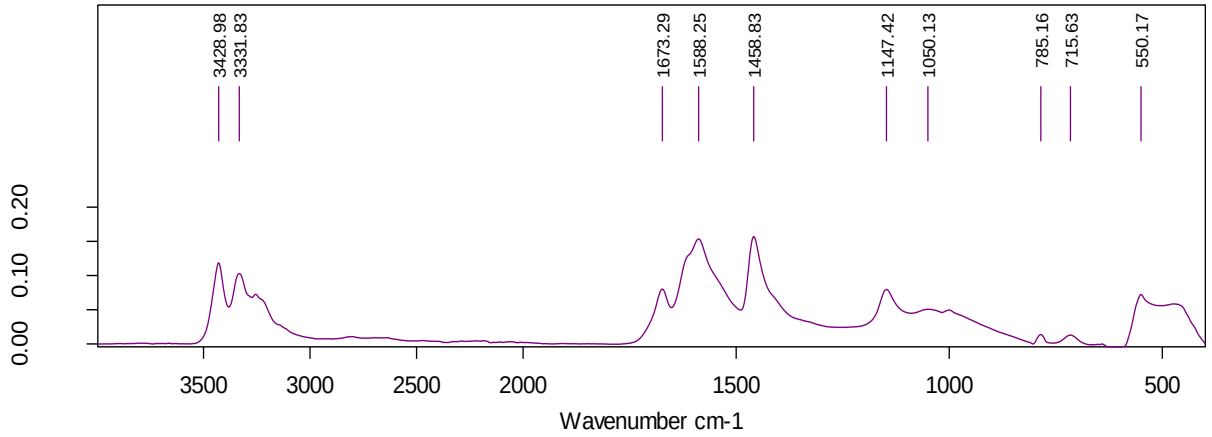

Figure A2-22: FT-IR spectrum of Urea.

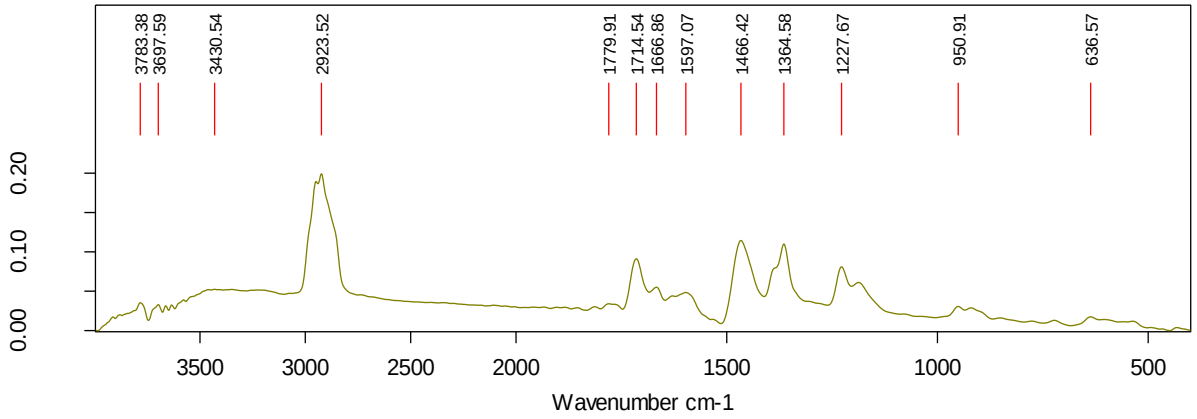

Figure A2-23: FT-IR spectrum of PIBSA-UREA (sample-10).

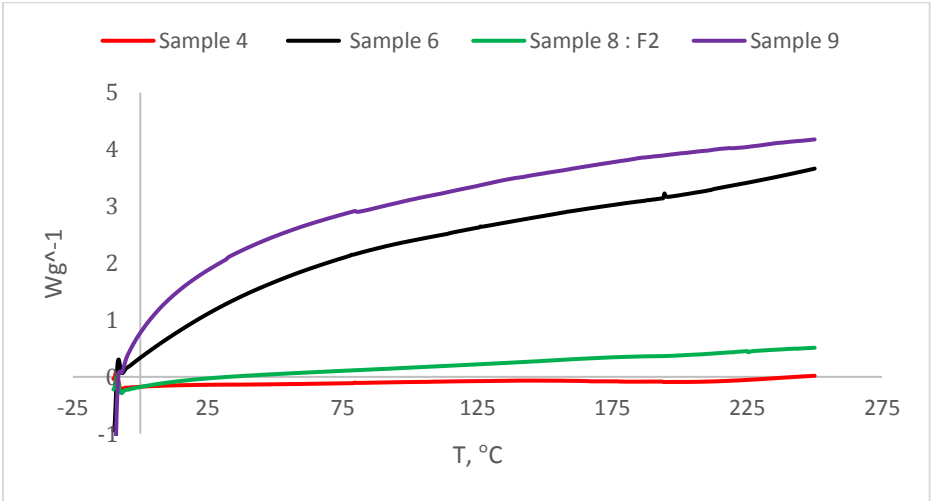

Figure A2-24: DSC plot of samples-4, -6, -8: F2 and -9.

A3. Appendix to Chapter 3

Theoretical aspects of BFDH and Growth Morphology methods

The purely geometric BFDH method was used for rough estimation of growth morphology. This method is based on the principle that crystal symmetry is related to possible growth planes by means of translational symmetry operators, which treat growth of higher order planes in preference to the lower order ones, and ease of adding a growth plane of atoms or molecules is proportional to its thickness (Eq. 3-4).

$$\boldsymbol{D_{hkl}} \sim \frac{\mathbf{1}}{\boldsymbol{d_{hkl}}} \qquad \textit{Eq. 3-1}$$

The D_{hkl} is the center to face distance and d_{hkl} is the lattice to plain spacing. Thinner growth planes grow faster and have larger center-to-face distance. This method does not account for the energy of the chemical nature and bonding in the crystal[41].

More accurate Growth morphology method, which is an extension of BFDH method, was used to deduce geometries and energetic characteristics of morphologically important crystal growth faces of *II-AN* and *IV-AN*. The relative measure of the normal growth rate of the [106] form is the attachment energy - $\boldsymbol{E_{att}}$, which is defined as the potential energy released on attachment of a growth slice to a growing crystal surface [41,118,119].

$$\boldsymbol{D_{hkl}} \sim \frac{\mathbf{1}}{\boldsymbol{E_{(hkl)att.}}} \qquad \textit{Eq. 3-2}$$

The attachment energy - $\boldsymbol{E_{att}}$ is calculated for a series of suitable slices (h k l), which are deduced from a Donnay-Harker prediction Eq. 0-2, where $\boldsymbol{E_{slice}}$ = energy of a growth slice at $\boldsymbol{D_{hkl}}$ of thickness $\boldsymbol{d_{hkl}}$, and growth rate is inversely proportional to $\boldsymbol{E_{att}}$ (Eq. 0-3).

$$\boldsymbol{E_{att}} = \boldsymbol{E_{latt}} - \boldsymbol{E_{slice}} \qquad \textit{Eq. 3-3}$$

Table A3-1: ***Selected potentials and functional forms for non-bond interactions***

Potential name	Functional form	Units	Description	Forcefield
van der Waals				
LJ 9 6	$E = D_0\left[2\left(\frac{R_0}{R}\right)^9 - 3\left(\frac{R_0}{R}\right)^6\right]$	D_0 : kcal/mol	Equilibrium well depth	COMPASS II
		R_0 : Å	Equilibrium distance	
		E : -	Distance offset	
LJ 12 6	$E = D_0\left[\left(\frac{R_0}{R}\right)^{12} - 2\left(\frac{R_0}{R}\right)^6\right]$	D_0 : kcal/mol	Equilibrium well depth	Dreiding
		R_0 : Å	Equilibrium distance	
Morse Dispersion	$E = D_0[X^2 - 2X]f_s - (1 - f_s)\frac{C_6}{R^6}$ where: $X = \exp\left(-\frac{y}{2}\left(\frac{R}{R_0} - 1\right)\right)$ $f_s = \frac{1}{1 + \exp(20(R - R_c))}$	C_6 : kcal/mol /Å^{-6}	Dispersion C6 parameter	COMPASS II
		D_0 : kcal/mol	Equilibrium well depth	
		R_0 : Å	Equilibrium distance	
		R_c : Å	Morse Dispersion switching distance	
		y : -	Unitless scaling factor	
Hydrogen Bond				
LJ 12 10	$E = D_0\left[5\left(\frac{R_0}{R}\right)^{12} - 6\left(\frac{R_0}{R}\right)^{10}\right]\cos^4\phi$	D_0 : kcal/mol	Equilibrium well depth	Dreiding
		R_0 : Å	Equilibrium distance	
Coulombic				
Shielded (LIN-R-ε)	$E = C\frac{q_i q_j R_0}{\varepsilon R^2}$ where: C = 332.0647/(kcal/mol)Å/e^2 is a unit conversion factor R_0 = 1 Å	q_i, q_j : e		Dreiding
		ε : -	Relative dielectric constant	
		R_0 : Å	Equilibrium distance	
Coulombic (CONST-ε)	$E = C\frac{q_i q_j}{\varepsilon R}$ where: C = 332.0647/(kcal/mol)Å/e^2 is a unit conversion factor	q_i, q_j : e		COMPASS II
		ε : -	Relative dielectric constant	
Bond Increment Charges				
Simple	$q_i = \delta_i + \sum_j \delta_{ij}$	δ_{ij} : e	Bond increment charge between bonded particles i and j	COMPASS II
		δ_i: e	Charge associated with the ForcefieldType on i	

Table A3-2: Calculated partial atomic charges for individual Ammonium and Nitrate ions (gas phase)

Atom	Charge[a], *eV*	Charge[b], *eV*	Charge[c], *eV*
NH	- 0.774701	-0.744	-0.6553
H	0.443675	0.443	0.41384
NO	0.896259	0.898	0.6329
O	- 0.632086	-0.632	-0.5464

a. From CompassII [76];
b. From restricted electrostatic potential (RESP) fit in AMBER package [76];
c. From empirical fitting of NH_4^+ and NO_3^- parameters with GULP code [114];

Table A3-3: Forcite GO optimization convergence criteria

Value	Coarse	Medium	Fine	Ultra-fine
Energy (kcal/mol)	0.002	0.001	1×10^{-4}	2×10^{-5}
Max. force (kcal/mol/Å)	2.5	0.5	0.005	0.001
Max. stress (GPa)	2.5	0.5	0.005	0.001
Max. displacement (Å)	0.05	0.015	0.001	$1x10^{-5}$

Table A3-4: Partial atomic charges for the truncated side chain succinic anhydride forms as derived from ESP fit analysis in DMol³ and Forcite (CompassII)

HG-	**-CH_3**		**-$[IB]_1$**	**-$[IB]_2$**	**-$[IB]_3$**	**-$[IB]_4$**
Head group	CompassII q, *eV*	Dmol³ ESP q, *eV*	Dmol³ ESP q, *eV*	Dmol³ ESP q, *eV*	Dmol³ ESP q, *eV*	Dmol³ ESP q, *eV*
C1	0.562	0.566	0.549	0.568	0.572	0.574
C2	-0.053	0.256	0.156	0.183	0.139	0.137
C3	-0.106	-0.461	-0.446	-0.471	-0.509	-0.513
C4	0.562	0.692	0.683	0.664	0.689	0.692
O1	-0.450	-0.453	-0.437	-0.443	-0.436	-0.438
O2	-0.450	-0.466	-0.466	-0.457	-0.458	-0.460
O3	-0.224	-0.391	-0.391	-0.385	-0.397	-0.396
Tail						
C5	-0.159	-0.476	-0.518	-0.501	-0.582	-0.592
C6	-	-	0.516	0.461	0.474	0.537
C7	-	-	-0.649	-0.630	-0.542	-0.683
C8	-	-	-	0.786	0.822	0.818
C9	-	-	-	-0.608	-0.621	-0.576
C10	-	-	-	-	0.800	0.794
C11	-	-	-	-	-0.620	-0.514
C12	-	-	-	-	-	0.750
C13	-	-	-	-	-	-0.563

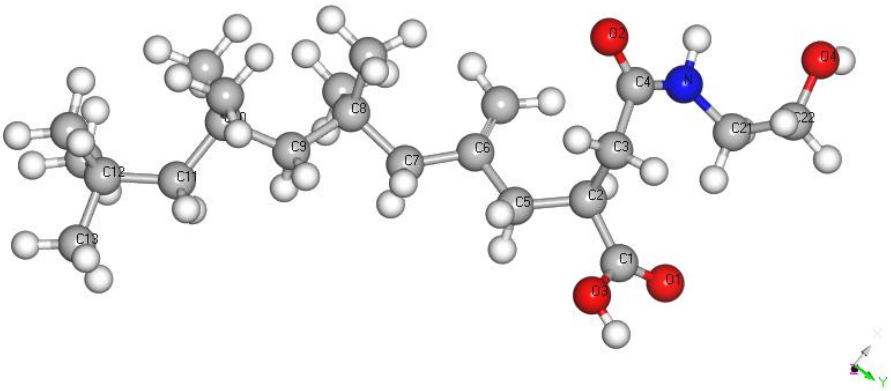

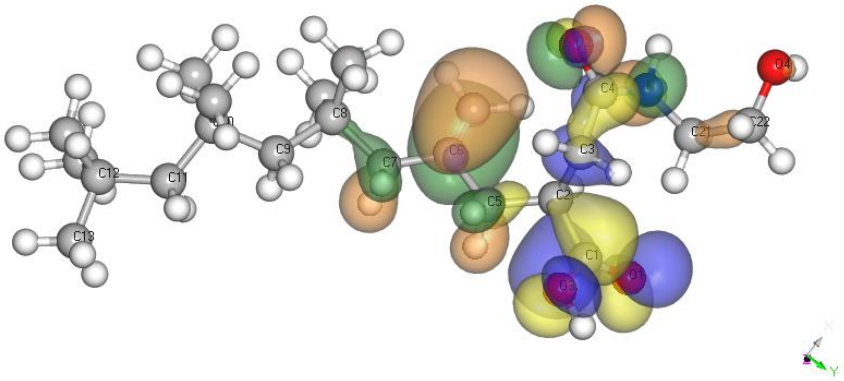

***Isosurface colour map**: **LUMO** Yellow - (-) values, blue - (+) values; **HOMO** - Brown - (-) values, green - (+) values*

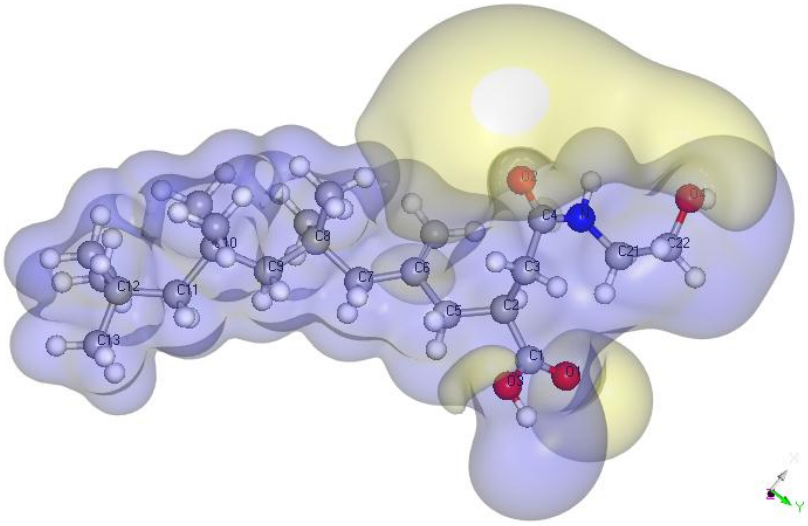

***Isosurface colour map**: Yellow - (-) values, blue - (+) values*

Scheme A3-1: Numbering and colour scheme for [IB]$_4$SA-MEA-cis conformation (top); HOMO-LUMO isosurface (middle) and calculated electrostatic potential (bottom).

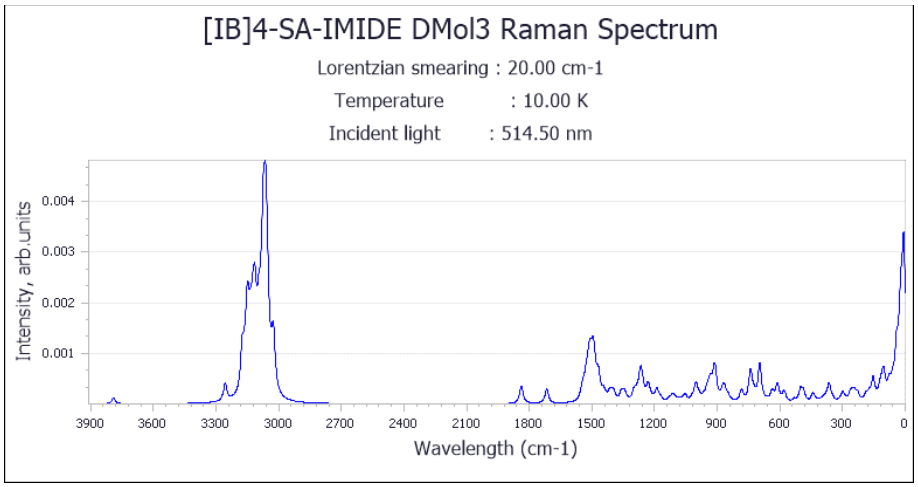

Figure A3-1: Calculated Raman spectrum for [IB]$_4$SA-IMIDE.

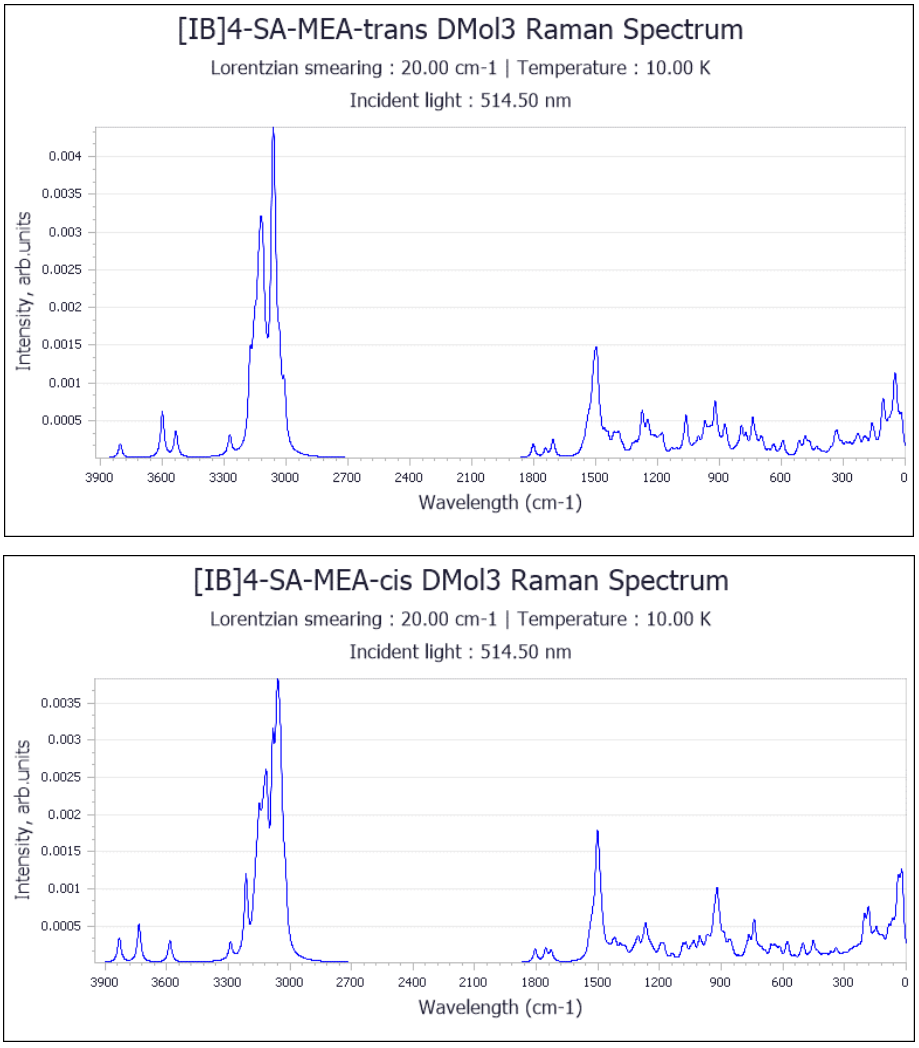

Figure A3-2: Calculated Raman spectrum for [IB]$_4$SA-MEA-trans and [IB]$_4$SA-MEA-cis conformations.

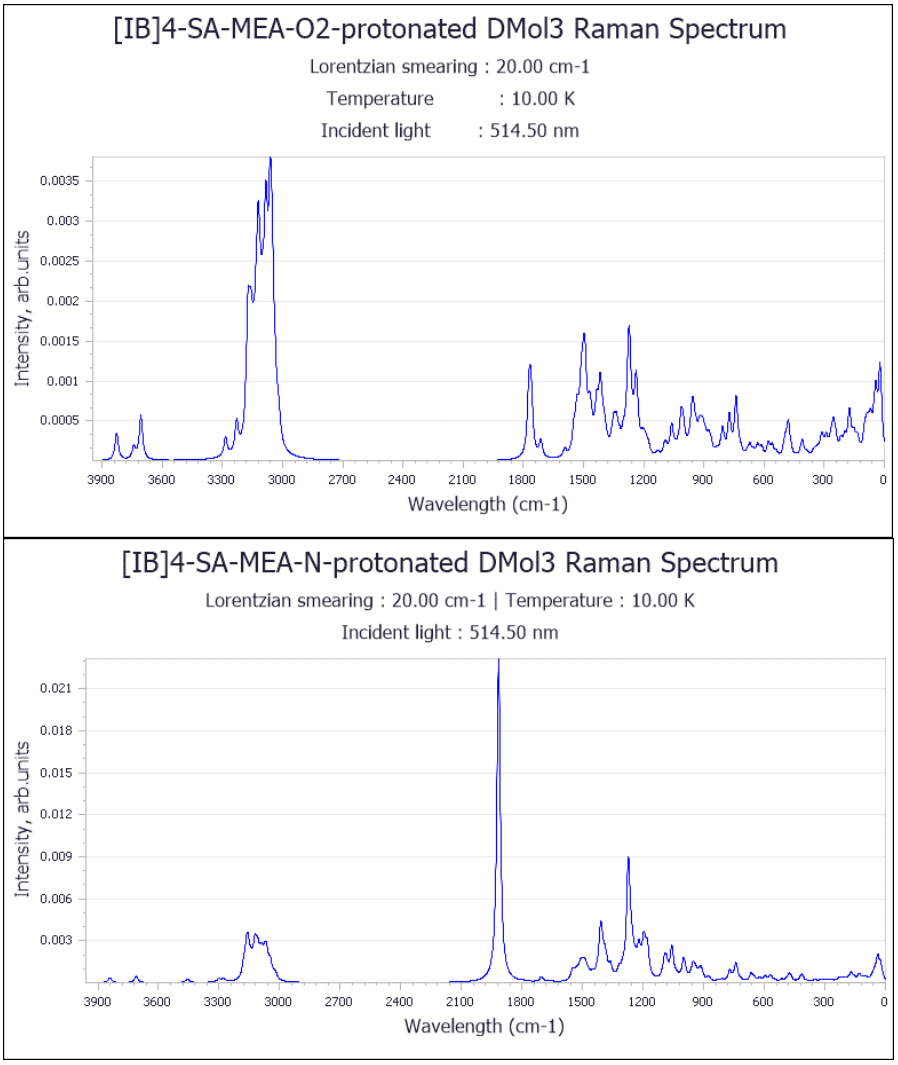

Figure A3-3: Calculated Raman Spectra for [IB]$_4$SA-MEA, [IB]$_4$SA-MEA$_{O2\text{-}protonated}$ and [IB]$_4$SA-UREA$_{N\text{-}protonated}$.

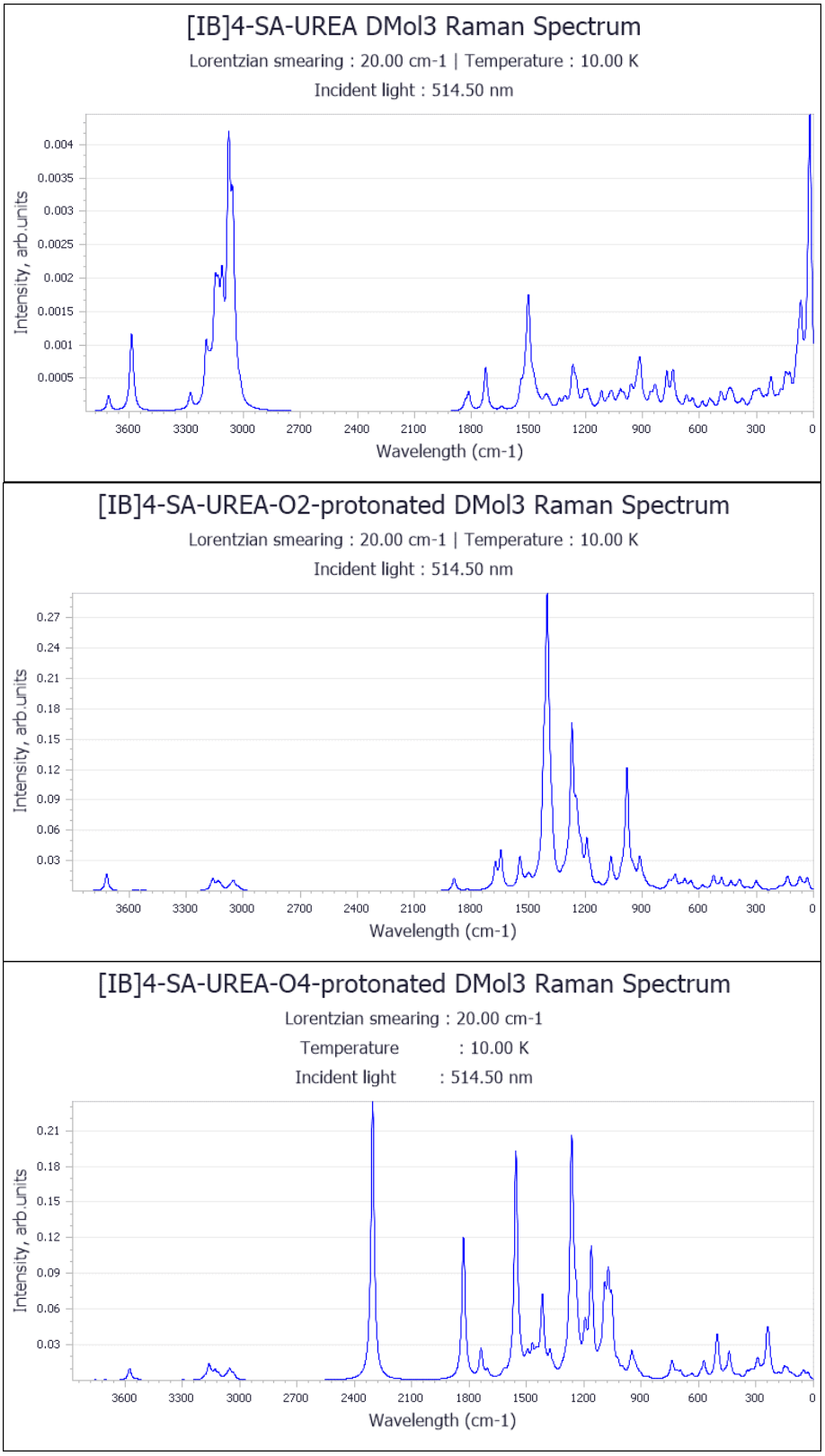

Figure A3-4: Calculated Raman spectra for [IB]$_4$SA-UREA, [IB]$_4$SA-UREA$_{O2\text{-protonated}}$ and [IB]$_4$SA-UREA$_{O4\text{-protonated}}$.

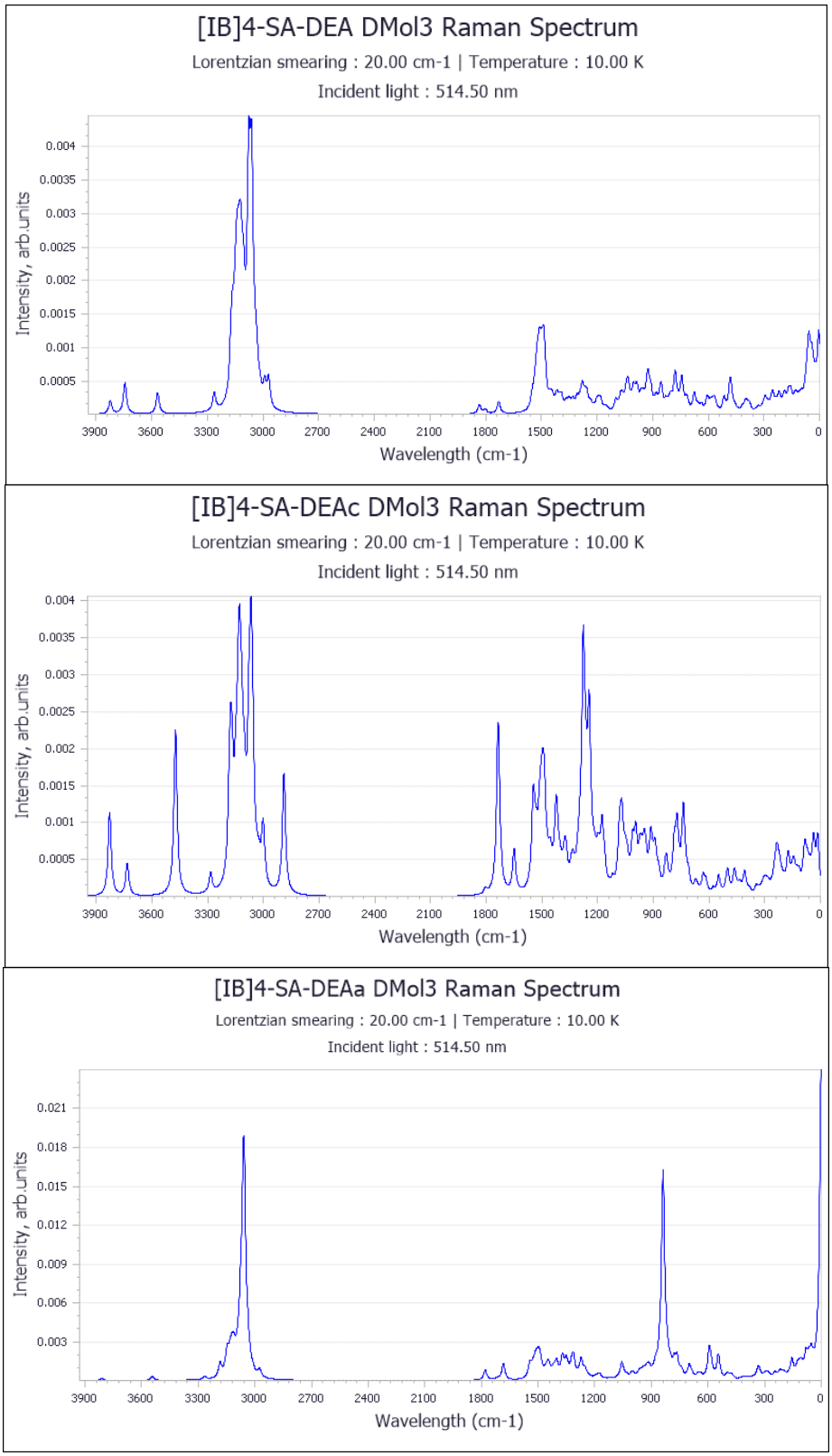

Figure A3-5: Calculated Raman spectra for [IB]$_4$SA-DEA, [IB]$_4$SA-DEAc and [IB]$_4$SA-DEAa.

Table A3-5: Experimental and calculated geometric parameters for II-AN and IV-AN

	***IV*- NH_4NO_3**				***II*-NH_4NO_3**			
	From exp. (Choi 1972)	***Calc. CASTEP*** [57]	***Calc. DMol³ (this work)***	***Calc. Compass II (this work)***	***From exp. (Lucas 1979)***	***Calc. CASTEP*** [57]	***Calc. DMol³ (this work)***	***Calc. Compass II (this work)***
Cell parameters								
a	5.745	5.8008	6.029	5.208	5.7193	5.7808	6.0641	5.179
b	5.438	5.4072	5.822	4.731	5.7193	5.7808	6.0641	5.179
C	4.942	5.0362	5.1843	4.283	4.9326	4.8355	5.1029	4.352
Vol, Å³	154.394	157.96	181.973	105.529	161.347	161.591	187.65	116.729
N1-H1	0.987	1.0352	1.0368	1.008	0.9880	1.0352	1.036	1.008
N1-H2	0.992	1.0296	1.0302	1.009	0.9880	-	-	-
N2-O1	1.226	1.2882	1.301	1.250	1.239	1.2366	1.283	1.253
N2-O2	1.222	1.2425	1.259	1.249	1.212	1.2652	1.250	1.251
Angles								
∠H1-N1-H1	115.7	111.4	110.976	109.8	109.47	109.5	109.527	109.75
∠H1-N1-H2	107.9	109.2	109.188	109.6			109.527	
∠H2-N1-H2	109.4	108.5	109.087	108.3			109.360	
∠O1-N2-O2	120.0	118.9	118.960	119.7	120.8	120.0	120.114	120.2
∠O2-N2-O2	120.0	122.1	122.079	120.7	118.4	119.9	119.771	120.2
Close contacts								
N1-H1---O1								
H1---O1	**2.050**	**2.057**	**2.168**	**1.71**	**2.658**	**2.705**	**2.634**	**2.084**
N1---O1	2.971	nr**	3.324	2.646	3.069	nr**	3.059	4.207
∠N1-H1---O1	154.4	1.519	150.50	141.41	105.2	102.9	104.716	125.380
N1-H2…O1								
H2---O1	2.161	2.107	2.303	1.71	-	-	-	-
N1---O1	3.147	-	3.324	3.786	-	-	-	-
∠ N-H---O	172.6	171.9	170.45	169.59	-	-	-	-
N1-H1…O2								
H1---O2	2.326	2.31	2.351	1.891	2.022***	1.880	1.957	1.554
N1---O2	3.200	nr**	3.145	2.788	2.982	nr**	2.987	2.445
∠ N1-H1---O2	147.0	148.7	151.259	146.5	163.3	169.5	170.17	143.99

*Experimental data for ND_4NO_3
**not reported
***From unit cell with replotted experimental coordinates

Table A3-6: Calculated habit faces with BFDH and Growth morphology methods with Dreiding FF for II-AN and IV-AN (in vacuum)

BFDH				Growth morphology			
hkl	**d_{hkl}**	**c2p distance, Å**	**Total facet area, %**	**d_{hkl}**	**c2p distance, Å**	**Total facet area, %**	**E_{att} (Total), kcal mol $^{-1}$**
IV-AN							
(0 0 1)	4.94	20.23	23.39	4.942	23.31	3.09	-23.31
(1 1 0)	3.95	25.32	44.67	-	-	-	-
(1 0 1)	3.75	26.69	17.04	3.75	24.18	24.84	-24.17
(0 1 1)	3.66	27.34	14.16	3.66	19.72	43.68	-19.72
(1 1 1)	-	-	-	3.08	29.31	2.217	-29.31
(2 0 0)	2.87	34.81	0.74	2.87	29.02	10.19	-29.02
(0 2 0)	-	-	-	2.72	23.63	11.36	-23.63
(2 1 0)	-	-	-	2.26	31.65	4.609	-31.65
Aspect ratio	***1.743***			***1.849***			
II-AN							
(0 0 1)	4.93	20.27	22.83	-	-	-	-
(1 1 0)	4.04	24.73	47.02	-	-	-	-
(1 0 1)			30.15	3.74	-22.02	56.48	-22.02
(1 1 1)	-	-	-	3.13	-26.36	5.60	-26.36
(1 1 -1)	-	-	-	3.13	-26.36	5.60	-26.36
(2 0 0)	-	-	-	2.85	-23.31	32.24	-23.31
Aspect ratio	***1.744***			***1.499***			

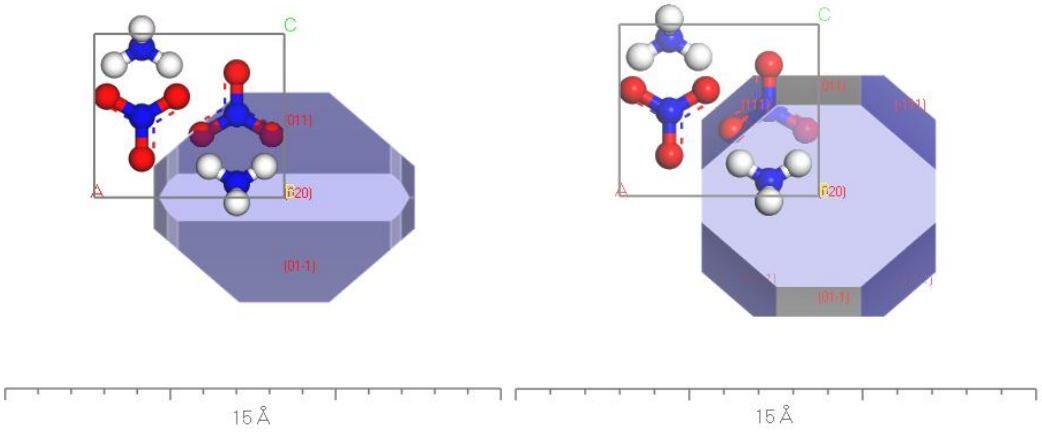

Figure A3-6: Growth morphology calculated crystal habit of IV-AN with Dreiding (left) and CompassII (right) force-fields.

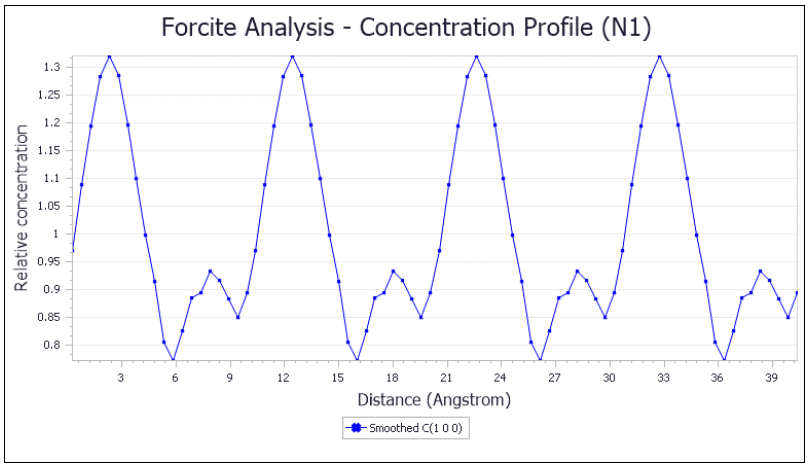

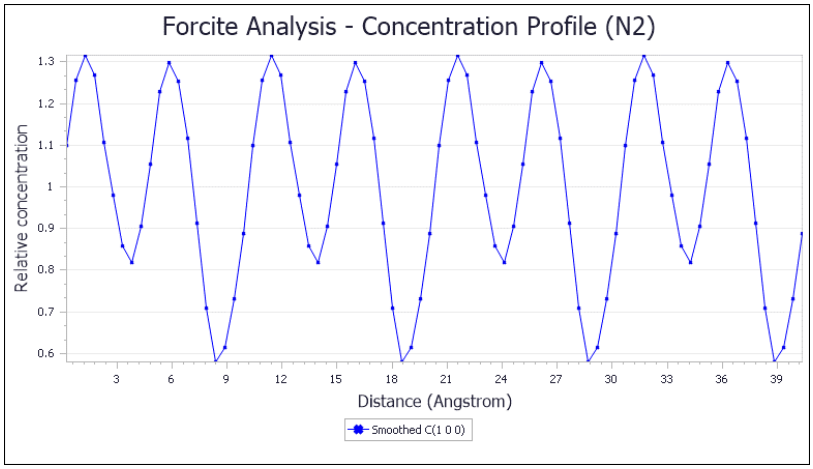

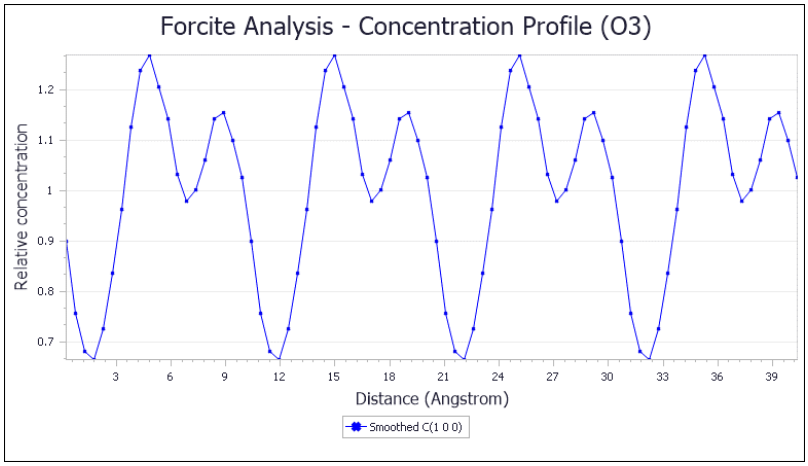

Figure A3-7: Concentration profiles for center atoms for CompassII aqueous ammonium nitrate (1:1:1) supercell (9x9x9SC).

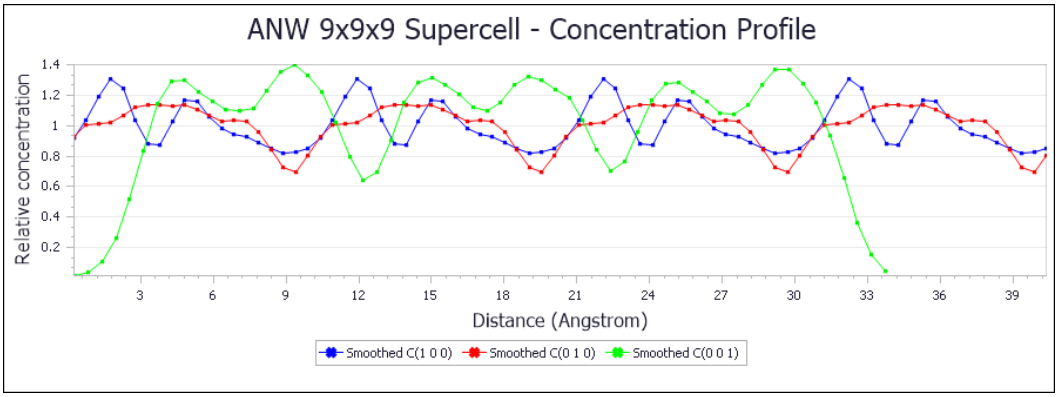

Figure A3-8: Concentration profile for CompassII aqueous ammonium nitrate (1:1:1) supercell (9x9x9SC).

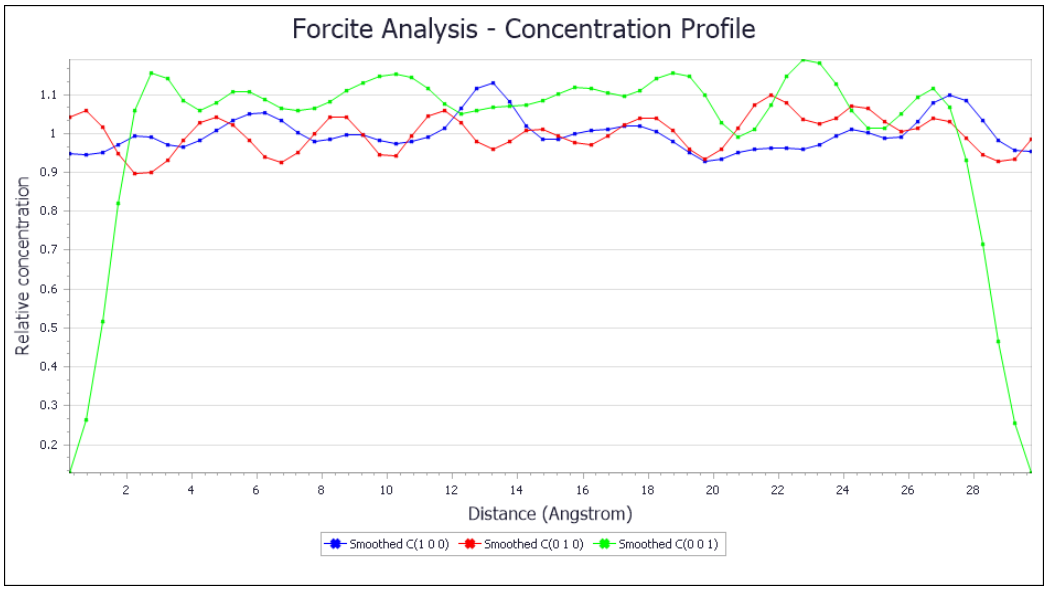

Figure A3-9. Concentration profile for CompassII water supercell (W900).

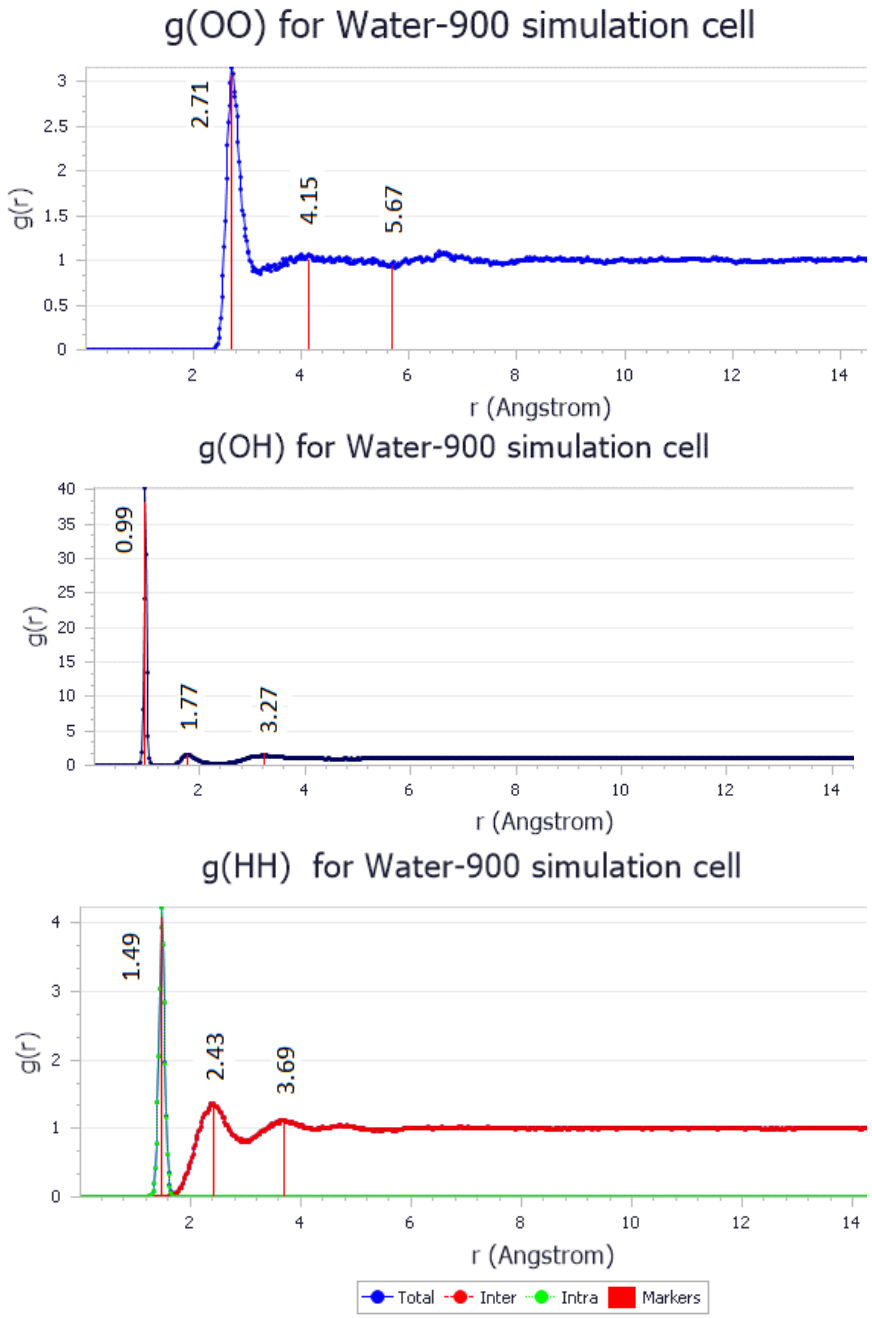

Figure A3-10: Calculated radial distribution functions for CompassII water simulation cell (W900).

*Table A3-7. Adsorption energies of PIB-based polymers to growth faces of II- and IV-*AN *in vacuum slab model*

	E_{ads} to (101), kcal mol^{-1}		**E_{ads} to (111), kcal mol^{-1}**		**E_{ads} to (200), kcal mol^{-1}**		**E_{ads} to (020), kcal mol^{-1}**	**E_{ads} to (011), kcal mol^{-1}**	**E_{ads} to (001), kcal mol^{-1}**
	ANII	***ANIV***	***ANII***	***ANIV***	***ANII***	***ANIV***	***ANIV***		
E_{att}, kcal mol^{-1}	**-56.86**	**-59.40**	**-53.10**	**-52.16**	**-41.15**	**-51.95**	**-30.07**	**-49.98**	**-53.45**
HR-PIB	-26.30	-15.29	-27.05	-26.26	-26.48	-26.92	-27.74	-28.26	-26.52
HR-PIBSA	-37.03	-55.86	-37.86	-51.03	-51.60	-46.55	-51.53	-50.99	-54.16
HR-PIBSucc	-44.79	-45.71	-54.13	-47.12	-44.62	-49.57	-44.77	-59.00	-64.74
PIBSA-MEAn	-58.71	-75.31	-69.53	-42.83	-59.55	-69.05	-37.66	-40.94	-41.26
PIBSA-$MEA_{N\text{-proton.}}$	-57.17	-78.43	-80.78	-84.39	-77.19	-56.52	-60.13	-59.14	-78.75
PIBSA-MEAa	-65.23	-85.21	-71.49	-72.69	-60.67	-59.92	-72.17	-77.80	-84.62
PIBSA-MEAz	-85.43	-87.81	-72.44	-71.03	-68.24	-85.56	-70.63	-83.22	-90.75
PIBSA-UREAn	-55.40	-68.56	-55.06	-79.31	-44.20	-62.19	-37.34	-75.60	-84.83
PIBSA-UREAc	-68.78	-68.06	-52.01	-74.04	-60.15	-62.24	-52.78	-57.98	-96.16
PIBSA-UREAa	-57.75	-75.67	-62.40	-53.89	-50.23	-47.10	-51.05	-78.44	-83.90
PIBSA-UREAz	-73.07	-82.08	-70.26	-70.78	-55.11	-57.18	-58.34	-81.69	-100.66
PIBSA-IMIDE	-50.90	-57.70	-51.92	-50.51	-49.21	-55.77	-49.55	-48.46	-50.90
PIBSA-DEEA	-52.64	-63.70	-45.52	-54.23	-34.97	-57.20	-47.49	-78.33	-67.50
PIBSA-DEAn	-68.20	-79.14	-51.79	-61.79	-48.63	-66.36	-55.44	-74.47	-58.50
PIBSA-DEAc	-52.54	-75.18	-49.07	-58.54	-46.82	-52.20	-47.46	-65.68	-40.51

*Table A3-8: Adsorption energies of truncated surfactants to growth faces of II- and IV-*AN *in vacuum slab model*

	E_{ads}, to (101), kcal mol^{-1}		**E_{ads} to (111) , kcal mol^{-1}**		**E_{ads} to (200), kcal mol^{-1}**		**E_{ads} to (020) , kcal mol^{-1}**	**E_{ads} to (011) , kcal mol^{-1}**	**E_{ads} to (001) kcal mol^{-1}**
	IIAN	IVAN	IIAN	IVAN	IIAN	IVAN	IVAN		
***Eatt,* kcal mol^{-1}**	**-56.86**	**-59.40**	**-53.10**	**-52.16**	**-41.15**	**-51.95**	**-30.07**	**-49.98**	**-53.45**
Dodecane*	-13.18	-13.49	-14.9	-11.47	-14.1	-13.26	-14.15	-14.69	-14.31
H_2O	-20.91	-18.97	-20.75	-20.32	-17.34	-17.66	-15.42	-21.88	-28.86
NH_4^+	-30.28	-23.18	-22.20	-27.46	-13.31	-12.00	-13.05	-40.67	-65.01
NO_3^-	-43.00	-46.32	-27.99	-32.07	-18.92	-18.89	-14.48	-42.53	-36.50
CH_3COOH	-24.11	-27.24	25.24	-24.81	-20.91	-20.42	-27.13	-24.15	-27.13
CH_3Succ-acid	-32.91	-36.20	-36.33	-37.13	-32.18	-28.02	-24.20	-24.25	-49.47
CH_3SA	-26.47	-27.28	-20.59	-21.53	-19.62	-18.67	-17.33	-24.25	-19.15
CH_3SA -MEAn	-40.46	-51.33	-34.51	-35.49	-32.67	-40.00	-23.19	-38.76	-42.22
CH_3SA -MEAa	-58.15	-62.65	-49.77	-51.36	-33.21	-37.45	-28.51	-55.59	-59.66
CH_3SA -UREAn	-50.69	-45.21	-44.55	-45.43	-36.05	-32.52	-27.72	-38.34	-62.02
CH_3SA -UREAa	-41.88	-52.28	-42.86	-49.01	-32.91	-31.76	-32.13	-52.93	-66.58
CH_3SA -IMIDE	-21.55	-38.81	-35.14	-26.39	-27.85	-25.37	-21.27	-30.74	-38.85
CH_3SA –DEEA	-35.65	-37.61	-39.20	-33.65	-21.41	-30.10	-25.34	-38.29	-25.16
CH_3SA –DEAn	-41.57	-39.75	-32.68	-34.80	-33.22	-32.87	-25.92	-37.27	-57.81
CH_3SA –DEAc	-36.41	-45.23	-38.66	-36.09	-25.80	-34.15	-37.38	-44.82	-39.69
CH_3SA –bisMEAn	-43.19	-47.54	-44.54	-36.81	-35.87	-35.64	-28.39	-35.97	-41.89
CH_3SA –bisMEAc	-50.35	-45.34	-53.86	-55.15	-32.61	-36.22	-29.87	-61.71	-42.90
CH_3SA –bisMEA2c	-80.46	-49.42	-47.16	-88.56	-57.02	-38.72	-35.24	-96.06	-51.10

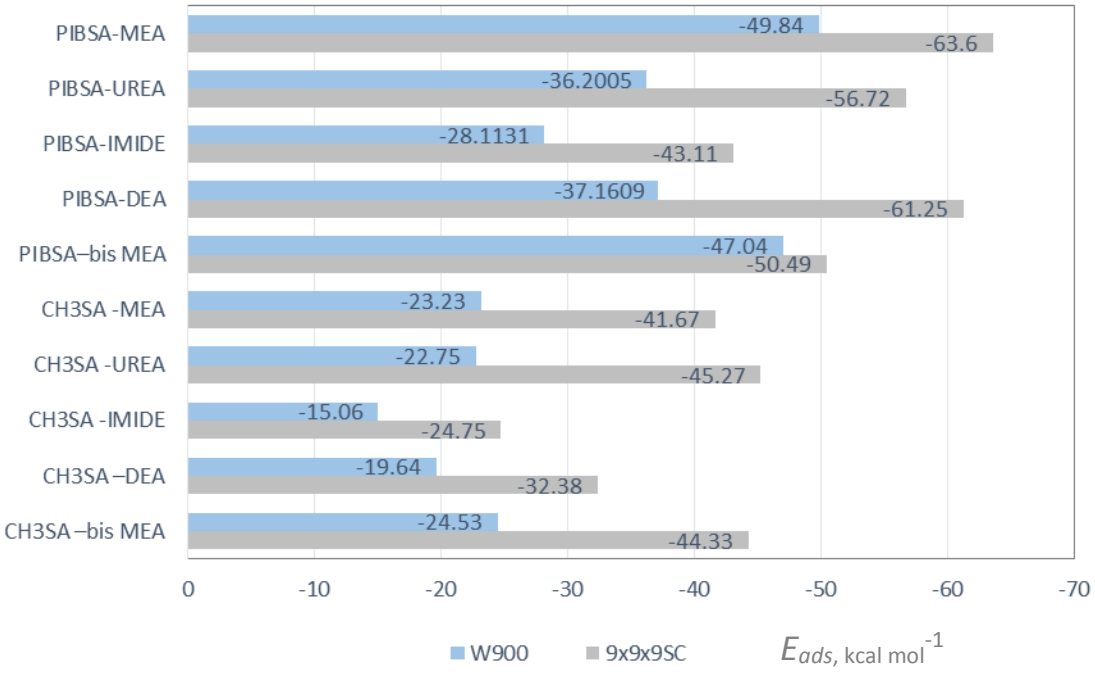

Figure A3-11: Plot of Eads for neutral forms of polymeric and truncated surfactants to amorphous surfaces (W900 and 9x9x9SC).